UNIVERSITY OF SOUTHAMPTON

Observational constraints on the progenitors of Type Ia Supernovae

by

Georgios Dimitriadis

A thesis submitted in partial fulfillment for the degree of Doctor of Philosophy

in the

Faculty of Physical Sciences and Engineering

Department of Physics and Astronomy

December 2017

UNIVERSITY OF SOUTHAMPTON

Abstract

Faculty of Physical Sciences and Engineering
Department of Physics and Astronomy

Doctor of Philosophy

Observational constraints on the progenitors of Type Ia Supernovae

by Georgios Dimitriadis

This thesis investigates observational signatures and provides constraints on the progenitors of Type Ia Supernovae (SNe Ia), one of the most powerful cosmological probes, with a profound impact on understanding the evolution of the universe. By exploiting rich observational datasets, from powerful transient surveys, and extensively analysing them, we provide an insight into the long-standing progenitor problem.

At first, we investigate the late-time evolution of the SN Ia light curve. Using the Palomar Transient Factory (PTF) observations of SN 2011fe, added with external literature data, we achieve an unprecedented photometric coverage of the late-time light curve of a SN Ia, spanning from 200 to 1600 days after maximum, with remarkable temporal density. A combination of photometry and spectroscopy at these phases allows us to construct a pseudo-bolometric light curve and physical models that describe the behaviour of it are considered. Our main results are the explanation of the bolometric light curve by radioactive inputs of the ^{56}Ni and ^{57}Ni decay chains, with the estimated amount of ^{57}Ni to be relatively large, indicating a high central density explosion environment. Moreover, our pseudo-bolometric light curve is not consistent with models that have complete trapping of the produced charged leptons, with models that allow for positron/electron escape or an infrared catastrophe (IRC) adequately describing the evolution. Finally, we studied a sample of 49 PTF SN Ia with late-time photometric coverage, finding no significant deviation on their light curve evolution compared to SN 2011fe, and provide an upper limit on the hydrogen rich material at the site of the explosion to be $\leq$0.87 $M_\odot$.

For the last part, we turn our focus to the spectroscopic class of 91T-like overluminous SNe Ia, by studying two members of this class: SN 2014eg and SN 2016hvl, for which we present their rich data set and provide physical parameters that describe them. Our results show that the highly reddened SN 2014eg is a slightly less luminous 91T-like, with a ^{56}Ni mass of 0.573 $M_\odot$, with indications of circumstellar material (CSM) at the site of the explosion, while SN 2016hvl is a 91T-like with 0.767 $M_\odot$ mass of ^{56}Ni. Finally, we study the host galaxies of the PTF 91T-like SNe Ia, and we find that they preferentially explode in active galaxies, with moderate to high star formation rates and a range in their stellar masses.

αυτό είναι ένα αστέρι

είπε ο δάσκαλος

όχι

είναι μια έκρηξη

είπε ο μαθητής

Thessaloniki,

somewhere on a wall, close to the university

*crude translation: this is a star, said the teacher. No, it's an explosion, said the student

Contents

List of Figures

List of Tables

Abbreviations

ADU	**A**nalog-**D**igital **U**nits
ATEL	**A**stronomer's **TEL**egram
BFN	**B**ox **F**itler **N**arrow
BFW	**B**ox **F**itler **W**ide
BPS	**B**inary **P**opulation **S**ynthesis
C/O WD	**C**arbon/**O**xygen **W**hite **D**warf
CCD	**C**harged **C**oupled **D**evice
CSM	**C**ircum**S**tellar **M**edium
DD	**D**ouble **D**egenerate
Dec.	**Dec**lination
DIB	**D**iffuse **I**nterstellar **B**and
DLR	**D**irectional **L**ight **R**adius
DOF	**D**egrees **O**f **F**reedom
DTD	**D**elay **T**ime **D**istribution
ESO	**E**uropean **S**outhern **O**bservatory
FWHM	**F**ull **W**idth at **H**alf **M**aximum
FOV	**F**ield **O**f **V**iew
HVG	**H**igh **V**elocity **G**radient
IGM	**I**nter**G**alactic **M**edium
IME	**I**ntermediate **M**ass **E**lement
IPE	**I**ron **P**eak **E**lement
IR	**I**nfra**R**ed
IRC	**I**nfra**R**ed **C**atastrophe
ISM	**I**nter**S**tellar **M**edium
JD	**J**ulian **D**ay

LCO	**L**as **C**umbres **O**bservatory
LCOGT	**L**as **C**umbres **O**bservatory **G**lobal **T**elescope
LVG	**L**ow **V**elocity **G**radient
MJD	**M**odified **J**ulian **D**ay
MW	**M**ilky **W**ay
NIR	**N**ear **I**nfra**R**ed
NSE	**N**uclear **S**tatistical **E**quilibrium
NTT	**N**ew **T**echnology **T**elescope
PESSTO	**P**ublic **E**SO **S**pectroscopic **S**urvey for **T**ransient **O**bjects
pEW	**p**seudo**E**quivalent **W**idth
PSF	**P**oint **S**pread **F**unction
PTF	**P**alomar **T**ransient **F**actory
R.A.	**R**ight **A**scension
S/N	**S**ignal to **N**oise
SD	**S**ingle **D**egenerate
SED	**S**pectral **E**nergy **D**istribution
SFH	**S**tar **F**ormation **H**istory
SFR	**S**tar **F**ormation **R**ate
SN(e)	**S**uper**N**ova**e**
SN(e) Ia	Type **Ia** **S**uper**N**ova**e**
sSFR	**s**pecific **S**tar **F**ormation **R**ate
UT	**U**niversal **T**ime
UV	**U**ltra**V**iolet
WLR	**W**idth **L**uminocity **R**elationship

Declaration of Authorship

I, GEORGIOS DIMITRIADIS, declare that this thesis titled, 'OBSERVATIONAL CONSTRAINTS ON THE PROGENITORS OF TYPE IA SUPERNOVAE' and the work presented in it are my own. I confirm that:

- This work was done wholly or mainly while in candidature for a research degree at this University.
- Where any part of this thesis has previously been submitted for a degree or any other qualification at this University or any other institution, this has been clearly stated.
- Where I have consulted the published work of others, this is always clearly attributed.
- Where I have quoted from the work of others, the source is always given. With the exception of such quotations, this thesis is entirely my own work.
- I have acknowledged all main sources of help.
- Where the thesis is based on work done by myself jointly with others, I have made clear exactly what was done by others and what I have contributed myself.

Signed:

Date:

Acknowledgements

The careful reader of this manuscript may spend time on deciphering the dense context, complex equations and colourful plots, without realising the feelings hidden behind them. I will attempt to pay tribute to the amazing people responsible for these feelings, struggling to keep it short, but allowing for proper recognition.

First and foremost, I am deeply grateful to my supervisor, Mark Sullivan, for giving me the opportunity, the support and the guidance that a PhD student needs. By now, you are not just a teacher of astrophysics for me, but a mentor on how science should be done. It's been a privilege to be your student.

I would like to extend my gratitude to Dr. Jacco Vink and Dr. Charalambos Moustakidis, for their opportunities in the past that led me to where I am now. Special thanks to Alekos, for laying the groundwork.

To the Southampton Supernova Group. I learned so much from you, and had wonderful moments, I wouldn't change a thing. Szymon, Miika, Cosimo, Chris, Charlotte, Claudia and Mike, thank you for the amazing 4 years. Special thanks to Regis; your passion for astronomy and your dedication to the subtlest details on research is an inspiration. Also, I made the John Gardner Pass mate, you should be proud!

To Mat. I cannot simply describe my gratitude to you. You showed me the way to do it, I will try to follow it. If I become half a scientist and person you are, I will have succeeded in life.

During my PhD, I have been fortunate to visit Chile and see from up close the beauties of this incredible country. I am grateful to PESSTO for giving me this chance. What I will remember most, is the time I spent there with two of my closest colleagues and, by now, true friends. Rob, you were the first person I met in Southampton, I have been at your stag and your wedding, I climbed a mountain with you, I played perudo with you. Thanks for being there. Chris, we started this together, we traveled the world together, we wrote our first papers together, we wrote our thesis together, we will graduate together. You made my time here special.

To all my Southampton friends. James (for the music, the talks and the palafico), Aarran (you know why mate), Sam (for only spilling my beer 3 times), Andy (for being the most reliable pub mate) and Fred (theoretical physicist by name, astronomer at heart), you are a huge part of the best 4 years of my life. Joe, I hope I put your scoring skills at test (and a small tip for the next time: I always fall on my right side). I am proud to call you my friends. Special thanks to Boon, Juan, Stew, Alex, Sadie, Sam, Becca,

Dave, Pete, John, Noel, and Vicky, for making a pleasure to come into work everyday, especially the Fridays. Juri, Miguel and Simone, you were the best housemates I could have, thanks for making the PIG parties legendary. Thanks for all the memories, I hope we make many more of them in the future.

To all my friends back in Greece; Babis, Sakis, Maria, Thanasis, Christina, Danai, Natalia, Folias, Charis, Natassa ('latreia'), Nikoleta and so many others, you mean the world to me. Special thanks to three of them: Koutounidi, your attitude towards life and our late night talks with a lot of tsipouro influenced me the most. Vasili and Artemi, thanks for letting me crash at your place, and for all the memories the last 15 years. I am indebted to you all.

Petro, Garo, Gianni, Natassa and Doukissa, thanks for making me feel that I have never left. I will hold in my mind the summer nights at 'avlitsa' with much love.

In the last 6 years that I have been away from home, I came to realise the importance of family in a person's life, something that I, somehow, forgot or took it for granted. With this in mind, I would like to thank my grandparents, for raising me up and being so gentle and caring. Papou, thanks for making me realise what I want to be in my life. To my brother; you are the most stable thing in my life, an unbreakable bond that only two brothers can understand. Thank you for everything. To my mother; I was never good at words, you know that. I love you more than anything in the world, thank you for being strong for us all this time.

Finally, the most difficult part to write. This thesis is dedicated to the only person that will not be able to read it. The person that was most proud of what I chose to do, observe explosions in the sky. The explosion in my sky, my father. We did it Dad.

For my Father.

Chapter 1

Introduction

Type Ia supernovae (SNe Ia) have assumed a major role in cosmology as standardisable candles over the last 25 years and continue to attract considerable interest as astrophysical phenomena in their own right. Although decades of intensive study have led to significant breakthroughs in our understanding of these systems, many questions remain unanswered. Perhaps the most important is the underlying physical mechanism that leads to the explosion, including the configuration of the progenitor system. There is a general theoretical and observational consensus that SNe Ia are caused by the explosive thermonuclear burning of the degenerate material of a carbon-oxygen white dwarf star (WD) in a binary system, with the light curve primarily sustained by the radioactive decay of ^{56}Ni synthesised in the explosion. The nature of the companion star to the white dwarf, however, remains uncertain.

While the majority of SNe Ia constitute a rather homogeneous class, with small variations on light curve parameters, such as the maximum luminosity and its decline rate, a considerable variety of peculiar objects have been discovered, challenging our understanding of the phenomenon. These 'non-normal' events show the characteristic nucleosynthetic output of a thermonuclear explosion, but with distinct, primarily spectroscopic, behaviour. The simplest explanation of the nature of these objects is that they originate from different progenitor systems and/or explosion mechanisms than their 'normal' relatives.

In the modern era of astronomy, high quality and quantity observational data provide an invaluable tool for extracting information towards understanding the underlying physics of these mysterious objects.

1.1 The Supernovae Family

Supernovae (SNe) are the manifestation of the catastrophic endpoint of stellar evolution. These cataclysmic explosions can outshine their host galaxy light several times, and be visible several months after their peak brightness. While the clear distinction between novae and supernovae became obvious early after their discovery (Baade & Zwicky, 1934), targeted spectral and photometric observations were able to reveal the presence of several classes, with different physical origins and diverse evolution of the phenomenon. In Fig. 1.1, we show a simplified classification scheme, adapted from Turatto (2003), with their observed fractions, estimated from the Lick Observatory Supernova Search (LOSS; Li et al., 2011a), shown in Fig. 1.2.

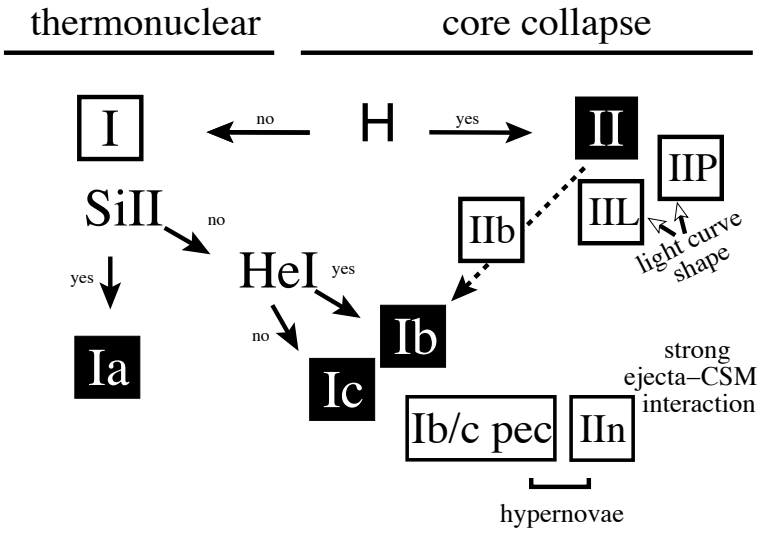

FIGURE 1.1: Simplified classification scheme of Supernovae classes (Fig. 1 from Turatto 2003).

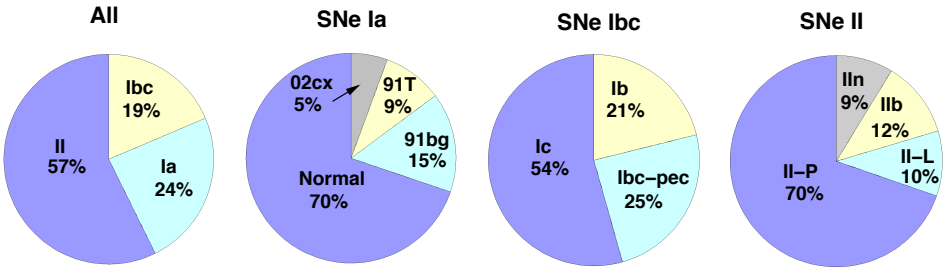

FIGURE 1.2: The observed fractions of the subclasses of SNe in a volume-limited sample (Fig. 9 from Li et al. 2011a).

SNe have historically been divided into two broad categories: Type I, for which no hydrogen emission is observed, and Type II, where a strong P-Cygni hydrogen profile dominates the spectrum. Furthermore, within the Type I class, several subclasses

have been defined. The presence of blueshifted silicon absorption, particularly Si II λ6347,6371, often referred to as the 6150Å feature, and other elements such as Ca, Mg and S, are the defining spectral characteristics of the Type Ia Supernova (SN Ia).

Since the early '90s, the improvement of observational capabilities, mainly because of the introductions of cameras equipped with charge coupled devices (CCDs), the technological developments in image subtraction techniques and the employment of dedicated synoptic SN surveys, have revealed a plethora of transient classes within the SN family. In the next section, we will focus on the SN Ia class of events and its diverse sub-family.

1.2 Type Ia Supernovae and their observational characteristics

SNe Ia define a unique class of transients, with unique observational characteristics. Firstly, they show a remarkable uniformity in their spectroscopic and photometric characteristics: the absence of hydrogen and the presence of a deep absorption feature at 6150Å , attributed to blue-shifted Si II are the defining spectral characteristics. The spectral evolution reveals a stratification of the ejected explosion ashes, from possible unburned carbon and oxygen at the surface to intermediate mass elements (IMEs) and, finally, iron peak elements (IPEs) close to the centre. The peak luminosity of the explosion is noticeably uniform and, finally, SNe Ia occur in both early- and late-type galaxies, in contrast with the core-collapse ones: this means that the progenitor of the explosion is an old stellar object. All of the above observational characteristics can be attributed to the thermonuclear explosion paradigm: a thermonuclear runaway that unbinds a degenerate carbon/oxygen white dwarf (C/O WD), close to the Chandrasekhar mass limit (Hoyle & Fowler, 1960; Wheeler & Hansen, 1971). Nevertheless, minor variations have been observed, challenging our understanding of the nature of the phenomenon. For an extensive review of the SNe Ia diversity, we refer to Taubenberger (2017).

In Fig. 1.3, we present the distribution of the SN Ia transients and their sub-classes, in the peak luminosity – decline rate space (Taubenberger, 2017). The majority of SNe Ia form a homogeneous class of objects, which we refer as 'normal' SNe Ia, shown in grey crosses. Their behaviour in this phase space is remarkable, with only minor small variations: the intrinsically brighter events have broader light curves (faster decline rates) and vice-versa. This astonishing feature, first observed by Phillips (1993), is the 'width–luminosity relation' (WLR), initially formulated with a handful of events, but subsequently confirmed with hundreds of other SNe (Hicken et al., 2009; Folatelli et al., 2010). This behaviour allows for the standardisation of their luminosity and their

use as distance indicators, and resulted in an outstanding discovery that changed our understanding of the cosmos: the accelerating universe and the Dark Energy (Perlmutter et al., 1998; Riess et al., 1998).

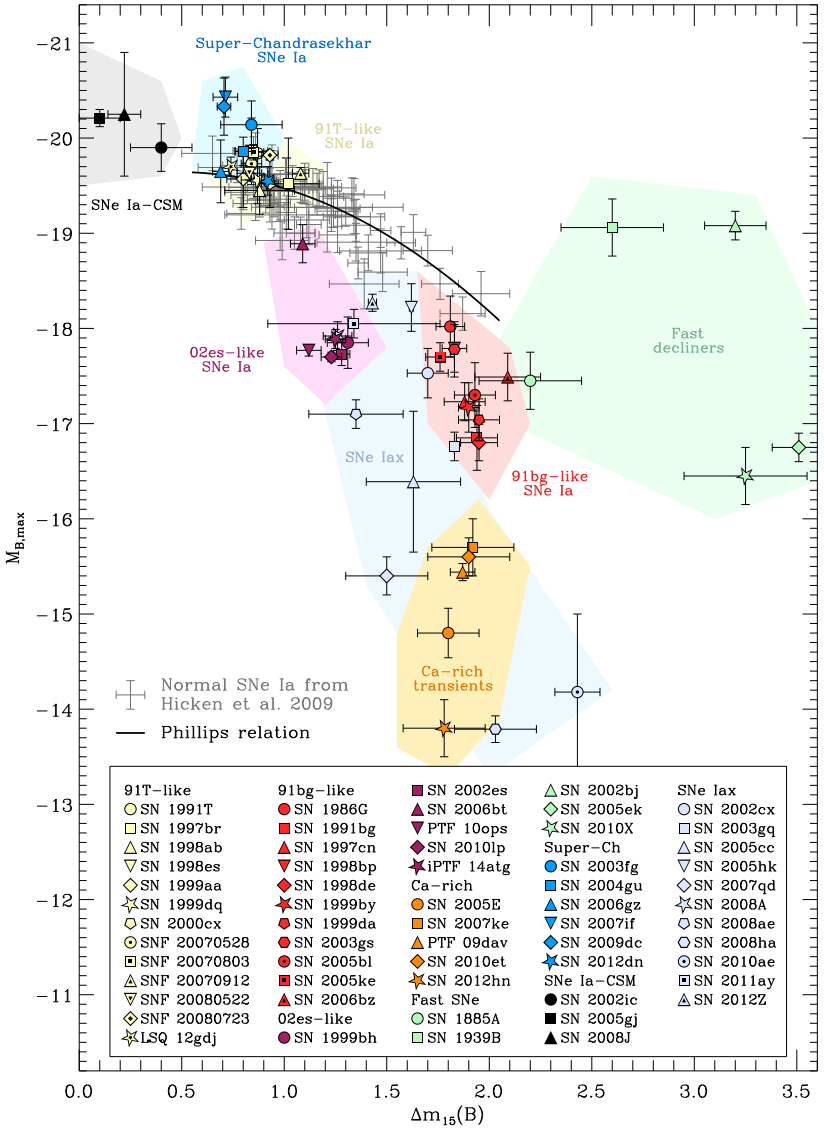

FIGURE 1.3: Absolute peak magnitude vs decline rate ($\Delta m_{15}(B)$, the decline within 15 days from peak in B-band) of various transient events of thermonuclear origin (Fig. 1 from Taubenberger 2017).

Next to this well-defined family of 'normal' SNe Ia, a variety of other transients exist. These events either do not follow the WLR or show peculiar spectroscopic behaviour. The 'traditional' two peculiar classes, that represent the extremes of the WLR, have been named by the two prototypical events of their class: SN 1991bg (Filippenko et al., 1992a), a subluminous and fast-declining SN Ia and SN 1991T (Filippenko et al., 1992b), a bright and slow-declining one. In recent years, other distinct classes of events have emerged, which, among others, include the '02es-like' peculiar subluminous transients

(Ganeshalingam et al., 2012), the faint calcium-rich explosions (Perets et al., 2010), the 'Super-Chandrasekhar' SNe Ia (Hicken et al., 2007), the peculiar SNe Iax (Foley et al., 2013) and the 'interacting' SN Ia–CSM (Silverman et al., 2013a).

While all of the 'normal' SNe Ia and their peculiar sub-classes have a thermonuclear origin, it is evident that their varied photometric and spectroscopic behaviour is due to different physical processes, explosion mechanisms and progenitor scenarios. In the next section, we will start from the basics, reviewing the physics that drives the evolution of the phenomenon.

1.3 The Physics of Type Ia Supernovae

In the following section, we will introduce the physical processes involved in explosive fusion, the nucleosynthetic yields obtained under various explosion mechanisms, and describe how these shape the two main observables of SNe Ia, the light curve and the spectrum.

1.3.1 Explosive Nucleosynthesis

As it was already mentioned in section 1.2 and outlined in the review of SNe Ia nucleosynthesis by Seitenzahl & Townsley (2017), the basic model for SNe Ia remains established, with the realisation that if a near-Chandrasekhar mass CO WD is incinerated, the resulting ejecta structure produces a transient that is spectroscopically similar to a SN Ia (Nomoto et al., 1984). However, exactly how the incineration is initiated and propagated is still unclear. Nevertheless, the nucleosynthetic output of such processes and the observed synthesized ejecta are well defined and can broadly be described in Fig. 1.4, where the products of burning depend on the local fuel density: high densities lead to more complete processing to IPEs in nuclear statistical equilibrium (NSE), while lower densities limit the nuclear processing to Si-group IMEs.

These two distinctions are closely related to the mode of the propagation of the thermonuclear burning front. Solutions to the hydrodynamical equations allow for this combustion wave to propagate either as a subsonic deflagration wave (where the flame propagates microscopically by heat conduction and turbulence) or as a supersonic detonation wave (where the flame is driven by a shock wave). In Fig. 1.4, a M_{Ch} WD burned by a detonation, with no opportunity to expand (solid green), will produce nearly all IPEs, while a lower mass star will produce only about 0.6 $M_{\odot}$ of IPEs, with the balance being mostly IMEs (dashed orange).

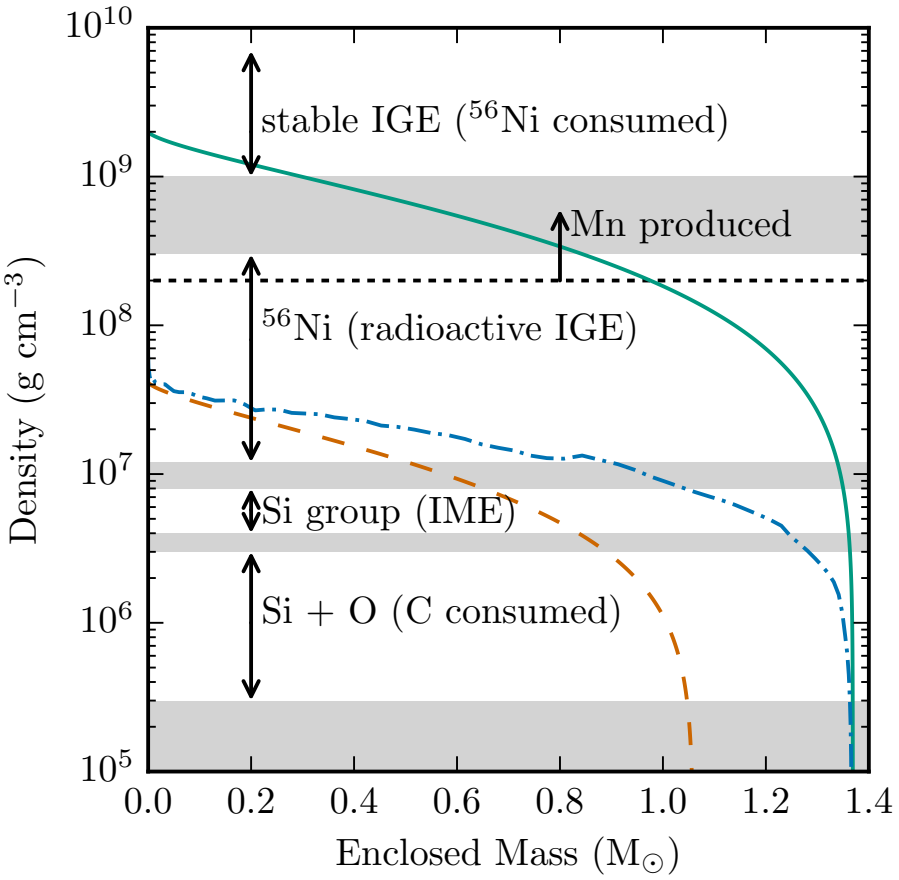

FIGURE 1.4: Density structures of various CO WD models as a function of its mass (Fig. 1 from Seitenzahl & Townsley 2017). Different profiles of WDs shown include a WD close to the Chandrasekhar mass (solid green), a 1.05 $M_\odot$ WD (dashed orange), and a delayed detonation profile (dot-dashed blue).

One of the most well-studied and promising explosion model requires a deflagration-to-detonation, known as 'delayed detonation' (Khokhlov, 1991). In this approach, a transition occurs from deflagration to the (explosive) detonation, which sufficiently explains the ejecta stratification. A model like this is shown, in Fig. 1.4, in dot-dashed blue, producing similar yields to the low-mass incineration, favouring more IMEs. IF no transition occurs, the resulting SN Ia would be subluminous (describing sufficiently peculiar SN Ia subclasses, such as the Iax, Magee et al., 2016) while a prompt detonation results in extremely efficient burning, with the ejecta consisting almost exclusively of IPEs.

The local fuel density also determines the production of stable IPEs, such as ^{54}Fe and ^{58}Ni. As seen in Fig. 1.4, these yields are only produce in densities higher than 10^8g cm^{-3}, associated mainly with CO WDs above about 1.2 $M_\odot$, which can only be formed by accretion. These neutron-rich elements are synthesised in high densities due to conversion

of protons to neutrons by electron captures. Other neutron-rich elements that may be produced in these conditions are the radioactive ^{57}Ni and ^{55}Co (decaying to ^{57}Fe and ^{55}Mn, respectively). Moreover, neutron enrichment also decreases the amount of radioactive ^{56}Ni available to power the observed bright transient.

Vigorous theoretical work is currently performed on the explosion and the consecutive nucleosynthesis of various thermonuclear explosion models. At the same time, accurate observations of neutron-enriched and non-enriched isotopes in the solar distribution and comparison of them with the theoretical yields of the explosion models is a ongoing topic of study.

1.3.2 Photometric evolution

In Fig. 1.5, we show the photometric evolution of a typical SN Ia, SN 2005cf (Wang et al., 2009a). Observations are presented in five optical photometric bands, spanning from ~3500 to 8000 Å (UBVRI). The evolution of transient phenomena is usually presented in the rest–frame 'phase', τ, measured in days, where $\tau = 0$ is the B-band maximum.

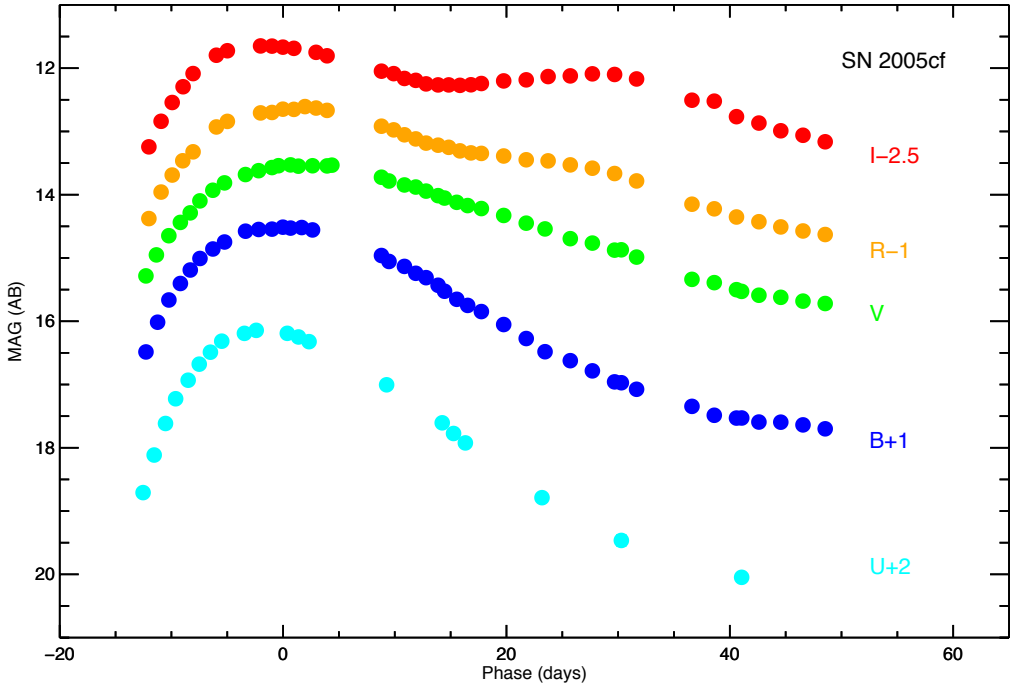

FIGURE 1.5: Multi-band light curve of SN 2005cf, a typical SN Ia. The apparent magnitudes of U (cyan), B (blue), V (green), R (orange) and I (red) are shifted according to offsets marked on the plot.

SNe Ia typically rise from their first light to peak brightness over a period of ~19 days (Firth et al., 2015). The decline rate varies, both in terms of its absolute peak brightness

(see section 1.2) and as a function of wavelength. While the 'blue' optical light curves (UBV) decline uniformly during the first two weeks from maximum, the redder bands (RI) show a distinct plateau, that lasts ~ 10-15 days, which varies in strength from SN to SN. After ~40 days from peak, the light curve declines linearly (in magnitude space).

The power source that drives the evolution of the light curve is the radioactive decay of iron peak elements (IPEs), that are synthesised during the explosion of the C/O WD. During the first few hundred days, the principle contributor is ^{56}Ni, which radioactively decays to ^{56}Co and, later, ^{56}Fe:

$$^{56}\mathrm{Ni} \xrightarrow{t_{1/2}=6.08\,\mathrm{d}} {}^{56}\mathrm{Co} \xrightarrow{t_{1/2}=77.2\,\mathrm{d}} {}^{56}\mathrm{Fe} \tag{1.1}$$

(Arnett, 1982; Pinto & Eastman, 2000a). Recent studies, using the European Space Agency satellite INTEGRAL (Winkler et al., 2003) have confirmed the presence of this decay chain in SN 2014J (Fossey et al., 2014), by detecting ^{56}Ni (Diehl et al., 2014) and ^{56}Co (Churazov et al., 2014) lines, with properties in agreement with the canonical thermonuclear explosion model.

The amount of ^{56}Ni (which is the most abundant synthesised radioactive nuclide) is, at least for the 'normal' SN Ia, the parameter that drives the WLR (however, see Scalzo et al. 2014a for the influence of the total ejecta mass and Kasen & Woosley 2007 for the effect of the spectroscopic and colour evolution). Most of the energetic output of the decay is in the form of γ-rays, that heat the expanding ejecta, creating optical and near-infrared (NIR) photons. The escape of the first photons from the ejecta initiates the rise of the light curve, and, as the ejecta expand, more photons produced deeper in the ejecta escape. The homologous expansion makes the ejecta less opaque with time, increasing the amount of escaped energy and the light curve reaches its maximum when the energy that is radiated is equal to the energy deposited by the decay. This peak bolometric luminosity is related to the total amount of synthesised ^{56}Ni, known as Arnett's Rule (Arnett, 1979, 1982). The width of the light curve is primarily driven by the photon diffusion time (Pinto & Eastman, 2000b), which is related, to the first order, with the total ejecta mass: larger amounts of ejecta force the photons to spend longer time in them, increasing the diffusion time and 'stretching' the light curve.

As the ejecta continue to expand, they become transparent to the high-energy γ-rays, which increasingly escape thermalisation. The light curve declines faster than that expected from the radioactive decay, up to the point when the contribution of lower-energy products of decay, such as positrons, become dominant. Then, the light curve declines exponentially (in flux space), broadly matching the decay of ^{56}Co. At even later

times, other longer-lived decay chains may also contribute, a topic discussed in detail in Chapter 3.

In this context, the explanation for the peculiar photometric behaviour of the 'classical' extremes of the WLR is rather straightforward (see also Scalzo et al., 2014b): higher amounts of synthesised ^{56}Ni and ejecta mass cause the light curve to be brighter and broader (91T-likes) while the opposite results in fainter and faster explosions (91bg-likes). The existence of 'transitional' objects in both of these classes, such as SN 1999aa (Krisciunas et al., 2000), a slightly fainter 91T-like, and SN 1986G (Phillips et al., 1987), an intermediate 'normal'–91bg-like event, exemplifies this argument. The extent to which this may apply to the other peculiar thermonuclear transients is still under debate, but different configurations of progenitor systems and explosion mechanisms are the most probable answer.

1.3.3 Spectroscopic evolution

A collection of typical SNe Ia spectra at maximum light is presented in Fig. 1.6. The spectra presented are template spectra of a 'normal' SN Ia (Hsiao et al., 2007), and the two 'classical' extremes: a 91T-like (blue) and a 91bg-like (red) from Nugent et al. (2002), with distinctive spectral features labelled on the plot.

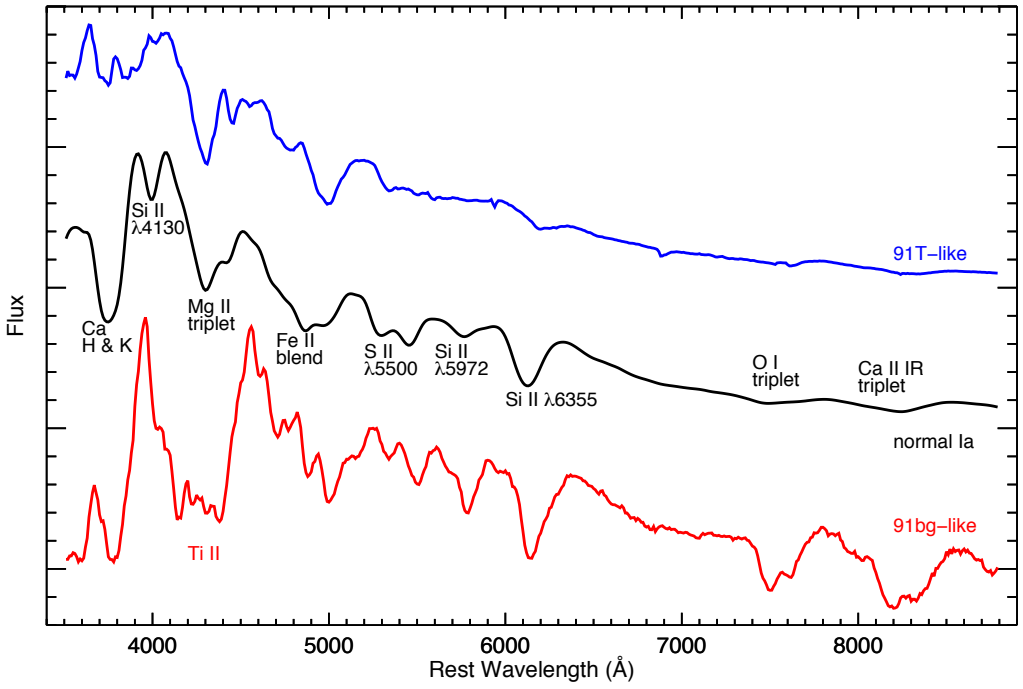

FIGURE 1.6: Rest frame spectra of a 'normal' (black), a 91T-like (blue) and a 91bg-like (red) SN Ia, at maximum light. We mark distinctive absorption features on the plot.

SN Ia spectra detail important information about the explosion and the stratification of the elements synthesised. At the early phases, the main spectral features are due to iron peak elements (IPEs), such as Fe II and Co II, and a range of intermediate mass elements (IMEs), such as Si II, Ca II, S II, O I and Mg II, while, in a few cases, traces of unburned C II has been observed (e.g. Cartier et al., 2014). All of the absorption lines are significantly blueshifted ($\sim 10,000\,\mathrm{km\,s^{-1}}$) and broadened due to the rapid expansion after the explosion. These spectral features are super-imposed on a pseudo-continuum that resembles a blackbody, with a distinctive deficit of UV flux, due to line blanketing of the IPEs at that wavelengths. As the SN evolves, the relative contribution of the iron-group elements increases, as the photosphere recedes into the ejecta and, finally, with the ejecta becoming optically thin, forbidden emission lines of Fe II and III dominate.

Measurements of the velocities and strengths of these distinctive features is a powerful tool to probe the underlying physics and describe the variations in the SN Ia family, reflecting at the same time the photometric diversity. Commonly used schemes include the Wang et al. (2009b) division to two groups based in the Si II λ6355Å velocity at peak brightness (with SNe Ia having velocities of ≥12,000 km $\mathrm{s^{-1}}$ exhibiting a narrower range in both peak luminosity and light curve width) and the Benetti et al. (2005) three group division according to the temporal evolution of the Si II velocity: a FAINT group, consisting of the 91bg-like events, a high-velocity gradient (HVG) group, which includes the bulk of the 'normal' SN Ia population and a low-velocity gradient one (LVG) that corresponds to the 91T-like type. As can be seen in Fig. 1.6, the strength of the IMEs absorption features also reflects a spectroscopic–photometric sequence, trending from strong to weak pseudo equivalent widths (pEWs; for example see Nugent et al., 1995) from the 91bg-like to 91T-like SNe. Nugent et al. (1995) attribute this spectroscopic–photometric sequence primarily to temperature differences, likely to be due to the total amount of ^{56}Ni produced in the explosion.

As for the rest of the peculiar SNe Ia, the spectroscopic diversity becomes much more complex, pushing our understandings to the limits. As a full description is beyond the scope of this thesis, we will only mention the case of the 'interacting' SN Ia–CSM. This subclass is relevant to our work, as a unique class of bright objects, with slow photometric evolution and spectroscopic similarity to 91T-likes, and a spectroscopic feature clearly distinct from the other SNe Ia: a broad Hα component that is the outcome of the interaction of the ejecta with locally deposited circumstellar medium (CSM).

1.4 The progenitor problem of SNe Ia

The identity of the exploding object in a SN Ia is universally agreed: in the 'standard' thermonuclear model (Hoyle & Fowler, 1960; Wheeler & Hansen, 1971), SNe Ia are explosions of C/O WDs that undergo a thermonuclear runaway that incinerates the star. Strong observational evidence on the C/O WD origin has been provided by extremely early observations of SN 2011fe (~4 hr after explosion; Nugent et al., 2011; Bloom et al., 2012b), constraining the initial primary radius of the exploding object to $R_p \leq 0.02\,\mathrm{M}_\odot$. The WD accretes matter to the point when, due to compression, fusion of carbon to IPEs (Colgate & McKee, 1969) initiates, releasing the nuclear binding energy which is absorbed from the WD material and converted to kinetic energy that unbinds the star. Strong arguments in favour of this paradigm include the absence of hydrogen and helium in SNe spectra, the fact that the energy obtained from the thermonuclear burning minus the binding energy matches the kinetic energy, the uniformity of their light curves and spectra, and the observations of SNe Ia at environments where star formation has ceased (see Maoz et al., 2014, for a recent review).

However, a major problem arises: the mass distribution of WDs peaks at $\sim 0.6\ \mathrm{M}_\odot$ (Liebert et al., 2005), while the mass limit for a (non-rotating) C/O WD is $\sim 1.38\ \mathrm{M}_\odot$ (i.e. the Chandrasekhar limit). This means that the C/O WD must grow in mass to reach ignition, and the realistically conceivable configuration that this may happen in is a (close) binary. The nature of the companion star that provides this 'extra' mass to the WD is still under debate. Moreover, the explosion mechanism that initiates the burning and the underlying physical processes are not fully understood.

These questions, collectively refereed to in the SN community as the 'progenitor problem', are a topic of vigorous ongoing research, both theoretically and observationally. In the following sections, we will describe the main progenitor systems that have been proposed and their observational evidence.

1.4.1 Progenitor systems

The most popular progenitor models that have been proposed in the past years can, broadly, be divided into two categories: the Single Degenerate (SD; Whelan & Iben, 1973) scenario, where the companion is a non-degenerate star, and the Double Degenerate (DD; Iben & Tutukov, 1984) scenario, where the binary consists of two WDs.

In the SD scenario, the C/O WD accretes hydrogen/helium rich material from a non-degenerate secondary, either through Roche-lobe overflow or through the wind of the donor. The mass of the WD approaches the Chandrasekhar limit, decreasing its radius

and increasing its density, and finally reaching an instability that initiates the thermonuclear runaway. In this configuration, the donor star can be a main-sequence (van den Heuvel et al., 1992), a sub-giant (Han & Podsiadlowski, 2004), a red-giant star (Patat et al., 2011b) or a helium star (Tutukov & Yungelson, 1996), with each case including various configurations based on the pre-supernova binary stellar evolution (Wang & Han, 2012a).

A major theoretical complication of the SD channel is relatively narrow range of the (net) mass accretion rate ($\sim 10^{-8} - 10^{-7}$ $M_\odot$ yr^{-1}). For this rate, stable nuclear burning of hydrogen to helium is possible (Nomoto, 1982), with these systems expected to resemble the supersoft X-ray sources (SSXs; van den Heuvel et al., 1992). A higher rate of accretion likely leads to engulfment of the donor in a common envelope, due to the expansion of the accretor, and cease of mass growth (however, see Hachisu et al. 1996 for a possible solution to this problem). Lower accretion rates lead to accumulation of the accreted hydrogen and a subsequent 'nova' eruption that ejects the accreted material. Similar issues are found in the helium star channel: the accumulated He layer may ignite in lower mass compared to hydrogen, but possible He novae may prevent the WD mass growth.

For the DD scenario, the accreted mass to the exploding more massive WD (primary) originates from a less massive (secondary) WD, which is brought close to the primary by the emission of gravitational radiation. With the secondary tidally disrupting in a timescale of a few orbital periods, this channel avoids the issues of inefficient mass growth, compared to SD. However, studies have shown that this high accretion rate leads to an off-centre carbon ignition that converts carbon to oxygen (O) and neon (Ne). Subsequently, the O+Ne WD undergoes an 'accretion-induced collapse' to a neutron star (Nomoto & Iben, 1985; Saio & Nomoto, 2004; Shen et al., 2012), i.e. not a SN Ia explosion. On the other hand, if the deposition of the mass of the disrupted WD happens 'violently' ('violent merger'; Pakmor et al., 2010, 2011, 2012), complex structures of high temperature and density on its surface may ignite and lead to a SN Ia. Variants of the DD scenario include collisions of WDs, instead of spiralling due to gravitational-wave losses, in dense stellar environments, or in triple systems, where the third member is a low-mass star, in orbit to the primary. The resonances in the triple system due to the non-degenerate star may increase gravitational losses and lead to head-on collision of the inner WD binary (Katz & Dong, 2012).

Alternative scenarios include explosions caused by the detonation of a He surface, in a binary consisting of a C/O WD and a He WD companion ('double detonation'; Woosley & Weaver, 1994; Bildsten et al., 2007; Sim et al., 2010) or in a 'violent merger' configuration (Shen & Bildsten, 2014), super-Chandrasekhar mass models (Maeda & Iwamoto, 2009,

particularly for bright SNe Ia), rotationally-supported massive WDs in spin-up/spin-down SD models (Di Stefano et al., 2011), the 'core-degenerate' model (Kashi & Soker, 2011), WD and M-dwarf binary systems (Wheeler, 2012) and single-star progenitors (Iben & Renzini, 1983).

In order to test the validity of the aforementioned models, parallel studies on the explosion mechanisms and the formation of the observables has been performed, focusing on hydrodynamical explosion models and radiative transfer codes (e.g. see Hillebrandt & Niemeyer, 2000; Hillebrandt et al., 2013). This is a crucial step towards the final answer: a viable progenitor scenario must be able to reproduce the observed light curves and spectra, and at the same time provide a robust explosion mechanism, in order to account for the homogeneity of SNe Ia, but still allow for the intrinsic variability of the observed sequence.

1.4.2 Observational evidences

In recent years, there has been a huge effort to systematically obtain observational data towards disentangling the progenitor problem. In general, the observational approaches could be divided into three broad categories: searching for the progenitor systems in pre-explosion data, investigating the properties of the event for progenitor hints, and searching for progenitor signatures on (presumed) SN Ia remnants (SNRs).

The search for progenitor candidates, for the SD channel, mainly focuses on recurrent novae (RNe) systems (della Valle & Livio, 1996), cataclysmic variables that have experienced more than a single nova eruption over the past century. Two of the most promising ones are U Sco and RS Oph, with WD masses close to the Chandrasekhar limit; however, the extent of that being true has been disputed (Schaefer, 2013). Moreover, the number of the RNe in our Galaxy is too low (60–100; Schaefer, 2010) to be considered a significant fraction of SN Ia progenitors. For the SSXs, both Di Stefano (2010) and Gilfanov & Bogdán (2010) have argued for their deficiency; for the He-rich SD channel no explicit cases have been reported; while for identifying rapidly-rotating WDs, measured rotations are observed to be very slow (Kawaler, 2004), although extremely difficult to measure. The situation seems more promising for the DD scenario, since recent surveys have found several candidate WD binaries, close to the Chandrasekhar limit (Napiwotzki et al., 2007; Badenes et al., 2009).

A more promising (although limited, due to the distances of the host galaxies) method is to directly detect the progenitor in pre-explosion images of the position where the SN exploded. Nielsen et al. (2012) used archival X-ray images to rule out SSXs at the location of the explosion for ten nearby SNe Ia, however, the most tight constrain comes

from the nearby SN 2011fe, where Li et al. (2011b) used optical pre-explosion imaging of M101 to exclude luminous red giants and most He stars.

While the direct imaging of the progenitor could provide unambiguous evidence, high quality archival data are required, which are not always present. Thus, studying the events themselves for traces of progenitor information has been the most successful approach. These attempts mainly focus on testing whether individual progenitor scenarios and explosion mechanisms are able to reproduce the (multi-band) photometric evolution and the observed velocity structure and chemical stratification of the ejecta. This is achieved by employing hydrodynamical modelling and radiative transfer prescriptions to obtain synthetic light curves and spectra, and then compared with single events or samples of them (e.g. Blondin et al., 2011; Röpke et al., 2012; Mazzali et al., 2014; Cartier et al., 2016). A promising method developed recently is the study of the late-time light curves. Since this approach is a substantial part of this thesis, we refer for more details in Chapter 3, where we apply this method to SN 2011fe.

Traces of hydrogen in a SN Ia spectrum could be strong evidence for the SD scenario. Maguire et al. (2016) searched for swept-up hydrogen in high resolution spectra of 11 nearby SNe Ia, with one tentative detection, but the SN Ia-CSM subclass Silverman et al. (2013a) is the most promising candidate for a SD SN Ia. Within a similar context, DD mergers predict substantial amounts of unburned C and O at high velocities ($> 12,000\,\mathrm{km\,s^{-1}}$), which is seen in ~30 % of the Carnegie Supernova Sample (CSP; Folatelli et al., 2012) and in individual objects, most notably SN 2011fe (Nugent et al., 2011; Parrent et al., 2012).

Another observational diagnostic for the SD scenario is the interaction of the SN ejecta with the non-degenerate companion. Kasen (2010) argues that the collision of the SN ejecta with the donor should produce detectable optical and UV emission at the early phase of the light curve, with Wang et al. (2012) finding UV excess in one SN (out of four), and Cao et al. (2015) reporting strong (but declining) UV emission from iPTF14atg within four days of its explosion. However, sample studies on early UV excesses rule out companion stars with masses $\geq 6\ \mathrm{M}_\odot$ (Hayden et al., 2010; Bianco et al., 2011).

SN 2006X is the most prominent object with direct CSM detection: Patat et al. (2007) have detected temporal variation of the Na I doublet, immediately after the explosion, which can be interpreted as arising from ionisation–recombination of Na in a CSM shell-like structure, predicted also by hydrodynamical simulations of RNe (Mohamed et al., 2013). Even more compelling is the strong statistical preference for blueshifted Na I doublet absorption features, attributed to mass outflows prior to the explosion (Sternberg et al., 2011; Maguire et al., 2013). Moreover, smaller total-to-selective absorption ratio

TABLE 1.1: Observational evidence for two families of SNe Ia, table 5 of Maguire et al. (2013)

Family 1	Family 2
More luminous	Less luminous
Broader light curve	Narrower light curve
Lower Si II λ4130 pEW	Higher Si II λ4130 pEW
Stronger high-velocity features	Weaker high-velocity features
Late-type host	Early-type host
Lower $M_{\rm stellar}$	Higher $M_{\rm stellar}$
Higher specific SFR	Lower specific SFR
Blueshifted Na I absorption	No Na I absorption
'prompt'	'delayed'

R_V may also suggest the presence of CSM dust in a subclass of SNe Ia (Wang et al., 2009b; Folatelli et al., 2010).

Indirect methods of detecting CSM also include the search for early radio and X-ray emission from the SN: the interaction of the ejecta with the CSM matter may produce synchrotron emission, with Hancock et al. (2011) providing an upper limit on the average companion stellar wind mass loss rate that rules out intermediate- and high-mass companions, while Russell & Immler (2012) derive an upper limit from the thermal X-rays emitted by the interaction of the SN shock with the CSM that excludes massive or evolved stars as companions. The strongest limits come again from SN 2011fe, both in X-rays (Horesh et al., 2012) and radio (Chomiuk et al., 2012), ruling out red giant donors or more evolved stars.

Finally, searches for surviving non-degenerate companions in SNRs provide further evidence for the DD scenario, as among SNRs suspected to originate from SN Ia, none has revealed conclusive detection of a surviving SD donor (e.g. see review of Vink, 2012).

Overall, most of the observational evidence are in favour of the DD scenario. However, SNe Ia with a SD origin have been identified, suggesting that the total population consists of a mixture of a dominant DD and a secondary SD channel, with the fraction of them remaining to be estimated (Scalzo et al., 2014b). Indications of two 'families' of SNe Ia have been observed, outlined in Table 5 of Maguire et al. (2013): Family 1 includes more luminous and slow declining events, with lower strengths of absorption features and blueshifted Na I D absorption, while Family 2 exhibits the opposite properties. Additionally, the galaxies that host Family 1 SNe Ia appear to be late-type, with lower mass and higher specific star formation rates compared to Family 2. We will expand on the host galaxy properties of SNe Ia in the next section.

Whether this observed division is due to a 'two-component' progenitor model of two (possibly widely diverse) progenitor channels acting the same time, or a single, self-consistent model with varying physical properties remains to be seen.

1.5 Host galaxies of SNe Ia

An observational characteristic that distinguishes SNe Ia from the other SN classes is the fact that they occur both in young and old stellar populations (Branch & van den Bergh, 1993). Moreover, observations suggest that the most luminous (i.e. those with the broadest light curve) occur preferentially in late-type galaxies (Hamuy et al., 1996), while subluminous events tend to occur in early-type ones (Howell, 2001). This implies that there is a range in the time delay between the star formation and the SN explosion from much less than 1 Gyr to at least several Gyr (Sullivan et al., 2006), categorized in terms of (perhaps distinct) populations of 'prompt' and 'delayed' SNe Ia (Mannucci et al., 2006). Moreover, the SN properties have been shown to correlate with the host galaxy star formation rate (SFR; Sullivan et al., 2006), stellar mass (Sullivan et al., 2006, 2010) and metallicity (Gallagher et al., 2008), as seen in Maguire et al. (2013) and outlined in Table 1.1.

Investigation of the physical origins for the these differences can be performed by measuring the delay-time distribution (DTD), a theoretical measure of the SN rate as a function of the delay time, since different progenitor scenarios require different DTDs. Theoretical delay times for DD scenarios, which are driven by the loss of angular momentum through gravitational waves emission, predict a DTD $\sim t^{-1}$, in agreement with observed volumetric SN rates (Dilday et al., 2010; Graur et al., 2011; Perrett et al., 2012), while suggestions for some SD channels may also follow this relation (Maoz et al., 2012). However, Sullivan et al. (2006) proposed a 'two-component' progenitor population, with a 'prompt' channel of ~100-500 Myr delay time, and a 'tardy' channel of ~5 Gyr that can also represent the SN Ia rate.

A different approach is the construction of theoretical DTDs via binary population synthesis (BPS) codes, simulations of large samples of initial binaries (e.g two main sequence stars orbiting with a certain period) with different initial parameters (masses, periods) and star formation histories (Wang & Han, 2012b; Ruiter et al., 2009; Claeys et al., 2014). While there are a lot of systematic uncertainties in both the SD and the DD treatment, the situation again slightly favours the DD channel, however, both of them are unable to reproduce the normalised (i.e. the Hubble-time-integrated number of SNe) observed DTDs (e.g. Figure 8 of Maoz et al., 2014).

In summary, DTDs predicted from DD models reproduce the observed SNe Ia rates, but modern studies with better treatment on the DTDs, particularly with information below ~1 Gyr, will potentially disentangle the problem. Moreover, understanding the systematics of both DD and SD models in the context of their host galaxies and the observed correlations between SN and host properties will be beneficial towards the final answer.

1.6 Thesis outline

This thesis consists of observational studies regarding the long-standing progenitor problem of SNe Ia. The source of the data are provided by modern surveys with excellent capabilities on discovering and following-up local SNe Ia, making them ideal experiments for investigating SNe Ia progenitors. Towards this end, the thesis can be divided in two categories: a) The investigation of the late-time light curves of SNe Ia, a recently developed method to directly constrain explosion models by measuring the nucleosynthetic yields for diagnosing the density of the exploding WD, and, b) the analysis of the 91T-like overluminous subclass of SNe Ia, in terms of their unique photometric, spectroscopic and environmental properties. An outline of this work is as follows:

In Chapter 2, I provide details of various observational projects that I have been involved in, from which the majority of the data presented here originate from. These include the Palomar Transient Factory (PTF), the Public ESO Spectroscopic Survey for Transient Objects (PESSTO) and the Las Cumbres Observatory Supernovae Key Project (LCO SN Key Project). Moreover, I will introduce some basic data analysis techniques, widely used in this thesis: the image subtraction pipeline, the light curve fitting and the spectral mangling.

In Chapter 3, I examine the late time evolution of the light curve of SN 2011fe. After briefly introducing this important SN Ia, I present the observed late-time PTF light curve, alongside external photometric and spectroscopic data. I describe a method to construct a bolometric light curve and, by analysing it, I outline possible theoretical models for its interpretation.

In Chapter 4, I investigate the late-time light curve behaviour of a sample of PTF SNe Ia. I describe a method to compare them with the well-established SN Ia evolution, based on our work on SN 2011fe, and the SNe Ia-CSM evolution, exemplified by PTF11kx, drawing conclusions on the limit of Hα presence at the late times.

In Chapter 5, I focus on the overluminous subclass of SNe Ia, the 91T-likes, by studying the rich data sets of two representative members, classified by PESSTO: SN 2014eg and

SN 2016hvl. After presenting their extensive photometric and spectroscopic observations, I analyse the data in the context of their progenitor systems, focusing, among other indicators, on their local environments.

In Chapter 6, I turn to the global properties of the 91T-like SNe Ia host galaxies. I use the PTF SNe Ia sample in the Sloan Digital Sky Survey (SDSS) footprint as the source for my data, I identify the correct host of each SN and, by fitting the observed spectral energy distribution of the host, I recover its mass and star formation. I investigate any preference of 91T-likes to occur in specific environments and discuss the implications on their progenitor systems.

In Chapter 7, I summarise my results, and provide an observational framework that can improve similar studies in the future.

Chapter 2

Observations, Data and Techniques

Before beginning our scientific studies, in this chapter we first give some brief details on the various projects and algorithms that provide the fundamental framework for our analysis. We will describe the surveys from which the majority of our data originate. These include the Palomar Transient Factory (PTF), the Public ESO Spectroscopic Survey for Transient Objects (PESSTO) and the Las Cumbres Observatory Supernovae Key Project (LCO SN Key Project). Moreover, we will outline some of the techniques we use on the analysis of our photometric and spectroscopic data.

2.1 Palomar Transient Factory - PTF

The Palomar Transient Factory (PTF; Law et al., 2009; Rau et al., 2009) was a rolling, wide-field transient survey, covering the northern hemisphere and dedicated to systematically explore the optical transient phase space, with characteristic timescales from minutes to months. The success of PTF is illustrated by the substantial number of SNe discovered during its 4-year operation (2009–2012), and the scientific impact it had on the exploration of the Universe in the time domain.

PTF operated with the CFH12k camera (Rahmer et al., 2008) mounted on the Samuel Oschin 48-in telescope at the Palomar Observatory (P48 telescope), with data mostly taken in a Mould R-band filter ($R_{\rm P48}$) interspersed with some g-band ($g_{\rm P48}$) observations. The field of view (FOV) was ~7.3 square degrees with a plate scale of 1.0″ pixel^{-1}. The survey covered an area of the sky of ~ 8000 square degrees in the typical 3 to 5 day

cadence. The limiting magnitude in good conditions was $R_{\rm P48} \simeq 20.5$ mag (Frohmaier et al., 2017) with the typical 60s exposure.

During the 4-year operation of PTF, almost 50,000 transient astrophysical objects were detected. The classification of these potential SN candidates was performed as follows: the candidate SN transients were ranked by employing machine-learning techniques (Bloom et al., 2012a) and then visually confirmed by PTF collaborators or citizen scientists via the 'Galaxy Zoo: Supernova project' (Smith et al., 2011), and sent for spectroscopic classification, with additional monitoring for the most interesting ones.

Photometric characterisation and follow-up was performed mainly with the 60-in Palomar telescope, while for the spectroscopic classifications a wider network of other telescopes were used: the Palomar Hale Telescope, the Keck telescopes, the Lick Observatory 3m telescope, the Gemini-N telescope and the University of Hawaii 88-in telescope. A follow-up Marshal was designed for an efficient and rapid response to targets relevant to the appropriate science program, which acted as the main tool for distribution of the follow-up facilities. All the reduced images of PTF are publicly available through the Infrared Science Archive at IPAC[1], while the classification spectra are available through the WISeREP archive[2] (Yaron & Gal-Yam, 2012).

During the experiment's course, several predefined long-term surveys were carried out. The primary experiments designed to discover optical transients were the 5 day cadence survey (5DC) and the dynamic cadence experiment (DyC). The 5DC experiment monitored an active area of $\sim$ 2700 square degrees, with a mean cadence of 5 days. Observations were performed with the $R_{\rm P48}$-band filter, and typically two 60s exposures, separated by 1hr, were taken at each epoch for the individual field. The DyC experiment focused on exploring events with shorter timescales (1m to 3d), with notable successes in discovering new or rare type of transients, such as faint-and-fast '.Ias', Ca-rich halo transients and Luminous Red Novae (for a review see Kasliwal, 2012).

The importance of studying SNe Ia has already been discussed in Chapter 1. Towards this goal, PTF has substantially contributed to SN cosmology, by discovering 1250 SNe Ia in the nearby smooth Hubble flow ($0.03 \leq z \leq 0.14$). Moreover, several hundred were followed in detail, in order to both explore systematic effects in cosmological studies (such as the intrinsic SN colour–luminosity relation under the effect of dust reddening, the impact of the environment, or the evolution of the progenitor system with redshift), and for systematic and unbiased studies of the physics of the phenomenon (Maguire et al., 2014; Pan et al., 2014, 2015; Firth et al., 2015).

[1] http://irsa.ipac.caltech.edu/
[2] http://wiserep.weizmann.ac.il/

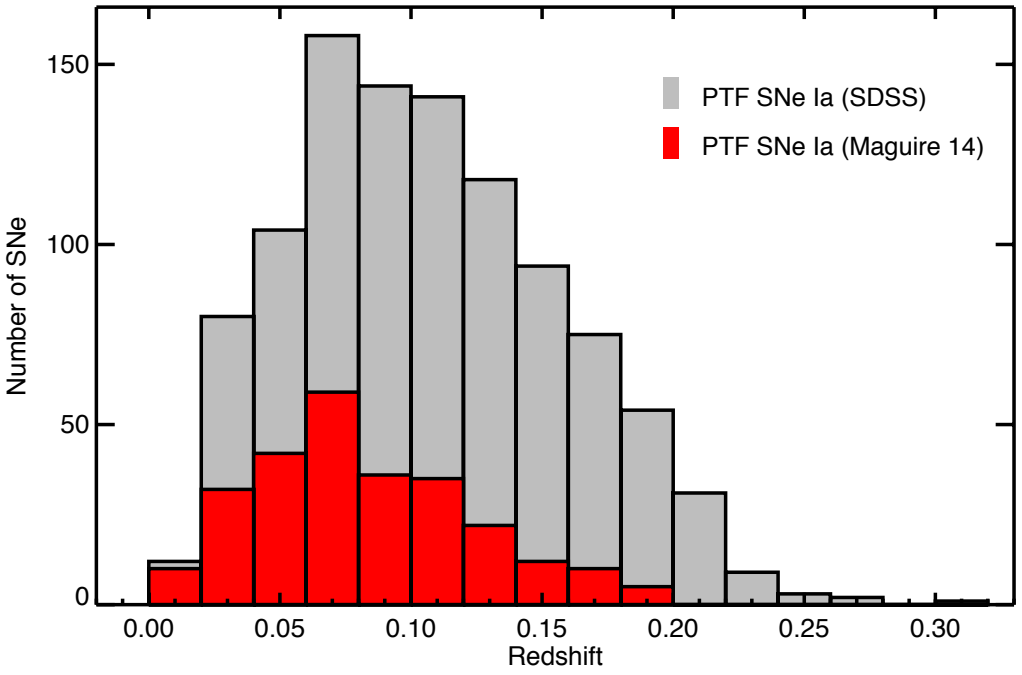

FIGURE 2.1: Redshift distribution of the PTF spectroscopically confirmed SNe Ia, located in SDSS. The total number of events is 1024 (out of a total of 1250), with a median redshift of 0.1. Overplotted is the sub-sample of the 263 (out of a total of 265) SNe Ia of Maguire et al. (2014), with a median redshift of 0.076.

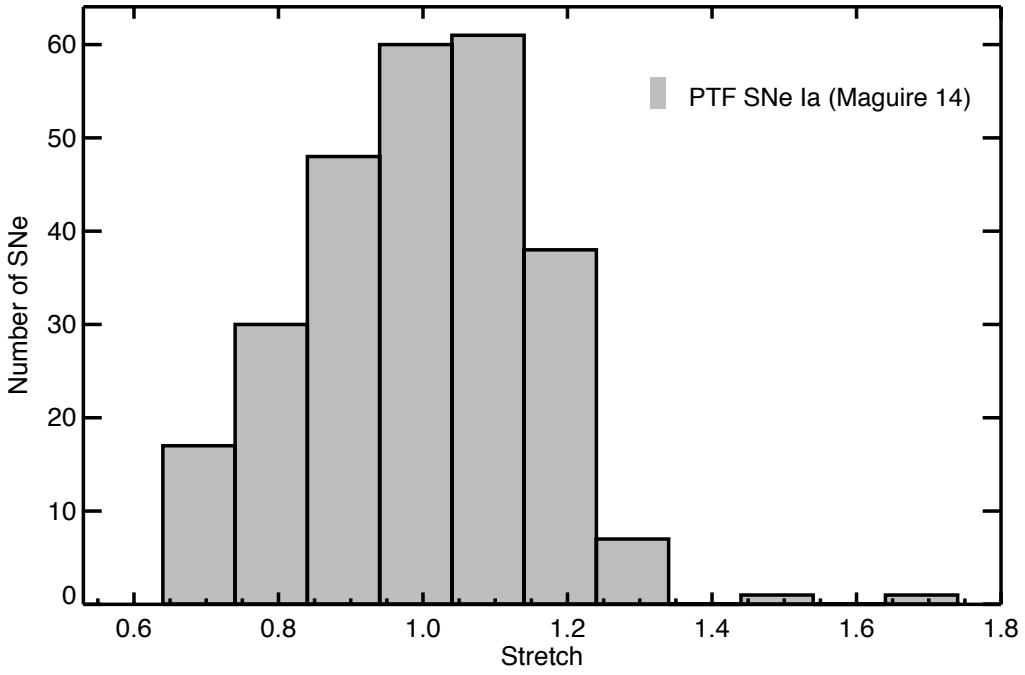

FIGURE 2.2: Stretch (see Section 2.4.2) distribution of the PTF low-z SN Ia sample from Maguire et al. 2014. The median stretch is 0.99.

At the sample studies of SNe Ia we perform in this thesis, and particularly in Chapters 3 and 6 , our parent sample is the Maguire et al. 2014, which initially contains 264 (out of 1250) SNe Ia, for which multi-band photometric follow-up was performed and sufficiently high signal-to-noise ratio (S/N) that at least the velocity and pseudo-equivalent width of the Si II 6150Å feature can be measured. Further quality cuts, imposed by the scientific goals of our studies, are specifically addressed at the corresponding chapters. In Fig. 2.1, we present the distribution in redshift of the Sloan Digital Sky Survey (SDSS; Frieman et al., 2008) sample of the PTF SN Ia (grey) and the low-z sample of Maguire et al. 2014 (red), with the distribution in stretch of the low-z sample shown in Fig. 2.2.

2.2 Public ESO Spectroscopic Survey for Transient Objects - PESSTO

The Public ESO Spectroscopic Survey for Transient Objects (PESSTO; Smartt et al., 2015) is a public spectroscopic follow-up survey, composed of a wide variety of transient research groups within the European Southern Observatory (ESO), with a principal science goal to deliver high-quality optical and NIR spectroscopic time series, primarily of rare or unusual transient events. In this section, we will give an overview of the survey and describe the PESSTO pipeline, used for the reduction and calibration of the majority of our data.

2.2.1 PESSTO – Overview

PESSTO uses the 3.58m New Technology Telescope (NTT) of the European Southern Observatory (ESO), while the instruments used are the ESO Faint Object Spectrograph and Camera 2 (EFOSC2; Buzzoni et al., 1984) in the optical and the Son OF ISAAC (SOFI) (Moorwood et al., 1998) in the near-infrared (NIR).

PESSTO was allocated 90 nights per year, for a total of 5 years (2012–2016), extended for 2 more years under the ePESSTO program, with observations from August until April. Each year, a month's run consists of 3 sub-runs of 4, 3 and 3 nights. Target selection for classification is performed via the PESSTO Marshall, a web-based data aggregator, that collects information from various sources, including feeder surveys such as the La-Silla Quest, Pan-STARRS, ASASSN and OGLE-IV, as well as the Astronomers Telegram (ATEL) and the IAU Central Bureau for Electronic Telegrams (CBET). The Marshall also acts as a real-time collaboration and communication platform, that allows PESSTO members to prioritise and track the observations of their targets of interests.

To date[3], PESSTO has classified 1168 transients and actively followed 254. The latest data release[4] (PESSTO SSDR3) includes 1977 optical and NIR spectra of follow-up objects (151 SNe, 10 super-luminous SNe, 2 supernova imposters, 3 Tidal Disruption Events, 1 unclassified object and 1 AGN), in addition to 1098 optical classification spectra of transients for which follow-up was not pursued. The PESSTO Paper Library[5] consists of 60 peer-reviewed papers, covering a wide range of scientific interest, such as thermonuclear and core-collapse SNe, superluminous SNe, tidal disruption events and gravitational-wave optical counterparts.

The University of Southampton Supernova Group is an integral part of PESSTO, both in terms of scientific impact and providing observers. My observing experience with PESSTO comprises of 29 observing nights (November 2014, December/January and October/November 2015) as a 3rd, 2nd and lead observer respectively, with 27 ATELs submitted. My responsibilities included the target selection and night planning, quick data reductions of spectral measurements, classifications of transients and the writing of every night's ATEL.

PESSTO have been incredibly successful in classifying and monitoring SNe during the last 4 years. However, there is always room for improvement. The communication between the observer and the Primary Investigators (PIs) could be better: while the PESSTO Marshal provides an excellent framework for all the members of the collaboration to exchange information, sometimes, and especially considering high priority targets with time pressure, communication needs to be more clear. Moreover, an option for the PI to automatically upload OBs to the Marshal, in the case where the generic PESSTO OBs are not sufficient for the scientific outcome needed, can also be beneficial. Finally, PESSTO and its successor(s) should expand their scientific interests and goals out to other optical transients and not be limited to SNe. This can be accomplished with the participation to the collaboration of scientists with a more diverse background, such as GRBs and gravitational waves. ePESSTO is currently moving to that direction.

2.2.2 PESSTO – Data reduction pipeline

An advantage of PESSTO is the use of fixed set-ups for both EFOSC2 and SOFI spectroscopy, which allows for rapid and uniform distribution of the final data products to the PESSTO survey members and the public.

EFOSC2 uses the ESO#40 CCD, giving a 2D science image with 1024×1024 physical pixels, with a plate scale of 0.24″ pixel^{-1}. The field size for every observation is 4.1×4.1

[3] http://www.pessto.org/index.py
[4] http://eso.org/rm/api/v1/public/releaseDescriptions/88
[5] http://www.pessto.org/index.py?pageName=pesstopapers

TABLE 2.1: PESSTO spectroscopic settings

Instrument	Grism	Wavelength (Å)	Dispersion (Å pixel^{-1})	Resolution (Å)
EFOSC2	#13[a]	3650–9250	5.5	18.2
	#11	3345–7470	4.1	13.8
	#16	6000–9995	4.2	13.4

[a]Used for classification and follow-up

arcmin. The three spectroscopic set-ups (Table 2.1) are Gr#13 (used for classification and follow-up), Gr#11 and Gr#16 (used for follow-up), with appropriate blocking filters for the Gr#16 grism to remove second-order effects. The width-slits used for all the grisms are either 1″ or 1.″5, depending on the seeing at the time of the observation. The gain and readout noise, measured by PESSTO observations during 2012–2013, are constant and estimated to be 1.18 e$^-$/ADU and ~12.5 e$^-$. Moreover, from the same observations, the bias level of the CCD appears to be stable within 5–10% of the mean level (212 ADU).

A custom-made reduction pipeline was developed by Stefano Valenti, based on the basic python packages numpy, pylab, pyraf and pyfits, and it is publicly available through the PESSTO wiki[6]. All the PESSTO data, presented and analysed in this work, have been processed through this pipeline. For EFOSC2 spectroscopy, the data processing steps are summarised below:

1. Bias subtraction: A set of 11 bias frames are taken each afternoon of EFOSC2 observations and are used to create a nightly master bias, which is subtracted from all EFOSC2 data taken on that night. No dark current correction is applied, since the dark current is estimated to be less than 3.5 e$^-$ pix^{-1} h^{-1}, negligible for the typical PESSTO exposures (600–1800 s).

2. Flat fielding: Once per subrun of 3–4 nights, PESSTO takes sets of spectroscopic flatfields during the afternoon, for each combination of the spectroscopic set-up (grisms, sorting filters and slit widths). The illumination for these flats is external ('dome flats'), which are then combined and normalised to give a master flat that can be associated with every science observation taken on the subrun. Moreover, for Gr#16, where significant fringing is observed above ~7200 Å, three calibration flat field exposures with an internal lamp are taken immediately after the science exposure.

[6]http://wiki.pessto.org/

3. Wavelength calibration: The wavelength calibration for EFOSC2 is achieved with the use of arc frames from the two installed helium and argon lamps, generally taken in the evening before the observations. No arc frames are taken during the night, but instead we use the evening arc frames adjusted with a linear offset, as measured from either the skylines (for exposures longer than 300s) or the atmospheric absorption lines (for shorter exposures) of the science image. This linear shift is calculated by cross-correlating the observed spectrum with a series of library rest-frame spectra.

4. Cosmic Ray removal: The PESSTO pipeline employs the python implementation of the cosmic ray rejection algorithm LACOSMIC (van Dokkum, 2001), at the central pixel ± 100 pixels in the spatial dimension around the object.

5. Object extraction and background subtraction: The PESSTO pipeline uses the pyraf implementation of the standard IRAF task apall to extract the target and subtract the background. Each science spectrum has an associated sky background spectrum and an error spectrum, estimated as the standard deviation of the variance of the science spectrum.

6. Flux calibration: PESSTO uses a set of 9 spectrophotometric standards that can be found on the PESSTO wiki. The standard observing strategy indicates 3 observations (at the beginning, middle and end of night) of at least 2 different stars, in all of the instrumental set-ups (grisms, filter and slit width combinations). From the 3 observations, sensitivity functions are derived and a spectrophotometric standard is chosen by the reducer, typically the one closest in time to the science observation. Note that, for the PESSTO data releases, a master sensitivity function is created monthly and then applied to the final reduced spectra.

7. Telluric absorption correction: The data reduction pipeline uses a model to correct for the H_2O and O_2 atmospheric absorption, computed in Patat et al. (2011a). The procedure creates a model atmospheric absorption spectrum of gaussians, smoothed to the resolution of each instrumental set-up and re-binned to the appropriate pixel dispersion. Then, the pipeline scales the model spectrum to match the intensities of H_2O and O_2 absorptions to the ones observed in the spectrophotometric standards, and each science spectrum is divided with the closest in time model spectrum.

The pipeline produces fully reduced and flux-calibrated spectra of the instrumental set-ups shown in Table 2.1. For the Gr#11 and Gr#16 arms, we combine the reduced spectra by scaling one of them to match an overlapping wavelength region. Typically, a region of choice is one where SN features are not expected to be present, but we note that

this depends on the phase of the phenomenon. Since most of our observations in Gr#11 and Gr#16 are up until ~40d after peak, the wavelength region we choose is redward of the Si II 6150Å feature and blueward of Hα, between 7000–7200 Å. Finally, the spectral flux calibration is corrected by adjusting them to external calibrated photometry, as described in Section 2.4.4.

2.3 Las Cumbres Observatory SN Key Project

The Las Cumbres Observatory Global Telescope (LCOGT; Brown et al., 2013) is the first general–purpose, flexibly–scheduled, multi–instrument optical observatory, designed explicitly to pursue astronomical research in the time domain. Its deployment was motivated by the need of flexible facilities that can provide time–sampled data over a range of temporal cadences, dataset durations, and observing modes in a routine and systematic way. Some of the key scientific objectives are the study of SNe and dark energy, extra-solar planets, solar system objects and other time variable phenomena, such as GRBs, microlensing, stellar oscillations, variable stars and AGNs.

The study of SNe within LCOGT has been primarily realized by the Next-Generation Sample of Supernovae Key project and its successor, the Global Supernova Project. The aim of the project is to obtain light curves and spectra of ~200 SNe per year (both thermonuclear and core-collapse). Observations ideally start within hours of discovery, and focus on those SNe caught soon after explosion. LCOGT provides photometry and spectroscopy, operating a wide range of observing sites and telescopes around the globe. For photometry, the 1-m telescopes used in this work are located at the McDonald (ELP), the Cerro Tololo (LSC), the Sutherland (CPT) and the Siding Spring (COJ) observatories. The camera mounted on the telescopes was the Santa Barbara Instrument Group (SBIG) STX-16803, which was gradually replaced with the SINISTRO camera. A summary of the imager characteristics is presented in Table 2.2. Imaging used in this work has been performed in Bessel B V and SDSS g' r' i' filters, with their transmission fractions shown in Fig. 2.3. We overplot a typical SN Ia spectrum at maximum light, to show the correspondence of its dominant spectral features with each photometric band.

The LCOGT images are reduced via the custom-made BANZAI Python pipeline[7], which performs bias–dark subtraction and flat-field correction (with several bias, dark and flat-field images obtained at each epoch), source detection and astrometric solution from Astrometry.net (Lang et al., 2010).

[7] https://github.com/LCOGT/banzai

TABLE 2.2: LCOGT imager characteristics

Instrument	Format (pixels)	FOV (arcmin)	Pixel size (arcsec)	Readout noise (e^-)	Gain (e^-/ADU)
SBIG[a]	4096×4096	15.8×15.8	0.464	13.5	1.4
SINISTRO[b]	4096×4096	26.5×26.5	0.389	12.0	1.0

[a]2×2 binning,[b]1×1 binning

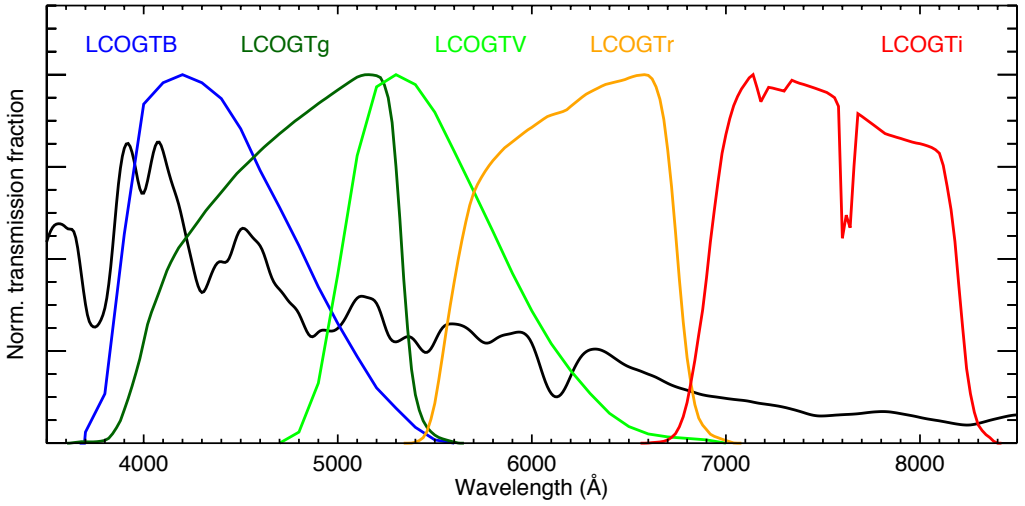

FIGURE 2.3: LCOGT filter transmission curves, together with a template SN Ia spectrum at maximum light.

LCOGT spectra used in this work were obtained with the FLOYDS spectrograph, installed on the 2-m telescopes at Haleakala (OGG) and Siding Spring (COJ). FLOYDS is a low resolution, low dispersion robotic spectrograph, designed for SN classification and monitoring. The wavelength range is large (3200–10000 Å) and the resolution varies between R~300–600, depending on wavelength. The raw spectral data are reduced internally in the LCO with a pipeline similar to the PESSTO pipeline (Section 2.2.2).

Under the collaboration of PESSTO with LCOGT, I was responsible for triggering the PESSTO photometric follow-up campaigns within LCOGT. My responsibilities also included monitoring the campaigns, checking the image quality and adapting observation strategies and, finally, providing a connection between LCOGT and PESSTO, for administrative issues. My involvement begun on May 2014 and lasts up until now.

2.4 Data analysis techniques

In this section, we will outline some basic data analysis techniques, both photometric and spectroscopic, that we use extensively throughout this work. This consists of the photometry pipeline (Section 2.4.1), the light-curve fitting tool (Section 2.4.2), the extinction correction laws (Section 2.4.3), the spectral 'mangling' (Section 2.4.4) and the *s*-correction (Section 2.4.5).

2.4.1 Photometry

The calibration and extraction of photometry of the PTF and LCOGT reduced images, used throughout this study, is performed with a single, custom-made, pipeline, used extensively in earlier PTF papers (see, e.g., Ofek et al., 2014; Firth et al., 2015, for particular details). The pipeline is based around a classical image-subtraction concept. A deep reference image is constructed using data prior to the first detection of the SN, which is then photometrically aligned, astrometrically registered and re-sampled to each image containing the SN light (the science image). The point spread function (PSF) of the resampled and science images are determined from isolated point sources in the images, and the image with the best seeing is degraded to match the PSF in the worst seeing image, using a similar technique to that of Bramich (2008). The reference image is then subtracted from the science image, producing a 'difference' image containing only objects that have changed their flux level between the reference and science image epochs. The SN position is then measured from the difference images that have a very high signal-to-noise (S/N) of the SN, and then PSF-fitting photometry measured at this fixed position in all images after the SN was first detected.

The calibration is achieved with nearby stars within the science image of the SN. Depending on the location of the SN in the sky, we use standard stars from either the Sloan Digital Sky Survey (SDSS; York et al., 2000) Data Release 12 (Alam et al., 2015) or the AAVSO Photometric All-Sky Survey (APASS; Henden & Munari, 2014).

All PTF photometry in this thesis is measured by me, using this pipeline. Moreover, I contributed to the update of the pipeline in order to process LCOGT images, and subsequently used it to obtain LCOGT photometry.

2.4.2 Light curve fitting

An essential part of our photometric analysis relies on the accurate and physically motivated modelling of the SN light curve. To this end, we make extensive use of the

light-curve fitter SIFTO (Conley et al., 2008), a light-curve analysis tool, initially developed for the Supernova Legacy Survey (SNLS; Astier et al., 2006), that empirically models a SN Ia light-curve, providing parameters such as the light-curve width (quantified by the parameter strech), the time of maximum light in the rest-frame B-band (t_{max}), the peak magnitude and a colour parameter C that represents the $B-V$ colour of the SN at peak (for SNe with photometric data in more than one filter; note that this is not the case for data originating from single-band surveys, such as PTF). SIFTO fits the observed flux, manipulating a spectral template that provides the spectral energy distribution (SED) at a given epoch and synthesising an observer-frame light-curve on a given redshift. The time-axis of the fitting template is adjusted with the dimensionless stretch factor s, for which the input template has $s = 1$. An example of a SIFTO fit is shown in Fig. 2.4 for the golden-standard SN 2005cf (Wang et al., 2009a), for which we calculate $s = 0.973 \pm 0.006$ and $\mathrm{MJD}_{max} = 53533.36 \pm 0.04$, $Mag_B^{Max} = 13.643 \pm 0.007$ and $B - V_{max} = 0.081 \pm 0.009$.

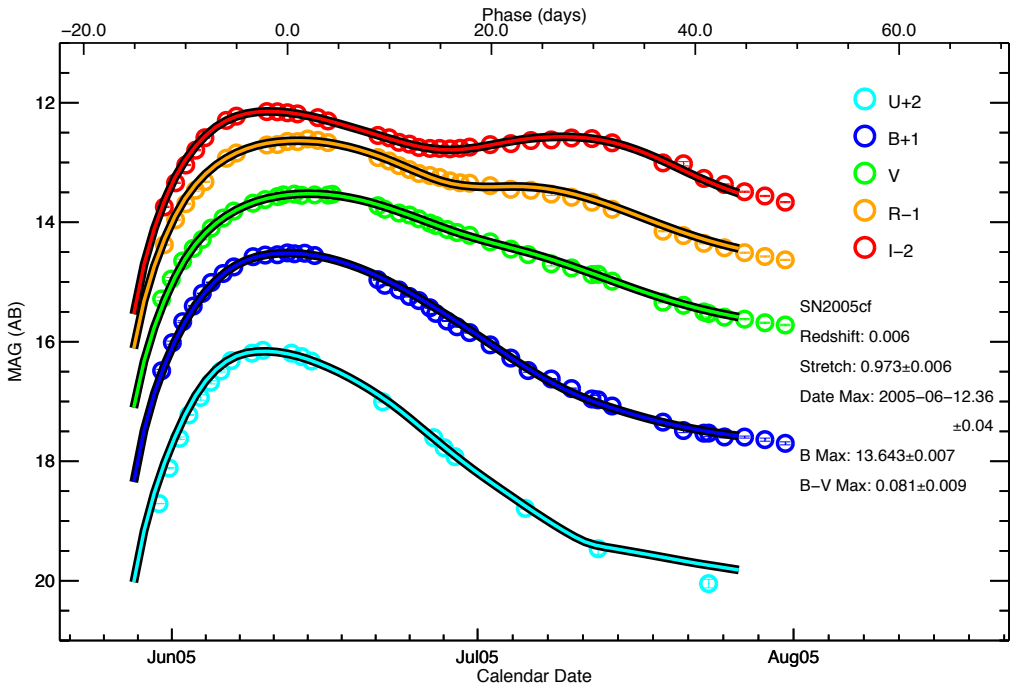

FIGURE 2.4: The light-curve of SN 2005cf (Wang et al., 2009a). We over-plot the SIFTO fit with solid lines and we report the calculated stretch and time of maximum light in the legend.

We note that throughout this work, we will refer to the time (in days) from maximum light as the phase, where:

$$\mathrm{phase} = \frac{t - t_{max}}{1 + z}, \tag{2.1}$$

where t is the time of a photometric point, t_{max} is the SIFTO measured time of maximum light and z is the redshift (we include the time dilation effect due to the redshift).

2.4.3 Extinction correction

While the intrinsic colour at maximum light of a (normal) SN Ia is correlated with its intrinsic peak brightness (redder SNe are intrinsically fainter; Tripp, 1998), the colour excess from extinction on the line of sight due to Milky Way (MW), the intergalactic medium (IGM) or the host galaxy is not. While the host-galaxy reddening is, in principle, unknown (and a substantial amount of this work is focusing on this issue), the extinction due to MW can be derived using the works of Schlegel et al. (1998) and Schlafly & Finkbeiner (2011). Normally, the extinction is characterised with the total-to-selective absorption ratio R_V:

$$R_V = \frac{A_V}{E(B-V)}, \tag{2.2}$$

where A_V is the V band reddening and $E(B-V)$ is the colour excess. The extinction at a given wavelength is then parametrized as:

$$\frac{A(\lambda)}{A_V} = a(x) + \frac{b(x)}{R_V}, \tag{2.3}$$

where $a(x), b(x)$ are empirically derived polynomial coefficients (Cardelli et al., 1989; Fitzpatrick, 1999), with the MW ISM having a mean value of $R_V = 3.1$. In this work, whenever it is noted, we extinction-correct our photometry or our spectra for MW using the Cardelli et al. (1989) law, with $R_V = 3.1$.

2.4.4 Spectral mangling

As discussed in section 2.2.2, a standard method to ensure proper flux-calibration of spectra is to 'modify' them by applying a multiplicative factor and retrieve a synthetic spectrum that matches the observed photometric colours. The need for this additional flux-calibration is based on various systematic uncertainties on the original spectral flux-calibration, such as slit losses, uncertainties on the spectrophotometric flux standard or the use of spectrographs with multiple grisms. This task is crucial, particularly when we use spectra to estimate physical parameters, such as a (pseudo-)bolometric flux or the host-galaxy extinction at the line of sight. A widely-used procedure that serves this purpose is the 'mangling' technique (Hsiao et al., 2007; Conley et al., 2008).

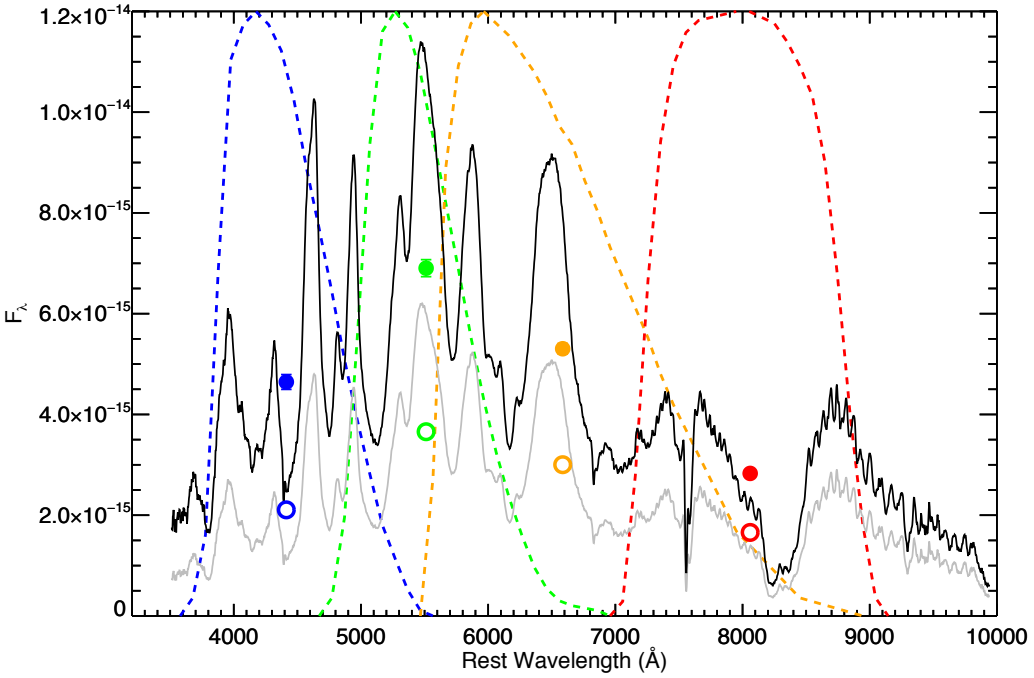

FIGURE 2.5: The +25d spectrum of SN 2005cf (grey) from Garavini et al. (2007) and the corresponding synthetic 'mangled' spectrum (black). We over-plot the spectrophotometric fluxes of B (blue),V (green), R (orange) and I (red) as open circles and the equivalent photometric ones (corrected for MW extinction) as full circles, at their effective wavelengths. We additionally show the response functions of the observed filters in dashed lines, using the same colour scheme.

The multiplicative factor in this approach is a set of splines, as a function of wavelength, with knots at the effective wavelengths of the observed photometric filters. Non-linear least-squares fitting determines the spline that smoothly scales the spectrum to the correct photometric colours. We note that either the input spectrum or the photometric colours are de-reddened for MW dust on the line of sight, with the prescription described in section 2.4.3. An illustration is presented in Fig. 2.5, where we 'mangle' the +25d spectrum of SN 2005cf from (Garavini et al., 2007) to the observed photometry of the SN, shown in Fig. 2.4.

A systematic uncertainty involved in this procedure is the choice of the input observed photometry at the given spectral epoch, since usually the photometry is not performed at the same time with spectroscopy. Whenever that is the case, we use either the SiFTO fits (as in Fig. 2.5), linear fits between two photometric epochs or more elaborate fits such as splines. At late times (phase > +40d), when the SN is expected to decline linearly with time (in magnitude space) due to radioactive decay, we may use linear fits to the late-time data set, particularly when we see random variations on the observed photometry from the linear decline.

2.4.5 S-corrections

A well-known issue in SNe photometric studies is the systematic differences obtained, when combining data from different telescopes and bandpasses. A popular approach to address this problem is the so-called *s*-correction (Stritzinger et al., 2002), a technique that combines the knowledge of a telescope's instrumental bandpasses with spectrophotometry, in order to correct the observed magnitudes from different telescopes and bandpasses to a common system.

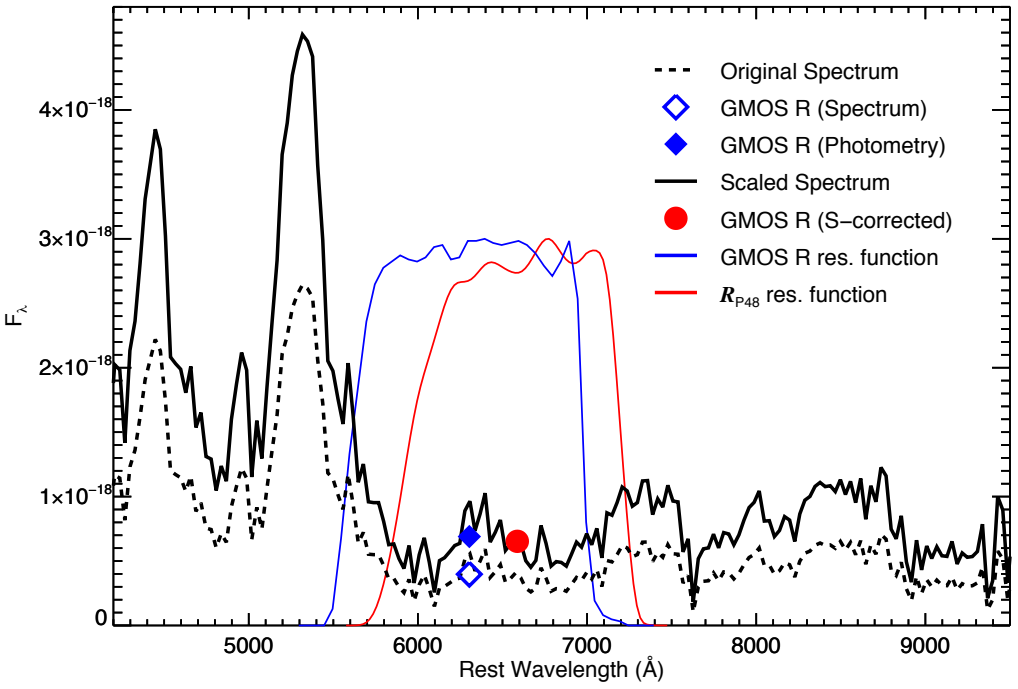

FIGURE 2.6: An illustration of the *s*-correction technique we use in our work. For this specific example, the SN 2011fe 1034 d spectrum (dashed black line), with a spectrophotometric GMOS R magnitude of 24.61 (open blue diamond) is scaled (solid black line) to a photometric GMOS R magnitude of 24.01 (filled blue diamond). The *s*-corrected magnitude is calculated by integrating the scaled spectrum over the R_{P48} bandpass, giving a mag of 23.97 (filled red circle). We over-plot the instrumental response functions of GMOS R (blue solid line) and R_{P48} (red solid line). All magnitudes are reported in the AB magnitude system. The spectra are binned to 30 Å for illustration purposes.

A description of the procedure is illustrated in Fig. 2.6. In this example, we *s*-correct a GMOS R photometric point of SN 2011fe at 923 d after maximum to a R_{P48} magnitude system, using the 1034 d spectrum of the SN. The procedure is as follows:

1. For the non-R_{P48} photometric point (e.g GMOS R), we choose the closest-in-time spectrum.

2. We scale the chosen spectrum to the photometric flux in the GMOS R bandpass.

3. We integrate the scaled spectrum over the R_{P48} bandpass.

Ideally, *s*-corrections should be applied to similar filters with respect to their instrumental bandpasses (for example, Johnson R to SDSS r'). Moreover, the success of this technique depends heavily on the dense temporal coverage of the SN, in order to be able to sufficiently probe momentary changes in the spectrum, and broad wavelength coverage, to capture the complete evolution of the SED. We note that at the extremely late times that we study in Chapter 3, Section 3.3.2, the evolution of the SN SED is remarkably constant, and *s*-corrections applied for data separated monthly or even more is justified.

2.5 Summary

In this Chapter, we have described the experiments that our data originate from, and various procedures we employ in the analysis of these data sets. We have given an overview of PTF, PESSTO and LCOGT and introduced the photometric pipeline, SIFTO, the MW extinction correction, the spectral 'mangling' and the *s*-correction.

In the next Chapter, we begin our science investigations. We will present and analyse the late-time light curve of one of the most distinguished discoveries of PTF, SN 2011fe, and explore the photometric and spectral behaviour of SNe Ia at these extreme epochs. We will demonstrate the importance of these approach on revealing information on the explosion mechanism and the progenitor system of this remarkable event.

Chapter 3

The late-time light curve of SN 2011fe

The importance of late-time studies of Type Ia Supernovae (SNe Ia) has gained popularity in the SN community during the last years. While theoretical work has been performed even from the early '80s, only recently real progress has been made on the observational side. This has been achieved due to the improvement of observational capabilities in the modern era, and the deployment of powerful all-sky surveys, capable of efficiently monitoring the night sky.

In this chapter, we will examine the late time evolution of SN 2011fe, by analysing the behaviour of the late-time light curve, complemented with spectroscopic data spread over this phase range. The main source of photometric data comes from the Palomar Transient Factory (PTF), the survey that discovered the SN, which provides a densely sampled coverage down to $R \simeq 22$ mag, up until 620 days after explosion. Literature data are added to the study at later times, in order to achieve an unprecedented photometric coverage for a SN Ia, up to 1600 days after explosion. In this chapter, we firstly introduce SN 2011fe in the context of its discovery and its early photometric and spectroscopic follow-up and early scientific results. We then present the PTF late-time light curve, complemented with external data, and describe a method to construct the bolometric light curve. We outline possible theoretical models to interpret the light curve, and, finally, discuss the implications of our study, in the context of the SN Ia progenitor problem.

3.1 SN 2011fe: Discovery and early scientific results

3.1.1 Discovery

SN 2011fe (PTF11kly) was discovered by PTF (Chapter 2.1) on 2011 August 23 UT (at MJD 55797.2), at an apparent magnitude of $g = 17.3$ mag (Fig. 3.1). Its host galaxy was the face-on spiral galaxy M101, located at a distance of 6.4 Mpc (Shappee & Stanek, 2011). Fits to the early time data give an inferred epoch for the emergence of the first photons of MJD 55796.687 ± 0.014 (Nugent et al., 2011). The SIFTO light curve fitter (Conley et al., 2008) measures a stretch of 0.98 ± 0.01 and a $B - V$ colour at maximum light of -0.07 ± 0.02 mag (Mazzali et al., 2014), together with an epoch of maximum light in the rest-frame B-band of 55814.30 ± 0.06 (2011 September 10.4 UT); all phases in this chapter are given relative to this epoch. These numbers are all indicative of a normal SN Ia. The SALT2 light curve fitter (Guy et al., 2007) gives similar results (Pereira et al., 2013). The Milky Way extinction was $E(B-V)_{\rm MW} = 0.009$ mag, and a measurement of the host galaxy extinction along the line-of-sight to the SN gives $E(B-V)_{\rm host} = 0.014 \pm 0.002$ mag (Patat et al., 2013a).

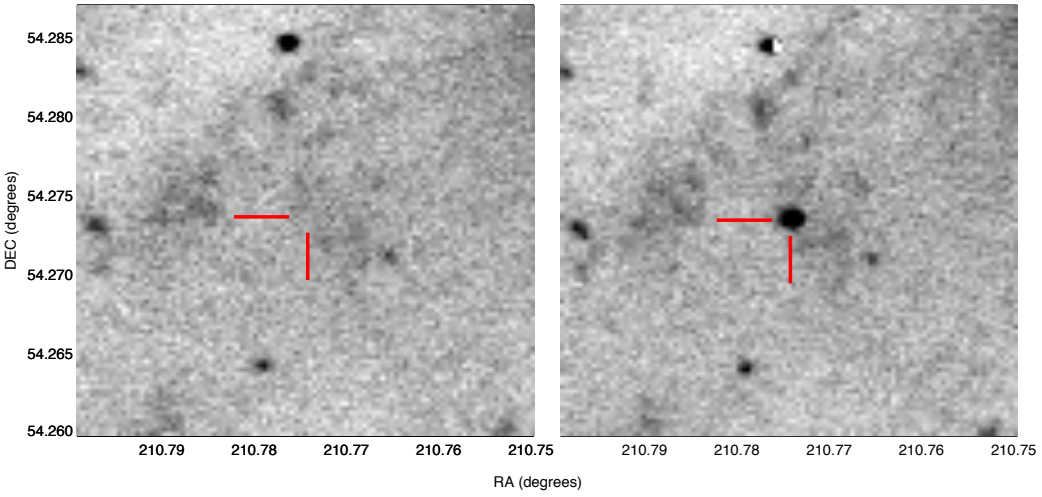

FIGURE 3.1: PTF g-band image stamps at the location of SN 2011fe. Left: The 2011-08-23T05:17:16.711 UT image, with a non-detection at the location of SN 2011fe up to a 3σ upper limit of 21.196 mag. Right: The 2011-08-24T03:59:20.661 UT image, where the SN is detected with 17.375 ± 0.015 mag. The red cross indicates the position of the transient at $\alpha = 14^{\rm h}03^{\rm m}05^{\rm s}.83$, $\delta = 54^{\rm o}16'25".2$ (J2000.0).

The event has a remarkably rich data set, making it the most well-studied SN Ia to date, with excellent spectroscopic (Nugent et al., 2011; Parrent et al., 2012; Pereira et al., 2013; Mazzali et al., 2014, 2015; Taubenberger et al., 2015; Graham et al., 2015; Shappee et al., 2013; Patat et al., 2013b; Foley & Kirshner, 2013) and photometric (McClelland et al., 2013; Matheson et al., 2012; Richmond & Smith, 2012; Munari et al., 2013; Tsvetkov

et al., 2013; Zhang et al., 2016; Shappee et al., 2016) coverage. Rigorous theoretical and observational work has been undertaken, providing a plethora of information on its progenitor system with notable successes.

3.1.2 Early scientific results

A review of the early scientific findings from studies of SN 2011fe can be found in Kasen & Nugent (2013). Here, we briefly summarise the main results.

- The extremely early discovery of SN 2011fe and the rapid response to photometric and spectroscopic follow-up of the event were able to provide significant constraints at the radius of the exploding object (Nugent et al., 2011). Simple scaling arguments indicate that the early luminosity of a SN Ia explosion is proportional to the progenitor's radius:

$$L \propto \frac{E_0 R_0 c}{M \kappa}, \tag{3.1}$$

  where E_0 is the total energy of the explosion, R_0 and M are the radius and mass of the exploding object, κ is the opacity and c is the speed of light. Comparing the earliest photometric point after the explosion and assuming reasonable physical parameters for E_0, M and κ (10^{51} erg, 1 $M_\odot$ and 0.2 $cm^2 g^{-1}$ respectively), an estimation of $R_0 \leq 0.02\, R_\odot$ is derived. Moreover, for this value of R_0, the mean density is $\overline{\rho} \geq 10^5\, \overline{\rho}_\odot$, giving extra indication of the compactness of the exploding object. These strict limits are broadly consistent with the realisation that the progenitor exploding object of SN 2011fe and, hence, of any SN Ia, is a WD.

- While the fact that the exploding object of a SN Ia is a WD was historically suspected to be true, the nature of the companion star that provides the surplus mass to the WD remains uncertain. Assuming that the WD is in a binary formation, two important observational constraints have been placed for SN 2011fe. Firstly, *HST* pre-explosion images of M101 reveal no optical source at the location of the SN (Li et al., 2011b), with derived mass limits of $M \leq 2.2 - 3.5\, M_\odot$, excluding companion stars larger than red giants. Secondly, under the assumption of the SD scenario, the SN ejecta are expected to interact directly with the (relatively close-by) companion, overrunning it and forming bright shock emission from the impact. The re-shocked ejecta's emission should dominate the SN luminosity at this early stage (first days after explosion), with varying amplitude due to the viewing angle and/or the mass of the companion (Kasen, 2010). Bloom et al. (2012b) put an

upper limit of the companion's radius $R_c \leq 0.01 - 0.1 R_\odot$, depending on orientation effects, excluding any red giant or solar-type stars.

- Tight constrains have also been placed due to the low-density CSM around the explosion centre of SN 2011fe. Most of the SD channels predict substantial mass outflows, either stable or episodic, prior to the explosion, from mass lost by the donor star. These outflows potentially form a dense CSM, as opposed to the DD scenario, where potential mass outflows are expected to be limited. All of the diagnostic studies regarding the presence of CSM around SN 2011fe have been unsuccessful, most notably any possible time variation of narrow absorption lines in high-resolution spectra (no time evolution of Na I doublet and Ca II H&K; Patat et al., 2013b) and X-ray (Horesh et al., 2012) or radio (Chomiuk et al., 2012) emission from the SN ejecta's interaction with the CSM, with upper limits on the mass loss of the companion of $\dot{M} \leq 4 \times 10^{-5}$ and $\dot{M} \leq 10^{-8}\,M_\odot\,yr^{-1}$ (for a wind terminal velocity of $100\,km\,s^{-1}$), respectively. These limits rule out most of the SD scenarios involving a RG companion star (or a more evolved one), but allow for MS companions.

- Regarding the explosion mechanism, SN 2011fe, with its normal peak brightness, revealed a, typical for normal SNe Ia, ^{56}Ni synthesised mass of $\sim 0.5 - 0.6\,M_\odot$, with its spectral series confirming the well-understood nucleosynthetic output of Ia explosions. However, the explosion model comparisons of Röpke et al. (2012) are unable to firmly disentangle whether popular SD (3D delayed-detonation) or DD ('violent merger') models reproduce the spectral evolution of SN 2011fe, giving slight preference to the DD one. On the contrary, Mazzali et al. (2015), by applying abundance tomography at nebular *HST* spectra, obtain satisfactory matches of the main late-time spectral features for the Mazzali et al. (2014) 'ρ-11fe' model (with a ^{56}Ni mass of $\sim 0.45\,M_\odot$), a model with high central density and a structure that matches the low-energy delayed detonation models of a Chandrasekhar-mass WD in a SD configuration, disfavouring significantly sub-Chandrasekhar models and mergers with individual WD masses significantly below the Chandrasekhar mass.

Overall, while arguments in favour of a SD origin have been presented, there is an almost unanimous consensus that SN 2011fe was a normal SN Ia, originating from the DD channel. However, one should always keep in mind that, while SN 2011fe is representative of the bulk population of the so-called normal SNe Ia, the fact that its progenitor system is constrained in substantial detail does not exclude the possibility of the presence of other progenitor channels for the peculiar or, even, other normal SNe Ia. Ongoing investigation, either on single-object or statistical and sample studies of SNe Ia are

crucial. Moreover, the investigation of unexplored areas of studies, such as the very late-time evolution of the phenomenon, may provide additional information towards solving the long-standing progenitor question.

3.2 The late-time light curve of a SN Ia

The shape of a SN Ia bolometric light curve is driven by the energetic output of the radioactive decay, and the opacity of the (homologously) expanding ejecta into which the decay energy is deposited. The principle contributor for the first few hundred days after explosion is ^{56}Co, generated from the decay of the most abundant radioactive synthesised nuclide, ^{56}Ni. Most of the energy in the decay of ^{56}Co is emitted in the form of γ-rays and the rest in charged leptons, such as positrons and electrons, both of which are thermalised in the expanding ejecta, creating optical and near-infrared (NIR) photons. As the ejecta expand and the column density decreases as t^{-2}, the ejecta become transparent to the high-energy γ-rays which increasingly escape thermalisation. This leads to an observed light curve decline that is faster than that expected from the radioactive decay, until, after about 75–250 days (Childress et al., 2015), when the contribution of positrons/electrons becomes dominant (e.g., Arnett, 1979) and the bolometric light curve is expected to settle on to a decline broadly matching that of ^{56}Co. This assumes that the majority of charged leptons get trapped in the ejecta; the extent to which these get trapped is uncertain (e.g., Cappellaro et al., 1997; Milne et al., 2001), but models with full positron/electron trapping are consistent with the late-time optical/near-IR observations of several SNe Ia (e.g., SN 2000cx: Sollerman et al., 2004; SN 2001el: Stritzinger & Sollerman, 2007; SN 2003hv: Leloudas et al., 2009; SN 2012cg: Graur et al., 2016).

At even later epochs, other longer-lived decay chains may also contribute, in particular the chains of ^{57}Ni and ^{55}Co (Seitenzahl et al., 2009; Röpke et al., 2012). Both chains have decay steps with half-lives of several hundred days, longer than ^{56}Co, leading to a slowly declining energy input and thus a predicted flattening in very late-time (>500–600 days) SN Ia light curves. The first evidence for such nuclides has been claimed for the nearby SN Ia SN 2012cg (Graur et al., 2016), and a slow-down in the decline of the optical/NIR light curves has been observed in other SNe Ia after ~600 days (Cappellaro et al., 1997; Sollerman et al., 2004; Leloudas et al., 2009). Spectral modelling of the late-time SN 2011fe spectra also seems to require additional energy input from ^{57}Co (Fransson & Jerkstrand, 2015).

In principle, an accurate determination of the mass of these other longer-lived nuclides provides a promising diagnostic tool to distinguish between different explosion mechanisms and, in turn, different progenitor scenarios (see section 1.3.1). Theoretical modelling shows that models with burning at higher central white dwarf densities predict higher ^{57}Ni/^{56}Ni mass ratios, since ^{57}Ni is a neutron-rich isotope that is produced in greater abundance in neutron rich environments, such as near-Chandrasekhar mass explosion models. Lower central density models, such as white dwarf mergers, generally predict lower ratios (for example, see Röpke et al., 2012; Seitenzahl et al., 2013).

A major complication is the accurate determination of the bolometric light curve. A robust theoretical prediction is the 'infrared catastrophe' (IRC), a predicted thermal instability that occurs at ~500 d after maximum light (Axelrod, 1980). During the nebular phase up until the onset of any IRC, cooling of the SN ejecta results from optical and near-IR transitions, dominated by Fe II and Fe III. However, as the ejecta expand and the temperature decreases to ~2000 K, the cooling is instead predicted to become dominated by fine structure lines in the mid-IR with excitation temperatures of ~500 K. This is predicted to result in rapid cooling, and the thermal emission moving from the optical/near-IR to the mid/far-IR; only ~5% of the deposited energy would emerge in the optical/near-IR at 1000 days after maximum light (Fransson & Jerkstrand, 2015).

This rapid decrease in luminosity in the optical/near-IR has never been observed in SN Ia light curves (e.g., Sollerman et al., 2004; Leloudas et al., 2009), which is not consistent with predictions from model light curve codes (Kozma & Fransson, 1998a,b). The reason is unclear. One possibility is that at least part of the SN ejecta is kept at temperatures above that at which the IRC occurs due to clumping in the ejecta (Leloudas et al., 2009). Lower density regions cool more slowly and may therefore remain above the limit for the IRC, thus maintaining some flux output in the optical/near-IR. Another possibility is that optical/near-IR luminosity can be maintained by a redistribution of UV flux into the optical wavebands, due to non-local scattering and fluorescence (Fransson & Jerkstrand, 2015). Other possible complications include 'freeze-out' (Fransson & Kozma, 1993), where the assumption that radiated luminosity is equal to the deposition of energy from radioactive decay (heating is balanced by collisional excitation cooling), breaks down. This occurs when the cooling time scale becomes longer than the expansion time scale, making necessary the inclusion of detailed time-dependent ionisation models.

The number of SNe Ia with the high-quality late-time data needed to make progress with these issues remains small: events must be both very nearby and (ideally) suffer from only minimal absorption from dust along the line of sight, keeping them visible in the optical until very late times. Moreover, it is advantageous if the SN is located in the outskirts of its host galaxy, avoiding possible crowding from nearby stars and

simplifying the photometry at late times. For all of the above reasons, SN 2011fe, with its minimum absorption on the line of sight and its close proximity (section 3.1.1) is the best candidate for extensive follow-up studies in these extremely late times.

3.3 The observed late-time light curve of SN 2011fe

Our first task is to compile a complete photometric and spectroscopic data set on SN 2011fe, covering the phase regime from 200 up to 1600 days after explosion. Firstly, we introduce the new observations presented in this chapter, i.e., a new late-time light curve from the PTF survey. We also describe the significant amount of photometric and spectroscopic data that we use from the literature. Finally, we will present the complete late-time light curve of SN 2011fe.

3.3.1 PTF Data

The main source of photometric data of this study come from PTF (Chapter 2.1), for which all data we analyse are publicly available through the Infrared Science Archive at IPAC[1]. For the PTF light curve, we employ the pipeline presented in Chapter 2.4.1. Note that SN 2011fe was bright enough to saturate the PTF camera when around peak brightness, and these saturated images are discarded from our analysis. The bulk of the data were taken in the R_{P48} filter (although g_{P48} data were also taken around maximum light), and thus we restrict the PTF analysis to R_{P48} in this work. Our PTF light curve of SN 2011fe is presented in each entirety in Appendix A, Table A.1. The photometry covers 819 R_{P48} images over PTF and iPTF, with typical science, reference and difference images, shown in Fig. 3.2.

SN 2011fe is clearly detected (i.e., $> 3\,\sigma$ significance) in individual PTF images up until around 400 d after maximum light. After these epochs, the data measured from the individual images, with typical 60 s exposure times, are mostly formal non-detections ($< 3\,\sigma$ significance in any individual frame). However, much deeper limits can be reached by co-adding the PTF data to increase the sensitivity. This technique has previously been used on PTF data to successfully detect pre-cursor events to core collapse SNe that lie below the formal detection limit of PTF (Ofek et al., 2013, 2014; Corsi et al., 2014; Strotjohann et al., 2015).

There are several choices as to how to perform this co-adding. The individual science images could be co-added prior to image subtraction; the individual difference images

[1] http://irsa.ipac.caltech.edu/

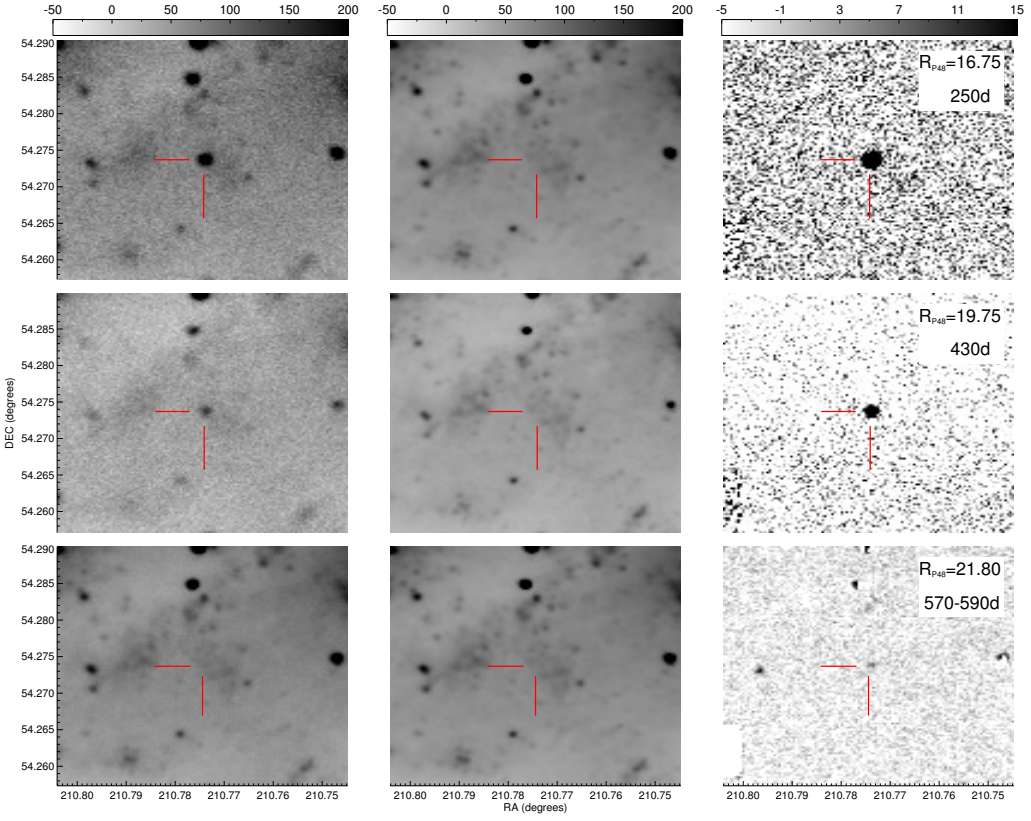

FIGURE 3.2: Late-time images of SN 2011fe. The left column shows the science image, the centre column the reference image, and the right column the difference image. The corresponding phases of SN 2011fe are (top to bottom) +250 days, +430 days and an average of 40 images over 570-590 days, with the measured $R_{\rm P48}$ magnitudes indicated on the figure. The reference images indicate a low surface-brightness of M101 at the position of the SN (see also the pre-explosion *HST* imaging presented in Li et al., 2011b).

could be co-added prior to the photometric measurement; or the co-adding can be performed on the individual photometric data points produced by the pipeline. The first two of these options have a significant disadvantage, in that the PSF size and shape in the individual images may change significantly over the averaging period, which may last up to several tens of nights. Thus we instead choose to average the individual flux measurements made from each PTF observation.

In order to test the fidelity of the subtraction pipeline at these faint flux levels, we insert artificial SNe ('fakes') into the unsubtracted science images, and then test how accurately these fluxes can be recovered after image subtraction and averaging of the PSF photometric measurements. We inserted 2300 fake point sources at random positions, but with each fake having the same magnitude in each frame chosen to lie over the range $19 < R_{\rm P48} < 24$. We then run the image subtraction pipeline on all images, and measure the PSF flux of the fake SNe in each individual frame. These individual measurements

are then averaged together to give a final recovered magnitude, exactly as for the real SN 2011fe light curve. The result of this test is shown in Fig. 3.3.

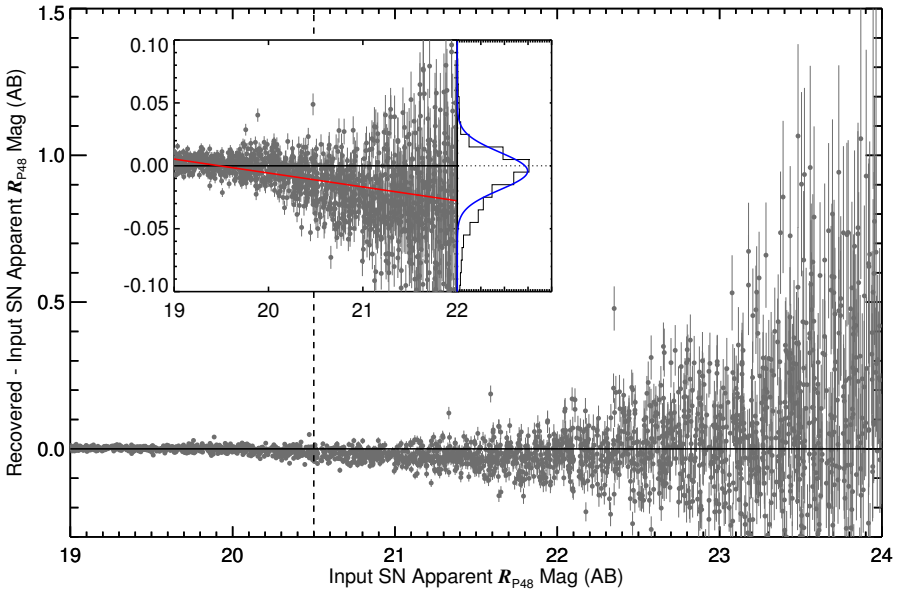

FIGURE 3.3: The fake SN tests on PTF imaging data (see section 3.3.1). The main panel shows the difference between the recovered and input fake SN magnitudes for 2300 fake SNe, as a function of the input fake SN magnitude. The recovered magnitudes have been averaged over the period 200 to 700 days after maximum light of SN 2011fe, with the vertical error-bars showing the uncertainty in the averaged magnitude. The vertical dashed line denotes the typical limiting magnitude in any individual PTF image ($R_{\rm P48}$ = 20.5). The inset shows the histogram of the magnitude differences over $19 < R_{\rm P48} < 22$, with the best-fitting Gaussian over-plotted on the histogram in blue. The red line denotes the linear correction we apply to the pipeline photometry.

The pipeline generally performs well. For the epoch range we are particularly interested in (+200 to +700 days), when SN 2011fe is expected to be at $R_{\rm P48} \simeq 19 - 22$, we calculate a mean offset of −0.006 with a 0.019 $1\,\sigma$ standard deviation. The outliers on the distribution are found mainly on the fainter side of the magnitude space, especially at mag > 21, where naturally the pipeline under-performs.

3.3.2 Other Data

As well as the new PTF light curve data for SN 2011fe, we also use complementary photometric data from other sources. In particular, we use data from Tsvetkov et al. (2013) from the Crimean Astrophysical Observatory (1m CAO) out to ~600 d, and imaging from the Gemini-N telescope (GMOS North) from Kerzendorf et al. (2014) at around ~900 d, for which we make no attempt to correct for any background light and use it as published. We also use photometric data from the Large Binocular Telescope (LBT) at

~500-1600 d and *HST* imaging from the Shappee et al. (2016) *HST* program at epochs >1000 d (*HST* proposals 13737 and 14166).

These data are compiled together in Appendix A, Table A.2. Note that, unlike the PTF and the LBT light curve, none of these data are based on difference imaging, i.e. there is the possibility of contamination from background light from M101. However, deep pre-explosion *HST* imaging reveals no objects within 0.2" at the position of the SN to a 3-σ limit of 26.6 mag, in F606W (Li et al., 2011b), and thus the late-time *HST* data will be only negligibly contaminated by background light.

Our analysis also requires spectroscopic data, for the calculation of s-corrections (see Chapter 2.4.5), in order to correct the magnitudes estimated from different telescopes and bandpasses to a common system (in this case, $R_{\rm P48}$), and pseudo-bolometric luminosities. A significant amount of spectral data on SN 2011fe at late-time already exist, and we use optical data from the Lick Observatory 3-m telescope, the 4.2-m William Herschel Telescope (WHT), and the 10-m Keck-I and Keck-II telescopes, and near-IR data from LBT. We download all spectra from the WISeREP archive[2] (Yaron & Gal-Yam, 2012), and details are presented in Appendix A, Table A.3.

3.3.3 The late-time light curve of SN 2011fe

In Fig. 3.4, we present the late-time photometry of SN 2011fe obtained from PTF. The PTF coverage is shown from around +200 d when the supernova was $R_{\rm P48} \sim 16$, through to +1200 d, when the SN was not detected even in measurements averaged over several weeks. There was no PTF coverage from around +620 d to +780 d, as the field was not included in the iPTF survey during this period. We also show the other (s-corrected to the $R_{\rm P48}$) ground- and space-based optical data. Such a procedure assumes that our spectra match the SEDs of the SN on the photometric epochs. We check this in Fig. 3.5, where we compare the late-time photometric V-R colour of SN 2011fe with the equivalent colour calculated from the available spectra. The photometric and 'spectral' colours are consistent, with no indication of a mis-match between the colours calculated from the spectra and those from the photometry.

We identify three distinct regions of interest in the $R_{\rm P48}$ light curve. The first corresponds to 200 to 400 d, the second to 400 to 600 d and the third to 600 to 1600 d. During the first and third regions, the light curve is declining linearly in magnitude space (but with different slopes), qualitatively consistent with a light curve powered by radioactive decay. During the first period, we calculate a slope of 1.53 ± 0.09 mag per 100 days (consistent with similar studies of SNe Ia in the R band, see Milne et al., 2001; Lair et al., 2006)

[2] http://wiserep.weizmann.ac.il/

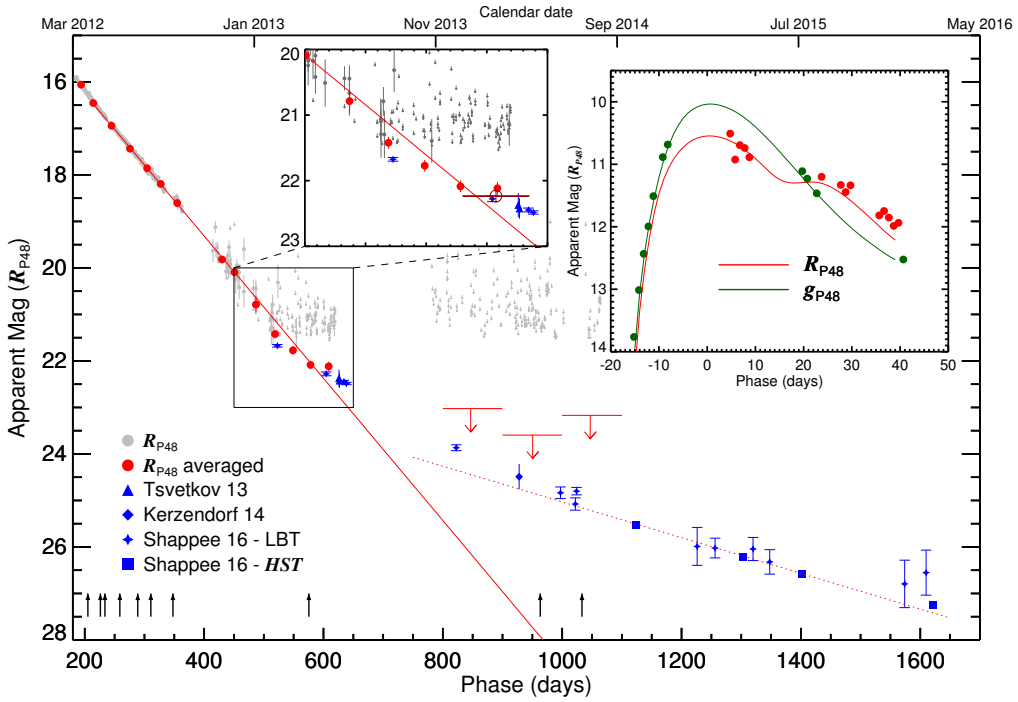

FIGURE 3.4: The SN 2011fe late-time R_{P48}-band light curve as a function of phase in days since maximum light. The light grey points show every individual PTF observation; when the significance of the detection is $< 3\sigma$, an upper limit is plotted at 3σ. The red filled circles are averages of the PTF data in bins of 25 days. The literature photometric data are plotted as blue symbols and the sources are given in the legend; all are originally observed in some form of R-band filter (see Appendix A, Table A.2) and s-corrected in the figure to R_{P48} (see Chapter 2.4.5 for details). The black vertical arrows correspond to the epochs of the spectral sample (see Appendix A, Table A.3). The red solid line is a linear fit over the region of +200 to +600 d, and the red dashed line a fit over +700 to +1620 d. The left inset shows a zoom of the region between +450 to +650 d, with the dark red open circle showing the averaged magnitude between $\sim 580 - 640$d. The right inset shows the light curve around maximum light, together with fits from the SIFTO light curve fitter. Uncertainties are always plotted, but are often smaller than the data points.

and in the third region a slope of 0.37 ± 0.12 mag per 100 days. In the second region, the light curve appears to deviate from a simple linear radioactive decay, showing a faster decline for ~100 d followed by an apparent flattening over the next ~50 d. The final PTF measurement is consistent with the Tsvetkov et al. (2013) R-band measurement at 625 d.

3.4 Towards a bolometric light curve

A more detailed and quantitative investigation requires a bolometric light curve covering wavelengths from the ultraviolet (UV) to the infrared (IR). However, there are

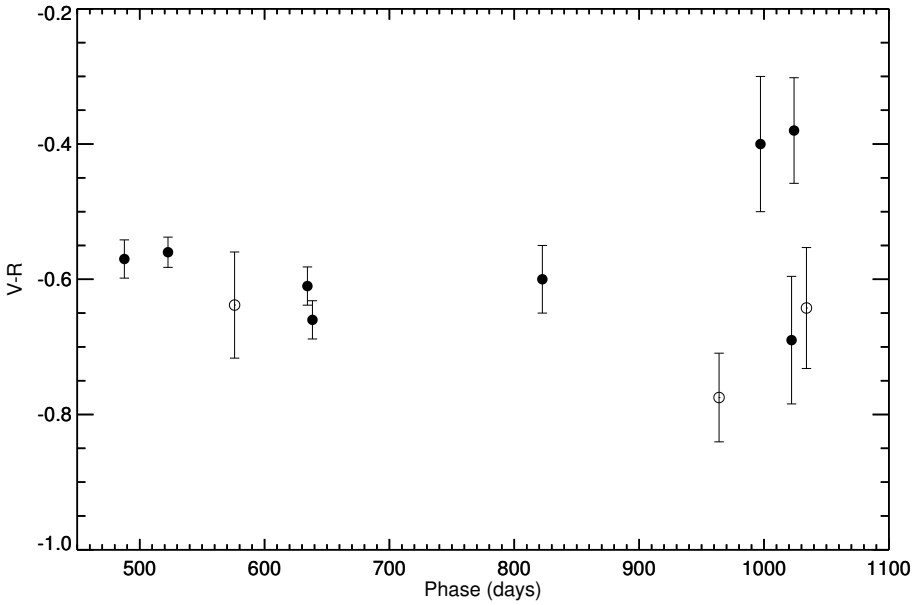

FIGURE 3.5: The *V*-*R* colour of SN 2011fe at late times. Full black circles are the photometric LBT colour from Shappee et al. (2016), and open black circles denoted the spectroscopic colour of the 576, 964 and 1034 d spectra (see Appendix A, Table A.3). Uncertainties are reported in 1 σ confidence.

few published observations in the near-IR of SN 2011fe at these late phases: the latest spectroscopic observation is at ≃250 d (Mazzali et al., 2015), while for photometric observations, available data include LBT (*J* band) and *HST* imaging, both presented in Shappee et al. (2016). Thus a true bolometric light curve is not possible to directly construct, and we restrict ourselves to constructing a bolometric light curve based only on the optical data where good spectral coverage does exist, which we hereafter refer to as a 'pseudo'-bolometric light curve. We then correct for the likely near-IR contribution in our model, based on data from SN 2011fe and other events, when analysing this pseudo-bolometric light curve.

Table A.3 describes the published spectral data available, and three of these late-time spectra, at 348 d, 576 d and 1034 d, are shown in Fig. 3.6. We introduce two pseudo-bolometric box filters, a wide 'BFW' filter from 3550-9500 Å, and a slightly narrower 'BFN' filter covering 4500-9500 Å. The narrower BFN filter is designed for the narrower wavelength coverage of the 576 d spectrum. These two filter responses are also shown in Fig. 3.6, together with the $R_{\rm P48}$ filter response. The spectral features clearly evolve over these phases, principally with the disappearance of the [Fe III] line at 4700 Å. Most relevant for the $R_{\rm P48}$ filter is the weakening of the 7200 Å feature relative to the other stronger lines at bluer wavelengths (see Taubenberger et al., 2015).

We flux-calibrate the spectra in Table A.3 by estimating the $R_{\rm P48}$ magnitude on the

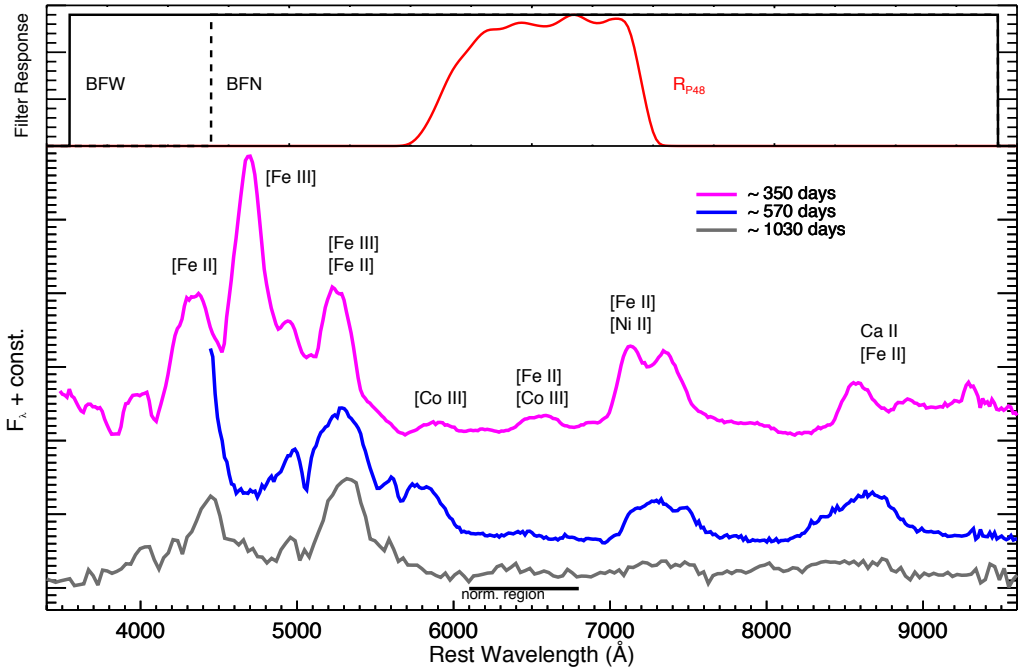

FIGURE 3.6: Lower panel: Comparison of three late-time optical spectra of SN 2011fe at (from top to bottom) 348 d, 576 d and 1034 d. Common nebular lines are marked. Upper panel: The filter responses of the R_{P48} filter (red), the wide bolometric box filter (BFW, solid black) and the narrow bolometric box filter (BFN, dashed black).

epoch of the spectral observation using linear interpolation. For the +576 d spectrum that coincides with the apparent break in the light curve, we average the photometry from +550 to +650 d instead of using linear interpolation. We rescale each spectrum so that it reproduces the estimated R_{P48} apparent magnitude when integrated through that filter, and then measure the pseudo-bolometric fluxes by integrating through the BFW or BFN filters as appropriate. This is, essentially, a flux-space 'bolometric correction' for the R_{P48} data determined on each epoch on which a spectrum exists.

We then extend the bolometric corrections made on epochs on which spectra exist, to any epoch on which we have R_{P48} data. To do this, we check the stability of the bolometric correction by plotting the ratio of the flux in R_{P48} to the flux in the BFW and BFN filters in Fig. 3.7. The two ratios evolve slowly as a function of time, with the relative flux in the R_{P48} filter generally increasing. The exception to the trend is the data point from the spectrum at +576 d in the BFN filter, where there is an apparent drop in the ratio. This is temporally coincident with the apparent break in the R_{P48}-band light curve (Fig. 3.4).

We fit a simple smooth spline function to the BFN ratio data to interpolate over this time period, superimposed on a linear fit to the remaining epochs for interpolation at other epochs (Fig. 3.7). We scale this spline fit to the BFW data, and combined with a

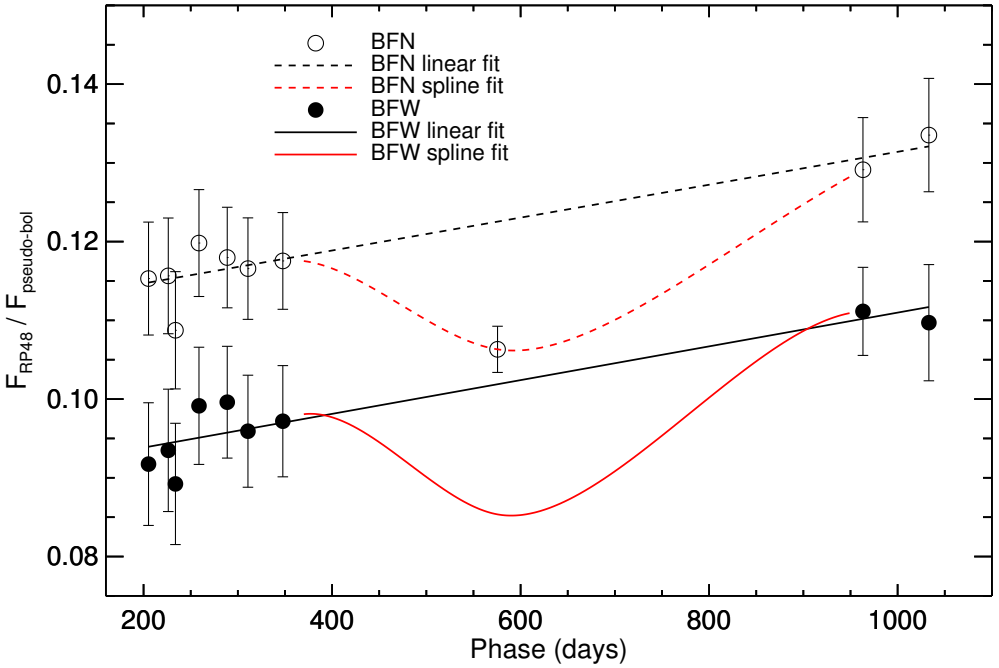

FIGURE 3.7: The ratio of the flux in the R_{P48} filter to that in the BFN filter (open circles) and the BFW filter (filled circles) for the spectral sequence in Table A.3. Overplotted are the linear (black) and spline (red) fits for the BFN filter (dashed lines) and the BFW filter (solid lines). The BFW spline is a rescaled version of the BFN fit, and is not independent.

linear fit to the other BFW data. This process allows us to translate the *R*-band data on any epoch into a pseudo-bolometric luminosity, and thus construct a pseudo-bolometric light curve, presented in Appendix A, Table A.3.

3.5 Analysis of the bolometric light curve

We now turn to the analysis of the radioactive decay chains that may explain the shape and evolution of the pseudo-bolometric light curve of SN 2011fe. Our goals in this section are two-fold. The first goal is to confirm that the shape of the pseudo-bolometric light curve can be explained in terms of the radioactive decay chains that are expected to be present, including ^{57}Co and ^{55}Fe (e.g., Seitenzahl et al., 2014; Graur et al., 2016; Shappee et al., 2016). The second goal is to attempt to robustly determine the relative amounts of ^{56}Co, ^{57}Co and ^{55}Fe that are required to reproduce the pseudo-bolometric light curve evolution. We first introduce the framework of our modelling and the assumptions and then discuss procedures for adjusting the model luminosity to account for near-IR contributions.

3.5.1 Analysis framework

Several different decay chains may contribute at different levels during the time period that we are sampling. These produce not only γ-rays and positrons but also electrons and X-rays that can be thermalised and deposit their energy in the expanding SN ejecta. At the late-time epochs that we study here, when the SN ejecta become increasingly optically thin, the delay between the energy deposition from the radioactive decay and the emission of optical radiation becomes short, and the light curve time-scale becomes driven by the various decay chains.

We consider three decay chains that are likely to contribute to the bolometric output:

$$^{56}\mathrm{Ni} \xrightarrow{\mathrm{t}_{1/2}=6.08\,\mathrm{d}} {}^{56}\mathrm{Co} \xrightarrow{\mathrm{t}_{1/2}=77.2\,\mathrm{d}} {}^{56}\mathrm{Fe} \tag{3.2}$$

$$^{57}\mathrm{Ni} \xrightarrow{\mathrm{t}_{1/2}=35.6\,\mathrm{h}} {}^{57}\mathrm{Co} \xrightarrow{\mathrm{t}_{1/2}=271.2\,\mathrm{d}} {}^{57}\mathrm{Fe} \tag{3.3}$$

$$^{55}\mathrm{Co} \xrightarrow{\mathrm{t}_{1/2}=17.53\,\mathrm{h}} {}^{55}\mathrm{Fe} \xrightarrow{\mathrm{t}_{1/2}=999.67\,\mathrm{d}} {}^{55}\mathrm{Mn} \tag{3.4}$$

where the half-life is given in each case. Note that in each of these chains, one of the decay steps is significantly longer than the other; thus we make the approximation that only ^{56}Co, ^{57}Co and ^{55}Fe are important in our late-time ($t > 200$ d) light curve analysis (we neglect other decay chains such as ^{44}Ti as they will be sub-dominant for many years; e.g., Seitenzahl et al., 2009).

Under these approximations, the bolometric luminosity L for a given decay chain is

$$L_A(t) = \frac{2.221}{A} \frac{\lambda_A}{\mathrm{days}^{-1}} \frac{M(A)}{\mathrm{M}_\odot} \frac{q_A^l f_A^l(t) + q_A^\gamma f_A^\gamma(t) + q_A^x}{\mathrm{keV}} \times \exp(-\lambda_A t) \times 10^{43} \mathrm{erg\ s}^{-1}, \tag{3.5}$$

where t is the time since explosion, A is the atomic number of the decay chain, $M(A)$ is the initial mass synthesised, λ_A is the decay constant, q_A^l, q_A^γ and q_A^x are the average energies per decay carried by the (electrically charged) leptons, γ-rays and X-rays, and f_A^l and f_A^γ are the fractions of the leptons and γ-rays absorbed in the ejecta, i.e. that contribute to the luminosity. Under the assumption of homologous expansion, these fractions are time-dependent and are given by

TABLE 3.1: Radioactive decay constants and energies per decay

Nucleus	λ_A days^{-1}	q^γ [keV]	q^x [keV]	q^l [keV][a]
^{56}Co	8.975e-3	3606.0	1.587	124.61
^{57}Co	2.551e-3	121.6	3.6	17.814
^{55}Fe	6.916e-4	–	1.635	3.973

[a]Including e^+, Auger e^- and IC e^-

$$f_A^{l,\gamma}(t) = 1 - \exp\left[-\left(\frac{t_A^{l,\gamma}}{t}\right)^2\right], \tag{3.6}$$

where $t_A^{l,\gamma}$ corresponds to the time when the optical depth, $\tau_A^{l,\gamma}$, for positrons/leptons or γ-rays becomes unity, i.e. $\tau_A^{l,\gamma} = \left(t_A^{l,\gamma}/t\right)^2$. In this framework, the effective opacity for each species, $k_A^{l,\gamma}$, is proportional to t_A^2. Under the leptonic contribution channel, we include positrons, Auger and internal conversion electrons.

The values for the decay energies and constants are presented in Table 3.1, and can be found at the National Nuclear Data Center[3].

In our analysis, we make the following simplifications:

1. We fix $t_{56}^\gamma = 35$ d. This parameter is not well-measured by the late-time pseudo-bolometric light curve, but is well-constrained in the literature: Sollerman et al. (2004), Stritzinger & Sollerman (2007) and Leloudas et al. (2009) have calculated t_{56}^γ for SN 2000cx, SN 2001el and SN 2003hv to be $t_{56}^\gamma = 31.5$, 35, and 32.5 d respectively, while Zhang et al. (2016) infer $t_{56}^\gamma = 34.5$ d for SN 2011fe. We include the (small) contribution to the heating from ^{56}Co γ-rays even at very late times.

2. We fix $t_{57}^\gamma = 160$ d. This parameter is, again, not well-measured. The main γ-ray contribution from ^{57}Co are the low-energy 14.4, 122.1 and 136.5 keV lines. For the 14.4 keV, we assume complete trapping. For the 122.1 and 136.5 keV ones, we use a value for t_{57}^γ that suggests a 10% trapping at 500 days.

3. We treat t_{56}^l, t_{57}^l and t_{55}^l as free parameters in some of the fits, i.e., we do not assume full trapping of the leptonic channel.

4. We assume complete trapping of the low energy X-rays.

[3]http://www.nndc.bnl.gov

3.5.2 The non-optical contribution

The pseudo-bolometric light curve (section 3.4) is based only on optical data. We must therefore account for the radiation emerging at non-optical wavelengths by either correcting the data, or by adjusting the model. Here we choose to adjust the model, keeping our data as close to the observations as possible.

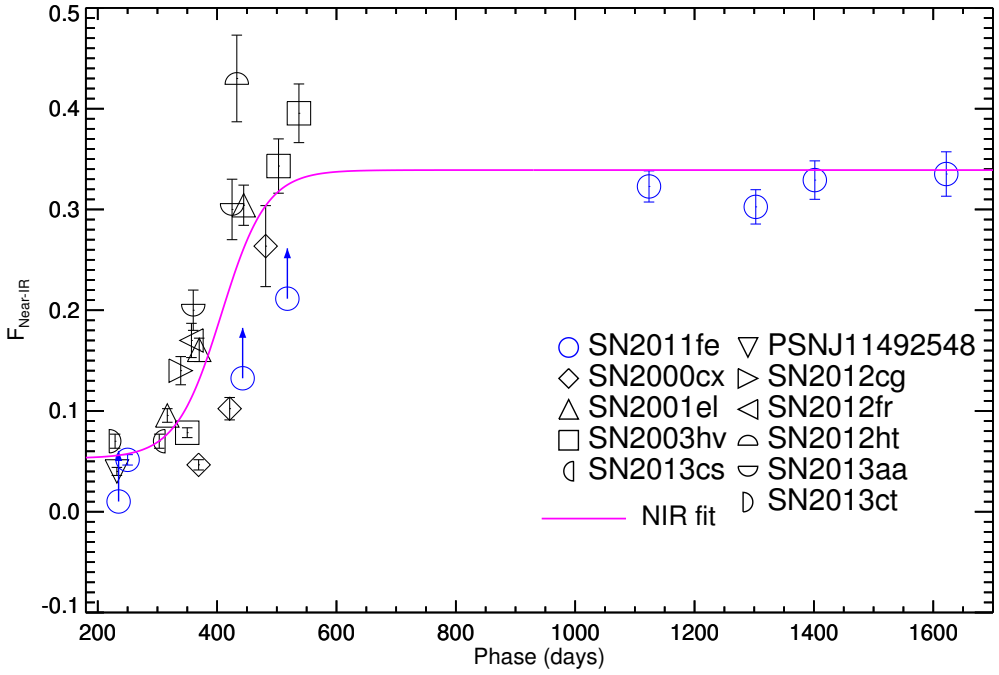

FIGURE 3.8: The Near-IR contribution, $F_{\mathrm{near-IR}}(t)$ (equation 3.7), for SNe Ia taken from the literature; see section 3.5.2. The blue points show data for SN 2011fe. The magenta line corresponds to the functional form that we adopt in our fitting to SN 2011fe.

In Fig. 3.8, we present the total near-IR contribution for SN 2000cx, SN 2001el and SN 2003hv based on broad-band imaging (Sollerman et al., 2004; Stritzinger & Sollerman, 2007; Leloudas et al., 2009). We also use near-IR estimates based on nebular spectra of 7 SNe Ia taken from Maguire et al. (in preparation) and observed in the optical and near-IR with the Very Large Telescope (VLT) XShooter spectrograph. Finally, we include a point for SN 2011fe obtained by integrating the available near-IR spectrum at 250 d (Table A.3), the near-IR LBT data (plotted with upward arrows, since they are only *J*-band observations) and the *HST* data from Shappee et al. (2016) at later phases. Note for the literature SNe Ia the rapidly increasing near-IR flux contribution over 400–600 d, as flux is presumably redistributed from the optical to the near-IR. This generally leads to optical light curves declining more rapidly than near-IR light curves over these epochs due to the decreasing temperature in the ejecta and the consequently

increased importance of the near-IR [Fe II] lines (e.g. Sollerman et al., 2004; Leloudas et al., 2009).

The calculation of the near-IR contributions of SN 2000cx, SN 2001el and SN 2003hv were performed as follows. The published light-curve magnitudes were extinction corrected and converted to fluxes, with linear interpolation for the missing epochs. The optical fluxes were used to adjust the available spectra of SN 2011fe so that the spectra reproduce the optical colours, using the 'mangling' technique of Hsiao et al. (2007) and Conley et al. (2008), and then integrated through the 'BFW' filter (or the 'BFN' filter, adding the appropriate correction from section 3.4), thus calculating the optical part of the bolometric light curve. The near-IR *JHK* fluxes were integrated over their effective filter area. The near-IR contribution is then defined as:

$$F_{\rm nir}(t) = \frac{L_{\rm nir}(t)}{L_{\rm opt}(t) + L_{\rm nir}(t)} \tag{3.7}$$

While the absolute contributions differ from SN to SN, the general shape is similar, indicating a colour evolution over ~300–600 d that shifts flux from the optical to near-IR wavelengths. We fit a simple functional form, based on the logistic or sigmoid function, to these data to model this near-IR contribution as a function of time. While a more complex near-IR colour evolution is possible, leading to a local maximum at ≃650 d, seen in SN 2003hv (Fig. 8 of Leloudas et al., 2009), we will retain this simple functional form, mainly because the last data point of SN 2003hv is based on extrapolating the light curve, under the assumption that the $J - H$ and $H - K$ colours do not change, making the final calculation highly speculative.

The final model luminosity, $L_{\rm model}(t)$, that we fit to our pseudo-bolometric light curve is then

$$L_{\rm model}(t) = [L_{55}(t) + L_{56}(t) + L_{57}(t)] \times [1 - F_{\rm nir}(t)] \tag{3.8}$$

where L_{55}, L_{56} and L_{57} are given by equation (3.5), and $F_{\rm nir}$ is determined as detailed above.

We also estimate the contribution of mid-IR emission over 500–600 d from the *Spitzer* light curve obtained with the Infrared Array Camera (IRAC) channels 1 and 2 (at 3.6 and 4.5 μm respectively) presented in Johansson et al. (2014). We can only estimate an upper limit, but find a total mid-IR contribution of ~1 per cent, indicating that little flux is emitted in the mid-IR region at these epochs. We defer a discussion of the far-IR region (and a possible IRC) to the next section. Finally, we note that the contribution

at UV wavelengths smaller than 3500 Å is expected to be small, since it is dominated by optically thick lines, and the only SN 2011fe nebular UV spectrum shows little UV flux (Friesen et al., 2017).

3.6 Results

The late-time pseudo-bolometric light curve of SN 2011fe derived in section 3.4 is shown in Fig. 3.9. In this section, we consider a range of different model fits to this light curve and attempt to constrain the various fit parameters.

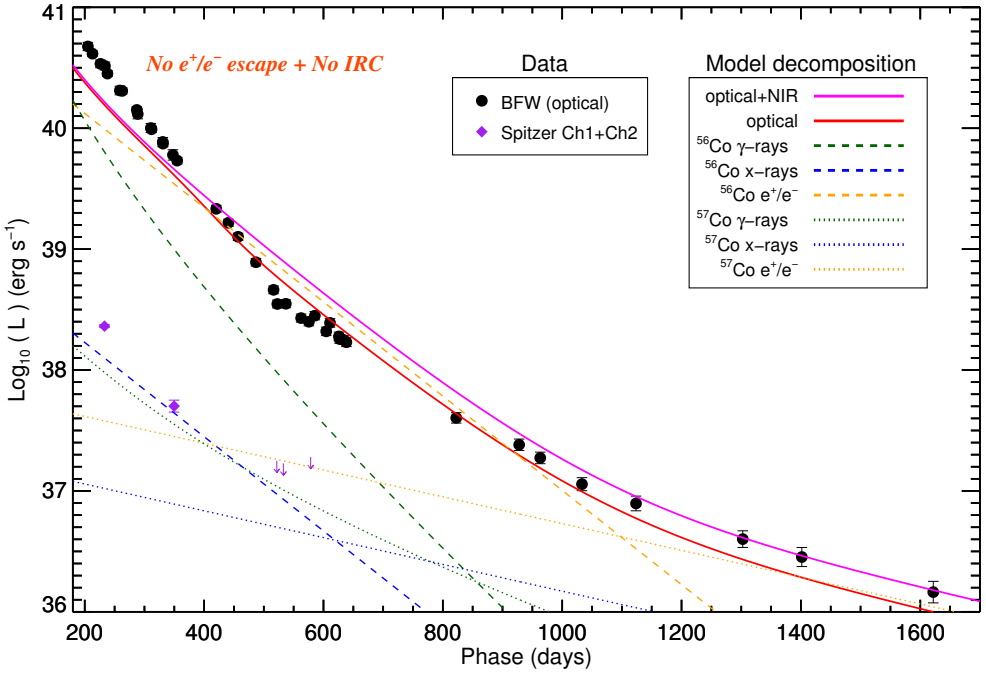

FIGURE 3.9: The pseudo-bolometric light curve of SN 2011fe shown as filled black circles; see section 3.4 for details of the light curve construction. This figure shows the fit of the *Case 0* model (section 3.6), assuming complete positron/electron trapping and no emergent far-IR flux. The magenta line is the total (optical plus near-IR) bolometric luminosity, and the red line is the final model fit to the pseudo-bolometric light curve data based on equation (3.8), once the near-IR contribution is accounted for. The mid-IR *Spitzer* light curve (Johansson et al., 2014) is plotted as purple diamonds and upper limits. We include the decomposition of our model into the two decay chains of $A = 56$ and $A = 57$, separated into the γ-ray, X-ray and positron/electron components, shown in the legend.

We begin by fitting equation 3.8, including all three decay chains (equation 3.2 to equation 3.4), directly to the data, assuming full trapping of positrons/electrons and no flux emerging at $\lambda > 2.5\,\mu$m (Fig. 3.9), which we refer to as *Case 0*. The best-fitting parameters are reported in Appendix B, Table B.1 and we include a smaller version in Table 3.2 for illustration purposes. This provides a very poor fit to the data with a reduced χ^2

TABLE 3.2: The best-fitting parameters for the modelling of the pseudo-bolometric light curve of SN 2011fe

Model	$M(56)$ ($M_\odot$)	$M(57)$ ($M_\odot$)	$M(57)/M(56)$ $(^{57}Fe/^{56}Fe)_\odot$ [a]	t^l_{56} (days)	t^l_{57} (days)	χ^2_{DOF}
Case 0	0.179(0.003)	0.004(0.001)	0.963(0.114)	—	—	24.09
Case 1	0.461(0.041)	0.014(0.005)	1.322(0.473)	233(30)	886(427)	2.47
Case 1 [b]	0.442(0.035)	0.015(0.007)	1.47(0.731)	249(32)	812(551)	2.25
Case 2	0.355(0.017)	0.021(0.003)	2.571(0.346)	—	—	2.08
Case 2 [b]	0.357(0.018)	0.022(0.003)	2.627(0.391)	—	—	1.96

[a] Assuming $\left(^{57}Fe/^{56}Fe\right)_\odot = 0.023$ (Asplund et al., 2009)
[b] excluding 550-650d

(the χ^2 per degree of freedom) of $\chi^2_{DOF} \simeq 24$ for 36 degrees of freedom. The model cannot simultaneously fit the data over 200–400 d and over 900–1600 d, and prefers a low ^{56}Ni mass ($M(56) = 0.18\,M_\odot$).

This $M(56)$ is significantly lower than other independent estimates. Mazzali et al. (2015) estimated $M(56) = 0.47 \pm 0.05\,M_\odot$ from nebular spectroscopy. Pereira et al. (2013) used the bolometric light curve around peak brightness to estimate $M(56) = (0.44 \pm 0.08) \times (1.2/\alpha)\,M_\odot$, where $\alpha = 1.2 \pm 0.2$ is the ratio of bolometric to radioactivity luminosities (instead, assuming $\alpha = 1.0 \pm 0.2$ would give $M(56) = 0.53 \pm 0.11\,M_\odot$). This suggests that the model needs a way to lose energy outside of the optical/near-IR wavebands. We next consider two ways in which this could occur.

For *Case 1*, which we refer to as the 'positron/electron escape case', we allow the positron/electron escape fractions (t^l_{56}, t^l_{57}) to be free parameters in the fit. We then find (Table 3.2) $M(56) = 0.461 \pm 0.041\,M_\odot$, $M(57) = 0.014 \pm 0.004\,M_\odot$ and $M(55) = 0.0\,M_\odot$, with a much improved fit quality ($\chi^2_{DOF} \simeq 2.5$ for 34 degrees of freedom, Fig. 3.10). This fit provides strong evidence for the presence of the ^{57}Ni decay chain. The fit also requires a considerable positron/electron escape over the phase range of 200–600 d; for example, at 500 d ≃75 per cent of the leptonic energetic output escapes the ejecta. The inferred trapping functions for this fit are shown in Fig. 3.11.

We can estimate the density ratio n_{57}/n_{56} for the SN material in order for the low energy Auger and internal conversion electrons from the ^{57}Co decay to have the same escape likelihood as the high energy ^{56}Co positrons. The escape likelihood for the charged leptons is $\sim 1/n_A\sigma_A$, where σ_A is the total cross section for Coulomb scattering, which, in turn, is $\sim \epsilon_A^{-2}$, where ϵ_A is the energy per decay (see Table 3.1). Using these scaling relations, we find $n_{57}/n_{56} = (\epsilon_{57}/\epsilon_{56})^2 \simeq 0.02$. From our fits, and since the opacity k^l_A is proportional to t^2_A, we recover $n_A \sim t_A^{-2}$. From our estimates for the trapping time scales, we estimate $n_{57}/n_{56} = (t_{56}/t_{57})^2 \simeq 0.07$.

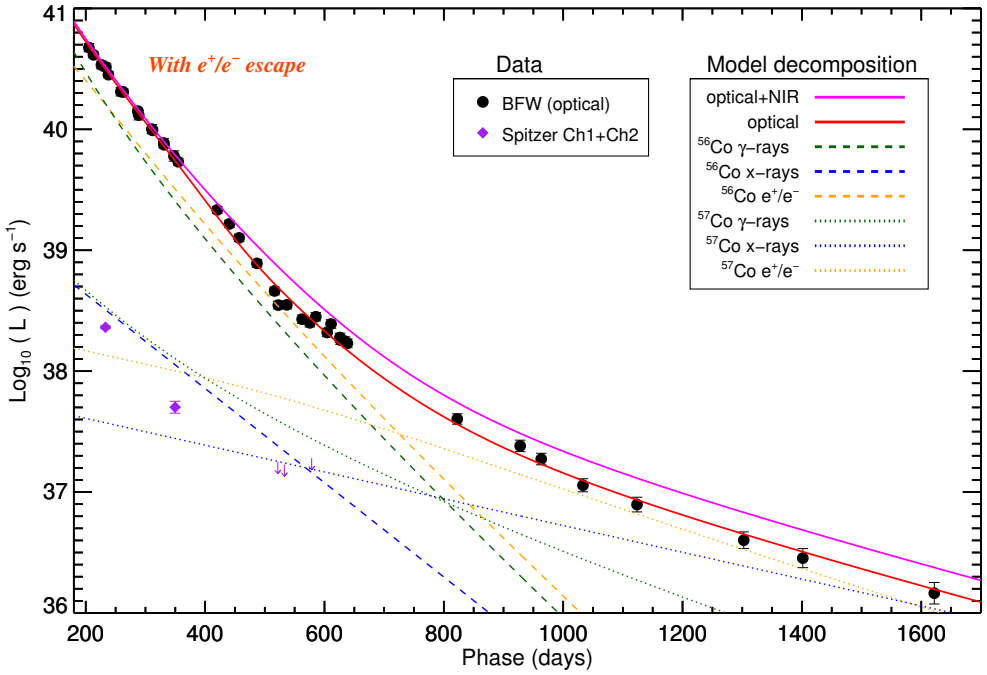

FIGURE 3.10: The pseudo-bolometric light curve of SN 2011fe shown as filled black circles; see section 3.4 for details of the light curve construction. This figure shows the fit of the *Case 1* model (section 3.6), allowing for positron/electron escape and assuming that the optical light curve and near-IR corrections (section 3.5.2) account for all of the emerging photons. Fig. 3.12 shows the fit of the *Case 2* model, which does not allow of positron/electron escape but instead allows for luminosity to emerge at wavelengths greater than 2.5 μm.

The inferred ^{56}Ni mass, $M(56) = 0.461\,M_{\odot}$, is consistent with other independent estimates (see above). The small difference compared to that from nebular spectroscopy (around 3 per cent) could be attributed to some part of the spectral energy distribution that is not covered by the pseudo-bolometric filter or near-IR correction. Generally, however, this fit provides evidence that the pseudo-bolometric light curve and the near-IR modelling are accounting for most of the emitted photons, *assuming* that the charged leptons are able to escape the ejecta.

Note that from around +500 d onwards, the optical bolometric light curve begins to decline faster, before beginning to flatten just before +600 d. This behaviour, particularly the flattening, is not well reproduced by our simple model, although the faster decline occurs at the same time as flux is being redistributed to the near-IR (Fig. 3.8). We therefore also fit the bolometric light curve excluding the phase range of 550–650 d, where the underlying behaviour is not well-understood and shows a different apparent decay rate. The parameters are again reported in Table 3.2 – these are close to the original fit values, but with an improved $\chi^2_{\rm DOF}$.

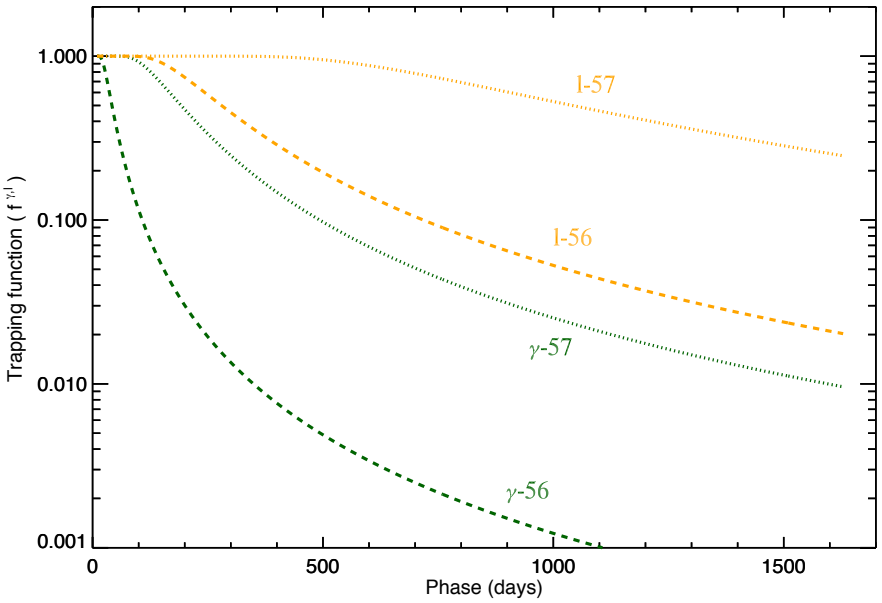

FIGURE 3.11: The inferred trapping functions for γ-rays ($f^{\gamma}(t)$) and positrons ($f^{l}(t)$), from equation (3.6), resulting from the *Case 1* fits. The green lines correspond to γ-rays with t^{γ}_{56} = 35 d (dashed) and t^{γ}_{57} = 160 d (dotted) that are assumed for ^{56}Co and ^{57}Co decay respectively. The yellow lines correspond to the leptonic trapping from the ^{56}Co decay, t^{l}_{56} = 233 d (dashed), and the leptonic trapping for ^{57}Co decay, t^{l}_{57} = 886 d (dotted).

Although we have accounted for the non-optical luminosity in our fitting up to 2.5 μm, there are strong theoretical reasons to expect significant mid/far-IR luminosity at late-times due to the IRC. Therefore, in *Case 2* we use a different approach for the non-optical contribution. Motivated by the fact that there has not been any strong observational evidence for positron/electron escape in SNe Ia, we investigate the 'IRC case', where a substantial amount of flux is shifted to far-IR wavelengths. For this, we fit a model where we force complete positron/electron trapping for the full bolometric light curve; in other words, we fix f^{l}_{A} in equation (3.5) to 1. This final model luminosity then will be

$$L_{\rm model}(t) = [L_{55}(t) + L_{56}(t) + L_{57}(t)] \times \left[1 - F_{\rm non-opt}(t)\right] \tag{3.9}$$

where L_{55}, L_{56} and L_{57} are given as before, by equation (3.5), and $F_{\rm non-opt}$ corresponds to the *total* non-optical contribution, for which we assume the same logistic functional form as in Fig. 3.8, but with a limit at 200 d to be $\simeq$1 per cent. We then fit for $M(56)$, $M(57)$, $M(55)$ and the total non-optical contribution. The result is plotted in Fig. 3.12 and again reported in Table 3.2.

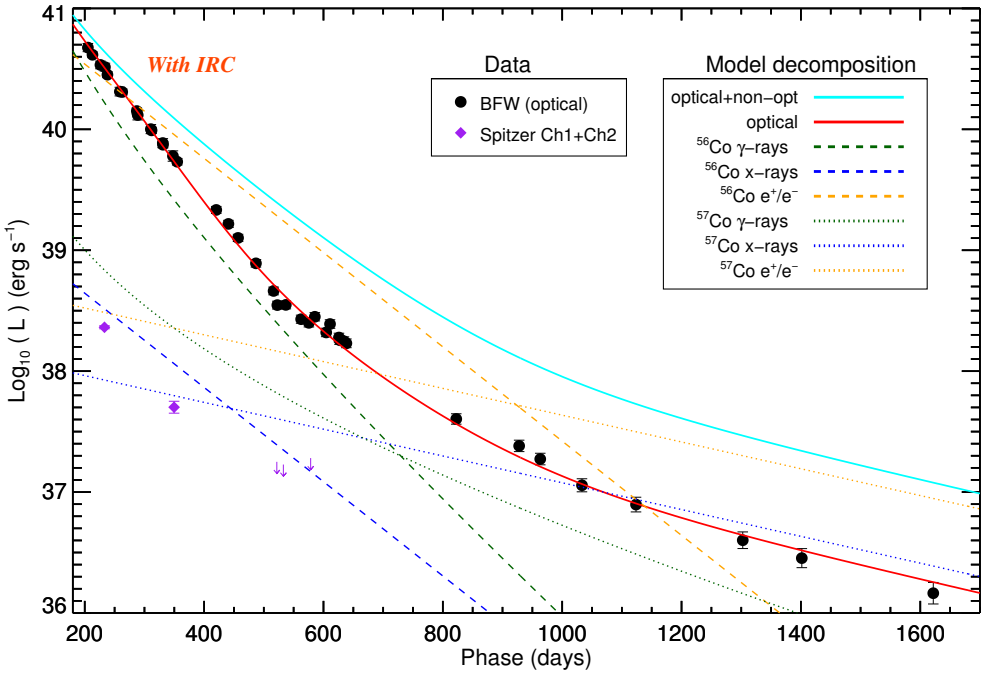

FIGURE 3.12: As Fig. 3.10, but for the *Case 2* model that accounts for flux emerging at $\lambda > 2.5\,\mu$m (i.e., an infrared catastrophe; IRC) and assumes full positron/electron trapping. Here, the cyan line denotes the inferred total (optical+near-IR+mid/far-IR) bolometric light curve of the SN.

For this fit, we find $M(56) = 0.355 \pm 0.017\,M_{\odot}$, $M(57) = 0.021 \pm 0.003\,M_{\odot}$ and $M(55) = 0.0\,M_{\odot}$ with $\chi^2_{\rm DOF} \simeq 2$ for 33 degrees of freedom. Note that this fit prefers a smaller $M(56)$, lower than previous estimates, indicating that at the earlier part of our bolometric light curve there still is 25 per cent of the flux that is still not probed. Fixing instead the $M(56)$ mass to $M(56) = 0.47\,M_{\odot}$, and allowing the non-optical contribution at 200 d to be unconstrained, we find $M(57) = 0.028 \pm 0.003\,M_{\odot}$ and a non-optical contribution at 200 d equal to 25 per cent, with $\chi^2_{\rm DOF} \simeq 2.04$ for 34 degrees of freedom.

The inferred non-optical contribution increases to $\simeq 85$ per cent at 600 d. This is consistent with Fransson & Jerkstrand (2015), who estimated an 80 per cent non-optical/NIR contribution at 1000 d, although their models indicate that this flux is mainly emitted in the mid-IR. In this analysis, we have assumed a constant evolution of the non-optical contributions after +600 d, the approximate expected epoch of any IRC. This assumption may not be correct, and a colour evolution that decreases the near-IR flux and increases the mid/far-IR one is certainly possible, but not constrained by our data. Note that the *Spitzer* mid-IR flux from Johansson et al. (2014) is very small, although in the event of an IRC, the theoretical prediction is that the fine-structure lines will be redward of the mid-IR *Spitzer* filter bandpass.

3.7 Discussion

We now investigate other physical mechanisms that may contribute to the behaviour of the bolometric late-time light curve, and then discuss the implications of this study in the context of SN Ia explosion models and physics.

3.7.1 Other contributions to the late-time luminosity

Although this simple model provides a good fit to most of the pseudo-bolometric light curve data, other sources of luminosity cannot be ruled out that may effect the late-time light curve. We discuss these in turn (see also a similar discussion in the context of SN 2012cg in Graur et al., 2016).

3.7.1.1 A light echo

The flattening of the light curve of SN 2011fe from around 600 d could be explained by the presence of a dust cloud near the SN that scatters a fraction of the SN light towards the observer, a mechanism known as 'light echo'. Due to the different light travel times, the spectrum observed would then be an integrated combination of the scattered early-time spectra combined with the direct line-of-sight late-time spectrum. This behaviour has been demonstrated for several SNe Ia (e.g. Schmidt et al., 1994; Cappellaro et al., 2001; Drozdov et al., 2015), where the bolometric light curves evolve in a manner consistent with ^{56}Co up to >500–600 d, at which point the light curves flatten. The spectra also evolve from classical SN Ia nebular spectra over ~300–500 d, to spectra showing a blue continuum with broad absorption and nebular emission features super-imposed at ~500–600 d. Schmidt et al. (1994) and Cappellaro et al. (2001) can reproduce the late-time SN Ia spectra with a model light-echo spectrum, constructed by co-adding early-time spectra multiplied by a power-law scattering function, $S_\lambda \propto \lambda^{-\alpha}$, with $\alpha = 1, 2$ (for a more detailed approach see Marino et al., 2015).

While the late-time photometric behaviour of SN 2011fe partly resembles a light echo (e.g., the flattening at ~600 d), a light echo is unlikely to be responsible. The late-time spectra are considerably different to a blue-continuum light echo spectra. We demonstrate this following the procedure of Schmidt et al. (1994) and Cappellaro et al. (2001). We used the available early-time spectra of SN 2011fe from *WISEREP*, spanning −5 to +75 d, and after weighting them by the integrated luminosity at their observed epochs, correcting for reddening and using scattering laws as above, we co-add them constructing an expected light echo spectrum. In Figure 3.13, we compare the late-time

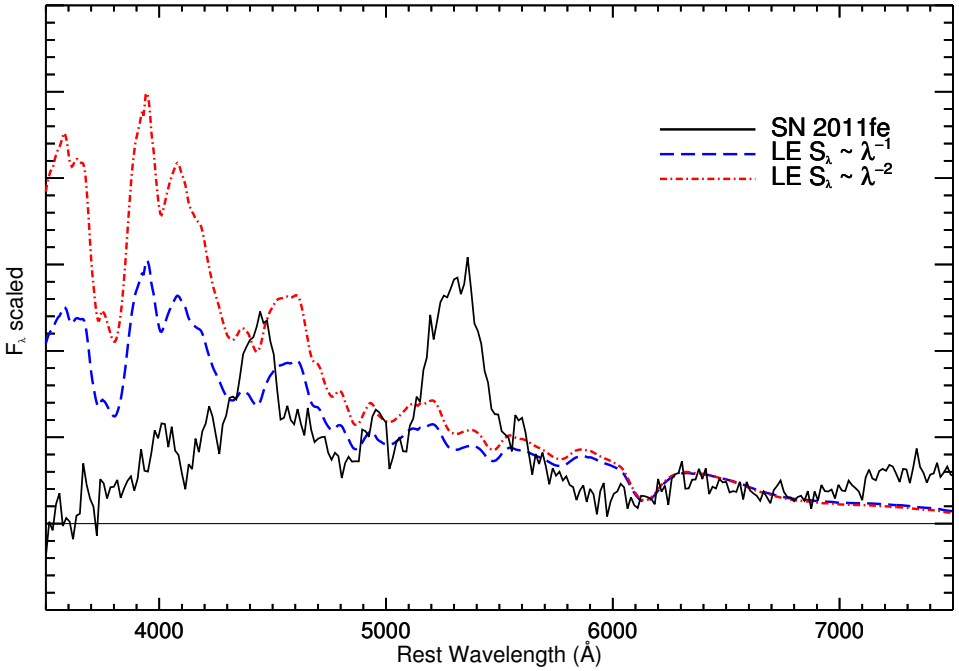

FIGURE 3.13: The +1030 d SN 2011fe spectrum (black solid line; Taubenberger et al., 2015), compared to two synthetic 'light echo' spectra constructed with scattering laws of $S_\lambda \propto \lambda^{-1}$ (blue dashed line) and $S_\lambda \propto \lambda^{-2}$ (red dashed-dotted line). For details see Section 3.7.1.

SN 2011fe spectrum with the two synthesised light echo spectra for the two different scattering laws with $\alpha = 1, 2$. We observe no similarities between the observed and synthetic spectra, and thus conclude that a light echo cannot significantly influence the SN 2011fe light curve. A similar study has been performed by Shappee et al. (2016), reaching similar conclusions.

3.7.1.2 Circumstellar material

A possible explanation for the brightness of SN 2011fe at these late epochs is that the light curve is contaminated by interaction of the ejecta with circumstellar material (CSM) around the explosion. While a complete investigation of these possibilities is beyond the scope of this work, we note that we do not see hydrogen in any of the late-time spectra, indicating little interaction with a CSM, with no hot black-body component and no narrow/intermediate emission lines of any element.

3.7.1.3 A surviving companion

Finally, we consider whether a surviving binary companion could also contribute significant luminosity at late times. If we fit the bolometric light curve with a simple ^{56}Co decline law and a constant luminosity component, simulating a surviving companion, we find $L_{\rm companion} = 7.7 \pm 0.6 \times 10^2\,L_\odot$, with $\chi^2_{\rm DOF} \simeq 8.6$ for 36 degrees of freedom. This upper limit would be consistent with a red giant or main-sequence star of $\sim 6\,{\rm M}_\odot$, but such a possibility is excluded by the analysis of the *HST* pre-explosion imaging by Li et al. (2011b) and stellar evolution timescales (however, less massive companions could have an increased luminosity due to interaction with the SN ejecta). Thus, again, this possibility seems unlikely, again as was also found in Shappee et al. (2016).

3.7.2 Implications

3.7.2.1 The infrared catastrophe or positron/electron escape?

We next investigate whether an infrared catastrophe (IRC) may have occurred in SN 2011fe, and discuss the implications of this phenomenon regarding the late light curve evolution. As discussed in the introduction, the IRC is the result of a rapid cooling in the ejecta, with the thermal emission moving from the optical/near-IR to the mid/far-IR. There is no published direct evidence for a dramatic IRC in SN 2011fe, either in the spectroscopy, where prominent optical emission lines are still seen (e.g., Taubenberger et al., 2015), or in other photometric studies (Kerzendorf et al., 2014).

However, in this work, we have shown that the pseudo-bolometric light curve is difficult to reconcile with the evolution expected from the ^{56}Ni and ^{57}Ni decay chains with models involving complete or nearly-complete trapping of the charged leptons. Such a model can be made to be consistent with the data in the presence of significant positron/electron escape.

We note that such a positron escape is disfavoured, since it would be difficult to explain the distribution of the observed positron signal from the Milky Way. Crocker et al. (2016) determine the required age of a putative stellar source of the Galactic positrons, constrained by the recently revised positron annihilation signal of the bulge, disc, and nucleus of our Milky Way (Siegert et al., 2016). Crocker et al. (2016) require the putative stellar source of the positrons to have an age of 3-6 Gyr and argue strongly against normal SNe Ia (with typical ages of 300–1000 Myr) as the main source of positrons in our Galaxy.

Therefore, taking into account the lack of any evidence for very high positron/electron escape from SNe Ia, we favour the interpretation of the late time light curve evolution as a redistribution of flux from the optical/NIR to the mid/far-IR, similar to an occurrence of an IRC.

3.7.2.2 Evidence for ^{57}Ni and ^{55}Co

The luminosity produced by the ^{57}Ni decay chain is unambiguously detected in this analysis; fits based just on ^{56}Ni cannot reproduce the observed evolution. In principle, a measurement of the ratio of the synthesised ^{57}Ni to ^{56}Ni masses ($M(57)/M(56)$) can possibly disentangle potential explosion mechanisms, and thus provide some insight into the progenitor system. A recent demonstration on the SN Ia SN 2012cg (Graur et al., 2016) claimed $M(57)/M(56) = 1.87^{+0.52}_{-0.48}$ (here we give all ratios in terms of the solar value of $\left(^{57}\mathrm{Fe}/^{56}\mathrm{Fe}\right)_{\odot} = 0.023$; see Asplund et al., 2009), increasing to a higher value of $2.96^{+0.83}_{-0.78}$ when enforcing $M(55) = 0$. Even more recently, Yang et al. (2017) obtained *HST* high precision photometry of SN 2014J and confirmed the presence of ^{57}Ni, with a ratio of $M(57)/M(56) = 3.5^{+0.41}_{-0.37}$. However, such measurements are clearly susceptible to assumptions made in the modelling, and thus systematic uncertainties, including, among others the bolometric correction, electron/positron escape, time-dependent effects etch.

Our fit ratios range from $M(57)/M(56) = 1.3$–2.5, i.e. super-solar. These values are broadly consistent with the ratios predicted for the one-dimensional W7 (1.7; Iwamoto et al., 1999), the two-dimensional (1.4-1.9; Maeda et al., 2010) and three-dimensional (1.3; Seitenzahl et al., 2013) delayed detonation models, but not with the 'violent merger' (1.1; Pakmor et al., 2012) model.

While the systematic uncertainties of the modelling are large, the (simple) models that we have investigated indicate a high $M(57)/M(56)$ ratio, in contradiction with Shappee et al. (2016), pointing to an explosion mechanism with relatively high central density of synthesised ^{56}Ni, in accordance with Mazzali et al. (2014). This kind of explosion mechanisms are associated with channels where accretion towards M_{Ch} occurs, a mechanism that is related to SD progenitor scenarios (however, see Fenn et al. 2016).

In all of the fits, we use a physical prior in the models that all of the synthesised masses must be greater than or equal to zero. The fits including ^{55}Co hit this limit for $M(55)$, precluding the calculation of uncertainties in this parameter. Relaxing this assumption gives a very small negative value for $M(55)$ with an uncertainty of $6.9 \times 10^{-3}\,\mathrm{M}_{\odot}$ and $1.6 \times 10^{-2}\,\mathrm{M}_{\odot}$ for *Case 1* and *Case 2*, respectively. The corresponding upper limit ratios are then $M(55)/M(57) = 0.47$ and 0.56; the corresponding predicted ratios for the two-dimensional delayed detonation models are $0.4 - 0.6$ (Maeda et al., 2010), for the

three-dimensional delayed detonation model (Seitenzahl et al., 2013) the prediction is 0.7, and for the violent merger model (Pakmor et al., 2012; Röpke et al., 2012) 0.25.

3.8 Summary

In this chapter we have presented a late-time optical *R*-band light curve for the type Ia supernova SN 2011fe, measured using data from the Palomar Transient Factory. Combining this light curve with other published photometric data from ground-based telescopes and the *HST*, and with ground-based spectroscopy, we have estimated the pseudo ('optical') bolometric light curve out to 1600 days after peak brightness. We also construct a model for the likely bolometric output in the near-IR. We analyse this light curve using a simple model of energy deposition from three possible decay chains (^{56}Ni, ^{57}Ni and ^{55}Co). The main findings are:

- The bolometric light curve for SN 2011fe can be broadly explained by the radioactive inputs from the ^{56}Ni and ^{57}Ni decay chains. The presence of the ^{57}Ni decay chain is required and is robustly detected in the analysis.
- The PTF *R*-band light curve has a noticeable rapid decline followed by a plateau over 500-600 days. While the rapid decline can be explained by a cooling ejecta and the emergence of [Fe II] lines producing increased near-IR flux, our simple models are unable to adequately explain the plateau feature in the light curve.
- The pseudo-bolometric light curve is not consistent with models that have full trapping of the produced charged leptons and no infrared catastrophe (IRC). An additional route for energy escape outside of the optical/near-IR is required.
- The bolometric light curve is consistent with models that allow for positron/electron escape. In this case, the best-fitting initial ^{56}Ni mass is $M(56) = 0.461 \pm 0.041\,M_{\odot}$, consistent with independent estimates from nebular spectroscopy analysis and Arnett's Law. However this model requires 75 per cent of the charged leptons to escape by 500 d.
- Alternatively, the data are also fully consistent with a model that has complete positron/electron trapping but does allow for a redistribution of flux to the mid-far IR, similar to an IRC (Axelrod, 1980). In this case, around 85 per cent of the total bolometric luminosity must be escaping at non-optical wavelengths by day 600 and onwards.
- For both of these scenarios, the amount of ^{57}Ni we estimate is relatively large, compared to popular explosion models. This large inferred mass indicates high central

density explosion environments, mainly predicted from SD progenitor channels and WD collisions.

- Including contributions from the ^{55}Co decay chain does not improve the quality of the bolometric light curve fits, although this is not well constrained by the dataset. We estimate an upper limit of ^{55}Co mass of $1.6 \times 10^{-2}\,M_{\odot}$.

This work has highlighted the significant systematic uncertainties that are involved in modelling the late-time light curves of SNe Ia, even within a very simple framework. Even though high-quality data were obtained for SN 2011fe during the late phases, a denser time sampling of photometric and spectroscopic late-time observations spanning the optical and infrared are needed for future similar events, particularly over the phase range of 400–800 days, where the ionisation state appears to change and a sharp colour evolution can occur (including mid and far-IR data where possible). We also neglected dependent effects in the modelling, such as freeze-out. While these effects are predicted to be small out to at least 900 days (Fransson & Jerkstrand, 2015), more detailed modelling may provide an improved interpretation of the very late-time light curve. Repeating this study for a larger sample of events will allow us to precisely measure and compare the nickel masses obtained from peak and late times, extracting information on the energetic output of the radioactive decay and confirm whether positron escape and/or an IRC is occurring.

Having established a knowledge of the late-time evolution of SN 2011fe, we turn our attention to the total PTF SN Ia sample. The work on SN 2011fe will provide the reference point, in order to perform, in the next chapter, a statistical study of the late-time light curves of other SNe, investigating the physical properties that shape the late-time behaviour of SNe Ia.

Chapter 4

Late time light curves of PTF Type Ia Supernovae

In this chapter, we will focus on the late-time light curves of SN Ia. Firstly, we will introduce the PTF SNe Ia sample and outline the quality cuts that we apply, towards constructing a representative sub-sample, suitable for late-time studies. We will then describe the method we implement to analyse the late-time light curves, in a statistically comprehensive approach, and present our results. Finally, we will discuss our findings in the context of the progenitor system of SNe Ia.

4.1 Introduction

As discussed in Chapter 1, while SNe Ia continue to be the most mature probe for measuring the accelerating expansion of the Universe, the nature of the progenitor system remains unknown. The controversy includes both the configuration of the binary, known as the single-degenerate (SD) and the double-degenerate (DD) progenitor system, but also the explosion mechanism that unbinds the degenerate star.

An important step towards extracting information regarding this open question has been achieved by PTF. As we already have shown in Chapter 2.1, PTF provided a nearly-complete sample of SNe Ia in the local universe, that span the whole range of the Phillips relationship (Fig. 2.2). Moreover, it provided two of the most well-studied local SN Ia, that represent the best candidates for the two main proposed progenitor channels: for the DD scenario, SN 2011fe (Nugent et al., 2011), discussed at length in Chapter 3 and, for the SD scenario, PTF11kx (Dilday et al., 2012), a SN Ia that showed clear signs of interaction between the SN ejecta and multiple components of circumstellar material

(CSM). The existence of both of these objects demonstrates that multiple progenitor channels contribute to the total population of SNe Ia, at least from the observational point of view.

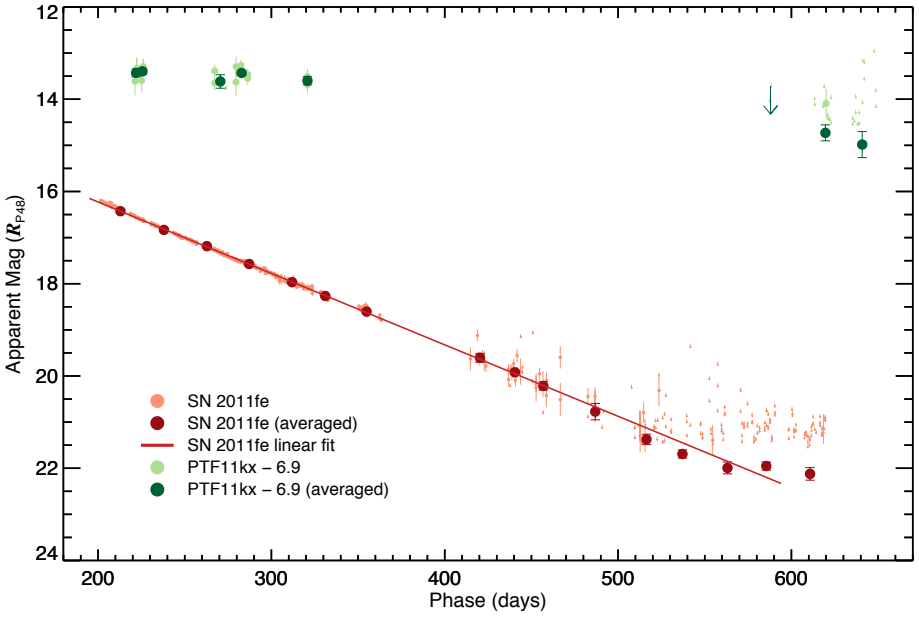

FIGURE 4.1: The late-time light curves of SN 2011fe and PTF 11kx. Individual observations are shown with light red (SN 2011fe) and light green (PTF 11kx), with dark red and dark green the averaged ones in bins of 25 days. The solid red line corresponds to the linear fit to SN 2011fe, similar to Fig. 3.4. The light curve of PTF 11kx has been shifted to the peak magnitude of SN 2011fe.

PTF11kx was discovered on 2011 January 16 UT by PTF, with its classification spectrum taken on 2011 January 26 UT. All of its early spectra show a resemblance with SN 1999aa, an over-luminous and slowly-declining SN Ia, super-imposed with a broad Hα component, an unambiguous sign of SN ejecta interacting with a hydrogen-rich CSM, at a radius of $\sim 10^{16}$ cm from the progenitor. The component's strength increased over time, revealing a complex shell-like CSM structure, with slower expanding material exterior to faster material, with velocities of $\sim 50 - 100\,\mathrm{km\,s^{-1}}$. Spectral observations at even later times (124–680 days after maximum) by Silverman et al. (2013b) strengthen the argument for the SN Ia-CSM nature of PTF11kx, showing that these blue-shifted and slow-moving features are directly related to, and probably previously ejected by, the progenitor system itself. Both of these studies argue that the spectral characteristics of PTF11kx are most consistent with a symbiotic binary progenitor system, similar to RS Oph (Patat et al., 2011b), that experienced multiple past nova eruptions during the mass-accretion phase (Moore & Bildsten, 2012). Recently, Graham et al. (2017) present spectroscopic observations of PTF11kx at 1342 days after maximum, demonstrating the persistence of the broad Hα component, with a similar profile as in the early-time

observations. In Fig. 4.1 we present the late-time light curve of PTF11kx, alongside SN 2011fe. PTF11kx is ~ 4 mags brighter than SN 2011fe at ~ 200 days after maximum, remaining ~ 7 mags brighter at ~ 600 days.

PTF11kx was not the only SN Ia with signs of interaction with its CSM. Other SNe Ia that showed similar properties include SN 1997cy (Turatto et al., 2000), SN 1999E (Rigon et al., 2003) and, most prominently, SN 2002ic (Hamuy et al., 2003) and SN 2005gj (Aldering et al., 2006). Silverman et al. (2013a) have conducted a systematic search for this rare subclass of SNe Ia, identifying 16 SN Ia-CSM objects, nine of them previously known (including SN 2002ic and SN 2005gj), and seven new discoveries from PTF, previously identified as Type IIn supernovae (SNe IIn). All of these objects appear to be somewhat more luminous than normal SNe Ia, with spectra resembling a 91T-like spectrum plus Hα emission. The hosts of these SNe appear to be late-type spirals or dwarf irregulars. Moreover, a statistical study by Leloudas et al. (2015) has shown that the connection of 91T-like SNe Ia with the SN Ia-CSM has a real physical origin, and they propose that 91T-like SNe Ia result from single degenerate progenitors. Finally, Fisher & Jumper (2015) argue that SD SNe Ia should preferentially be over-luminous 91T-like events, by analytically deriving certain conditions that lead to a transition from central ignitions to buoyancy-driven ones. They also calculate these events' contribution to the overall normal SN Ia rate, and find that these are not likely to exceed 1% of the total SN Ia rate, demonstrating the rare nature of these objects.

Our study in this chapter is directly motivated from the above works. Our goal is to perform the reverse study of Silverman et al. (2013a): Instead of spectroscopically looking for hidden SNe Ia in the PTF sample of SNe IIn, look photometrically in the PTF sample of SN Ia for events that show excessive brightness at late times compared to the normal SN Ia population and identify new SN Ia-CSMs, or less extreme versions of them, with a focus on the over-luminous ones. There are two main arguments for using PTF: 1) The PTF sample includes SN 2011fe and PTF11kx, the two extremes at the parameter space that we will investigate, providing a consistent approach, and 2) the wavelength range of the $R_{\rm P48}$ filter that was used for PTF covers the Hα region for local SNe Ia. In the next section, we will describe the quality cuts we employ on the parent PTF SN Ia sample for compiling a representative sub-sample, and the method we employ to identify possible candidates.

4.2 Sample selection

Our first task is to compile a sub-sample of the PTF SNe Ia that is suitable for the study we will perform. Ideally, we would like to study relatively close-by SNe Ia, in order to

be visible at late-times, with adequate photometric coverage. Moreover, we additionally require good photometric and spectral coverage around peak. This is equally important since we would like to be able to investigate possible correlations of the late-time light curve behaviour with photometric and spectroscopic indicators at peak, such as the width of the light curve and the subtype of the SN respectively.

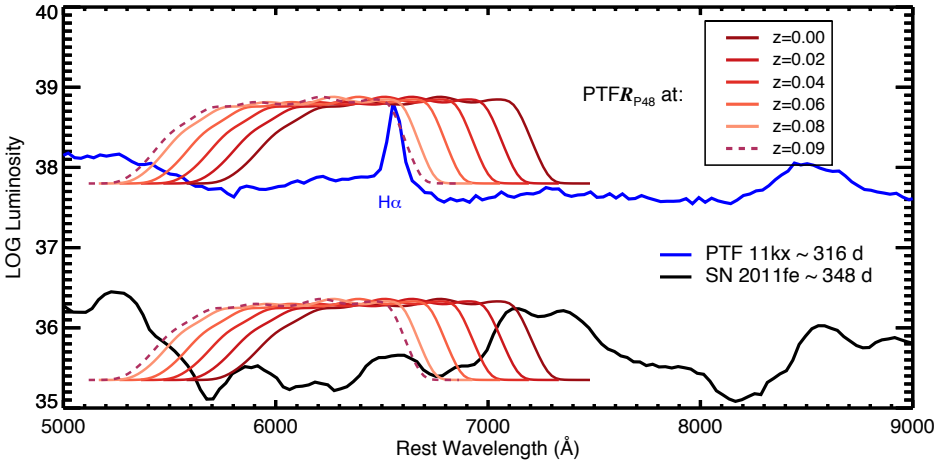

FIGURE 4.2: The late-time spectra of SN 2011fe (black) and PTF 11kx (blue). We over-plot the R_{P48} response function shifted blue-wards for different redshifts, reported at the upper-right legend, that mimics the redshift effect. Notice that, at $z = 0.09$ (red dashed line), the Hα component (at rest-wavelength of 6562 Å) reaches the red-ward edge of the filter. The SNe spectra are binned to 30 Å for illustration purposes.

Our initial quality cut we impose is motivated by the apparent magnitude of the SN. The median redshift of all PTF SNe Ia is 0.1, and at $z = 0.09$, a typical SN Ia has a peak apparent magnitude in $R_{P48} \simeq 18.5$. Intensive multi-colour and spectroscopic follow-up was restricted to objects with $z < 0.09$, in order to avoid selection effects. The same redshift cut has been made to other PTF papers (for example; Pan et al., 2014, 2015; Firth et al., 2015), while the initial redshift cut of Maguire et al. (2014) was $z < 0.2$. In this work, we will restrict ourselves to a more stringent cut of $z \leq 0.08$. The reason is demonstrated in Fig. 4.2. Since we are primarily interested at the region around Hα, we will exclude SNe with redshift $z \geq 0.08$, because any Hα component reaches the edge of the R_{P48} filter, and becomes susceptible to systematic instrumental uncertainties.

For the ~1250 SNe Ia that PTF discovered, Maguire et al. (2014) have performed a comprehensive statistical study on a sub-sample of 264 of them; they considered SNe Ia with good photometric quality (quantified with a cut at a stretch error $s_{err} < 0.15$) and adequate spectroscopic data (at least one spectrum up to +5d from maximum, measurement of the Si II λ6355 absorption component). We note that the stretch estimate of Maguire et al. (2014) is based on multi-band photometry (carried out by the PTF photometric follow-up program), while our data consist of only R_{P48} imaging. While our

TABLE 4.1: Number of SNe after each quality cut, described in section 4.2

Cut description	Number of SNe	Number of SNe discarded
PTF SN Ia parent sample	1250	–
Maguire et al. (2014)	264	986
With late-time data	86	178
With late-time data + Maguire et al. (2014)	56	30
$z \leq 0.08$	49	7

initial sample contains 86 objects with adequate coverage at late times, in order to have an accurate description of both the photometric and spectroscopic properties at peak, our final sample includes only SNe Ia that are included in Maguire et al. (2014).

A summary of our final sample is presented in Table 4.1, with redshift and stretch distributions shown in Fig. 4.3. We conclude that our sub-sample, consisting of 49 events, is representative of the total population of SNe Ia.

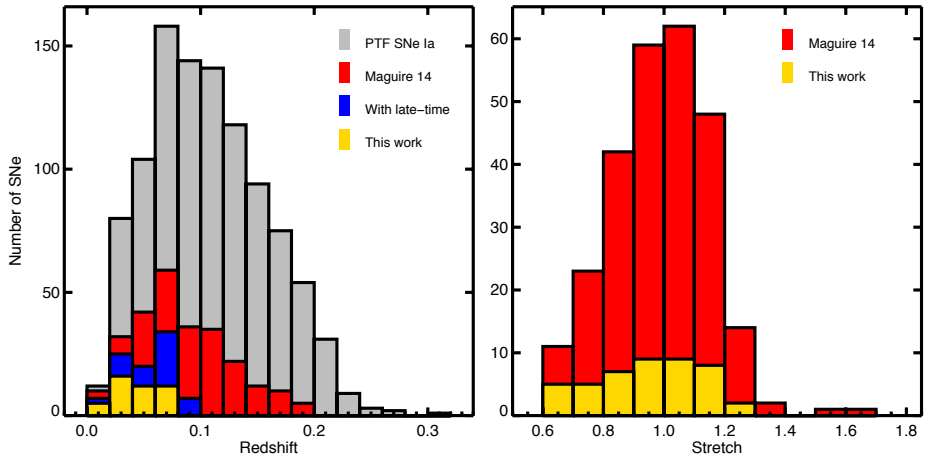

FIGURE 4.3: Redshift (left panel) and stretch (right panel) distribution of the parent PTF SNe Ia sample (grey), the Maguire et al. (2014) sample (red) and the sample analysed in this work (gold).

4.3 Analysis framework

After compiling the sample, according to section 4.2, we move to the description of the method we introduce to explore the late-time evolution of our SNe. We use the pipeline discussed in Chapter 2.4.1, with which we recover the photometry of our objects, and fit their light curves at peak with SiFTO (Chapter 2.4.2), recovering the time of maximum, the corresponding flux and the stretch parameter s. We then normalise the fluxes to the flux at peak, after correcting for MW extinction along the line of sight (Chapter 2.4.3).

We note that we do not attempt to correct for extinction from the host galaxy of the SN. We additionally employ a k-correction to the photometry: for the flux at peak, we k-correct using a template SN Ia spectrum at peak, while for the later times, we use the +348 days spectrum of SN 2011fe (Appendix A, Table A.3). As we have shown in Chapter 3, the shape of the SED of a SN Ia does not change significantly from ~200 up to ~600 days, particularly close to the R_{P48} wavelength range.

Since the limiting magnitude of PTF was ~21 mag, we expect that most of the data in our sample will be formal non-detections. Assuming that all SN Ia light curves are driven by radioactive decay at these late-times, we average our data, in order to achieve better sensitivity, in a similar manner as Chapter 3.3.3, with a 20 days time-bin.

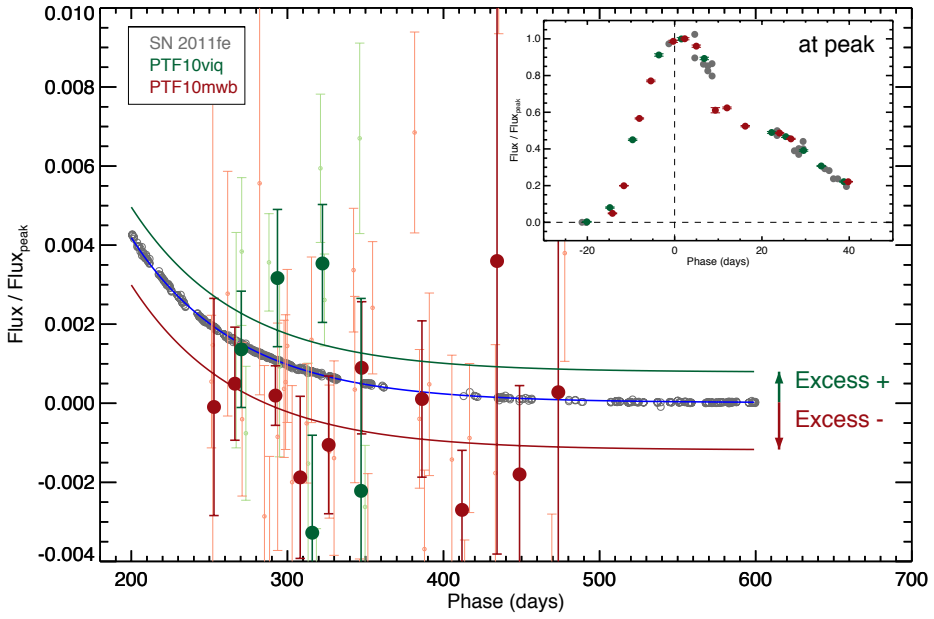

FIGURE 4.4: The late time R_{P48} flux light curves of SN 2011fe (grey circles), PTF10viq (green circles) and PTF10mwb (red circles), normalised to their flux at peak, with the light and dark colours corresponding to individual and 20d averaged photometric points respectively. The blue solid line corresponds to the exponential fit of SN 2011fe. The green and red solid lines are the exponential fits to PTF10viq and PTF10mwb, respectively, which correspond to the SN 2011fe fit plus a constant offset E, which we refer to as "Excess". The top right inset shows the same light curves at peak.

Initially, we restricted our analysis to the phase range of 200–400 days after maximum, not considering photometric data at later times. The choice of this approach was imposed by SN 2011fe: as we have shown in Chapter 3.3.3, at this phase range, the light curve declines linearly in magnitude space, consistent with radioactive decay, while at later phases, there is a deviation from it. However, in order to exploit as much of our data set, especially at these faint luminosity levels, we also extend our analysis to 200–600 days after maximum.

We perform this procedure for SN 2011fe, for which we fit a simple exponential decline at the phase of interest. This model encompasses the complex behaviour seen at 400–600 days after peak (Chapter 3, Fig. 3.4). Recovering the parameters of this fit, we fit all of the other SNe with the same model, adding an (constant) offset as a free parameter. We will define this offset as an excess (if the offset is positive) or deficiency (if the offset is negative) of the specific SN, compared to SN 2011fe (we will collectively refer to this parameter as "excess" E for the rest of this work). This approach *assumes* that all of our SNe decline with the same slope as SN 2011fe. An illustration of this method, with example light curves of PTF10viq (positive offset, excess) and PTF10mwb (negative offset, deficiency) is shown in Fig. 4.4.

4.4 Results

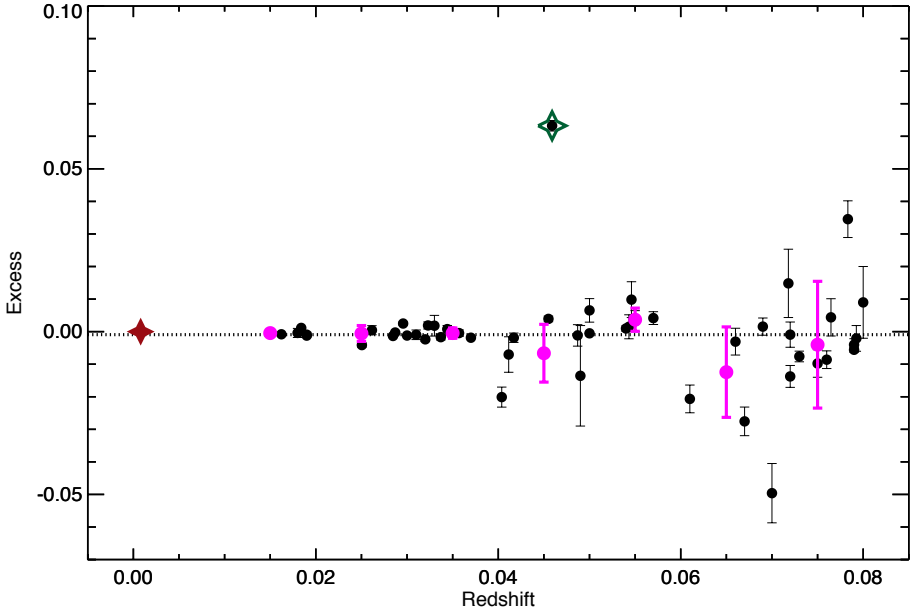

FIGURE 4.5: The excess of the SNe in our sample as a function of redshift. We overplot the SN 2011fe point (by definition $E_{11fe} \equiv 0$) with a red filled star and the PTF 11kx with a green open star. The dotted line indicates the median excess of the sample and the full magenta circles the average excess in a 0.01 redshift bin.

In Fig. 4.5, we present the excess E of our SN sample as a function of the redshift of the object. We also mark the location in this plot of SN 2011fe (filled red star) and PTF 11kx (open green star). We calculate the mean excess to be $E_{mean} \simeq -0.001$ with a standard deviation of ~ 0.014, slightly less than the excess of SN 2011fe, which by definition is $E_{11fe} \equiv 0$. The general trend on this plot indicates that the spread of the excesses increases at higher redshifts (thus, smaller peak apparent magnitudes and lower SNR). Nevertheless, within the uncertainties, the excesses we calculate are *generally* consistent

with SN 2011fe. PTF11kx is an obvious outlier, as it remains brighter in R_{P48} compared to SN 2011fe (thus, compared to any normal SN Ia) even at late times, due to the interaction of the ejecta with the CSM.

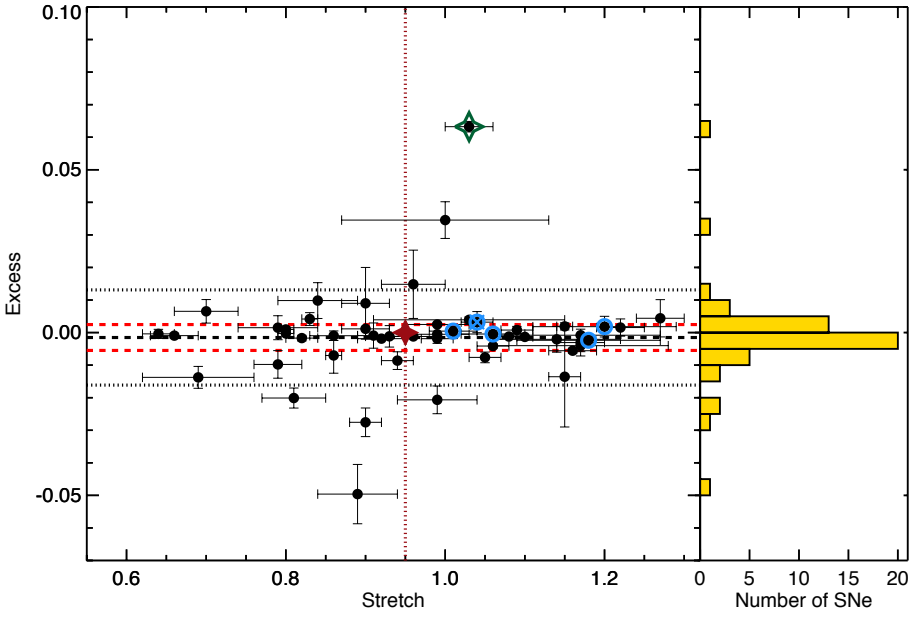

FIGURE 4.6: The late-time excess of the SNe in our sample as a function of stretch, colour-coded as Fig. 4.5. The black dashed line is the mean excess, while the black dotted lines correspond to the 1-σ standard deviation. The red dashed lines corresponds to the standard deviation adopting a sigma-clip cut of 4-σ. The red dotted vertical green line corresponds to the stretch of SN 2011fe. The 91T-likes of our sample are marked with open blue ones. We additionally mark PTF10iyc with a blue X (see text for details). We include the histogram of the excesses on the right-hand side of the plot.

In Fig. 4.6, we show the excess E as a function of stretch. The median stretch of our sample is $s = 0.96$, very close to the stretch of SN 2011fe ($s_{11fe} = 0.95$), meaning that our sample is representative of the total population of SNe in the width-luminosity relationship space (see also Fig. 4.3). We run SUPERFIT (Howell et al., 2005) on the available spectra of these objects and for all of them apart one, the best fits were normal SNe Ia. One SN, PTF10iyc, matches a 91T-like SN Ia.

Our sample includes four 91T-like SNe Ia (PTF 10hmv, 10qny, 10zai and 11gdh), for which we mark their excesses on the excess–stretch plot with open blue circles. All of them are consistent with zero excess.

Two objects that show remarkable positive excesses are 09fox and 10gnj, which are spectroscopically normal SNe Ia, but at $z > 0.07$. Moreover, SNe with significant negative excesses $E < -0.02$ are also at high redshift $z > 0.065$ and visual observations of their late time light curves reveals either poor photometric quality or, in some cases, bad host galaxy subtractions.

We find no strong preference for a SN Ia that shows (positive) excess to be over-luminous (high-stretched). A Pearson correlation test gives a value of $r = 0.10$, and if we exclude PTF11kx, $r = 0.09$, revealing no correlation between the excess of a SN Ia at late times with its stretch. Nevertheless, ongoing and future surveys, such as DES or LSST, with more powerful observing capabilities (particularly reaching fainter magnitudes with multi-colour observations) will be able to follow-up SNe Ia at very late times, and investigate their light curve evolution.

Shappee et al. (2013) provide a limit on the presence of Hα emission of $\leq$0.001 $M_\odot$, originating from the stripped hydrogen of a potential donor star in the SD scenario, using the 274d nebular spectrum of SN 2011fe. This is accomplished by scaling the models of Mattila et al. (2005) for the expected luminosity of the narrow Hα component, assuming a gaussian with FWHM of 1000 km s^{-1}, centred at the rest wavelength, for which the luminosity is 3.36×10^{35} ergs s^{-1} $\AA^{-1}$ for 0.05 $M_\odot$ stripped hydrogen material at 380 days after peak. A similar study was performed by Maguire et al. (2016) in a sample of 11 SNe, with one tentative detection, SN 2013ct, with ~0.007 $M_\odot$, and upper limits to the other 10 SNe (<0.001-0.058 $M_\odot$).

Using similar scaling relations, and since R_{P48} covers the Hα region (Fig. 4.2), we can place limits on the Hα emission, using our limits on the late-time excess of our SN sample. Adopting a conservative limit of the 1-σ standard deviation (dotted black line in Fig. 4.6), we obtain a 3-σ upper mass limit of $\leq$1.76 $M_\odot$ of stripped hydrogen. We can provide a stricter limit, by sigma clipping our late-time excess (using a σ cut of 4 standard deviations from the median) to exclude outliers. Adopting this approach, we find an upper mass limit of $\leq$0.51 $M_\odot$.

4.5 Summary

In this Chapter, we performed a sample study of the late-time light curves of the PTF SN Ia population. After introducing specifically designed quality cuts, appropriate for the scope of this work, we compile a sample of 49 SNe Ia. We constructed a method to compare our sample with the two well-observed PTF SNe Ia, the spectroscopically normal SN 2011fe and the Ia-CSM PTF11kx, which represent two extremes at the late-time light curve brightness. Our study reveals no correlation between flux excess at late times and high stretch, but a few number of events show modest excesses, spanning over the width-luminosity relationship range. We provide an upper limit on the hydrogen material ejected from the companion, in the SD scenario, of $\leq$0.51 $M_\odot$.

From our work, it is clear that PTF11kx is an outlier in the PTF SN Ia population. There are clear and distinct populations of 'normal' SNe Ia (the bulk of our SN sample) and H-rich SNe Ia (PTF11kx). Future work on this topic should include a repetition of this study with higher quality data from modern surveys.

Chapter 5

Overluminous Type Ia Supernovae with PESSTO: SN 2014eg and SN 2016hvl

While the majority of the thermonuclear explosions observed in the Universe is well described in the context of the thermonuclear runaway of a massive carbon-oxygen white dwarf (C/O WD) in a binary system, leading to the so-called normal Type Ia supernovae (SNe Ia), many other objects have shown discrepancies of their observational properties, implying possible distinct progenitor systems or explosion mechanisms. Modern surveys are able to discover a wide variety of 'non-normal' or 'peculiar' SNe Ia and dedicated follow-up experiments provide dense observational data towards explaining these deviations from the standard thermonuclear scenario.

In this chapter, we will examine the physical properties of the overluminous subclass of SNe Ia, colloquially known as 91T-likes, named after the prototypical event of this class, SN 1991T. To this end, we will present the discovery, the extensive photometric and spectroscopic follow-up observations and analysis of two overluminous SNe Ia, SN 2014eg and SN 2016hvl, classified and monitored by PESSTO and LCO (Chapter 2.2 and 2.3). We will focus on the study of the environment in which these events occurred, in order to provide clues on the progenitor system of this subclass.

5.1 Introduction

The huge increase in the number of SNe Ia discovered over the last few years has led to the revelation that distinct flavours of SNe Ia exist, showing distinct spectroscopic and

photometric behaviour. Different subclasses have been identified, usually based on early spectral characteristics (up until peak luminosity), most notably expansion velocities, line ratios and light-curve widths (Benetti et al., 2005), the absorption equivalent widths of Si II λ5972 and λ6355 (Branch et al., 2006) and the expansion velocity of Si II at maximum (Wang et al., 2009b). The early spectra of normal SNe Ia are dominated by intermediate mass elements (IMEs), such as Si, S, Ca and Mg, forming a well-defined homogeneous class, with a small variation of the light-curve behaviour, which is most likely driven by the mass of the synthesised radioactive ^{56}Ni.

For peculiar events such as SN 1991T (Filippenko et al., 1992b), the overall shape and colour evolution are relatively similar to normal SNe Ia, but their absolute peak magnitudes are somewhat brighter and the light curves decline slower, while the pre-maximum spectral evolution is the defining characteristic of this subclass: a featureless blue pseudo-continuum, strong Fe III absorption features and weak (or even absent) intermediate mass elements, which only develop around or after peak brightness. The expansion velocity of the ejecta, estimated via the Si II λ6355 feature, is low and appears to be constant. From all of the above, the general consensus is that 91T-like objects are part of the shallow-silicon class and the low-velocity-gradient group (indicating that the IMEs are confined to a narrow region), producing higher amounts of ^{56}Ni ($\geq 0.7\,M_{\odot}$) compared to normal Ias ($\approx 0.5\,M_{\odot}$). Similar to these objects are the 99aa-like SNe (SN 1999aa; Krisciunas et al., 2000), a transitional class of objects between normal Ias and 91T-likes.

An important observational characteristic of this subclass is that they predominantly occur in late-type galaxies (Howell, 2001), likely pointing to young stellar populations, with most of them displaying narrow galactic absorption features, indicating high absorption along the line of sight. This fact makes them excellent tools for studying galactic reddening laws, probing the local environment and, subsequently, providing indications on the progenitor system of the explosion.

Studies on the immediate environment of SNe Ia explosions, such as direct detection of Hα, temporal evolution of the narrow Na I D lines and the blueshifted structure of the absorbing material have provided contradicting results. An excess of blueshifted material, compared to redshifted one, has been unambiguously observed (Sternberg et al., 2011; Foley et al., 2012; Maguire et al., 2013), with individual objects, such as SN 2006X (Patat et al., 2007), SN 1999cl (Blondin et al., 2009), SN 2007le (Simon et al., 2009) and PTF11kx (Dilday et al., 2012), additionally showing a temporal evolution of their absorption profiles. However, direct detection of Hα on samples of normal SNe Ia (Maguire et al., 2016) have yet to be confirmed. In addition, it has been suggested that such nearby circumstellar material (CSM) could affect the colours of SNe Ia (Goobar, 2008), where other studies find that the dust responsible for the observed reddening of SNe Ia is

predominantly located in the interstellar medium (ISM) of their host galaxies (Phillips et al., 2013).

There have been indications of a connection between 91T-likes and SNe Ia-CSMs (Silverman et al., 2013b), events that are spectroscopically similar to 91T-like SNe, superimposed with Hα emission due to interaction with the CSM. SNe Ia-CSM provide some of the best evidence of the SD scenario. In order to investigate this possible connection, I have led the spectroscopic follow-up of young, nearby, 91T-like SNe Ia within PESSTO, photometrically supported by the LCO SN key project. To this date, rich data sets for four SNe have been collected and this project will continue for the next 2 years within ePESSTO. Current estimates on the rate of 91T-like SNe suggest that they make up of $\sim$10% of SNe Ia (in volume-limited samples, Li et al. 2011b). Furthermore, based on previous PESSTO experience, $\sim$5 events per year are classified as early 91T-likes, therefore we expect to classify and potentially follow 10-12 events over 2 years of ePESSTO. Our photometric follow-up strategy requires 3-4d cadence around peak and 7-10d cadence after 40d, in (u)BgVri, while for the spectroscopic follow-up, we require EFOSC2 gr#11 and gr#16 grisms around peak, while gr#13 after 40d of peak. In overall, 7-8 spectra before 40d (with 4-5d cadence) and 5-6 spectra after 40d (with 10d cadence) is optimal for probing the spectral evolution of the phenomenon. Moreover, NIR photometry with SOFI, particularly around peak, will allow us to probe the complete energetic output and constrain the host galaxy reddening law. Information on the observational set-ups are presented in Chapter 2.2 and 2.3. Here, we will present the data and the analysis of two well-observed SNe of this sample, SN 2014eg and SN 2016hvl.

5.2 Discovery

SN 2014eg was serendipitously discovered in the course of observing SN 2013fc (Kangas et al., 2016) by PESSTO. While obtaining NTT/EFOSC2 UBVRi subtraction templates of the host galaxy of SN 2013fc, ESO 154-G010, on 2014 November 16 UT, a new transient was discovered at coordinates α = $02^{h}45^{m}09^{s}.27$, δ = $-55^{o}44'16".9$ (J2000.0), with V = 17.5 (Kangas et al., 2014), with the last non-detection being from NTT/SOFI Ks-band on 2014 October 14 UT.

The SN lies 8″.7 east and 5″.35 north of the centre of ESO 154-G010 (Fig. 5.1), an SBa-type barred spiral galaxy, with a heliocentric redshift of 0.01863 ± 0.00008 and a recession velocity of 5586 ± 24 km s^{-1} according to NASA/IPAC Extragalactic Database (NED)[1]. The Galactic extinction along the line of sight is $E(B-V)_{MW}$ = 0.0257 ± 0.0003 mag (Schlafly & Finkbeiner, 2011).

[1] https://ned.ipac.caltech.edu/

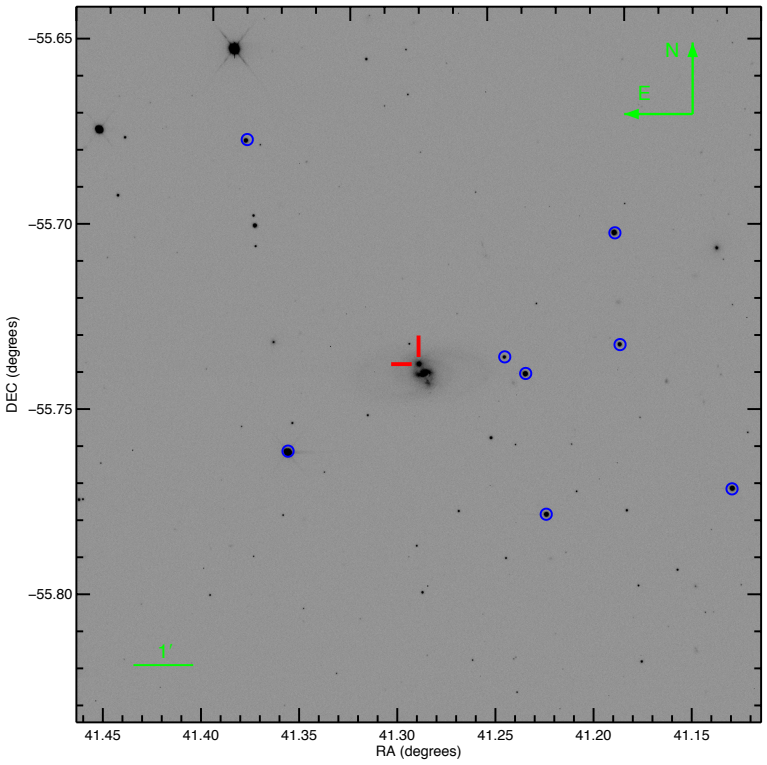

FIGURE 5.1: LCOGT V-band image of ESO 154-G010, taken on 2014 December 01 UT. SN 2014eg is marked with the red cross. The blue circles indicate the local standard stars on the field of the SN.

SN 2016hvl was discovered by the ATLAS survey (Tonry, 2011) at α = 06$^{\rm h}$44$^{\rm m}$02$^{\rm s}$.16, δ = 12°23′47″.8 (J2000.0) on 2016 November 04 UT, with c = 17.26 mag (c is a broad filter used by ATLAS, resembling an SDSS g′+r′), with $E(B-V)_{MW}$ = 0.3766 ± 0.0109 mag (Schlafly & Finkbeiner, 2011). Initially, the SN was associated with UGC 03524, a spiral galaxy with heliocentric redshift of 0.013092 ± 0.000007 and a recession velocity of 3925 ± 2 km s^{-1}. The SN lies 19″.2438 south and 22″.356 east from the centre of the galaxy (Fig. 5.2), with a separation of 29″.4. For a luminosity distance to UGC 03524 of 56.23 Mpc, the projected SN distance from the potential host is 8.05 kpc. However, deep pre-explosion images from the Pan-STARRS1 Survey (Chambers et al., 2016) DR1 (Flewelling et al., 2016) reveal a possible red satellite dwarf galaxy at 2″.299 west and 0″.781 south of the SN, with a 2″.44 separation, corresponding to a distance of 0.66 kpc from the SN location.

This dwarf galaxy is at α = 06$^{\rm h}$44$^{\rm m}$02$^{\rm s}$.0, δ = 12°23′47″.05 (J2000.0), 20″.0 south and 20″.0 east of the centre of UGC 03524, with a separation of 28″.05, or 7.65 kpc. In Fig. 5.3, we show the deep g (left) and i (right) images from Pan-STARRS1. The host is not visible at the g-band, but clearly visible in the i-band. We perform aperture

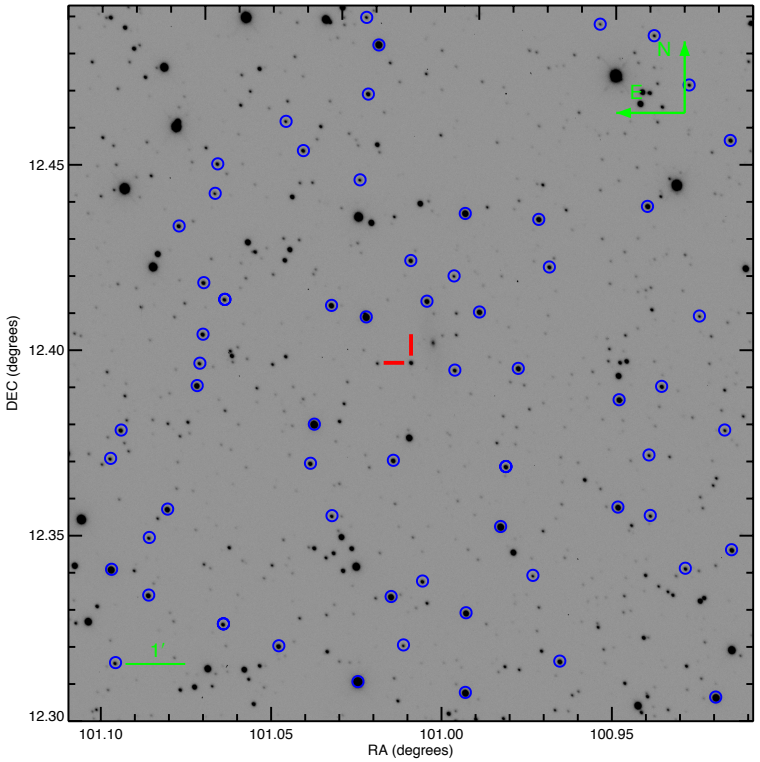

FIGURE 5.2: LCOGT V-band image of UGC 03524, taken on 2016 November 24 UT. SN 2016hvl is marked with the red cross. The blue circles indicate the local standard stars on the field of the SN.

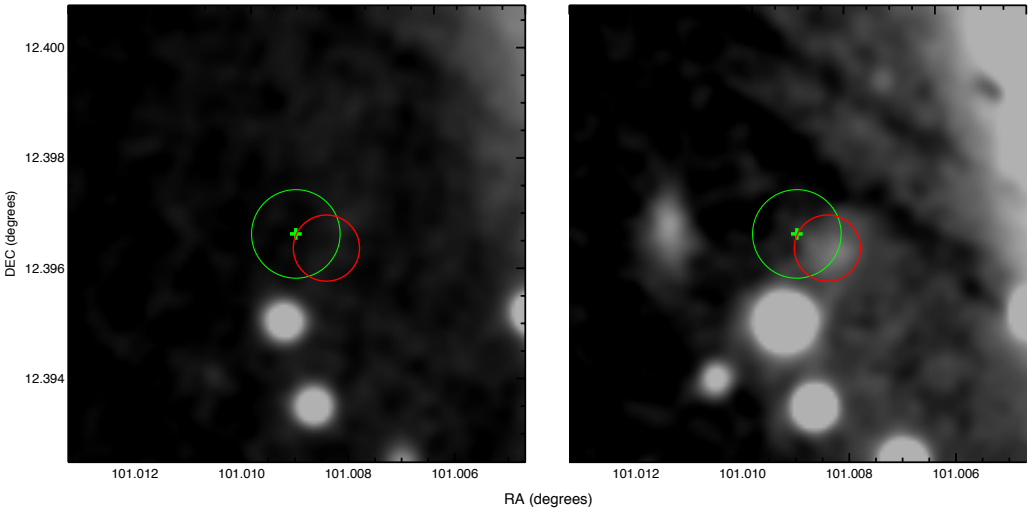

FIGURE 5.3: Pan-STARRS1 g (left panel) and i (right panel) at the location of SN 2016hvl, where north is up and east is left. The location of the SN is marked with the green cross, inside a circle of 4″. The red circle indicates the location of the potential host galaxy. The images have been smoothed with a Gaussian kernel for illustration purposes.

photometry at the location of the potential host at the griz deep-stack images of Pan-STARRS1, with an aperture of 4″, and we measure g = 23.218±0.282, r = 22.063±0.112, i = 21.582 ± 0.099 and z = 21.275 ± 0.162.

5.3 Observations

For both of the SNe, the classification was performed by PESSTO, with its standard classification spectral settings, outlined in Table 2.1. For SN 2014eg, a classification spectrum was taken on 2014 November 22 UT and analysed with the Supernova Identification package (SNID; Blondin & Tonry, 2007). The target was classified as a relatively young (~ 7 days before peak) SN Ia (1991T-like), at z = 0.018 (Smith et al., 2014a), while for SN 2016hvl, the classification was performed on 2016 November 06 UT, and SNID gave a match with a young (~ 10 days before peak) SN Ia (1991T-like), at z = 0.013 (Dimitriadis et al., 2016).

5.3.1 Photometry

Since both of the SNe were classified as local, young and peculiar SNe Ia, a follow-up campaign within PESSTO was initiated. High cadence optical imaging was performed with LCO (Chapter 2.3). Regarding SN 2014eg, the observations were taken from 2014 November 24 UT till 2015 March 18, from 7 days before peak to 105 days after peak. Given that the SN exploded in a region with significant galaxy background flux, it was necessary to acquire galaxy images when the SN had faded, to perform proper subtraction of the galaxy light. These galaxy templates were taken from 2015 September 18 UT onwards, at a phase of ≥ 285 days after peak. For SN 2016hvl, observations started on 2016 November 9 UT and the last images were obtained on 2017 April 5 UT (~8 days before peak to ~136 days after peak). No subtraction templates were taken, since the potential host, described in section 5.2 would not be detected in the LCO images.

The photometry was performed with our custom pipeline, as described in Chapter 2.4.1, and the results are presented in Tables C.1 and C.2, for SN 2014eg and SN 2016hvl, respectively.

5.3.2 Spectroscopy

As key science targets, SN 2014eg and SN 2016hvl were frequently observed by PESSTO. For SN 2014eg, we have acquired in total 9 optical spectra with EFOSC2 and 2 NIR spectra with SOFI. Additional higher-resolution spectra were obtained with XSHOOTER

TABLE 5.1: SN 2014eg Spectroscopy log

Date (UT)	MJD (days)	Phase (days)[a]	Telescope	Instrument	Exposure times (s)
2014 11 22	56984.25	−7.52	NTT	EFOSC2	1×600
2014 11 24	56986.26	−5.51	NTT	EFOSC2	2×1800[b]
2014 11 28	56990.13	−1.64	NTT	EFOSC2	2×1800
2014 11 30	56991.05	−0.72	VLT	XSHOOTER	1×600
2014 12 01	56992.18	+0.41	NTT	EFOSC2	2×1800
2014 12 14	57005.25	+13.48	NTT	EFOSC2	1×900
2014 12 15	57006.16	+14.39	NTT	SOFI	1×2160[c]
					1×3600[d]
2014 12 21	57012.24	+20.47	NTT	EFOSC2	1×900
2014 12 22	57013.20	+21.43	NTT	SOFI	1×3240[e]
2014 12 29	57020.02	+28.25	VLT	XSHOOTER	1×1800
2014 12 29	57020.10	+28.33	NTT	EFOSC2	1×900
2015 01 14	57036.13	+44.36	NTT	EFOSC2	1×1200
2015 01 28	57050.14	+58.37	VLT	XSHOOTER	1×1200
2015 02 14	57067.05	+75.28	NTT	EFOSC2	2×2700
2015 02 17	57070.06	+78.29	NTT	EFOSC2	2×2700

[a] MJD_{peak} = 56991.77 from SIFTO
[b] Only Grism#11
[c] Blue part
[d] Red part
[e] Only Blue part

TABLE 5.2: SN 2016hvl Spectroscopy log

Date (UT)	MJD (days)	Phase (days)[a]	Telescope	Instrument	Exposure times (s)
2016 11 05	57698.37	−11.99	NTT	EFOSC2	1×300
2016 11 06	57699.25	−11.12	NTT	EFOSC2	2×1500
2016 11 11	57703.61	−6.83	OGG	FLOYDS	1×1800
2016 11 15	57707.39	−3.09	OGG	FLOYDS	1×1800
2016 11 19	57711.49	+0.95	OGG	FLOYDS	1×1800
2016 11 21	57713.29	+2.73	NTT	EFOSC2	2×900
2016 11 24	57716.65	+6.04	COJ	FLOYDS	1×1800
2016 11 28	57720.35	+9.70	NTT	EFOSC2	2×900
2016 12 02	57724.31	+13.61	NTT	EFOSC2	2×900
2016 12 21	57744.28	+33.32	NTT	EFOSC2	2×900
2016 12 24	57746.50	+35.51	OGG	FLOYDS	1×2700
2016 12 26	57748.50	+37.49	COJ	FLOYDS	1×2700
2017 01 06	57759.25	+48.10	NTT	EFOSC2	1×1800
2017 01 16	57770.22	+58.93	NTT	EFOSC2	1×1800
2017 02 05	57789.16	+77.63	NTT	EFOSC2	1×2700
2017 02 17	57802.05	+90.35	NTT	EFOSC2	1×2700

[a] MJD_{peak} = 57710.52 from SIFTO

(Vernet et al., 2011), mounted on ESO Very Large Telescope. A summary of the observations is shown in Table 5.1. For SN 2016hvl a total of 10 optical spectra with EFOSC2 and 6 with the FLOYDS spectrograph from LCO were acquired. The spectroscopic log is presented in Table 5.2. Information regarding the resolution of the spectra and the data reduction procedures, for both EFOSC2 and FLOYDS, are presented in Chapter 2, sections 2.2.2 and 2.3 respectively.

5.4 Results

In the following section, we will present the photometric and spectral analysis of SN 2014eg and SN 2016hvl. Throughout our analysis, we will compare our results with 3 other well-studied SNe Ia: The prototypical SN of their class, SN 1991T, the transitional SN 1999aa and the normal SN 2011fe. For these SNe, the majority of the spectra were taken from the WISeREP archive[2] (Yaron & Gal-Yam, 2012). Photometric observations were obtained from the Open Supernova Catalog[3] (Guillochon et al., 2017) and consist of: for SN 1991T from Lira et al. (1998) and Altavilla et al. (2004), for SN 1999aa from Krisciunas et al. (2000) and Jha et al. (2006) and for SN 2011fe from Munari et al. (2013).

5.4.1 Light curves

We present the light curves of SN 2014eg and SN 2016hvl in Figures 5.4 and 5.5 respectively. Non-detections are shown as a 3-σ upper limit, and plotted with a downward arrow.

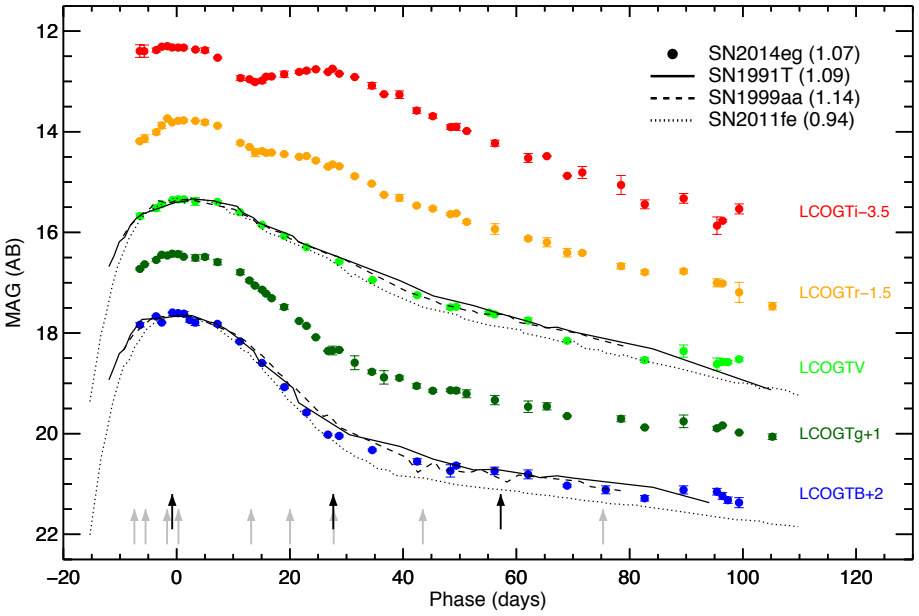

FIGURE 5.4: The BgVri light curves of SN 2014eg (full circles), shifted according to the offsets indicated in the plot. We compare the light curves with those of SN 1991T (solid lines), SN 1999aa (dashed lines) and SN 2011fe (dotted lines), normalised to SN 2014eg peak magnitudes. We report the stretch factor for each SN, inferred from SIFTO, at the top-right legend. The vertical arrows correspond to SN 2014eg's spectral series (Table 5.1), with grey indicating EFOSC2 and black Xshooter spectra.

[2] http://wiserep.weizmann.ac.il/
[3] https://sne.space/

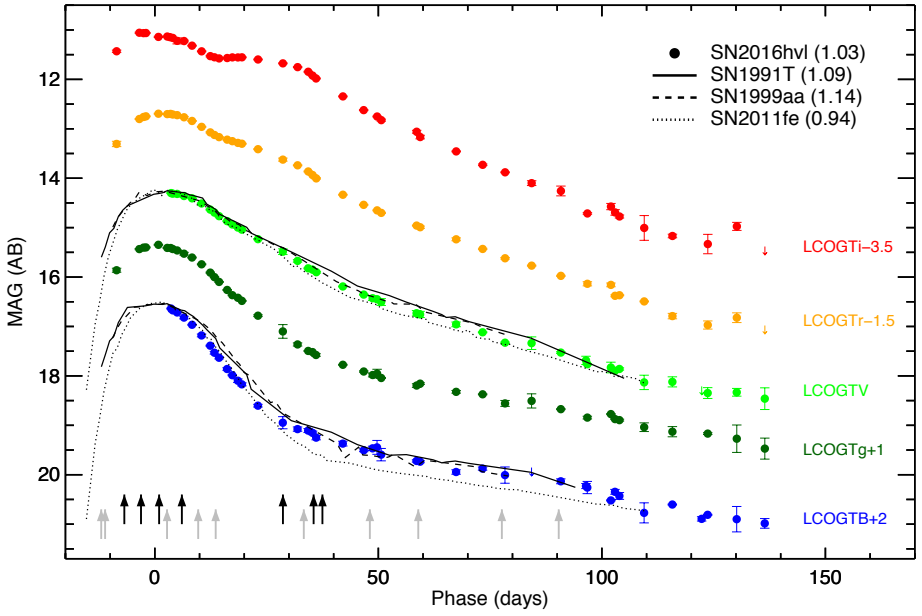

FIGURE 5.5: The BgVri light curves of SN 2016hvl (full circles), shifted according to the offsets indicated in the plot. The comparison SNe are also shown in a similar manner as in Fig 5.4. The vertical arrows correspond to SN 2016hvl's spectral series (Table 5.2), with grey indicating EFOSC2 and black FLOYDS spectra.

In these plots, we do not include the R and I-band light curves of our comparison sample, since the photometry of our SNe was performed in SDSS r′ and i′. We will apply proper s- and k-corrections when we will compare the colour evolution of the SNe.

We fit the SN 2014eg and SN 2016hvl light curves with SIFTO (see Chapter 2.4.2) and we estimate the epochs of maximum light of $MJD_{\rm max}^{\rm 14eg} = 56991.85 \pm 0.18$ and $MJD_{\rm max}^{\rm 16hvl} = 57710.52 \pm 0.29$, with stretch factors of $s_{\rm 14eg} = 1.073 \pm 0.022$ and $s_{\rm 16hvl} = 1.03 \pm 0.03$, while the B-V colours at maximum are $(B-V)_{\rm max}^{\rm 14eg} = 0.409 \pm 0.014$ and $(B-V)_{\rm max}^{\rm 16hvl} = 0.434 \pm 0.018$. From the SIFTO fits, we can also estimate the observed decline in 15 days in B-band, for which we calculate $\Delta m_{15}^{\rm 14eg} = 1.01 \pm 0.02$ and $\Delta m_{15}^{\rm 16hvl} = 1.00 \pm 0.02$. The templates SIFTO uses for the fitting fail to capture the strong secondary maximum of the 91T-like SNe Ia, pronounced in the redder bands. Thus, for SN 2014eg, we additionally fit only the B and V light curves, for which we find $MJD_{\rm max}^{\rm 14eg} = 56992.02 \pm 0.17$, $s_{\rm 14eg} = 1.033 \pm 0.021$, $(B-V)_{\rm max}^{\rm 14eg} = 0.402 \pm 0.015$ and $\Delta m_{15}^{\rm 14eg} = 1.01 \pm 0.03$. We do not attempt to perform the same exercise for SN 2016hvl, since the SN was observed in B and V-band at ≥3 days after maximum light.

From the light curves and the SIFTO fits, we find that both of the SNe are (as expected from the spectral classification) overluminous, with broad light curves. Moreover, both of them show significant reddening. This was expected for SN 2014eg, since it exploded in a star-forming spiral galaxy with significant absorption (see also Kangas et al., 2016),

but it was, initially, somewhat surprising for SN 2016hvl: the fact that we see significant reddening is an additional argument for the small dwarf irregular host, as seen in the deep PS1 images, compared to an explosion at a remote location of UGC 03524, where no significant absorption is expected.

5.4.2 Colour curves

Figure 5.6 shows the colour evolution of SN 2014eg and SN 2016hvl in B-V (left), V-r′ (top-right) and V-i′ (bottom-right), alongside the comparison sample. In order to be able to perform proper comparisons, we apply the appropriate s- and k-corrections. For SN 2014eg and SN 2016hvl, we k-correct the photometry using the 91T spectral templates produced by Peter Nugent (Stern et al., 2004). The spectral templates are mangled to the photometry of the SNe (at epochs were we have simultaneous observations in all the optical bands) as discussed in Chapter 2.4.4, and we perform the k-corrections by shifting the filter response functions to the redshift of each SN, calculating the rest-frame magnitude in each filter. For the comparison sample, we apply the same procedure and, in addition, we s-correct the final mangled and k-corrected spectral template to the filter responses of r′ and i′. For SN 1991T and SN 1999aa, we used the same spectral template as for SN 2014eg and SN 2016hvl, while for the normal SN 2011fe, we use the Hsiao et al. (2007) templates.

The overall colour evolution of all of the SNe is similar, apart from the obvious offset of the highly reddened ones, SN 1991T, SN 2014eg and SN 2016hvl. As can be seen, SN 2014eg's offset is prominent in the bluer colours and gradually decreases in the redder ones. The same is true for SN 2016hvl, but with a moderate offset.

A method to calculate the host galaxy's absorption along the line of sight was developed by Lira and illustrated in Phillips et al. (1999): By comparing the colour evolution of unreddened SNe Ia, the authors found that the B-V colours at 30-90 days past V maximum evolved similarly, since the spectra at these epochs are quite uniform. Thus, the observed colour excess can be attributed solely to the reddening due to dust or gas from the host galaxy. The Lira law (equation 1 in Phillips et al. 1999)

$$(B-V)_0 = 0.725 - 0.0118(t_V - 60), \tag{5.1}$$

where t_V is the phase relative to V-band maximum, is plotted as a solid black line at the left panel of Fig. 5.6. SN 2011fe and SN 1999aa, two SNe with minimal absorption (both from the MW and their hosts) follow the Lira law. SN 1991T has an offset that

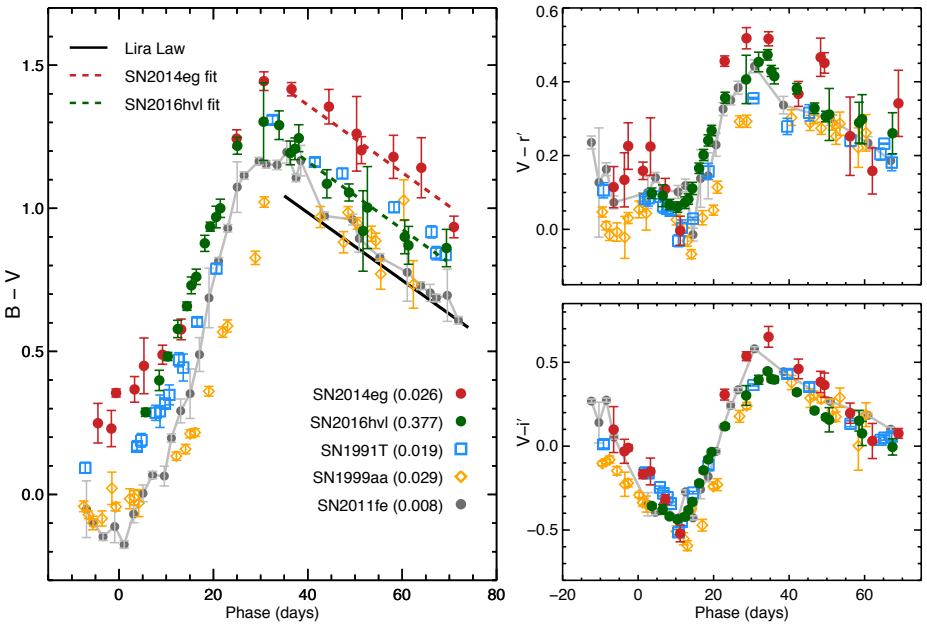

FIGURE 5.6: SN 2014eg (red filled circles) and SN 2016hvl (green filled circles) B-V (left), V-r′ (top-right) and V-i′ (bottom-right) colour evolution. The colours are compared with the ones of SN 1991T (open blue squares), SN 1999aa (open orange diamonds) and SN 2011fe (filled grey circles). The colours of the comparison sample were s- and k-corrected as described in the text. We correct the colours for Milky Way extinction, and we report in the legend the $E(B-V)_{MW}$ for each SN. At the B-V panel (left), we over-plot the Lira Law (solid black line) and the fits to the Lira Law for SN 2014eg (red dashed line) and SN 2016hvl (green dashed line).

corresponds to $E(B-V) \sim 0.2$ mag. Following Phillips et al. (1999), for SN 2014eg, we calculate $E(B-V)^{14eg}_{tail} = 0.393 \pm 0.054$ and for SN 2016hvl $E(B-V)^{16hvl}_{tail} = 0.184 \pm 0.053$.

A different approach for estimating the host galaxy absorption has been developed by Phillips et al. (1999) and updated in Folatelli et al. (2010): using the k-corrected peak magnitudes in B- and V-band, corrected for MW reddening, the pseudo-colours of low-reddened SNe from the CSP sample at maximum light are calculated and the dependence of them with the decline rate was investigated, providing relations that describe the colour excess as a function of Δm_{15}. They found (equation 3 in Folatelli et al. 2010)

$$(B^{max} - V^{max})_0 = -0.016(\pm 0.014) + 0.12(\pm 0.05) \times [\Delta m_{15}(B) - 1.1]. \quad (5.2)$$

Having established the behaviour of the pseudo-colours at maximum light for the unreddened SNe, it is trivial to estimate the host galaxy absorption for any other SN. Taking advantage of the fact that our optical photometry is performed in identical photometric bands as CSP, we followed the same procedure and we estimate, for SN 2014eg,

$E(B-V)^{14eg}_{max} = 0.392 \pm 0.018$. Once again, we do not perform this exercise for SN 2016hvl, due to poor coverage of B- and V-band near maximum.

Overall, we find that both of the SNe are affected by material along the line of sight. For SN 2014eg, we will adopt the weighted mean value of $E(B-V)^{14eg}_{host} = 0.3921 \pm 0.003$ and for SN 2016hvl $E(B-V)^{16hvl}_{host} = 0.184 \pm 0.053$.

5.4.3 Spectral evolution

In Fig. 5.7, we present the spectral series of SN 2014eg (left) and SN 2016hvl (right), obtained with the instruments as described in Tables 5.1 and 5.2. The spectra are mangled to the observed photometry, as described in Chapter 2.4.4, and we correct *only* for reddening due to Milky Way.

In general, the spectra show similar evolution, representative of the 91T-like subclass to which they belong. At early times (e.g. before peak luminosity), the spectrum is blue, with weak IME absorption lines. After peak, and particularly at ≥15 days after peak, the spectra are similar to normal SNe Ia. In the left panel of Fig. 5.8, we plot the early spectra of SN 2014eg (red) and SN 2016hvl (green), alongside SN 1991T (blue), SN 1999aa (orange) and SN 2011fe (grey) at similar epochs, at the wavelength range of ~3400–4500 Å. We over-plot with vertical dashed lines the expansion velocities of absorption lines of Ca H&K (at 17000 kms^{-1}), Si II λ4130 (at 10000 kms^{-1}), Fe III λ4421 (at 12000 kms^{-1}), Si III λ4568 (at 12000 kms^{-1}) and C III λ4648 (at 12000 kms^{-1}). From this plot, the difference between 91T-likes and normal SNe Ia is evident: The strength of the IME lines decreases from SN 2011fe to SN 1991T. Interestingly, there are hints of unburned carbon in SN 2016hvl, which is a common feature in 91T-likes (including 99aa-likes), but not in SN 2014eg (although this is expected to appear in phases ≤ 10 days from peak, for which no spectra are available). Moreover, the increased strength of the Fe III lines, absent in the normal SNe Ia, indicate high ionisation and temperature.

The fact that the explosion mechanism that leads to a 91T-like event produces higher temperatures than the normal SN Ia is also evident in the spectra at epochs around peak. The right panel of Fig. 5.8 shows the spectra of SN 2014eg, SN 2016hvl, SN 1991T, SN 1999aa and SN 2011fe, in a similar fashion as in the left panel. We also plot the expansion velocities of the absorption lines of the w-shaped S II λ5500, Si II λ5972 and Si II λ6355, at 10000 kms^{-1}. The w-shaped S II is fully developed in SN 2011fe and starts to appear in the 91T-likes, but is weaker. The same goes for the Si II lines, which are also weaker.

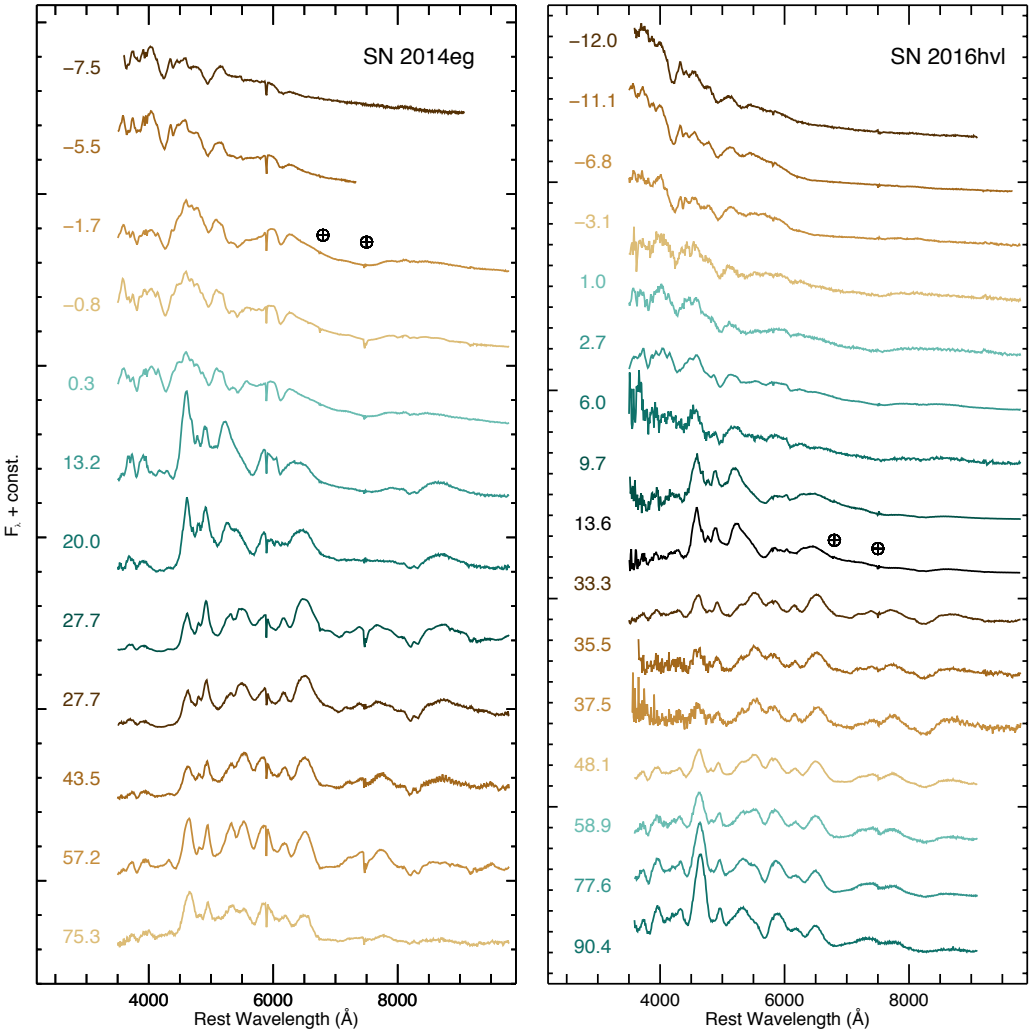

FIGURE 5.7: Optical spectroscopic sequence of SN 2014eg (left) and SN 2016hvl (right). Each spectrum is binned to 10 Å and shifted by an arbitrary offset for illustration purposes. All the spectra are mangled to the observed photometry and corrected for MW reddening for each SN. We mark with ⊕ the telluric features and we include the approximate phase of each spectrum at the left side of each one. Information on the spectra is presented in Tables 5.1 and 5.2, for SN 2014eg and SN 2016hvl respectively.

The observed trend in the strength of the features indicates the possibly common explosion mechanism but with different strengths, effective temperatures and masses of synthesised elements in the explosion, probing, in a spectral sequence, the observed width-luminosity relation of SNe Ia, as has been shown in Nugent et al. (1995).

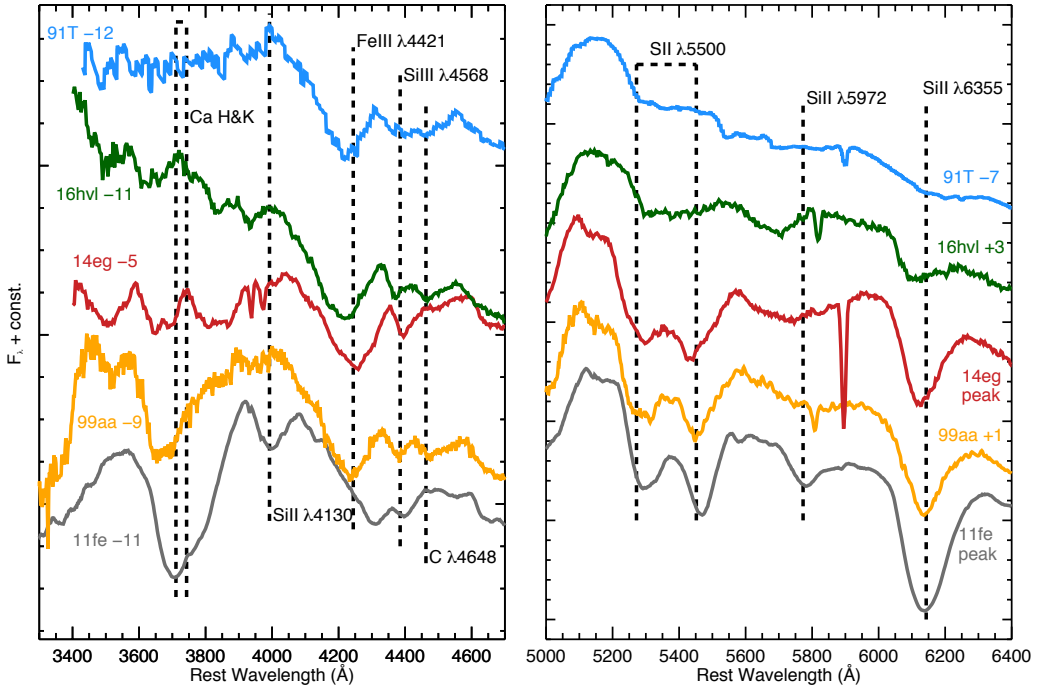

FIGURE 5.8: *Left panel:* Early (<5 days from peak) spectra of SN 2014eg (red) and SN 2016hvl (green), compared to spectra of SN 1991T (blue), SN 1999aa (orange) and SN 2011fe (grey) at similar phases. The vertical lines indicate common absorption lines, at expansion velocities of: Ca H&K at 17000 kms^{-1}, Si II λ4130 at 10000 kms^{-1} and Fe III λ4421, Si III λ4568 and C III λ4648 at 12000 kms^{-1}. *Right panel:* As in left panel, but for spectra at peak. Lines depicted are: S II λ5500, Si II λ5972 and Si II λ6355, at 10000 kms^{-1}.

5.4.4 Host galaxy absorption features in high resolution spectra of SN 2014eg

One of the most promising methods to probe the immediate environment at the site of the explosion is the study of the narrow absorption host galaxy features in high resolution spectra. In general, blueshifted material along the line of sight could be an indication of outflows, ejected from the binary system at a SD progenitor channel (however, see also Shen et al. 2013 for CSM in the double-detonation scenario). Moreover, any temporal evolution of the lines can potentially be attributed to expanding shells that evolve because of changes in the CSM ionization conditions due to the varying radiation field of the SN.

We have acquired in total three high resolution spectra of SN 2014eg with XSHOOTER (see Table 5.1), at phases of ∼-0.7, +28.2 and +58.4 from peak luminosity. The native resolution of XSHOOTER is $R = (\lambda/\Delta\lambda) = 4290$ and 7410 for the UVB (1″.0 slit width) and the VIS (0″.9 slit width) arm, respectively. The spectra reveal emission lines of multiple Hα and N II components. Visual inspection of the acquisition images and

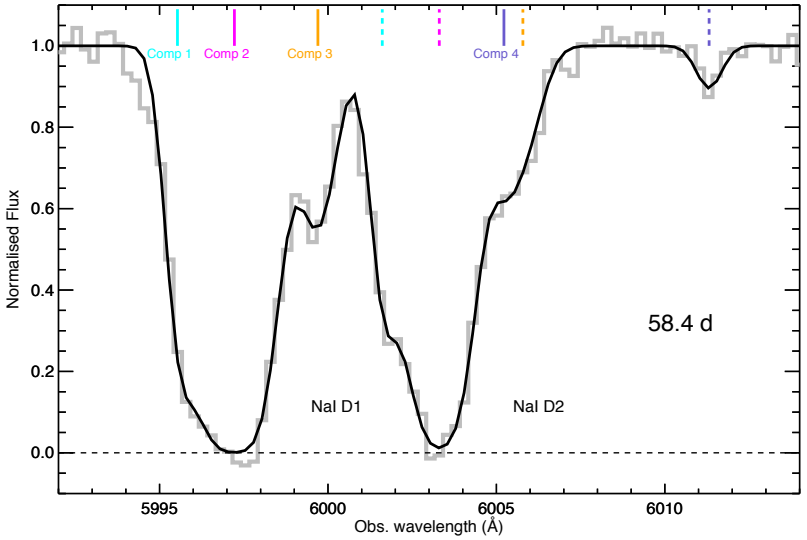

FIGURE 5.9: The 58.4 days after peak XSHOOTER spectrum of SN 2014eg (grey line) in observed wavelength, at the vicinity of the NaI D. We mark the observed minimum wavelengths of the four identified components (in cyan, magenta, orange and purple) with solid (NaI D1) and dahsed (NaI D2), respectively. The black line corresponds to the full 4-component Voigt profile fit.

the corresponding position of the slit, for each epoch of observation, demonstrates that the galaxy light included in the slit may originate from different parts of the galaxy. Moreover, the colour evolution of the SN, shown in section 5.4.2, makes clear that the SN is heavily reddened, and forces us to estimate a redshift not from the emission lines, but from the Na I doublet, shown in Fig. 5.9.

We identify four components: A saturated component, plotted in magenta, and three components, plotted in cyan, orange and purple, blueward, redward and redward respectively. We fit the Na I doublet using the Voigt profile fitting program, VPFIT[4], for which we recover the observed minimum wavelength and the column densities of neutral sodium of each component. The results of the fit are shown in Table 5.3.

The redshifts estimated for the saturated Na I component (component 1) are 0.018255, 0.018264 and 0.018248, with a mean of 0.018257 ± 0.000003. The strong Hα and N II components have a centroid at ~0.01825. In the following, we will adopt a redshift of z = 0.01826.

Using the work of Phillips et al. (2013), we can estimate the extinction on the line of sight: The authors have shown (their equation 4) that the V band extinction is correlated with the column density of Na I:

[4] http://www.ast.cam.ac.uk/~rfc/

TABLE 5.3: Host galaxy sodium absorption components in SN 2014eg (Fig. 5.9).

Spectrum	Min (Å)	Redshift	$\log_{10} N_{NaI}$ (cm^{-2})
		Component 1 (magenta)	
-0.7d[a]	5997.47	0.018255(0.000003)	13.944(0.039)
+28.2d[b]	5997.52	0.018264(0.000003)	13.882(0.025)
+58.4d[c]	5997.43	0.018248(0.000005)	13.949(0.058)
		Component 2 (cyan)	
-0.7d	5995.81	0.017973(0.000004)	13.336(0.177)
+28.2d	5995.87	0.017983(0.000004)	13.519(0.463)
+58.4d	5995.74	0.017961(0.000006)	13.215(0.192)
		Component 3 (orange)	
-0.7d	5999.88	0.018664(0.000007)	12.583(0.027)
+28.2d	5999.99	0.018683(0.000007)	12.531(0.029)
+58.4d	5999.91	0.018669(0.000008)	12.590(0.034)
		Component 4 (purple)	
-0.7d	6005.36	0.019593(0.000010)	12.249(0.289)
+28.2d	6005.47	0.019613(0.000013)	11.906(0.123)
+58.4d	6005.43	0.019606(0.000013)	12.036(0.084)

[a] $\chi^2_{DOF} = 5.22$
[b] $\chi^2_{DOF} = 4.97$
[c] $\chi^2_{DOF} = 1.44$

$$\log_{10} N_{NaI} = 13.180(0.003) + 1.125(0.005) \times \log_{10} A_V, \tag{5.3}$$

Substituting our column density values for each component, we estimate values of $A_V \simeq$ 4.8(0.4), 1.4(0.5), 0.295(0.016) and 0.15(0.09) respectively, for which, adopting a standard MW dust law ($R_V = 3.1$), corresponds to $E(B-V) \simeq$ 1.54(0.12), 0.44(0.16), 0.095(0.005) and 0.048(0.028).

However, Phillips et al. (2013) have shown that the most accurate spectral predictor of the individual SN extinction is the equivalent width of the diffuse interstellar band (DIB) at λ5780 Å. Moreover, the authors found that a quarter of the SNe of their sample display anomalously large Na I column densities, compared to the amount of dust extinction derived from their colours, and all of them show blueshifted profiles. In Fig. 5.10, we plot our three XSHOOTER spectra, in rest wavelength (adopting the aforementioned value of the redshift), at the expected vicinity of the DIB λ5780.

We identify a potential DIB λ5780 at $\lambda = 5781.3813 \pm 0.2178$ Å, with a FWHM of 1.8351 ± 0.6221, corresponding to an equivalent width of $EW = 0.0541 \pm 0.0186$ Å. Using equation 6 of Phillips et al. (2013)

$$\log_{10} \mathrm{EW}(5780) = 2.283(0.001) + \log_{10} A_V, \tag{5.4}$$

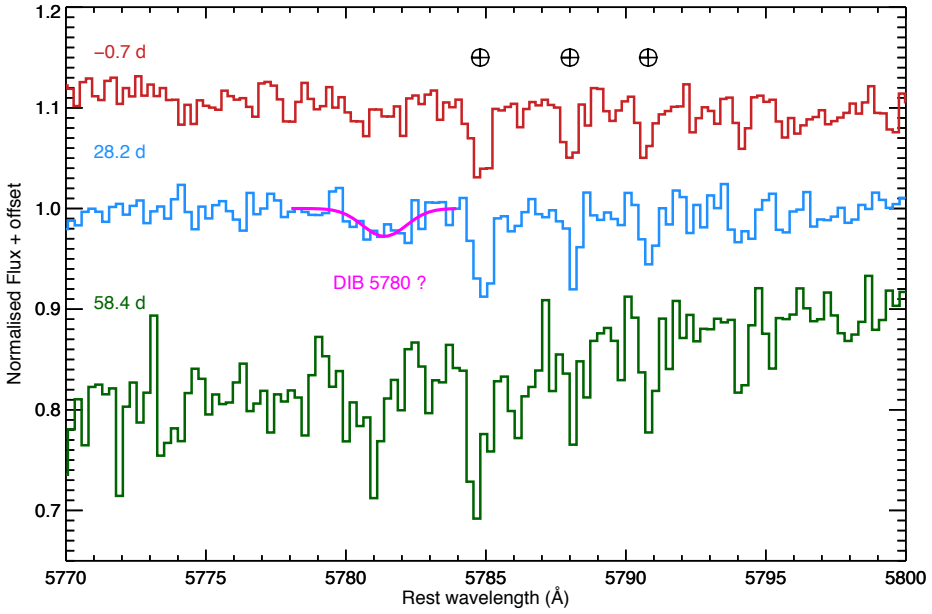

FIGURE 5.10: The XSHOOTER spectra of SN 2014eg at -0.7 (red), +28.2 (blue) and +58.4 (green) from peak luminosity, at ∼5770–5800 Å in rest wavelength. Telluric features are marked with ⊕. The absorption line at ∼ 5780 Å, shown in magenta, corresponds to the potential DIB λ5780.

where $\log_{10}$ EW(5780) is the equivalent width of the DIB λ5780 in mÅ, we find A_V = 0.28 ± 0.10, and using equation 7,

$$\log_{10} \mathrm{EW}(5780) = -9.433(0.004) + 0.889(0.004) \times \log_{10} \mathrm{N_{NaI}}, \tag{5.5}$$

we obtain $\log_{10} \mathrm{N_{NaI}}$ = 12.56 ± 0.18. For standard MW dust, our A_V value corresponds to $E(B-V)$ = 0.091 ± 0.031, which is in disagreement with the value estimated from the SN colours (section 5.4.2) and the saturated component Na I column density, but in agreement with component 3 (orange). The reason for this discrepancy can be either that there is a misidentification of the DIB *or* the true absorption of the host galaxy is indeed small, and the anomalously large absorption seen from the Na I doublet originates from another source on the line of sight, possibly CSM.

In Fig. 5.11, we plot the XSHOOTER spectra, converted to velocity space adopting z = 0.01826, for the Na I doublet, Ca H, Ca K and K I λ7665. We include the three components identified in Fig. 5.9 and presented in Table 5.3. We also show the velocity of the DIB λ5780 at the lower panel, derived from the fit in Fig. 5.10. We also plot the column densities and the derived redshifts of the 4 components in Fig. 5.12 as a function of time, color-coded as in Fig. 5.9.

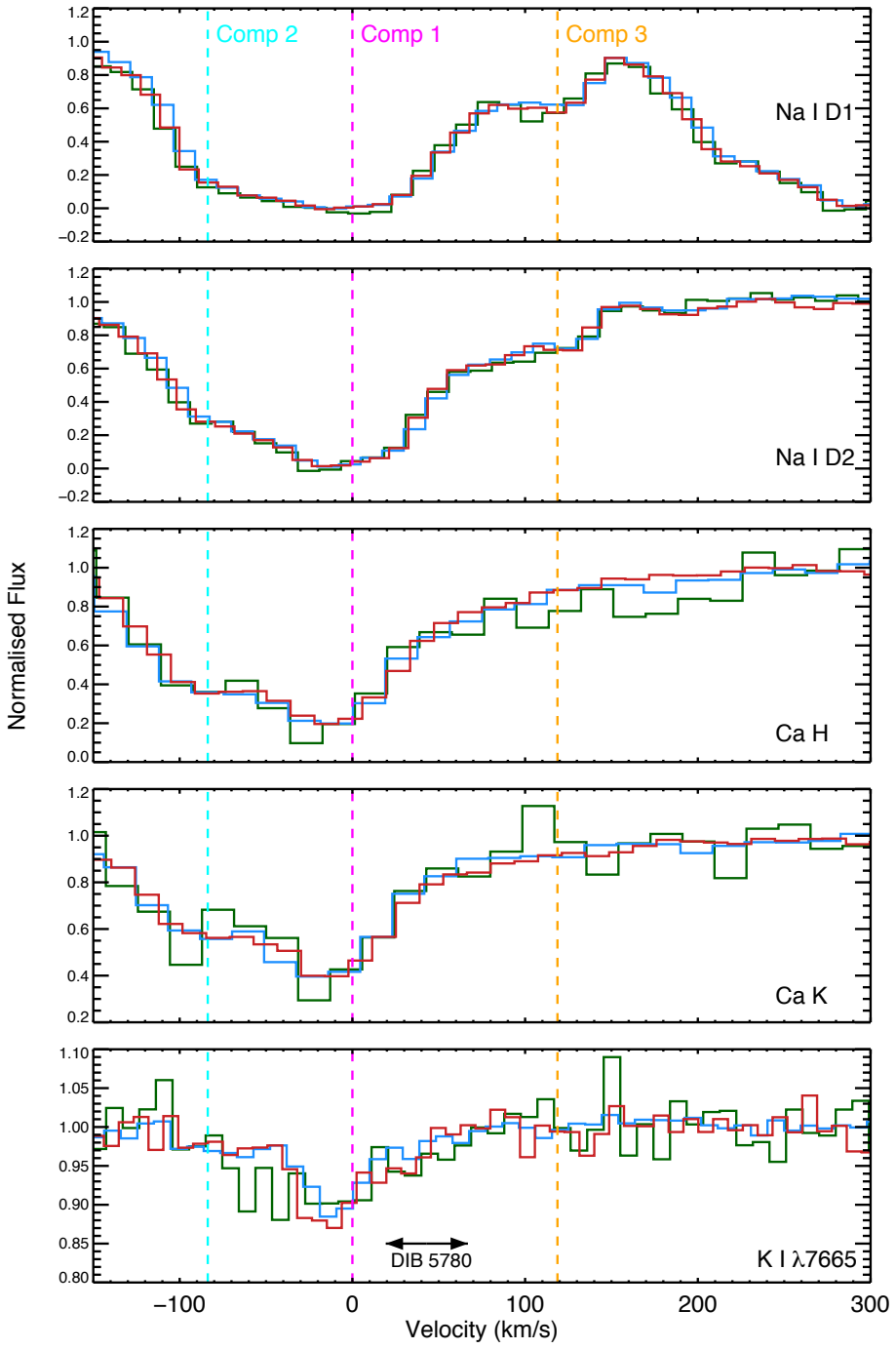

FIGURE 5.11: The XSHOOTER spectra of SN 2014eg at -0.7 (red), +28.2 (blue) and +58.4 (green) from peak luminosity. From top to bottom: NaI D1, NaI D2, Ca H, Ca K and K I λ7665. We over-plot with vertical dashed lines the corresponding velocities of Component 1 (magenta, 0 kms^{-1}), Component 2 (cyan, -84 kms^{-1}) and Component 3 (orange, +119 kms^{-1}). At the lower panel, we over-plot the velocity of the DIB λ5780 as $\pm 1\sigma$ error bar, derived from our fit in Fig. 5.10. Note that the velocity of Component 4 (400 kms^{-1}) is not shown.

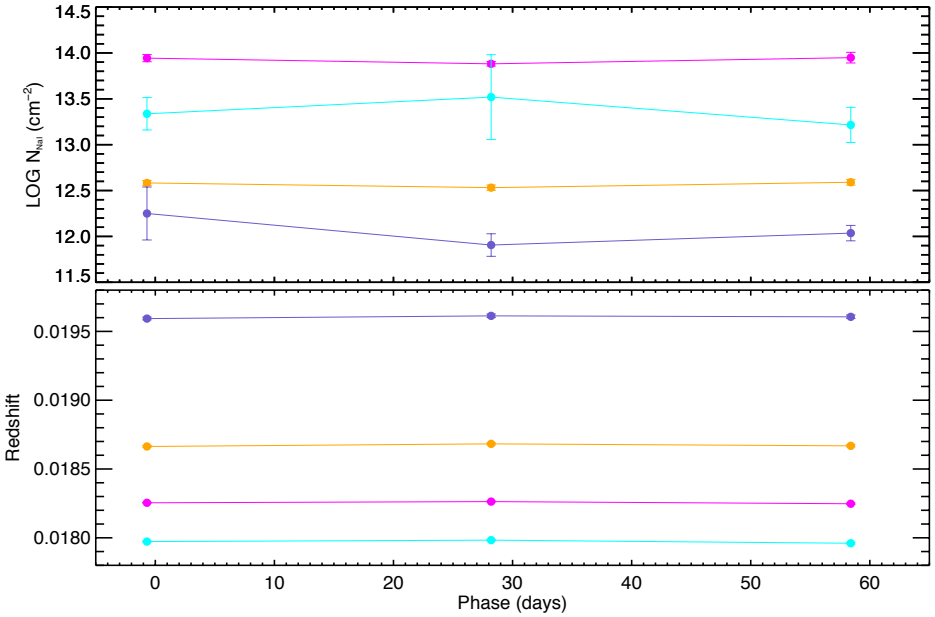

FIGURE 5.12: The estimated NaI column densities (top) and derived redshifts (bottom) of the 4 components, color-coded as in Fig. 5.9.

We do not see any appreciable temporal evolution in the absorption features, either in the blueshifted or the redshifted components. This means that, at least for the time range that our high resolution spectra are probing (-1 to 60 days from peak), no CSM in the form of expanding shell(s) is present, at distances of $\sim 10^{16}$ cm, as seen in other SNe Ia with time-varying absorption components (see section 5.1).

5.4.5 The reddening law of SN 2014eg

The fact that SN 2014eg exhibits anomalously large absorption motivates us to investigate in more detail the reddening towards the SN. A method to distinguish it has been presented in Folatelli et al. (2010), where the authors were able to prove that for highly reddened objects, such as SN 2014eg, the reddening law deviates from the MW adopted value of $R_V = 3.1$ towards lower values. In particular, for the highly-reddened SN 2005A and SN 2006X (which, according to Patat et al. 2007, shows signs of CSM) they find $R_V = 1.7 \pm 0.1$ and 1.6 ± 0.1 respectively, interpreted as multiple scattering (Goobar, 2008) by dense CSM in the vicinity of the SN. In order to be able to probe the reddening law, it is crucial to have photometric observations either in the UV or in the NIR at peak, which we do not have for SN 2014eg. However, we did acquire a NIR spectrum with SOFI at +14 days from maximum, for which by performing spectrophotometry we estimate $J = 16.64$, $H = 16.06$ and $K = 15.81$. The two NIR SOFI spectra are presented in Fig. 5.13. Since SN 2014eg is relatively similar to SN 2006X, and by examining the

NIR light curve of it (Friedman et al., 2015), we decide to use our measurement of the H-band, which shows a relatively smaller decline from peak to +14 days, of ∼0.2 mag, adopting $H = 15.86$.

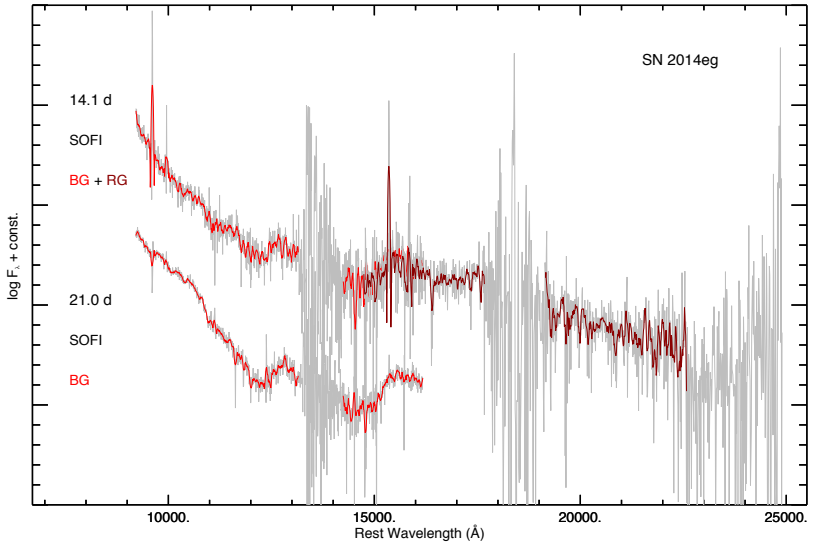

FIGURE 5.13: Near-infrared spectroscopic sequence of SN 2014eg. The grey lines display the raw spectra, while the red (Blue SOFI grism) and dark red (Red SOFI grism) lines show the spectra smoothed with a Savitzky-Golay polynomial smoothing filter (Savitzky & Golay, 1964), with a width of 50 Å. The spectra are shifted by an arbitrary offset for illustration purposes. The gaps of the smoothed spectra at $\sim 13,000 - 14,500$ and $\sim 18,000 - 19,000$ Å correspond to regions of high telluric absorption.

Following Folatelli et al. (2010), we calculate the colour excesses $E(V - X_\lambda)$, for bands $X_\lambda = BgVriH$, by k-correcting our photometry at peak with the Nugent 91T template and comparing it with the unreddened pseudo-colours at maximum from CSP (Table 3 of Folatelli et al. 2010) as a function of Δm_{15}. The final result is plotted in Fig. 5.14. By fitting the CCM model we find $R_V = 1.56 \pm 0.95$ and for the LMC dust Goobar 2008 power law with $p = -2.23 \pm 0.97$. We note that, for SN 2006X, Folatelli et al. (2010) found $R_V = 1.6 \pm 0.1$ and $p = -2.5 \pm 0.1$ respectively.

Kangas et al. (2016) have calculated a reddening law for ESO 154-G010, using data from SN 2013fc. For the Balmer decrement they favor a standard Cardelli-law with $A_V = 2.8 \pm 0,2$ mag, while by comparing the BVRI light curves of SN 2013fc to those of SN 1998S, they estimate $A_V = 2.9 \pm 0,2$ mag. While it is evidently clear that ESO 154-G010 is a particularly dusty galaxy, we note that the location of SN 2013fc is different compared to SN 2014eg: It is located closer to the nucleus, on top of a circumnuclear ring. Moreover, the authors assume a standard $R_V = 3.1$ law.

We conclude that there is clear indication that the material that causes the abnormal reddening of SN 2014eg is not MW-like dust in the ISM, but dust that is local to the

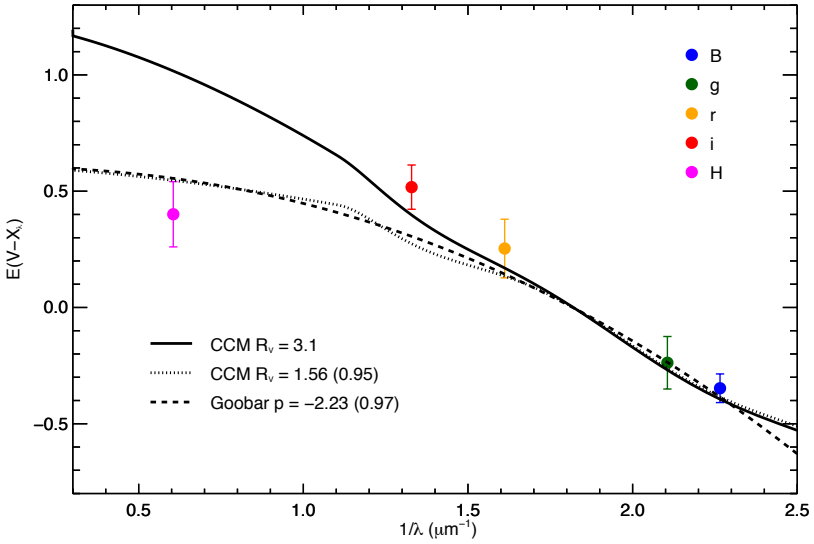

FIGURE 5.14: Colour excesses in the form of $E(V - X_\lambda)$, for bands $X_\lambda = BgVriH$, for SN 2014eg. We over-plot the CCM model with $R_V = 3.1$ with solid line and the two fits we perform: The fit of the CCM model with dotted line and the Goobar 2008 law, suitable for LMC dust grains, with their fitted values indicated at the legend.

SN, possibly CSM ejected by the companion in a SD scenario configuration.

5.4.6 The bolometric light curves of SN 2014eg and SN 2016hvl

Finally, we turn our focus on the bolometric luminosity of SN 2014eg and SN 2016hvl, and calculate important physical parameters that describe the phenomenon, such as the mass of ^{56}Ni, synthesised in the explosion, and the total mass of the ejecta. As noted in section 5.1, the well-established width-luminosity relation is primarily explained by different masses of radioactive ^{56}Ni synthesised: SNe with higher masses have higher luminosities and broader light curves. Accurate estimation of the ejecta mass may provide insights on whether the SN's explosion is sub-Chandra ($<< 1.4\,M_\odot$), Chandra ($\sim 1.4\,M_\odot$) or super-Chandra($>> 1.4\,M_\odot$), with different implications for the progenitor scenario. We note that we will calculate the bolometric luminosity in the optical bands, i.e. the pseudo-bolometric luminosity, and not the total luminosity. This does not affect significantly our results, since most of the flux of a SN Ia at these epochs is emitted at the optical bands.

In order to construct a bolometric light curve, an accurate determination of the luminosity distance and extinction of the host galaxy is crucial. For SN 2014eg, with a redshift of $z = 0.018252$, we adopt a distance modulus of $dm = 34.495$, which corresponds to a luminosity distance of 79.256±5.5 Mpc. As for SN 2016hvl, we will use the value for UGC 03524, that gives a distance luminosity of 57.9±4.1 Mpc, for a redshift of $z = 0.013$.

For the absorption on the line of sight, we use the values of $E(B-V)$ estimated in section 5.4.2 for the hosts: $E(B-V)^{14eg}_{host} = 0.392 \pm 0.018$ and $E(B-V)^{16hvl}_{host} = 0.184 \pm 0.053$. For the total-to-selective absorption ratio, R_V, we use the value we estimated in section 5.4.5, $R_V = 1.56$, for SN 2014eg, while for SN 2016hvl, since no strong absorption components from its host can be seen in the spectra, we will retain the normal MW dust value of $R_V = 3.1$. The values for the MW extinction on the line of sight are $E(B-V)^{14eg}_{MW} = 0.026 \pm 0.01$ and $E(B-V)^{16hvl}_{MW} = 0.377 \pm 0.01$, with $R_V = 3.1$.

We calculate the bolometric luminosity as follows: The photometry is extinction-corrected and k-corrected to the redshift of the SN, using the Nugent 91T template, and the fluxes of each optical band are recovered, for each epoch of observation that we have simultaneous BgVri observations. Then, a trapezoidal integration is performed at the resulting SED, and converted to luminosity. The results are shown in Fig. 5.15.

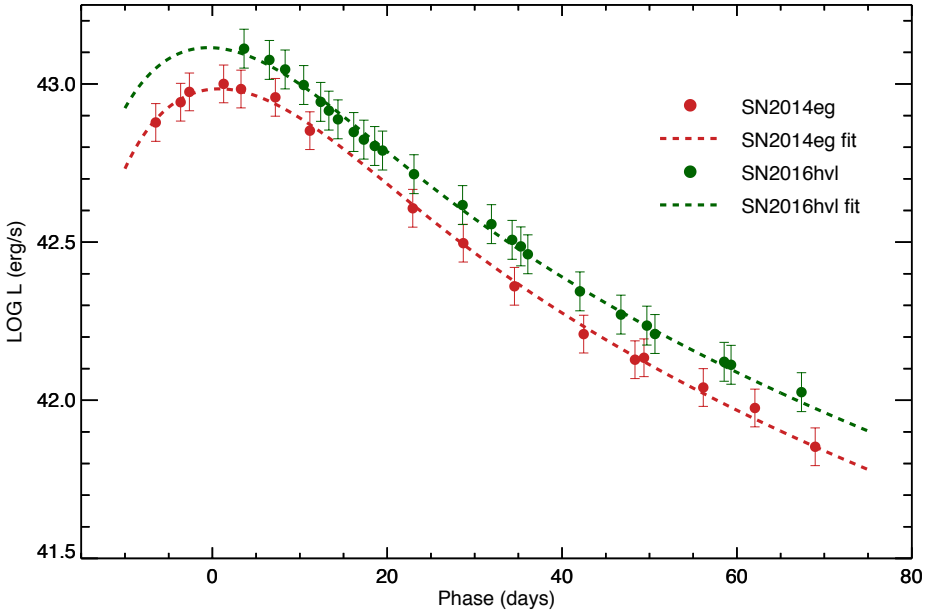

FIGURE 5.15: The pseudo-bolometric light curves of SN 2014eg (red circles) and SN 2016hvl (green circles). We include the fit of the luminosity, described in the text, as red and green dashed lines, for SN 2014eg and SN 2016hvl respectively.

We fit each bolometric light curve with a semi-analytical model derived according to the formalism of Arnett (1982): The bolometric light curve is powered by the deposition of energy released in the radioactive decay of ^{56}Ni to ^{56}Co. The free parameters of the model are the mass of ^{56}Ni M_{56}, the total ejected mass of the explosion M_{ejecta}, the rise time to peak t_0, the opacity of the ejected material κ and the total kinetic energy of the explosion E_k. The results we obtain are presented in Table 5.4.

We note that, for SN 2016hvl, simultaneous observations in all the photometric bands were performed only after peak, so we are unable to constrain t_0. In this case, we fix

TABLE 5.4: SN 2014eg and SN 2016hvl bolometric parameters

	SN 2014eg[a]	SN 2016hvl[a]
M_{56} ($M_\odot$)	0.595(0.028)	0.789(0.052)
$M_{\rm ejecta}$ ($M_\odot$)	1.320(0.093)	1.357(0.125)
t_0 (days)	19.07(1.74)	20.085(–)[b]
κ ($cm^2 g^{-1}$)	0.266(0.014)	0.249(0.031)
E_k($\times 10^{51}$ erg)	1.230(0.111)	1.255(0.145)
$\chi^2_{\rm DOF}$	0.105	0.078

[a] 1-σ uncertainties in parentheses
[b] Fixed parameter

the parameter adopting a value for the rise time equal to t_0 = stretch $\times$ 19.5, for which gives, for the stretch of SN 2016hvl (s = 1.07), t_0 = 20.085 days.

We find that SN 2016hvl has produced slightly more ^{56}Ni than SN 2014eg, with a value of $M_{56} \simeq 0.79\,M_\odot$, consistent with the values for a 91T-like type of SN Ia. The derived quantities for SN 2014eg are smaller than the ones of SN 2016hvl but generally larger than normal SNe Ia, confirming the transitional character of 99a-like SNe.

5.5 Summary

In this Chapter, we performed an extensive analysis of two overluminous SNe Ia, classified and followed-up by PESSTO and LCO. We presented the dense photometric and spectroscopic dataset of these two objects and focused on the analysis of the immediate environment at the site of the explosion. We confirmed the 99aa-like and 91T-like character of SN 2014eg and SN 2016hvl respectively and we provided hints on the progenitor system of SN 2014eg, by studying the reddening of the SN light curve and the high resolution spectra of it. We were able to derive a reddening law that indicates a possible presence of material local to the explosion site of the SN, in accordance with other similar, high-reddened events.

The importance of host galaxy studies of SNe Ia, in order to disentangle the progenitor problem, has already been established. Towards this goal, I will continue to collect data on the overluminous subclass of SNe Ia, under ePESSTO. Up to date, there are two more 91T-like events, SN 2017awz and SN 2017dfb, for which data are currently collected. Over the next 2 years of ePESSTO, we expect to classify and follow-up ~5-10 events, based on previous PESSTO experience. We stress the importance of NIR data around peak luminosity, since these data provide considerable leverage in order to constrain the nature of the absorption and provide insight on the progenitor system configuration.

Motivated by this work, in the following chapter, we will examine the host galaxies of the 91T-like SNe Ia. We will attempt to confirm a speculation in the SN community that 91T-like SNe Ia explode predominantly (if not exclusively) in late-type spiral galaxies and try to extract information on the reddening, in a statistical manner. This result will be important in providing constraints on the explosion mechanism and the progenitor channel of the overluminous SNe Ia.

Chapter 6

The host galaxies of the overluminous Type Ia Supernovae

An important observational characteristic that distinguishes thermonuclear from core-collapse supernovae (SNe) is the environment in which they occur: while core-collapse explosions happen exclusively in late-type galaxies, reflecting the fact that their progenitors are young massive stars, SNe Ia occur in both late-type (spiral or irregular) and early-type (elliptical) galaxies. This attribute is an indication of the older age of the exploding object, consistent with their carbon-oxygen white dwarf (C/O WD) origin.

While a correlation between the light curve decline rate with the host galaxy properties (fainter-faster SNe Ia are preferentially located in massive/older galaxies) has been observed, a targeted study on spectroscopically defined subclasses of SNe Ia has not yet been performed. With this in mind, in this Chapter we will investigate the 91T-like SN Ia subclass, and explore whether they have any indication to explode in specific environments. Such a preference will have implications on the progenitor system of these events, and potentially impact cosmological studies, by correcting for the SNe Ia host bias.

6.1 Motivation

Indications of different SN Ia flavours have long been observed. The 'width–luminosity relation' (WLR Phillips, 1993) reveals a continuum in the luminosity-decline rate phase space, with brighter SNe having broader light curves. Moreover, various spectral indicators, such as the pseudo equivalent widths (pEWs) of the silicon lines, indicate a relation

in temperature and ionisation of the ejecta: high temperature ejecta have lower silicon pEWs (Benetti et al., 2005; Blondin et al., 2012).

However, perhaps the strongest indication of discrete SN Ia families comes from studies on the host galaxies of the explosions. Family 1, as defined in Maguire et al. (2013), includes the broad-bright SNe Ia with low silicon pEWs, and preferentially occur in late-type, low mass galaxies with high specific star formation rates (Hamuy et al., 2000; Sullivan et al., 2006, 2010), compared to Family 2 (narrow-faint). At the same time, measurements of the delay-time distribution (DTD) and the SN rates show evidence for two distinct progenitor channels: a 'prompt' channel, with a short DTD and a 'delayed' one with longer DTDs. In this context, Family 1 favours the 'prompt' channel, with younger stellar environments and progenitor systems (Mannucci et al., 2006; Sullivan et al., 2006; Smith et al., 2012; Childress et al., 2013). With this in mind, a clear prediction is the preference of the highest stretch SNe Ia to occur in the youngest stellar systems.

While this two-component model for the production of SNe Ia is one of the possible answers to the progenitor question, theoretical delay times for DD scenarios are also in agreement with observed volumetric SN rates (e.g. Perrett et al., 2012), although the sparse information below ∼1 Gyr, where typical timescales of SD models lie (Sullivan et al., 2006), prevents accurate comparisons. However, *assuming* that the 'prompt-tardy' model is correct, SD models, for which the binary consists of a white dwarf (WD) and a MS or more evolved star, would favour Family 1 (however, the Di Stefano et al. 2011 spin-up/spin-down SD progenitors can potentially contribute to Family 2, due to their longer timescales), while DD channels favour Family 2. The detection of blueshifted NaI D absorption features in Family 1 SNe, with little NaI D absorption for Family 2, supports this idea: SD channels naturally predict outflows of circumstellar material (CSM) at the location of the explosion (Sternberg et al., 2011; Maguire et al., 2013).

The spectroscopic sub-class of the 91T-like SNe Ia is one of the primary candidates for a distinct group of events within the broad-bright family. An introduction of the properties for these explosions and their possible connection to the SD channel has already been argued in Chapters 4 and 5. In this Chapter, motivated by the work cited above, we will attempt to perform an analysis of the global properties of the 91T-like hosts of the PTF sample, comparing them with the general PTF SN Ia population, and examine whether they exclusively belong to the Family 1 group.

6.2 Host galaxy data

We now present the observational data of the PTF-SDSS SNe Ia sample we will use in our analysis. The SN Ia sample is already presented in Chapter 2.1. We here discuss the SDSS host photometric data, and the technique we use to identify the correct host for each SN.

6.2.1 Host galaxy photometric data

In this work, we use photometric data of the hosts of the PTF SN Ia sample that are located in the SDSS footprint. SDSS (York et al., 2000) performed deep imaging of $\sim$ 8400 deg^2 of high Galactic latitude sky, and more than 900,000 galaxies. The survey used the SDSS 2.5 m telescope (Gunn et al., 2006) located at at Apache Point Observatory, employing a wide-field CCD camera (Gunn et al., 1998) with an image size of 13.51×8.98 arcminutes, in the five SDSS optical bands (u′g′r′i′z′), with typical limiting magnitudes of 22.0, 22.2, 22.2, 21.3 and 20.5 respectively. For this work, we will use publicly available catalogue data, included in Data Release 12 (DR12; Alam et al., 2015), which we describe below.

We perform an SQL query at the Catalog Archive Server (CAS) using CasJobs[1], requesting observational data of sources flagged as galaxies that lie in a radius of 1 arcmin from the location of each PTF SN Ia. The relevant data for our analysis are twofold: Photometric observations in the five SDSS bands, and the parameters that describe the shape of the source. We retrieve the composite model fluxes and the associated uncertainties in u′g′r′i′z′ for each galaxy. This flux, dubbed as cModel Flux, is a linear combination of the best fit exponential and de Vaucouleurs profile to the source that best fits the image, and is recommended by SDSS to be used in galaxy sample studies, as opposed to PSF magnitudes/fluxes, suitable for bright point sources, or Petrosian magnitudes/fluxes, which tend to exclude the outer parts of galaxy profiles, especially for elliptical galaxies (Strauss et al., 2002). We also retrieve specific parameters that describe the ellipticity of the galaxy. These are the galaxy's ra and dec, the Petrosian radius in r′ band and the ellipticity Stokes parameters q and u. Finally, we also retrieve the angular separation of each SN with its potential host.

6.2.2 The DLR method

The correct identification of the host is not always straightforward (for example, see Sullivan et al., 2006): sometimes, the closest host (in projection) is not the correct

[1] http://skyserver.sdss.org/casjobs/

one. In order to tackle this problem, we employ the directional light radius (DLR) host matching method, initially developed by Sullivan et al. (2006) and applied in many other similar papers (Sako et al., 2014; Gupta et al., 2016). This method calculates the separation of the galaxy, normalised to its apparent size, with the SN that is potentially associated with: the separation of the SN from the candidate host is calculated in terms of each elliptical radius along a line that connects the SN position and the host galaxy centre. This separation is:

$$R_{\rm gal}^2 = C_{xx}(x_{\rm SN} - x_{\rm gal})^2 + C_{yy}(y_{\rm SN} - y_{\rm gal})^2 + C_{xy}(x_{\rm SN} - x_{\rm gal})(y_{\rm SN} - y_{\rm gal}), \tag{6.1}$$

with

$$C_{xx} = \cos^2(\theta)/r_A^2 + \sin^2(\theta)/r_B^2 \tag{6.2}$$

$$C_{yy} = \sin^2(\theta)/r_A^2 + \cos^2(\theta)/r_B^2 \tag{6.3}$$

$$C_{xy} = 2\cos(\theta)\sin(\theta)(1/r_A^2 + 1/r_B^2), \tag{6.4}$$

where r_A is the semimajor axis, r_B is the semiminor axis and θ is the position angle. In our case, the position angle is given by the Stokes parameters as

$$\theta = \frac{\arctan(u/q)}{2}, \tag{6.5}$$

the semimajor axis r_A is the Petrosian radius and the semiminor axis is

$$r_B = r_A \left(\frac{\sin 2\theta - u}{\sin 2\theta + u} \right) \tag{6.6}$$

For every SN in our sample, we assign an $R_{\rm gal}$ for each of the candidate hosts. An illustration of the method is shown in Fig. 6.1.

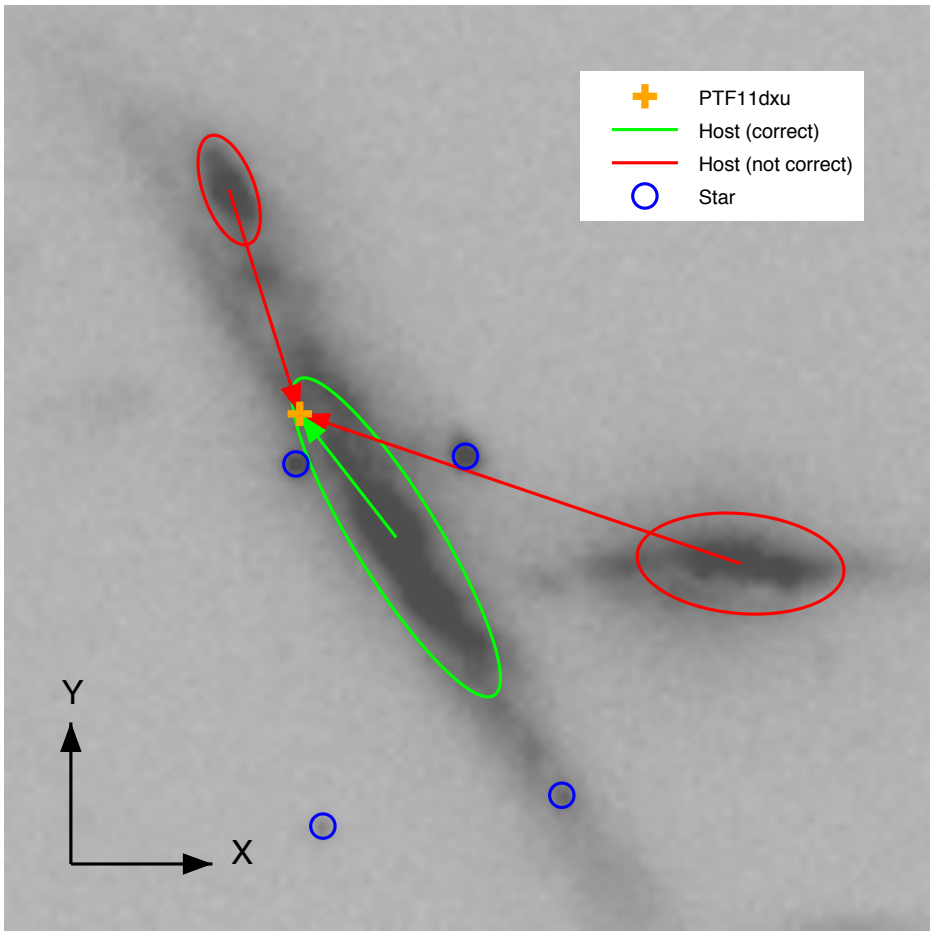

FIGURE 6.1: SDSS r′ image, in image coordinates (X,Y), at the location of PTF11dxu (orange cross), with an illustration of the directional light radius (DLR) host matching method. The three potential hosts, returned by the SDSS query, are shown as ellipses, as described in the text. The DLR method gives the correct host in green and disregards the other two (in red), according to the minimum DLR, presented in green and red arrows respectively. We also mark the position of foreground stars, in blue circles.

6.2.3 Further quality cuts

From the total of 1250 SNe Ia that PTF discovered, 1026 are in the SDSS footprint. Our SDSS query, as described in section 6.2.1 returned in total 15855 host galaxy candidates. We perform the DLR method for every SN and we initially record the potential hosts that have $R_{\rm gal} \leq 10$. With this cut, we recover in total 963 SN with potential hosts and 63 that we consider hostless. For these 963, our initial host sample consists of 1457 individual potential hosts.

In order to avoid spurious photometric sources in the SDSS photometry that may affect the correct identification, we employ an extra photometric quality cut: we require each potential host to have detections in g′r′i′, to ensure robust photometry, and, finally, we

TABLE 6.1: Number of host galaxy candidates and SNe passing each cut, described in sections 6.2.2 and 6.2.3

	No. of potential Hosts	No. of SNe
All host candidates	15855	1026
$R_{\rm gal} \leq 10$	1457	963
g′r′i′ detection + min($R_{\rm gal}$)	822	822
redshift + offset cut	804	804

associate as a true host to each potential SN the galaxy with the minimum $R_{\rm gal}$. With these cuts, we end up with 822 SNe and their associated hosts.

Two final quality cuts that we apply are a redshift cut of $z \geq 0.01$ (in order to avoid galaxies outside the Hubble flow) and an offset cut of 25 kpc, which we calculate from the angular separation of the SN with its host and the luminosity distance derived from the redshift of the SN. From the redshift cut, we disregard 3, and from the offset cut 15, which we also consider hostless. The final sample of the SNe and the hosts consists of 804 objects, and we summarise the quality cuts in Table 6.1.

6.3 Spectral energy distribution fitting

In order to characterise the global properties of the SNe Ia hosts, we estimate the stellar mass and the star formation rate (SFR) of the host galaxies of our sample. We use a custom fitting code also used in Sullivan et al. (2010). The code is similar to Z-PEG (Le Borgne & Rocca-Volmerange, 2002), while the templates are an expanded version of the ones based on the spectral synthesis code PÉGASE.2 (Fioc & Rocca-Volmerange, 1997). In particular, it is a set of 15 exponentially declining star formation histories (SFHs), with 125 age steps for each one, assuming a Salpeter (1955) initial mass function (IMF). The internal PÉGASE.2 dust prescription is not included in the templates, but instead we fit for extinction with $E(B-V)$=0 to 0.3 mag, with a step of 0.05 mag. After correcting the observed galaxy colours for MW reddening using the dust maps of Schlegel et al. (1998), the code fits them with the (total) 105 evolving spectral energy distributions (SEDs) and determines the best-fitting SED model by minimisation of the χ^2. The redshift of the host galaxy is fixed to the value of the SN redshift: this can either be the spectroscopic redshift estimated from galaxy emission lines in the SN spectrum, the spectroscopic redshift from the host galaxy spectrum taken during the PTF follow-up campaign or, in fewer cases, the redshift obtained from SNID (Blondin & Tonry, 2007) or SUPERFIT (Howell et al., 2005) fits of the classification or follow-up SN spectra.

The stellar mass $M_{\rm stellar}$ of the host galaxy is calculated by integrating the star formation history of the best-fitting SED model, subtracting the mass of the stars that have died.

TABLE 6.2: The classification scheme of the PTF SN Ia host galaxies sample

sSFR range	Star formation	Active or Passive
$\log_{10}$(sSFR)<-12.0	zero	Passive
-12.0≤$\log_{10}$(sSFR)<-10.6	low	Passive
-10.6≤$\log_{10}$(sSFR)<-9.5	moderate	Active
$\log_{10}$(sSFR)≥-9.5	high	Active

Since our data are purely photometric, we cannot determine the instantaneous SFR, but instead we estimate the recent SFR, averaging the SFR over the last 0.5 Gyr, as in Sullivan et al. (2006). We note that Sullivan et al. (2010) averages over the last 0.25 Gyr, stating that this choice provides similar results. We re-fitted our data with this value, finding no substantial differences in the results, thus we decided to keep the original value of 0.5 Gyr. We also record the specific star formation rate (sSFR), the SFR per unit stellar mass, for which we have $\log_{10}$(sSFR)=$\log_{10}$(SFR)-$\log_{10}(M_{\rm stellar})$. The uncertainties of these parameters are calculated by performing a Monte-Carlo simulation on the observed galaxy fluxes according to the uncertainties retrieved from SDSS.

6.4 Results

The goal of our analysis is to examine the dependence of the 91T-like SNe Ia properties on their environmental properties of their hosts, compared with the full SN Ia population. To this end, we will divide the SNe host galaxies into different groups, reflecting their recent star formation.

Sullivan et al. (2010) divides the host galaxies according to the sSFR. Galaxies with $\log_{10}$(sSFR)<-9.7 have smaller amounts of star formation relative to their stellar masses, and are classified as low sSFR, while those with a larger sSFR are classified as high sSFR. Smith et al. (2012) uses the same division, and also consider as passive galaxies with $\log_{10}$(sSFR)<-10.6, a value that represents the 'artificial edge' of the PÉGASE.2 templates. In our work, we consider 4 groups: Hosts with $\log_{10}$(sSFR)>-9.5 are considered as having high sSFR, hosts with -9.5<$\log_{10}$(sSFR)<-10.6 as moderate sSFR, hosts with -10.6<$\log_{10}$(sSFR)<-12.0 as low sSFR and hosts with $\log_{10}$(sSFR)<-12.0 will be considered as having a recent SFR of 0. In this scheme, outlined in Table 6.2, we will consider as 'active' the galaxies with high and moderate sSFR and 'passive' the galaxies with low or 0 sSFR.

6.4.1 Host galaxy properties

In Fig. 6.2, we show the distribution of our host galaxies sample in redshift (upper left), the SDSS r′ host galaxy apparent magnitude (upper right), the inferred DLR as discussed in section 6.2.2 (lower left) and the SN offset from the host centre in kpc (lower right). From the total of 804 host galaxies, and according to the scheme we introduced, we recover 641 active and 163 passive galaxies, with a ratio of ∼4, in accordance with Smith et al. (2012). The median χ^2 of the 804 fits is 2.1, while the equivalent values for active and passive galaxies are 1.9 and 3.1 respectively.

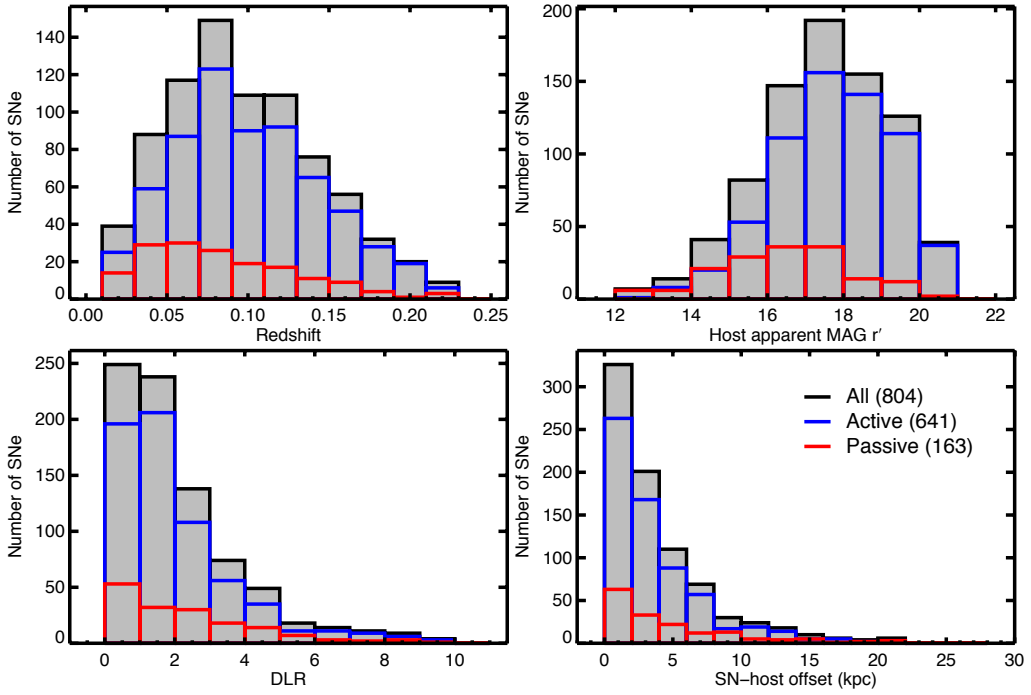

FIGURE 6.2: Distribution of the PTF SN Ia host galaxies in redshift (upper left), r′ host galaxy apparent magnitude (upper right), directional light radius (lower left) and SN offset from the host centre (lower right).

The distributions of $M_{\rm stellar}$ and SFR for the hosts of our sample is shown in Fig. 6.3. We note that from this point, we will present our results (and the corresponding units) in logarithmic space, e.g $\log_{10}(M_{\rm stellar})$, $\log_{10}$(SFR) and $\log_{10}$(sSFR), except where stated. The mean values of stellar mass and SFR for the complete sample is 10.331 $M_\odot$ and 0.191 $M_\odot yr^{-1}$. Splitting our sample into active and passive galaxies, we derive mean values of 10.228 $M_\odot$, (10.403 $M_\odot$ and 9.811 $M_\odot$ for the moderate sSFR and high sSFR, respectively) and 0.554 $M_\odot yr^{-1}$ (0.427 $M_\odot yr^{-1}$ and 0.860 $M_\odot yr^{-1}$) for the actives, and 10.735 $M_\odot$ (10.671 $M_\odot$ and 10.933 $M_\odot$ for the low sSFR and zero SFR, respectively) and -1.236 $M_\odot yr^{-1}$ (-0.558 $M_\odot yr^{-1}$ and -3.321 $M_\odot yr^{-1}$) for the passives respectively. This is

an expected result: galaxies with smaller sSFRs tend to have larger stellar masses, while the lower mass systems show increased star formation.

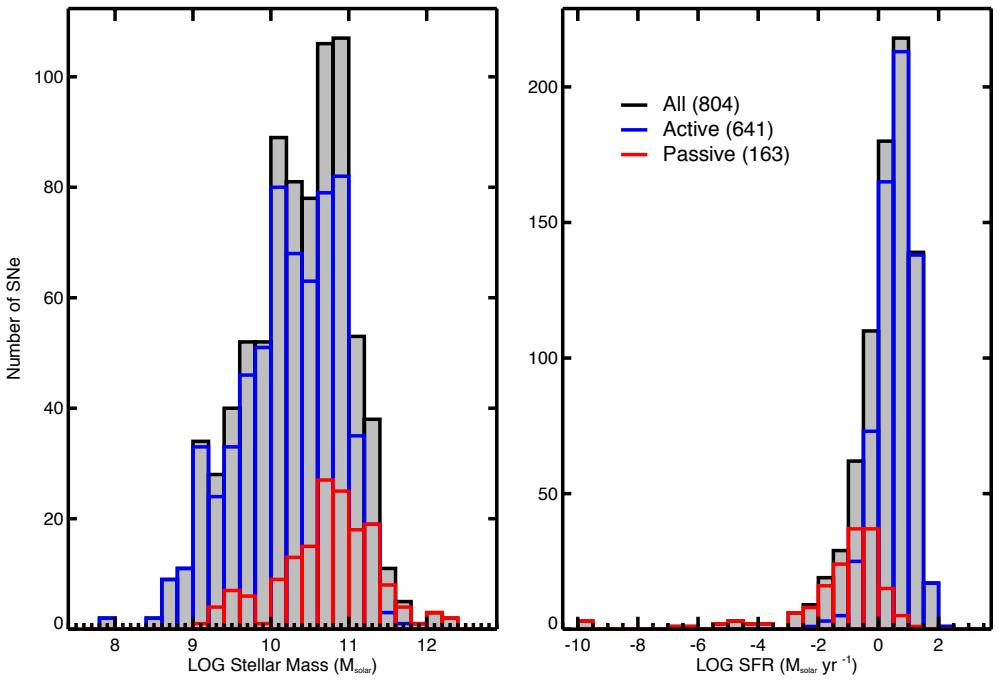

FIGURE 6.3: Distribution of the PTF SN Ia host galaxies in $M_{\rm stellar}$ (left) and SFR (right).

In Fig. 6.4, we plot the SFRs of our host galaxies sample versus their stellar mass, colour-coded according to the sSFR division scheme we introduced: high sSFR galaxies (189) are dark blue, moderate sSFR galaxies (452) are light blue, low sSFR galaxies (123) are light red and zero SFR galaxies (40) are dark red. The zero SFR galaxies are randomly plotted around $\log_{10}$(SFR)= −3.5, for illustration purposes. We measure a ratio of moderate to high sSFR galaxies of ∼2.4 and a ratio of low sSFR to zero SFR galaxies of ∼3.1. Our results are in accordance with Sullivan et al. (2010) and Smith et al. (2012): Our sample consists of ∼20% passive galaxies, with Sullivan et al. 2010 and Smith et al. 2012 ∼30% and ∼23%, respectively.

6.4.2 SN 91T-like host properties

A clear result of our study is the inferred SFRs of the 91T-like SNe Ia of our sample, marked with open green circles in Fig. 6.4. From the 26 events, we find that the host galaxies of 25 of them are active (21 in moderate sSFR galaxies and 4 in high sSFR), and 1 in a low sSFR passive galaxy. The mean mass of the active 91T-like hosts is 10.239 $M_\odot$ (10.429 $M_\odot$ and 9.389 $M_\odot$ for the moderate sSFR and high sSFR, respectively), while the mean SFR is 0.416 $M_\odot yr^{-1}$ (0.463 $M_\odot yr^{-1}$ and 0.753 $M_\odot yr^{-1}$). The only 91T-like

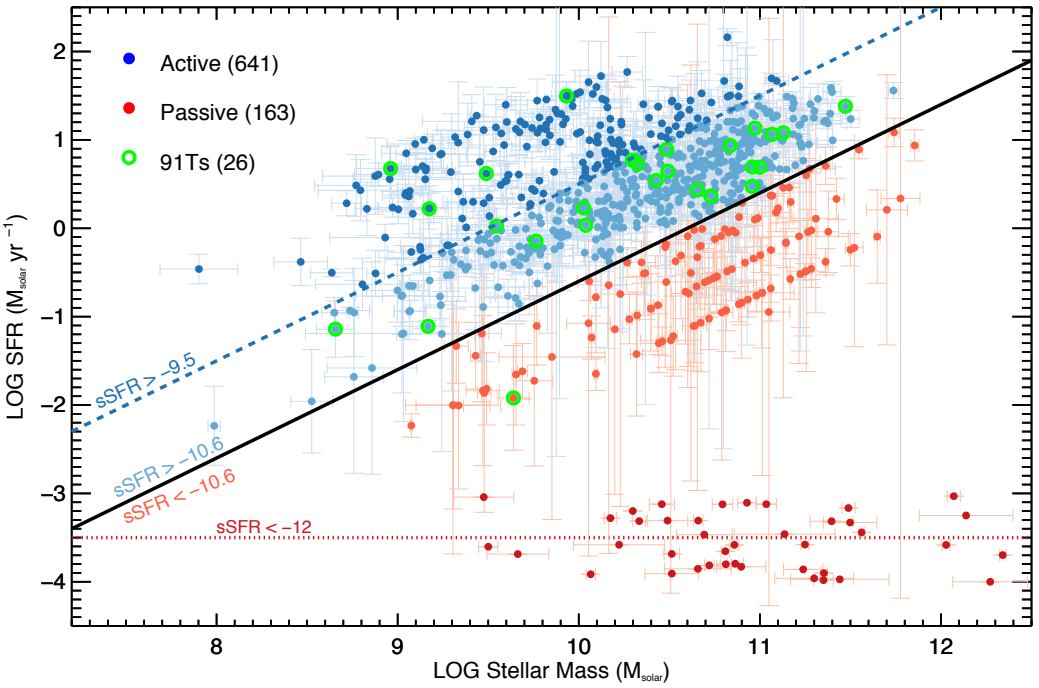

FIGURE 6.4: The distribution of the PTF SN Ia hosts in the $M_{stellar}$–SFR plane. The division between active and passive galaxies ($\log_{10}$(sSFR)>-10.6 and <-10.6, respectively) is shown as the black solid line. Active galaxies are plotted as blue full circles, for which the high sSFR are shown in dark blue and the moderate sSFR in light blue. Passive galaxies are plotted as red full circles, for which the low sSFR are shown in light red and the zero SFR in dark red. Note that, for the passive galaxies with SFR=0 are shown here as randomly distributed around $\log_{10}$(SFR)= −3.5. We mark the 26 91T-like SNe Ia in our sample with open green circles.

host in our sample consistent with a passive environment is a low sSFR host, with a mass of 9.639 $M_{\odot}$ and a SFR of -1.919 $M_{\odot}yr^{-1}$, which we note that it lies at the low end of the low sSFR mass and SFR distribution. We show the distribution of the sSFRs in Fig. 6.5, and the distribution of $M_{stellar}$ in Fig. 6.6. Interestingly, our results show that 91T-like SNe Ia do not preferentially explode in low-mass systems, but show a wide range that follows the active $M_{stellar}$ distribution. We overplot the SFR along the galaxy mass sequence (normalised to peak) found at the Salim et al. (2007) study of *GALEX* galaxies, expressed in the form of a modified Schechter function:

$$SFR = \log_{10}M * B * 10^{(\alpha+1)(\log_{10}M-\log_{10}M_0)} \exp(-10^{(\log_{10}M-\log_{10}M_0)}), \quad (6.7)$$

where B is a normalising factor, $\log_{10}M_0$ is the characteristic stellar mass and α is the low-mass slope, respectively. Their results are B=$5.96 \times 10^{-11}yr^{-1}$, $\log_{10}M_0$ = 11.03 and

$\alpha = -1.35$. A Kolmogorov-Smirnov test reveals that the 91T-like host mass distribution is drawn from this distribution with a likelihood of 97%.

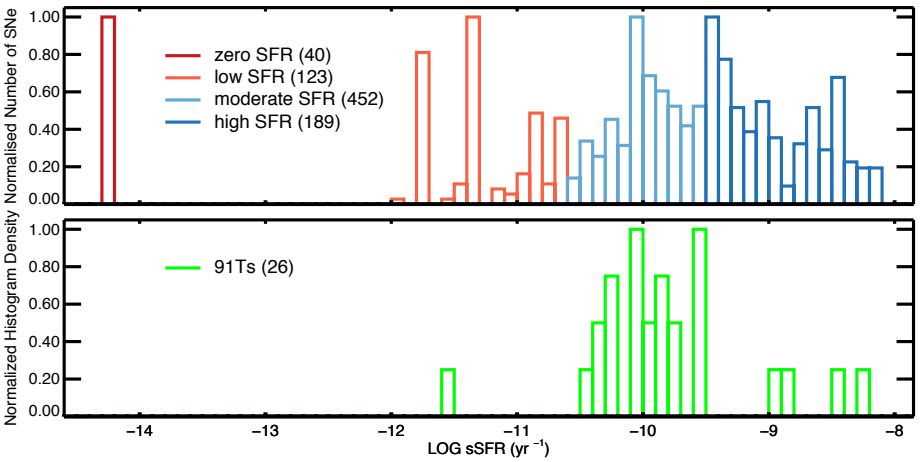

FIGURE 6.5: The normalised distribution of the PTF SN Ia host galaxies in specific star formation rate (sSFR), colour-coded according to Fig. 6.4. *Top panel*: Active hosts are shown in blue and passive hosts in red. *Bottom panel*: The 91T-like SN Ia host galaxies are shown in green.

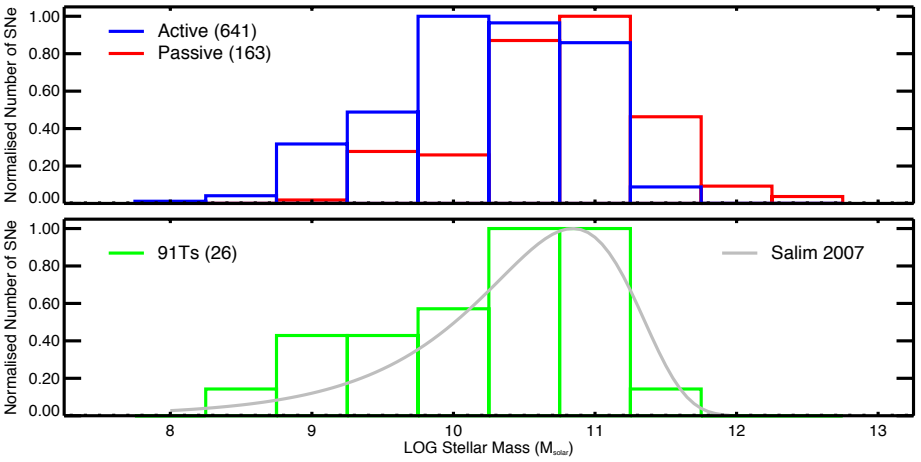

FIGURE 6.6: The normalised distribution of the PTF SN Ia host galaxies in host stellar mass. *Top panel*: Active hosts are shown in blue and passive hosts in red. *Bottom panel*: The 91T-like SN Ia host galaxies are shown in green. The solid grey line corresponds to the SFR distribution from Salim et al. (2007), normalised to peak.

We checked the validity of the classification of the 91T-like SNe of our sample, by fitting the available spectra, obtained during the PTF campaign, with SUPERFIT (Howell et al., 2005), confirming the 91T-like nature of the events. We show a collection of their earlier spectra in Fig. 6.7, colour-coded according to our division scheme. We also show the approximate phase of the spectrum, as given by SUPERFIT, at the left-hand side of each spectrum. 23 of our spectra were obtained early or around peak, while 3 of them at

later times ($> +7$ days from peak), and since the spectral characteristics of the 91T-like subclass manifest primarily at peak or before, we are confident of their classification.

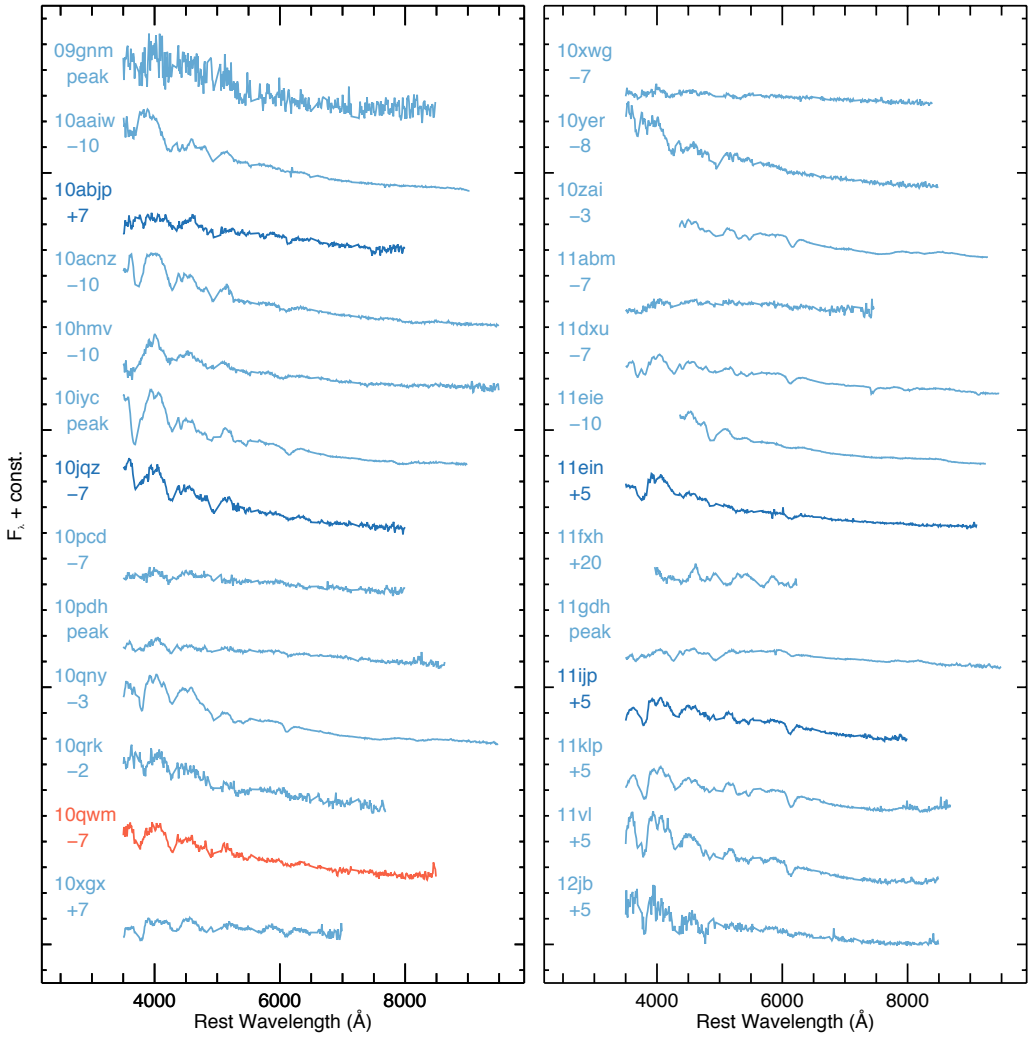

FIGURE 6.7: A collection of the 26 PTF 91T-like SNe Ia spectra of our host galaxy sample. The spectra are colour-coded as in Fig. 6.4: high sSFR are dark blue, moderate sSFR are light blue and low sSFR are light red. We report the classification phase, obtained by SUPERFIT at the left-hand side of each spectrum.

In Fig. 6.8, we show the SDSS stamps of the PTF 91T-like SN Ia host galaxies, where the host is centred at the image. We additionally add the star formation classification of the host at the bottom-right of each image. We summarize our results on Table 6.3.

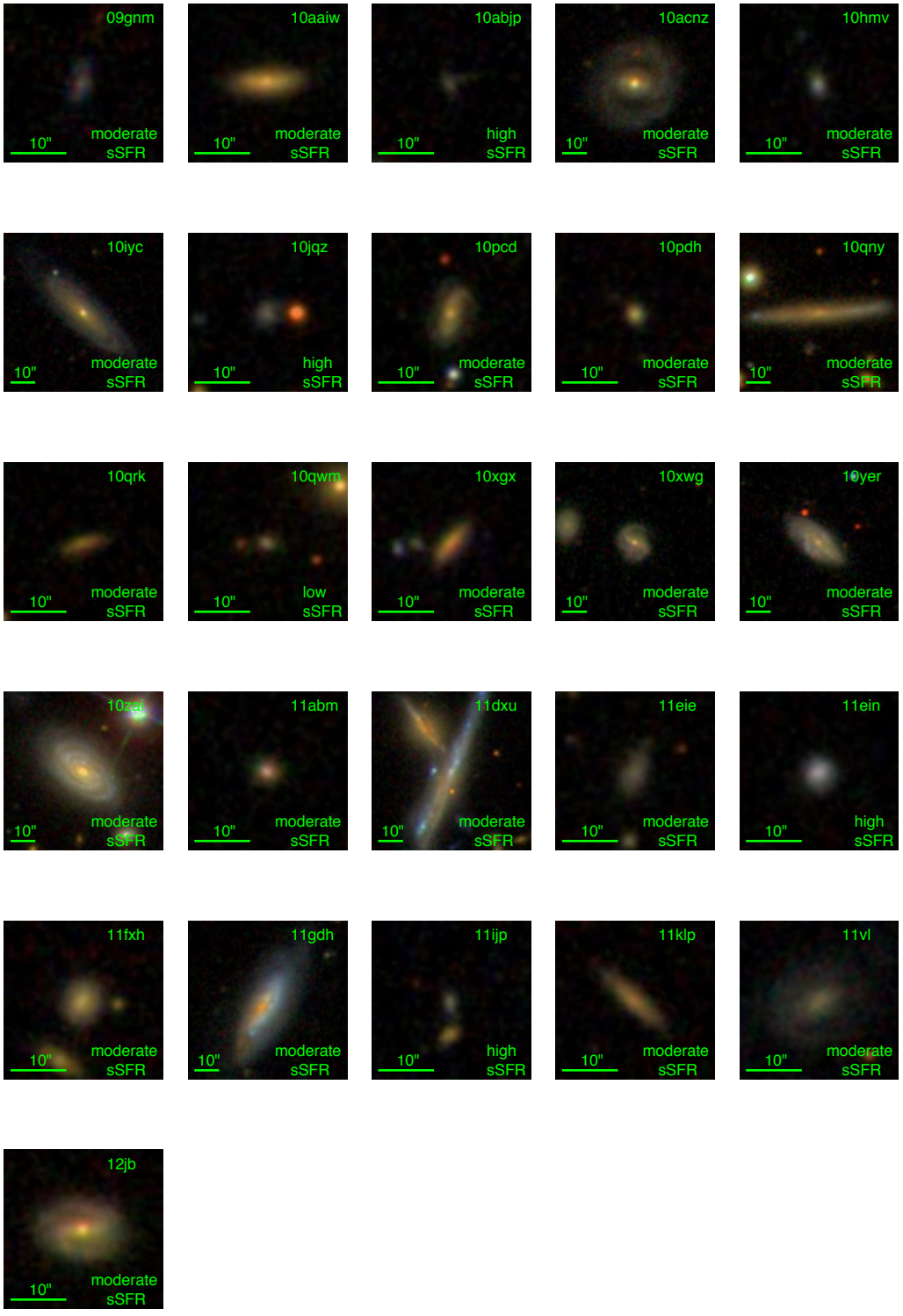

FIGURE 6.8: SDSS stamps of the 26 PTF 91T-like SNe Ia hosts of our sample.

TABLE 6.3: PTF 91T-like SNe Ia and their host properties

SN Name PTF	Ra	Dec	redshift	Host Ra	Host Dec	offset	Host Mass[a]	Host SFR[a]	Host sSFR[a]	Host classification[b]
	hh:mm:sss	dd:mm:sss		hh:mm:sss	dd:mm:sss	(kpc)	$\log_{10}M_{\odot}$	$\log_{10}M_{\odot}yr^{-1}$	$\log_{10}yr^{-1}$	
09gnm	02:47:31.572	-00:03:08.467	0.086	02:47:31.745	-00:03:10.188	2.94	9.55(0.25)	0.027(0.201)	-9.519(0.318)	m
10aaiw	01:09:21.151	15:44:08.117	0.060	01:09:21.022	15:44:06.612	2.08	10.66(0.02)	0.433(0.091)	-10.222(0.094)	m
10abjp	10:43:14.974	51:33:16.600	0.110	10:43:14.974	51:33:16.308	0.37	9.17(0.10)	0.221(0.523)	-8.953(0.534)	h
10acnz	11:44:58.656	58:39:42.303	0.062	11:44:56.292	58:39:45.756	12.70	10.73(0.07)	0.364(0.418)	-10.366(0.422)	m
10hmv	12:11:32.999	47:16:29.786	0.032	12:11:33.317	47:16:28.560	1.21	8.66(0.10)	-1.141(0.319)	-9.798(0.335)	m
10iyc	17:09:21.819	44:23:35.918	0.055	17:09:22.049	44:23:29.724	3.94	10.49(0.05)	0.893(0.221)	-9.593(0.226)	m
10jqz	12:27:49.559	10:42:23.616	0.120	12:27:48.784	10:42:24.948	15.81	8.96(0.19)	0.675(0.259)	-8.286(0.321)	h
10pcd	16:32:19.849	08:01:56.105	0.125	16:32:19.860	08:01:58.584	3.56	10.96(0.05)	0.474(0.216)	-10.483(0.226)	m
10pdh	16:51:31.439	44:23:30.123	0.134	16:51:31.435	44:23:30.804	1.04	10.04(0.03)	0.034(0.669)	-10.005(0.670)	m
10qny	16:09:31.296	22:20:10.535	0.033	16:09:30.682	22:20:09.924	3.06	10.43(0.06)	0.540(0.173)	-9.888(0.182)	m
10qrk	22:23:44.304	08:11:21.592	0.210	22:23:44.014	08:11:23.208	11.29	10.96(0.05)	0.693(0.201)	-10.266(0.208)	m
10qwm	22:02:50.185	08:23:38.283	0.101	22:02:50.150	08:23:37.896	0.72	9.64(0.09)	-1.919(0.592)	-11.559(0.598)	l
10xgx	00:12:23.149	02:30:44.060	0.142	00:12:23.242	02:30:44.208	2.27	11.00(0.08)	0.691(0.039)	-10.309(0.088)	m
10xwg	04:23:14.264	-05:05:49.801	0.093	04:23:14.292	-05:05:50.028	0.52	10.84(0.10)	0.937(0.277)	-9.900(0.294)	m
10yer	21:29:01.443	-01:25:48.310	0.050	21:29:01.358	-01:25:51.456	1.80	10.49(0.08)	0.646(0.253)	-9.846(0.264)	m
10zai	13:10:41.232	44:01:21.038	0.036	13:10:42.348	44:01:27.768	5.25	11.13(0.09)	1.080(0.115)	-10.049(0.147)	m
11abm	09:51:17.662	68:33:49.202	0.125	09:51:17.789	68:33:49.320	0.99	10.30(0.08)	0.769(0.380)	-9.528(0.389)	m
11dxu	16:12:44.831	28:17:02:292	0.025	16:12:44.674	28:17:10.068	2.09	10.03(0.05)	0.230(0.177)	-9.798(0.184)	m
11eie	15:14:12.122	20:46:32.409	0.039	15:14:12.139	20:46:34.104	0.73	9.17(0.09)	-1.109(0.067)	-10.277(0.110)	m
11ein	14:54:36.694	22:28:08:145	0.120	14:54:36.662	22:28:07.896	0.70	9.93(0.08)	1.497(0.167)	-8.435(0.185)	h
11fxh	21:35:17.329	04:43:09.217	0.133	21:35:17.472	04:43:10.596	3.98	10.97(0.07)	1.133(0.074)	-9.840(0.100)	m
11gdh	13:00:38.064	28:03:24.195	0.026	13:00:37.860	28:03:28.692	1.44	10.32(0.08)	0.727(0.030)	-9.598(0.085)	m
11ijp	21:47:11.133	-01:13:03.252	0.131	21:47:11.131	-01:13:02.316	1.39	9.49(0.31)	0.620(0.138)	-8.870(0.337)	h
11klp	22:17:28.418	18:17:03.479	0.174	22:17:28.414	28:17:13.542	20.47	11.07(0.07)	1.062(0.106)	-10.005(0.125)	m
11vl	16:28:40.679	27:43:32.954	0.045	16:28:40.282	27:43:39.864	4.23	9.76(0.07)	-0.147(0.062)	-9.910(0.095)	m
12jb	23:46:09.360	03:17:34.145	0.115	23:46:09.782	03:17:32.928	8.21	11.47(0.04)	1.380(0.112)	-10.092(0.117)	m

[a] 1-σ uncertainties in parentheses

[b] according to Table 6.2

The ratio of the 91T-like SNe Ia that occur at active galaxies over the passive ones is 25. In order to test the statistical significance of our result, we use a Bootstrap approach: we perform 100,000 random sample realisations of our total host galaxy sample, the 91T-like host sample and the non 91T-like host sample. For each realisation, we randomly select 26 hosts of each sample (26 being the total number of 91T-like hosts), allowing for replacement. With this approach, a specific host galaxy is allowed to be selected on multiple occasions, ensuring that the effect of outliers within the sample will be probed. For each of the randomly selected 26 hosts, we calculate their sSFR and divide them to active or passive, according the criterion illustrated in Fig. 6.4, and we record the ratio of the number of actives over passives. Note that, at some cases, we may recover zero active or passive galaxies. In this case, the nominal ratio will be 0 or infinity, but in our work, we replace the infinity with 26. A histogram of the bootstrapping is shown in Fig. 6.9.

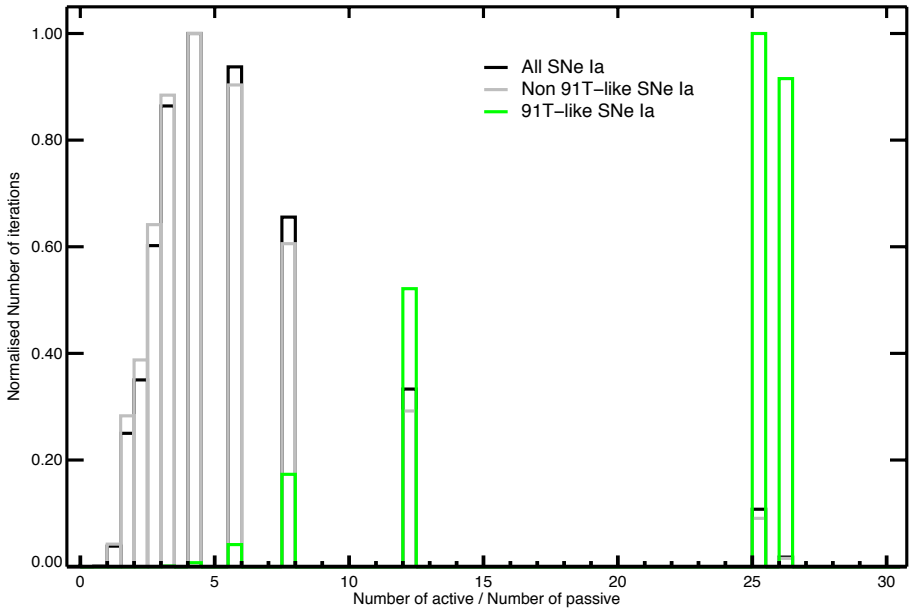

FIGURE 6.9: Normalised distribution of the number of active over passive galaxies for the complete sample (black), the non 91T-like sample (grey) and the 91T-like sample (green), for 100,000 bootstrap realisations. Ratio values at 0 and 26 represent a random sample with zero active and passive galaxies, respectively.

As expected, the peak of the distribution for both the complete sample and the non 91T-like one is centred at ~4, indicating that they are drown from the same parent population. On the contrary, the 91T-like host galaxies are skewed towards higher ratios of active to passive galaxies.

6.4.3 SN Ia properties as a function of host galaxy properties

Having established the fact that the host galaxies of 91T-like SNe Ia form a distinct group in terms of their star formation, we turn our analysis to investigating correlations between photometric and spectroscopic properties of SNe Ia with the host galaxy properties we derived. A study of the PTF SNe Ia properties has already been performed by Maguire et al. (2014), briefly discussed in Chapter 2.1. In this study, the authors have performed photometric and spectroscopic analysis of 264 low-z ($z < 0.2$) SNe Ia discovered and monitored by PTF, focusing mainly on spectral velocities and pseudo-equivalent width measurements of common absorption lines found in SNe Ia. From the total of 264 SNe in that work, 212 events overlap with our sample. From the 212 SNe, 175 occurred in active and 37 in passive galaxies, with a ratio of ~4.7 (while our complete host galaxy sample has a ratio of ~4).

Regarding 91T-likes, Maguire et al. (2014) analysed 8: PTF10acnz, PTF10hmv, PTF10iyc, PTF10jqz, PTF10qny, PTF10zai, PTF11dxu and PTF11gdh. The ratio between the number of 91T-likes to the total population is ~0.038, while the equivalent ratio of the complete host sample from section 6.4.3 is ~0.033. From those 8, 1 is in a high sSFR host and 7 in a moderate sSFR host. Unfortunately, PTF10qwm, the only 91T-like that occurred in a passive environment has not been studied in Maguire et al. (2014).

In Fig. 6.10, we show the stretch of the SN as a function of the host galaxy sSFR. We average the SN stretches, weighted by their errors, in bins defined by our sSFR division scheme (zero SFR, low sSFR, moderate sSFR and high sSFR). For the sSFR, we calculate the mean and standard deviation of it for each sSFR bin. A clear correlation is seen (reduced $\chi^2 = 0.6$): lower-stretch SNe Ia explode in lower star formation environments with older stellar populations, while higher-stretch events prefer high star formation galaxies with younger populations (see also Sullivan et al., 2010). We calculate, for the zero SFR, low sSFR, moderate sSFR and high sSFR hosts, mean sSFR values of -13.76 $M_{\odot}yr^{-1}$, -11.24 $M_{\odot}yr^{-1}$, -9.95 $M_{\odot}yr^{-1}$ and -8.94 $M_{\odot}yr^{-1}$ respectively. For the stretches, the values are 0.74±0.05, 0.88±0.03, 0.99±0.01 and 1.07±0.01 respectively.

As stated previously, Maguire et al. (2014) 91T-like sample consists of 8, well-measured events. From the remaining 18, we have reliable (which we define as at least 4 photometric points before and after peak) R_{P48}-band for 13 of them, which we add to our final sample. The 5 events that didn't make this quality cut are PTF10xwg, PTF11eie, PTF11ein, PTF11fxh and PTF12jb.

For the 91T-like events we calculate a mean stretch of 1.12±0.03 and a mean sSFR of -9.85 $M_{\odot}yr^{-1}$, with a standard deviation of 0.66 $M_{\odot}yr^{-1}$. The corresponding values in the moderate and high sSFR bins are 1.10±0.03 with -9.95(0.30) $M_{\odot}yr^{-1}$ and 1.16±0.06 with

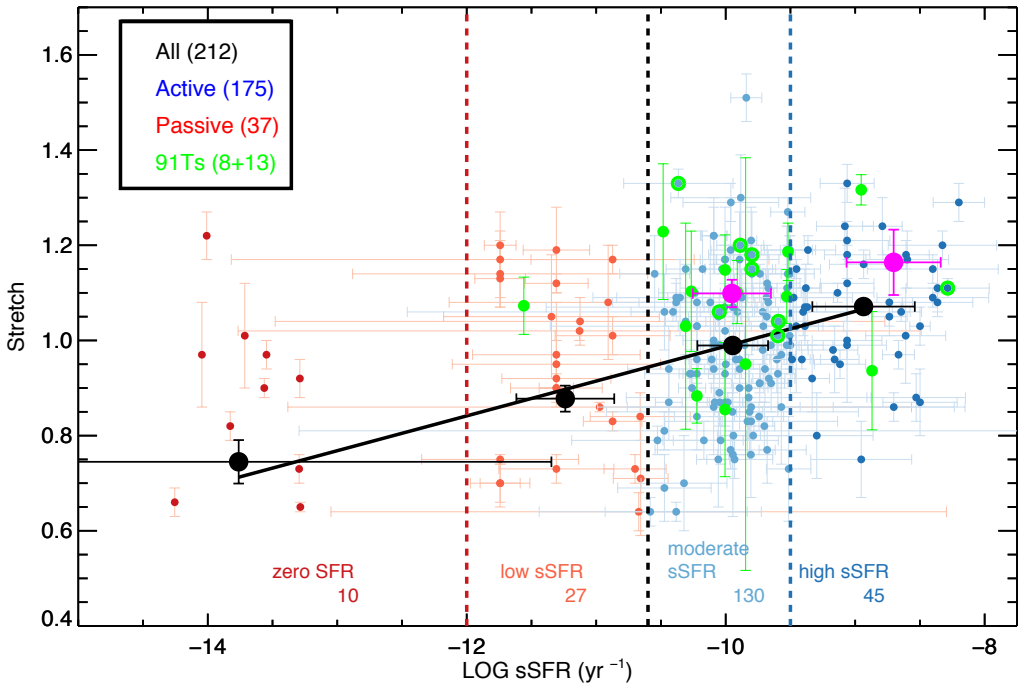

FIGURE 6.10: The SN Ia stretch, as a function of the host galaxy specific star formation rate, for the Maguire et al. (2014) sample we have host information. The host sample has been colour-coded as in Fig. 6.4, where the zero SFR hosts are shown randomly distributed around the mean of their sSFR, for illustration purposes. Full black circles are the averaged values in each sSFR bin, defined by our division scheme, shown in vertical dashed lines, while the black solid line is a linear fit to the averaged data. 91T-like hosts are marked with open (91T-likes in Maguire et al. 2014) and full (91T-likes *not* in Maguire et al. 2014) green circles, with their average value as full magenta circles.

-8.70(0.36) $M_{\odot}yr^{-1}$ respectively. While we recover the expected photometric behaviour of the 91T-like SNe (higher mean stretch than the complete sample), we see a preference of 91T-likes to occur in moderate sSF environments: the ratios between the number of 91T-likes to the total population, in each sSFR bin, are 0 (zero SFR), 0.03 (low sSFR), 0.13 (moderate sSFR) and 0.066 (high sSFR).

While the stretch of the SN is a well-established parameter that describes the variation of the light-curve behaviour (Phillips, 1993), it still is a *photometric* parameter: 91T-like SNe Ia are more luminous, and thus have broader light curves, but there are also high stretch SNe Ia that are not 91T-like. Since the 91T-like subclass has been defined according to the early to peak spectral behaviour, it is beneficial to investigate correlations of the host galaxy properties with a *spectroscopic* parameter, and more precisely, a spectral characteristic that distinguishes a normal SN Ia from a 91T-like one. The characteristic that fulfils this requirement is the behaviour of the Si II λ6355 absorption at peak (see also Chapter 5, Fig. 5.8). In the following, our 91T-like sample will consist *only* of the Maguire et al. (2014) 91T-likes, for which we have good spectroscopic coverage.

A caveat on this approach is that the spectral measurements for each SN are made at different phases. Benetti et al. (2005) have divided SNe Ia in two broad categories: high velocity gradient (HVG) SNe Ia, where the Si II velocity shows a rapid evolution, and low velocity gradient (LVG) SNe Ia, with moderate to no evolution. The later group consists of both normal and 91T-like events. This means that an estimate on the expansion velocity for a 91T-like event, being relatively constant, will depend weakly on the spectral phase, which is not the case for the normal SNe Ia. Thus, this effect will be, in principle, more pronounced in the normal SNe Ia, while for the 91T-like subclass, the effect will be smaller.

The results shown here are for the expansion velocities and pseudo equivalent widths (pEWs) of the spectrum closest to peak. As it can bee seen in Fig. 6.11, our 91T-like sample's 'closest-to-peak' spectra are at -2.86 days from peak, with a standard deviation of 3.85, while, for the global population, the phases are -1.81(4.1) and -2.27(3.98) for the SNe that exploded in active and passive galaxies, respectively.

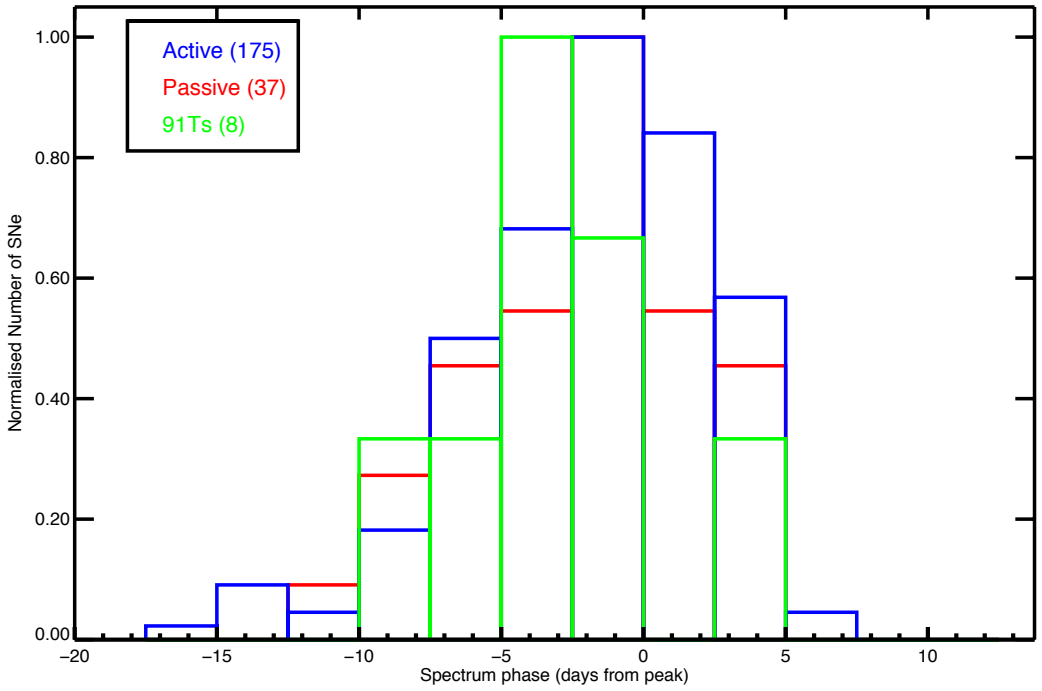

FIGURE 6.11: Distribution of the spectrum phase of the PTF SNe Ia used in this work.

We show the Si II λ6355 expansion velocity (in units of 10^3 km s^{-1}) and the Si II λ6355 pEW (in Å) as a function of the host galaxy sSFR in Fig. 6.12 and 6.13, respectively. For the mean values of the Si II λ6355 expansion velocity, divided as above, we recover 10,835±252, 11,688±134, 11,054±109 and 13,027±336 km/s respectively (the later value is relatively high due to some outliers with small error bars), with the linear fit giving a poor value for the reduced χ^2 (= 20.3). For the pEW, we estimate 92±9, 86±6, 75±3 and

71±5 Å, and the linear fitting having $\chi^2 = 0.25$, and consistent with a negative slope in 4.9-σ. The 91T-like estimates are 10,548±262 km/s and 43±7 Å. As expected, 91T-like hosts show a clear distinction compared with the total population.

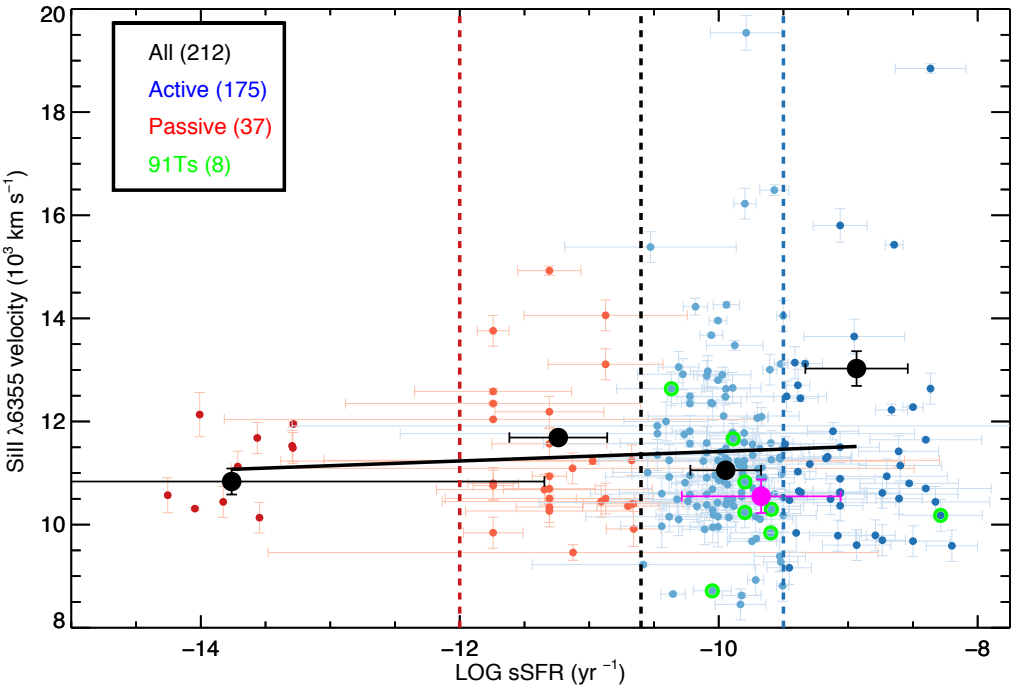

FIGURE 6.12: As in Fig. 6.10, but for the Si II λ6355 expansion velocity.

Finally, in Fig. 6.14, we show the distribution of the SN stretch versus the Si II λ6355 pEW. We divide our sample to low and high stretch SN ($s_{\rm low} < 1 \leq s_{\rm high}$), and weak- and strong-pEW SN, according to the mean pEW (pEW$_{\rm mean}$ = 76.8 Å), shown in black dashed lines. As expected, 91T-like events are exclusively at the high-stretch and weak-pEW end of the distribution, constituting ~ 12% of the total high-stretch–strong-pEW population. The percentage of the active hosts in each quadrant is 91.1% (high-stretch, strong-pEW), 80.4% (high-stretch, strong-pEW), 71.4% (low-stretch, strong-pEW) and 87.8% (low-stretch, low-pEW).

Our results are in accordance with works that find observational evidence of two different families of SNe Ia (Table 5 of Maguire et al., 2013): Our work suggests that 91T-like SNe form a distinct group, which is characterised by broader-brighter light curves, lower Si II λ6355 expansion velocities and pEWs that occur almost exclusively in active, late-type hosts with higher sSFR and younger stellar populations.

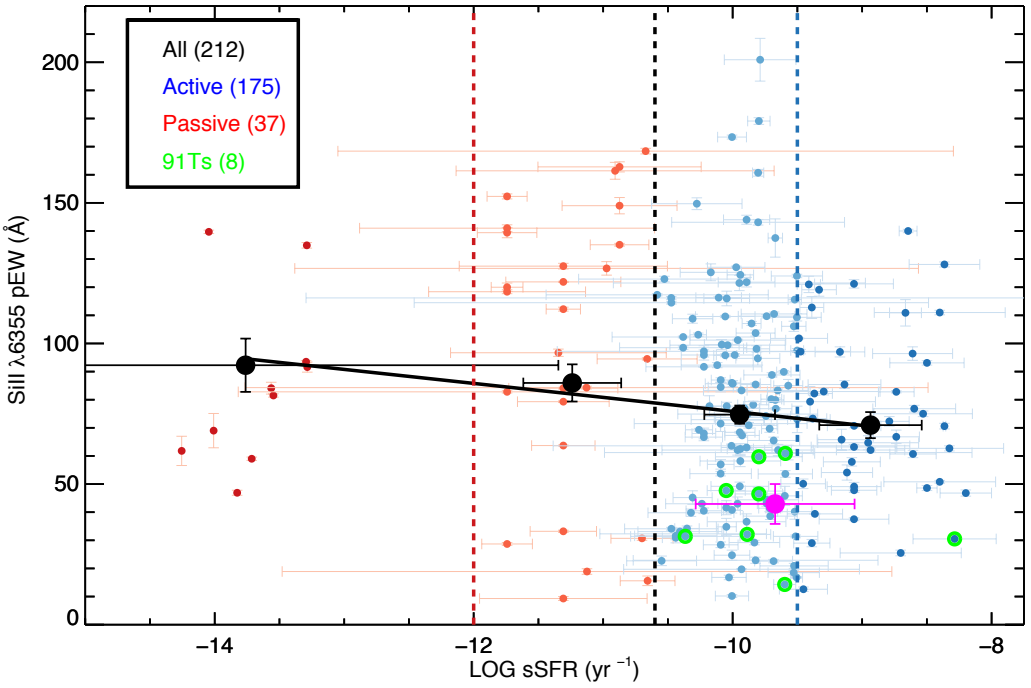

FIGURE 6.13: As in Fig. 6.10, but for the Si II λ6355 pseudo equivalent width.

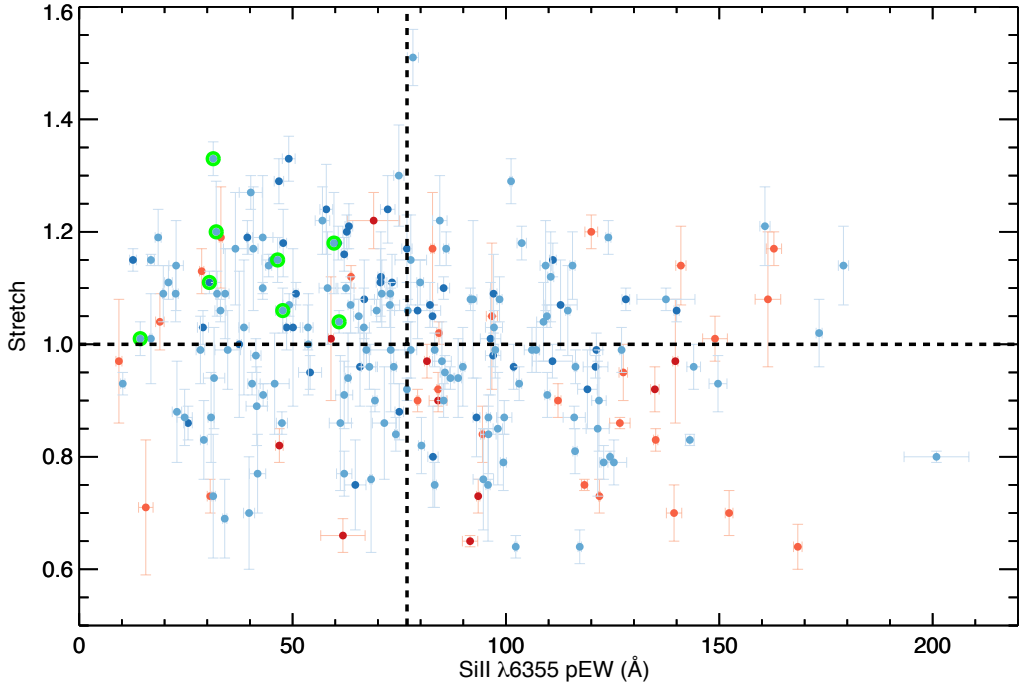

FIGURE 6.14: As in Fig. 6.10, but for the stretch vs the Si II λ6355 pEW. The black dashed lines correspond to $s = 1$ and pEW = 76.8 Å.

6.5 Summary

In this Chapter, we examined the global properties of the host galaxies of the PTF SNe Ia, focusing on the 91T-like spectroscopic subclass. We were able to identify host galaxies of 804 SNe Ia from the PTF parent sample that lies in the SDSS footprint and, by employing a method to fit the observed galaxy colours to spectral energy distributions of galaxy templates, recover properties such as the stellar mass and the star formation rate. We showed that, while our complete host galaxies sample is representative of the SN Ia population in terms of stellar mass and star formation, the hosts of 91T-like events show higher star formation and younger stellar progenitor populations. This result was also tested by exploring correlations between photometric and spectroscopic characteristics of 91T-likes, compared to normal SNe Ia, demonstrating the distinctive nature of their hosts. Our results are in accordance with suggestions in the literature that the 91T-like Type Ia Supernovae originate from the single degenerate scenario.

The class of 91T-like SNe Ia are, nowadays, routinely included on cosmological SNe Ia samples, although some studies have warned about the introduction of systematic biases. As it can be seen in Fig. 1.3, 91T-like SNe Ia are generally ~0.2 magnitudes brighter than the Phillips relation. Moreover, Reindl et al. (2005) find that the mean Hubble residual of the 91T-like family is -0.4 mag, while Folatelli et al. (2010), analysing the CSP sample of low-redshift SNe Ia, found that the four most-distant SNe have negative residuals (however, this can be an effect of small-number statistics) and (Scalzo et al., 2012), studying the properties of super-Chandra candidates in the Nearby Supernova Factory (Aldering et al., 2002) data set, found spectroscopic similarities between these SNe and 91T-like, having a mean Hubble residual of -0.56 mag. At the same time, many studies (e.g. Gallagher et al., 2008; Sullivan et al., 2010; Childress et al., 2013; Pan et al., 2014) find correlations between the properties of SNe Ia and the properties of their hosts; SNe Ia, after correcting for light curve width and colour, that occur in high-mass and low-sSFR galaxies are brighter, SNe Ia that decline faster happen in high-mass and low-sSFR galaxies and redder SNe Ia appear in massive, older, and higher metallicity hosts. While it is still not clear what drives these correlations, with possible explanations including dust, progenitor age and progenitor metallicity, a proper understanding of the physical origin of any SNe Ia subclass, such as the 91T-like, will be beneficial for future surveys, dedicated to measuring cosmological parameters.

While studying the global properties of the host galaxies of SNe has been proven to be beneficial, it would be more useful to be able to derive information on the local properties of the host. Moreover, an accurate estimation of the star formation requires high-quality spectroscopic data, at the location of the explosion.

Our 91T-like sample consists of 26 events, a relatively low number compared to the expected 91T-like population, for which volume-limited fractions show that they constitute ~10% of the total SNe Ia (Li et al., 2011a). The classification of them were performed in real-time by fitting the earlier spectra, mostly with SUPERFIT, and visually confirmed by PTF members using the PTF Marshal. This approach introduces a human bias; sometimes classifications may be ambiguous. Another potential issue is the galaxy light included in the SN spectrum: if this is strong then it tends to 'wash out' the Si II λ6355 absorption feature, making a definite classification ambiguous. As it can be seen in Fig. 6.14, there are SN with broad light curves and low Si II λ6355 pEW that are not included in our 91T-like sample, but potentially could be 91T-like. With this in mind, a proper classification scheme should include both spectroscopic *and* photometric information, particularly the absolute peak magnitude of the SN, estimated to be $0.2 - 0.3$ mag more luminous than the 'normal' SNe Ia (Blondin et al., 2012). This will allow us to increase the 91T-like sample and with a combination of dense photometric and spectroscopic datasets, spanning from the ultra-violet to the near-infrared, will provide a more robust statistical approach in studying this sub-class.

Chapter 7

Conclusion

In this thesis, we performed extensive observational studies of single or samples of Type Ia Supernovae (SNe Ia), with data originating from modern surveys with excellent capabilities for discovering, classifying and following-up local SNe: the Palomar Transient Factory (PTF), the Public ESO Spectroscopic Survey for Transient Objects (PESSTO) and the Las Cumbres Observatory SN Key Project (LCO SN Key Project). Our goal was to investigate potential observational signatures, explore the physical processes that describe the underlying physical mechanism leading to the explosion and the configuration of the progenitor system. Below we summarise our main results:

7.1 The late-time light curves of SNe Ia

In Chapter 3, we performed an extensive study of the late time evolution of SN 2011fe, one of the closest and best-studied SNe Ia of our times. Our PTF photometric coverage spans from 200–650 days after maximum, with remarkable temporal density, and by adding literature data from external sources, we achieved an unprecedented photometric coverage for a SN Ia, up to 1600 days after explosion. A combination of photometry with spectroscopy allowed us to construct a pseudo-bolometric light curve and investigate the physical processes that govern the evolution of SN 2011fe at the very late times. In Chapter 4, using the leverage of our understanding of the evolution of SN 2011fe at late times, we performed a sample study of the late-time light curve evolution of SNe Ia. We compared 49 SNe Ia, discovered and photometrically followed by PTF, with SN 2011fe and PTF11kx, a PTF SNe Ia of the Ia-CSM subclass, that represent the two extremes in the brightness phase space at late times (200-600 days after maximum), and provided upper limits on the hydrogen material deposited at the site of the explosion by a possible non-degenerate companion. We find:

- The bolometric light curve of SN 2011fe can be broadly explained by the radioactive inputs from the ^{56}Ni and ^{57}Ni decay chains.
- The PTF *R*-band light curve has a noticeable rapid decline followed by a plateau over 500-600 days. While the rapid decline can be explained by cooling ejecta and the emergence of [Fe II] lines producing increased near-IR flux, our models are unable to adequately explain the plateau feature in the light curve.
- The pseudo-bolometric light curve is not consistent with models that have full trapping of the produced charged leptons and no infrared catastrophe. An additional route for energy escape outside of the optical/near-IR is required.
- The bolometric light curve is consistent with models that allow for positron/electron escape. In this case, the best-fitting initial ^{56}Ni mass is $M(56) = 0.461 \pm 0.041\,M_{\odot}$, consistent with independent estimates from nebular spectroscopy analysis and Arnett's Law. However this model requires 75 per cent of the charged leptons to escape by 500 d.
- The data are also fully consistent with a model that has complete positron/electron trapping but does allow for a redistribution of flux to the mid-far IR, similar to an infrared catastrophe. In this case, around 85 per cent of the total bolometric luminosity must be escaping at non-optical wavelengths by day 600 and onwards.
- For both of these scenarios, the amount of ^{57}Ni we estimate is relatively large, compared to popular explosion models. This large inferred mass indicates high central density explosion environments, mainly predicted from SD progenitor channels and WD collisions.
- Including contributions from the ^{55}Co decay chain does not improve the quality of the bolometric light curve fits, although this is not well constrained by the dataset. We estimate an upper limit of ^{55}Co mass of $1.6 \times 10^{-2}\,\mathrm{M}_{\odot}$.
- In a sample of 49 SNe Ia with adequate late-time photometric coverage, we find no significant flux excess at late-time, compared to SN 2011fe.
- An outlier in our sample is PTF11kx, a SN Ia-CSM, that remains ~4-7 mag brighter than SN 2011fe at 200-600 days after maximum. This excessive brightness is attributed to the interaction of the SN ejecta with circumstellar material (CSM) expelled from the progenitor system at the pre-supernova stage
- Since our photometric coverage is in the PTF R_{P48} band, which at late-times will cover any hydrogen emission from a narrow Hα component, we were able to place an upper limit on the hydrogen rich material at the vicinity of the SN of $\leq$0.87 $\mathrm{M}_{\odot}$.

7.2 The overluminous SNe Ia subclass

In Chapter 5, we examined the physical properties of two overluminous SNe Ia, colloquially known as 91T-likes, discovered, classified and followed up by PESSTO and LCO, SN 2014eg and SN 2016hvl. We presented the dense photometric and spectroscopic dataset of these two objects and performed extensive analysis of the physical properties characteristic of their class. We find:

- SN 2014eg is a highly reddened overluminous SNe Ia, spectroscopically similar to SN 1999aa, a slightly less luminous 91T-like. We calculated a ^{56}Ni mass synthesised in the explosion of M_{56} = 0.59 $M_{\odot}$ and an ejecta mass of $M_{\rm ejecta}$ = 1.32 $M_{\odot}$.
- High resolution spectra of SN 2014eg reveal three components along the line of sight, with one strong blueshifted component at ~85 km s $^{-1}$. We constructed a reddening law and we provided hints of non-MW dust, close to the vicinity of the SN, a feature common to other similar, high-reddened events.
- SN 2016hvl is an overluminous SNe Ia, spectroscopically similar to SN 1991T. We calculated a ^{56}Ni mass synthesised in the explosion of M_{56} = 0.79 $M_{\odot}$ and an ejecta mass of $M_{\rm ejecta}$ = 1.36 $M_{\odot}$.

In Chapter 6, we performed a targeted study on the 91T-like subclass in the context of their host galaxies. We were able to identify the host galaxies of 804 PTF SNe Ia and estimated their star formation rate (SFR) and their mass by fitting their spectral energy distribution (SED) with galaxy templates, describing their global properties. We find:

- Our complete host galaxy sample is representative of the SN Ia population, in terms of stellar mass and star formation. From the total of 804 hosts, we find 641 with moderate to high SFR and 163 with low to zero SFR, with a ratio of ~4, in accordance with previous host galaxy studies.
- Our 91T-like sample, consisting of 26 events, preferentially explode in moderate to high star formation environments. We find 25 events occurring in active galaxies, 4 of them in high and 17 in moderate SFR hosts. One event occurred in low SFR galaxy, while no event has been found in a passive host. Statistical tests show that this result is significant, revealing the distinct nature of 91T-like SNe, in terms of their environments.
- We recover the general trend in the host galaxy stellar mass of the SN hosts: passive galaxies are on average more massive than the active ones. However, the

stellar mass of the 91T-like hosts in our sample is not preferentially at the low side of the distribution: 91T-like explode in a variety of hosts, in terms of their stellar mass.

- We explored correlations between the SN properties and their environments, confirming the general trend seen in previous studies: brighter and slower declining events preferentially occur in high to moderate star forming galaxies, with younger stellar progenitors. 91T-like events follow the same trend, with broader light curves and weaker Si II absorption features than the parent sample.

7.3 Future perspectives

Despite major effort, both theoretically and observationally, the SN Ia progenitor problem is far from being resolved. While there is a varying degree of evidence supporting both of the classical single degenerate (SD) and double degenerate (DD) scenarios, or contemporary variations of them, a definite answer to whether one, two or more mechanisms, with different contributions to the complete population, has not been provided. While the observational evidence seem to favour a DD origin, it is possible that no single model can describe all SNe Ia, opening the door to scenarios with low expected event rates.

On the theoretical side, substantial work needs to be done, mainly on the pre-supernova evolution of the binary: in a SD model, how accretion onto the WD proceeds and the influence of physical parameters such as mass transfer rate, composition and rotation; for the DD model, how ignition initiates and how subtle effects such as residual hydrogen or helium on the surface of the WD affect the explosion. Moreover, while hydro-simulations, radiative transfer algorithms and nucleosynthesis codes are currently successful in reproducing the early time observables, progress on the late time ones is still lacking. Finally, progress in theoretical delay time distributions (DTDs) will provide extra information on progenitor populations and ages, with more sophisticated treatment in binary population synthesis (BPS) codes. The tremendous increase on the computing power and the application of modern programming techniques guarantees future successes.

Turning to observations, our progress in only limited by the quality and quantity of data we can obtain. Time-domain astronomy is still a leading research field, with many surveys currently operating or planned for the future. For SNe Ia, we are now in the 'database' era, able to compile large subsamples of events and discover exotic transients that push our knowledge to the limits, without need for serendipitous discoveries of

only nearby events. Leading experiments currently happening include the All-Sky Automated Survey for Supernovae (ASASSN; Shappee et al., 2014), the Panoramic Survey Telescope and Rapid Response System (PanSTARRS; Chambers et al., 2016), the Asteroid Terrestrial-impact Last Alert System SN survey (ATLAS; Tonry, 2011) and the Dark Energy Survey (DES; Flaugher et al., 2015). Moreover, upcoming surveys such as the Zwicky Transient Facility (ZTF; Smith et al., 2014b), the VISTA Extragalactic Infrared Legacy Survey (VEILS; Hönig et al., 2017) and the Large Synoptic Survey Telescope (LSST; Ivezic et al., 2009) will generate large volumes of data and possibly unveil new classes of transients, within the thermonuclear paradigm. Future space telescopes will perform SN studies, such as the Wide Field Infrared Survey Telescope (WFIRST; Foley et al., 2017), the Euclid space mission (Astier et al., 2014) and the James Webb Space Telescope (JWST; Whalen et al., 2013), with the additional benefit on observing in the infra-red; not only observations will be unaffected by the dust along the line of sight, but also accurate bolometric light curves for SN will be determined, even at late times. Rapid spectroscopic follow-up with ground based facilities, focusing not only on the event itself (e.g. searching for hydrogen) but also its host galaxy features and their possible temporal evolution would be of substantial interest relating to the work presented here. Finally, the host galaxy properties of SNe Ia can arguably reveal important information on the nature of the progenitor system. SN Ia rates as a function of the stellar mass and the SFR, focusing also in SNe Ia subclasses, and their preference on occurring in specific galactic environments could be beneficial not only for the progenitor system, but also for cosmological corrections. The work presented here is a first step, and I will continue to pursue this research topic in the next years.

Appendix A

SN 2011fe: Photometric, spectroscopic and bolometric logs

TABLE A.1: PTF Photometry for SN 2011fe

MJD	Phase(days)[a]	Telescope	Filter	Mag(AB)	ΔMag(AB)
56016.201	201.65	P48	PTF48R	16.045	0.016
56016.263	201.72	P48	PTF48R	16.058	0.008
56017.170	202.62	P48	PTF48R	16.085	0.009
56017.214	202.67	P48	PTF48R	16.077	0.009
56017.245	202.70	P48	PTF48R	16.073	0.008
56017.463	202.91	P48	PTF48R	16.050	0.008
56017.507	202.96	P48	PTF48R	16.064	0.008
56019.322	204.77	P48	PTF48R	16.082	0.010
56019.415	204.87	P48	PTF48R	16.100	0.011
56019.450	204.90	P48	PTF48R	16.123	0.014
56020.376	205.82	P48	PTF48R	16.117	0.010
56020.405	205.85	P48	PTF48R	16.112	0.009
56020.435	205.88	P48	PTF48R	16.102	0.009
56021.250	206.70	P48	PTF48R	16.129	0.013
56021.313	206.76	P48	PTF48R	16.103	0.016
56021.348	206.80	P48	PTF48R	16.074	0.018
56021.385	206.83	P48	PTF48R	16.159	0.011
56021.415	206.86	P48	PTF48R	16.128	0.012
56022.321	207.77	P48	PTF48R	16.140	0.011
56022.356	207.80	P48	PTF48R	16.088	0.033
56022.387	207.83	P48	PTF48R	16.181	0.030
56023.336	208.78	P48	PTF48R	16.146	0.015
56023.370	208.82	P48	PTF48R	16.153	0.015
56023.489	208.94	P48	PTF48R	16.176	0.017
56024.164	209.61	P48	PTF48R	16.144	0.020
56024.199	209.64	P48	PTF48R	16.156	0.016

56024.426	209.87	P48	PTF48R	16.192	0.018
56024.466	209.91	P48	PTF48R	16.179	0.020
56025.139	210.58	P48	PTF48R	16.177	0.010
56025.177	210.62	P48	PTF48R	16.183	0.012
56025.255	210.70	P48	PTF48R	16.197	0.012
56026.158	211.60	P48	PTF48R	16.217	0.009
56026.160	211.60	P48	PTF48R	16.201	0.009
56026.196	211.64	P48	PTF48R	16.219	0.009
56026.234	211.68	P48	PTF48R	16.228	0.010
56026.256	211.70	P48	PTF48R	16.201	0.010
56026.306	211.75	P48	PTF48R	16.222	0.010
56027.247	212.69	P48	PTF48R	16.249	0.009
56027.282	212.73	P48	PTF48R	16.244	0.010
56027.311	212.75	P48	PTF48R	16.237	0.009
56033.146	218.59	P48	PTF48R	16.312	0.012
56033.285	218.72	P48	PTF48R	16.342	0.010
56033.432	218.87	P48	PTF48R	16.347	0.010
56034.368	219.81	P48	PTF48R	16.362	0.011
56034.397	219.83	P48	PTF48R	16.337	0.010
56034.432	219.87	P48	PTF48R	16.350	0.009
56035.399	220.84	P48	PTF48R	16.359	0.011
56035.429	220.87	P48	PTF48R	16.381	0.009
56035.460	220.90	P48	PTF48R	16.361	0.010
56035.495	220.93	P48	PTF48R	16.362	0.013
56036.384	221.82	P48	PTF48R	16.387	0.010
56036.413	221.85	P48	PTF48R	16.414	0.011
56036.443	221.88	P48	PTF48R	16.396	0.010
56037.387	222.82	P48	PTF48R	16.407	0.010
56037.416	222.85	P48	PTF48R	16.401	0.010
56037.454	222.89	P48	PTF48R	16.401	0.010
56037.494	222.93	P48	PTF48R	16.415	0.010
56038.168	223.60	P48	PTF48R	16.417	0.011
56038.221	223.66	P48	PTF48R	16.419	0.010
56038.391	223.83	P48	PTF48R	16.430	0.010
56038.466	223.90	P48	PTF48R	16.446	0.010
56039.381	224.81	P48	PTF48R	16.430	0.010
56039.411	224.84	P48	PTF48R	16.439	0.010
56039.443	224.88	P48	PTF48R	16.453	0.011
56040.349	225.78	P48	PTF48R	16.453	0.010
56040.378	225.81	P48	PTF48R	16.485	0.010
56040.457	225.89	P48	PTF48R	16.465	0.010
56040.488	225.92	P48	PTF48R	16.437	0.011
56041.383	226.82	P48	PTF48R	16.480	0.011
56041.413	226.84	P48	PTF48R	16.482	0.011
56041.443	226.88	P48	PTF48R	16.479	0.011
56045.238	230.67	P48	PTF48R	16.560	0.012
56045.326	230.76	P48	PTF48R	16.530	0.011
56045.358	230.79	P48	PTF48R	16.514	0.012

56046.262	231.69	P48	PTF48R	16.534	0.011
56046.299	231.73	P48	PTF48R	16.557	0.011
56046.328	231.76	P48	PTF48R	16.550	0.011
56046.477	231.90	P48	PTF48R	16.545	0.012
56047.178	232.61	P48	PTF48R	16.570	0.013
56047.298	232.73	P48	PTF48R	16.558	0.012
56047.306	232.73	P48	PTF48R	16.584	0.012
56047.336	232.76	P48	PTF48R	16.567	0.012
56047.355	232.78	P48	PTF48R	16.594	0.012
56047.401	232.83	P48	PTF48R	16.554	0.011
56048.306	233.73	P48	PTF48R	16.588	0.014
56048.371	233.80	P48	PTF48R	16.603	0.015
56048.401	233.83	P48	PTF48R	16.569	0.018
56049.362	234.79	P48	PTF48R	16.594	0.015
56049.391	234.82	P48	PTF48R	16.601	0.013
56049.422	234.85	P48	PTF48R	16.606	0.028
56049.474	234.90	P48	PTF48R	16.604	0.013
56050.396	235.82	P48	PTF48R	16.631	0.021
56050.499	235.92	P48	PTF48R	16.633	0.016
56058.165	243.58	P48	PTF48R	16.727	0.012
56058.194	243.61	P48	PTF48R	16.743	0.011
56058.225	243.64	P48	PTF48R	16.725	0.012
56059.162	244.58	P48	PTF48R	16.755	0.012
56059.265	244.68	P48	PTF48R	16.751	0.013
56059.296	244.71	P48	PTF48R	16.766	0.012
56059.444	244.86	P48	PTF48R	16.773	0.013
56059.481	244.90	P48	PTF48R	16.749	0.013
56060.270	245.69	P48	PTF48R	16.784	0.011
56060.301	245.72	P48	PTF48R	16.774	0.013
56060.365	245.78	P48	PTF48R	16.786	0.012
56060.465	245.88	P48	PTF48R	16.785	0.013
56061.279	246.69	P48	PTF48R	16.801	0.011
56061.309	246.72	P48	PTF48R	16.802	0.011
56061.377	246.79	P48	PTF48R	16.817	0.012
56061.461	246.88	P48	PTF48R	16.776	0.013
56062.284	247.70	P48	PTF48R	16.845	0.012
56062.314	247.73	P48	PTF48R	16.812	0.012
56062.343	247.76	P48	PTF48R	16.804	0.012
56063.264	248.68	P48	PTF48R	16.833	0.012
56063.294	248.71	P48	PTF48R	16.851	0.012
56063.358	248.77	P48	PTF48R	16.849	0.013
56064.274	249.69	P48	PTF48R	16.837	0.012
56065.186	250.60	P48	PTF48R	16.857	0.014
56065.237	250.65	P48	PTF48R	16.833	0.014
56065.289	250.70	P48	PTF48R	16.844	0.013
56066.273	251.68	P48	PTF48R	16.881	0.012
56066.304	251.72	P48	PTF48R	16.887	0.013
56067.276	252.69	P48	PTF48R	16.881	0.012

56067.318	252.73	P48	PTF48R	16.875	0.012
56067.380	252.79	P48	PTF48R	16.876	0.012
56068.318	253.73	P48	PTF48R	16.905	0.012
56068.348	253.76	P48	PTF48R	16.878	0.013
56068.377	253.79	P48	PTF48R	16.913	0.013
56068.433	253.84	P48	PTF48R	16.907	0.014
56068.471	253.88	P48	PTF48R	16.906	0.014
56069.283	254.69	P48	PTF48R	16.908	0.012
56069.312	254.72	P48	PTF48R	16.924	0.013
56069.409	254.82	P48	PTF48R	16.933	0.013
56070.326	255.73	P48	PTF48R	16.951	0.014
56070.381	255.79	P48	PTF48R	16.942	0.016
56070.418	255.83	P48	PTF48R	16.927	0.014
56071.326	256.73	P48	PTF48R	16.965	0.016
56071.372	256.78	P48	PTF48R	16.962	0.014
56071.402	256.81	P48	PTF48R	16.958	0.015
56071.432	256.84	P48	PTF48R	16.987	0.016
56071.463	256.87	P48	PTF48R	16.932	0.017
56075.195	260.60	P48	PTF48R	17.011	0.015
56075.226	260.63	P48	PTF48R	16.997	0.015
56075.274	260.68	P48	PTF48R	17.019	0.014
56076.176	261.58	P48	PTF48R	17.046	0.015
56076.216	261.62	P48	PTF48R	17.066	0.017
56076.272	261.68	P48	PTF48R	17.048	0.014
56077.183	262.59	P48	PTF48R	17.031	0.016
56077.246	262.65	P48	PTF48R	17.054	0.016
56078.168	263.57	P48	PTF48R	17.079	0.019
56078.206	263.61	P48	PTF48R	17.082	0.019
56078.236	263.64	P48	PTF48R	17.019	0.018
56079.171	264.57	P48	PTF48R	17.077	0.020
56079.199	264.60	P48	PTF48R	17.089	0.018
56079.229	264.63	P48	PTF48R	17.097	0.019
56081.172	266.57	P48	PTF48R	17.106	0.020
56081.203	266.60	P48	PTF48R	17.090	0.021
56081.232	266.63	P48	PTF48R	17.067	0.021
56082.203	267.60	P48	PTF48R	17.120	0.025
56082.233	267.63	P48	PTF48R	17.081	0.024
56083.254	268.65	P48	PTF48R	17.147	0.023
56083.291	268.69	P48	PTF48R	17.108	0.024
56083.321	268.72	P48	PTF48R	17.106	0.027
56084.224	269.62	P48	PTF48R	17.132	0.019
56084.438	269.84	P48	PTF48R	17.120	0.024
56084.467	269.86	P48	PTF48R	17.165	0.029
56085.396	270.79	P48	PTF48R	17.160	0.027
56085.426	270.82	P48	PTF48R	17.187	0.032
56085.455	270.85	P48	PTF48R	17.189	0.032
56086.390	271.79	P48	PTF48R	17.180	0.020
56086.419	271.82	P48	PTF48R	17.182	0.018

56086.449	271.84	P48	PTF48R	17.148	0.024
56087.352	272.75	P48	PTF48R	17.222	0.017
56087.382	272.78	P48	PTF48R	17.211	0.020
56087.412	272.81	P48	PTF48R	17.233	0.019
56088.319	273.71	P48	PTF48R	17.223	0.017
56088.348	273.74	P48	PTF48R	17.209	0.016
56088.377	273.77	P48	PTF48R	17.197	0.017
56089.279	274.67	P48	PTF48R	17.184	0.016
56089.308	274.70	P48	PTF48R	17.230	0.017
56089.338	274.73	P48	PTF48R	17.250	0.017
56090.241	275.63	P48	PTF48R	17.272	0.016
56090.272	275.66	P48	PTF48R	17.263	0.015
56090.311	275.70	P48	PTF48R	17.264	0.016
56091.272	276.66	P48	PTF48R	17.278	0.017
56091.309	276.70	P48	PTF48R	17.269	0.017
56091.340	276.73	P48	PTF48R	17.283	0.017
56092.281	277.67	P48	PTF48R	17.281	0.018
56092.311	277.70	P48	PTF48R	17.271	0.016
56092.341	277.73	P48	PTF48R	17.309	0.018
56093.273	278.66	P48	PTF48R	17.313	0.016
56093.304	278.69	P48	PTF48R	17.320	0.016
56093.335	278.73	P48	PTF48R	17.300	0.016
56094.238	279.63	P48	PTF48R	17.309	0.019
56094.268	279.66	P48	PTF48R	17.299	0.019
56094.302	279.69	P48	PTF48R	17.336	0.017
56095.245	280.63	P48	PTF48R	17.314	0.017
56095.276	280.66	P48	PTF48R	17.361	0.018
56095.305	280.69	P48	PTF48R	17.330	0.019
56096.218	281.61	P48	PTF48R	17.358	0.017
56096.249	281.64	P48	PTF48R	17.364	0.017
56096.279	281.67	P48	PTF48R	17.341	0.019
56097.188	282.58	P48	PTF48R	17.333	0.017
56097.228	282.62	P48	PTF48R	17.372	0.019
56097.258	282.65	P48	PTF48R	17.352	0.017
56098.178	283.56	P48	PTF48R	17.360	0.020
56098.207	283.59	P48	PTF48R	17.351	0.017
56098.236	283.62	P48	PTF48R	17.375	0.018
56099.187	284.57	P48	PTF48R	17.378	0.016
56099.218	284.60	P48	PTF48R	17.336	0.018
56099.247	284.63	P48	PTF48R	17.428	0.018
56100.176	285.56	P48	PTF48R	17.436	0.019
56100.205	285.59	P48	PTF48R	17.416	0.017
56100.234	285.62	P48	PTF48R	17.451	0.018
56101.189	286.57	P48	PTF48R	17.419	0.018
56101.222	286.61	P48	PTF48R	17.418	0.018
56101.252	286.64	P48	PTF48R	17.418	0.018
56102.178	287.56	P48	PTF48R	17.416	0.022
56102.207	287.59	P48	PTF48R	17.439	0.024

56102.237	287.62	P48	PTF48R	17.431	0.022
56103.177	288.56	P48	PTF48R	17.467	0.018
56103.206	288.59	P48	PTF48R	17.455	0.023
56103.236	288.62	P48	PTF48R	17.453	0.018
56104.216	289.60	P48	PTF48R	17.440	0.019
56104.245	289.63	P48	PTF48R	17.458	0.020
56105.203	290.58	P48	PTF48R	17.491	0.020
56105.233	290.61	P48	PTF48R	17.479	0.022
56105.262	290.64	P48	PTF48R	17.442	0.021
56106.179	291.56	P48	PTF48R	17.509	0.019
56106.215	291.59	P48	PTF48R	17.490	0.019
56106.245	291.62	P48	PTF48R	17.506	0.019
56107.232	292.61	P48	PTF48R	17.506	0.028
56107.261	292.64	P48	PTF48R	17.502	0.021
56108.179	293.56	P48	PTF48R	17.513	0.022
56108.209	293.59	P48	PTF48R	17.568	0.023
56108.239	293.62	P48	PTF48R	17.512	0.020
56109.179	294.56	P48	PTF48R	17.540	0.023
56109.209	294.59	P48	PTF48R	17.519	0.024
56109.239	294.62	P48	PTF48R	17.552	0.024
56110.182	295.56	P48	PTF48R	17.514	0.024
56110.211	295.59	P48	PTF48R	17.510	0.024
56110.260	295.64	P48	PTF48R	17.491	0.025
56111.181	296.56	P48	PTF48R	17.617	0.037
56111.210	296.59	P48	PTF48R	17.509	0.030
56111.240	296.62	P48	PTF48R	17.553	0.028
56112.181	297.56	P48	PTF48R	17.562	0.028
56112.230	297.60	P48	PTF48R	17.578	0.035
56112.260	297.64	P48	PTF48R	17.607	0.035
56113.181	298.56	P48	PTF48R	17.591	0.024
56113.241	298.61	P48	PTF48R	17.596	0.026
56114.209	299.58	P48	PTF48R	17.598	0.022
56114.239	299.61	P48	PTF48R	17.593	0.023
56115.180	300.55	P48	PTF48R	17.639	0.020
56115.210	300.58	P48	PTF48R	17.613	0.020
56115.239	300.61	P48	PTF48R	17.639	0.024
56116.185	301.56	P48	PTF48R	17.650	0.021
56116.216	301.59	P48	PTF48R	17.644	0.021
56116.246	301.62	P48	PTF48R	17.616	0.023
56117.178	302.55	P48	PTF48R	17.664	0.021
56117.211	302.58	P48	PTF48R	17.707	0.022
56117.216	302.59	P48	PTF48R	17.645	0.022
56117.247	302.62	P48	PTF48R	17.670	0.022
56118.181	303.55	P48	PTF48R	17.698	0.022
56118.211	303.58	P48	PTF48R	17.662	0.021
56118.241	303.61	P48	PTF48R	17.678	0.029
56119.178	304.55	P48	PTF48R	17.778	0.077
56119.208	304.58	P48	PTF48R	17.700	0.023

56119.238	304.61	P48	PTF48R	17.729	0.024
56120.255	305.62	P48	PTF48R	17.670	0.036
56120.284	305.65	P48	PTF48R	17.782	0.074
56122.304	307.67	P48	PTF48R	17.783	0.030
56122.334	307.70	P48	PTF48R	17.722	0.077
56122.367	307.73	P48	PTF48R	17.755	0.037
56123.278	308.64	P48	PTF48R	17.791	0.024
56123.308	308.67	P48	PTF48R	17.788	0.024
56123.339	308.71	P48	PTF48R	17.815	0.027
56124.269	309.63	P48	PTF48R	17.769	0.022
56124.300	309.67	P48	PTF48R	17.734	0.026
56124.331	309.70	P48	PTF48R	17.762	0.028
56125.273	310.64	P48	PTF48R	17.759	0.023
56125.316	310.68	P48	PTF48R	17.779	0.025
56125.346	310.71	P48	PTF48R	17.773	0.029
56126.186	311.55	P48	PTF48R	17.831	0.024
56126.216	311.58	P48	PTF48R	17.798	0.024
56126.247	311.61	P48	PTF48R	17.805	0.024
56127.255	312.62	P48	PTF48R	17.718	0.070
56128.189	313.55	P48	PTF48R	17.766	0.033
56128.249	313.61	P48	PTF48R	17.807	0.028
56129.179	314.54	P48	PTF48R	17.916	0.029
56129.209	314.57	P48	PTF48R	17.814	0.027
56129.239	314.60	P48	PTF48R	17.853	0.028
56130.179	315.54	P48	PTF48R	17.844	0.025
56130.209	315.57	P48	PTF48R	17.882	0.025
56130.241	315.60	P48	PTF48R	17.853	0.026
56131.177	316.54	P48	PTF48R	17.865	0.026
56131.208	316.57	P48	PTF48R	17.895	0.030
56131.241	316.60	P48	PTF48R	17.888	0.027
56132.174	317.53	P48	PTF48R	17.890	0.025
56132.205	317.56	P48	PTF48R	17.849	0.026
56132.235	317.59	P48	PTF48R	17.845	0.024
56133.175	318.53	P48	PTF48R	17.872	0.024
56133.209	318.57	P48	PTF48R	17.951	0.027
56133.239	318.60	P48	PTF48R	17.902	0.026
56135.174	320.53	P48	PTF48R	17.960	0.024
56135.205	320.56	P48	PTF48R	17.910	0.023
56135.234	320.59	P48	PTF48R	17.897	0.023
56136.175	321.53	P48	PTF48R	17.951	0.027
56136.205	321.56	P48	PTF48R	17.949	0.023
56136.236	321.59	P48	PTF48R	17.944	0.029
56137.191	322.55	P48	PTF48R	17.906	0.027
56137.223	322.58	P48	PTF48R	17.969	0.027
56137.254	322.61	P48	PTF48R	17.943	0.029
56138.173	323.53	P48	PTF48R	17.889	0.035
56138.202	323.56	P48	PTF48R	17.937	0.034
56138.233	323.59	P48	PTF48R	18.046	0.058

56143.165	328.52	P48	PTF48R	18.014	0.029
56143.195	328.55	P48	PTF48R	18.015	0.030
56143.235	328.59	P48	PTF48R	18.084	0.037
56144.167	329.52	P48	PTF48R	18.081	0.025
56144.198	329.55	P48	PTF48R	18.041	0.027
56144.228	329.58	P48	PTF48R	18.071	0.030
56145.168	330.52	P48	PTF48R	18.101	0.025
56145.231	330.58	P48	PTF48R	18.119	0.037
56145.263	330.61	P48	PTF48R	18.085	0.040
56146.168	331.52	P48	PTF48R	18.111	0.025
56146.228	331.58	P48	PTF48R	18.153	0.029
56146.258	331.61	P48	PTF48R	18.079	0.035
56147.170	332.52	P48	PTF48R	18.109	0.029
56147.206	332.55	P48	PTF48R	18.130	0.029
56147.246	332.59	P48	PTF48R	18.204	0.030
56148.170	333.52	P48	PTF48R	18.134	0.028
56148.219	333.57	P48	PTF48R	18.137	0.028
56148.250	333.60	P48	PTF48R	18.142	0.029
56165.165	350.50	P48	PTF48R	18.325	0.036
56165.199	350.53	P48	PTF48R	18.378	0.046
56165.229	350.56	P48	PTF48R	18.344	0.041
56166.150	351.48	P48	PTF48R	18.406	0.037
56166.197	351.53	P48	PTF48R	18.358	0.038
56166.227	351.56	P48	PTF48R	18.346	0.044
56167.144	352.48	P48	PTF48R	18.377	0.046
56167.191	352.52	P48	PTF48R	18.368	0.059
56167.220	352.55	P48	PTF48R	18.408	0.056
56168.146	353.48	P48	PTF48R	18.318	0.048
56168.230	353.56	P48	PTF48R	18.390	0.064
56169.145	354.47	P48	PTF48R	18.416	0.061
56169.198	354.53	P48	PTF48R	18.403	0.062
56169.229	354.56	P48	PTF48R	18.305	0.073
56170.146	355.47	P48	PTF48R	18.401	0.056
56170.199	355.53	P48	PTF48R	18.353	0.060
56170.229	355.56	P48	PTF48R	18.499	0.078
56177.138	362.46	P48	PTF48R	18.591	0.038
56177.208	362.53	P48	PTF48R	18.520	0.042
56178.137	363.46	P48	PTF48R	18.628	0.040
56178.170	363.49	P48	PTF48R	18.630	0.042
56229.548	414.83	P48	PTF48R	19.467	0.249
56233.547	418.82	P48	PTF48R	18.960	0.131
56234.535	419.81	P48	PTF48R	19.461	0.152
56236.531	421.81	P48	PTF48R	19.407	0.137
56237.550	422.82	P48	PTF48R	19.514	0.211
56238.536	423.81	P48	PTF48R	19.623	0.129
56251.498	436.76	P48	PTF48R	19.915	0.151
56251.531	436.79	P48	PTF48R	19.690	0.107
56252.487	437.75	P48	PTF48R	> 19.996	...

56252.517	437.78	P48	PTF48R	19.700	0.111
56253.485	438.75	P48	PTF48R	19.697	0.109
56253.515	438.78	P48	PTF48R	19.805	0.117
56254.480	439.74	P48	PTF48R	19.699	0.138
56254.510	439.77	P48	PTF48R	19.574	0.109
56255.477	440.74	P48	PTF48R	19.935	0.141
56255.508	440.77	P48	PTF48R	19.853	0.118
56256.474	441.73	P48	PTF48R	19.395	0.147
56256.513	441.77	P48	PTF48R	19.763	0.107
56258.477	443.73	P48	PTF48R	19.744	0.283
56258.506	443.76	P48	PTF48R	> 18.934	...
56259.467	444.72	P48	PTF48R	> 19.709	...
56259.496	444.75	P48	PTF48R	> 19.594	...
56265.476	450.73	P48	PTF48R	> 18.847	...
56265.505	450.76	P48	PTF48R	> 19.899	...
56267.444	452.69	P48	PTF48R	20.083	0.303
56267.474	452.72	P48	PTF48R	20.011	0.177
56269.438	454.69	P48	PTF48R	19.794	0.135
56271.441	456.69	P48	PTF48R	20.012	0.280
56271.470	456.72	P48	PTF48R	> 20.577	...
56273.428	458.67	P48	PTF48R	20.258	0.259
56273.458	458.70	P48	PTF48R	19.933	0.169
56281.412	466.65	P48	PTF48R	19.435	0.243
56281.443	466.68	P48	PTF48R	20.350	0.360
56297.362	482.59	P48	PTF48R	> 20.670	...
56297.425	482.65	P48	PTF48R	20.280	0.185
56301.472	486.70	P48	PTF48R	20.504	0.344
56301.519	486.74	P48	PTF48R	20.283	0.201
56305.568	490.79	P48	PTF48R	> 20.896	...
56306.373	491.59	P48	PTF48R	> 20.559	...
56322.553	507.76	P48	PTF48R	> 20.030	...
56324.376	509.58	P48	PTF48R	> 20.912	...
56324.413	509.62	P48	PTF48R	> 20.905	...
56324.450	509.65	P48	PTF48R	> 21.122	...
56327.369	512.57	P48	PTF48R	20.900	0.312
56327.506	512.71	P48	PTF48R	20.934	0.335
56327.542	512.74	P48	PTF48R	21.130	0.360
56328.446	513.65	P48	PTF48R	> 21.234	...
56329.559	514.76	P48	PTF48R	20.629	0.218
56330.361	515.56	P48	PTF48R	21.135	0.361
56330.570	515.77	P48	PTF48R	> 20.883	...
56335.421	520.62	P48	PTF48R	> 20.923	...
56335.537	520.73	P48	PTF48R	> 20.884	...
56336.344	521.54	P48	PTF48R	> 20.757	...
56336.555	521.75	P48	PTF48R	> 20.914	...
56337.341	522.54	P48	PTF48R	> 21.156	...
56337.565	522.76	P48	PTF48R	> 20.748	...
56338.339	523.53	P48	PTF48R	> 19.766	...

56338.400	523.59	P48	PTF48R	20.153	0.336
56340.537	525.73	P48	PTF48R	> 21.217	...
56340.566	525.76	P48	PTF48R	> 20.696	...
56341.536	526.73	P48	PTF48R	> 21.192	...
56341.566	526.76	P48	PTF48R	> 20.613	...
56342.328	527.52	P48	PTF48R	> 20.888	...
56342.388	527.58	P48	PTF48R	> 20.210	...
56345.423	530.61	P48	PTF48R	> 20.729	...
56345.460	530.65	P48	PTF48R	> 21.009	...
56345.497	530.68	P48	PTF48R	> 20.968	...
56354.405	539.59	P48	PTF48R	> 20.651	...
56354.434	539.61	P48	PTF48R	> 20.779	...
56354.464	539.64	P48	PTF48R	> 21.079	...
56356.477	541.66	P48	PTF48R	> 20.857	...
56356.506	541.69	P48	PTF48R	> 19.150	...
56362.359	547.53	P48	PTF48R	> 20.843	...
56362.389	547.56	P48	PTF48R	> 20.816	...
56362.418	547.59	P48	PTF48R	> 21.035	...
56363.441	548.61	P48	PTF48R	> 21.131	...
56363.471	548.64	P48	PTF48R	> 21.043	...
56363.505	548.68	P48	PTF48R	> 21.122	...
56367.499	552.67	P48	PTF48R	> 19.847	...
56367.529	552.70	P48	PTF48R	> 20.329	...
56368.402	553.57	P48	PTF48R	> 20.938	...
56368.432	553.60	P48	PTF48R	> 21.032	...
56369.412	554.58	P48	PTF48R	21.232	0.332
56369.442	554.61	P48	PTF48R	> 21.256	...
56369.471	554.64	P48	PTF48R	> 21.183	...
56372.256	557.42	P48	PTF48R	> 20.544	...
56372.285	557.45	P48	PTF48R	> 19.998	...
56372.315	557.48	P48	PTF48R	> 19.529	...
56374.459	559.62	P48	PTF48R	> 20.846	...
56374.488	559.65	P48	PTF48R	> 20.980	...
56374.518	559.68	P48	PTF48R	> 20.933	...
56375.490	560.65	P48	PTF48R	> 21.027	...
56375.520	560.68	P48	PTF48R	> 21.167	...
56376.247	561.41	P48	PTF48R	> 20.463	...
56376.276	561.44	P48	PTF48R	> 20.626	...
56376.306	561.47	P48	PTF48R	> 20.593	...
56385.469	570.62	P48	PTF48R	> 20.558	...
56385.501	570.66	P48	PTF48R	> 20.096	...
56386.248	571.40	P48	PTF48R	> 20.817	...
56386.279	571.43	P48	PTF48R	> 21.081	...
56386.310	571.46	P48	PTF48R	> 21.208	...
56387.445	572.60	P48	PTF48R	> 20.864	...
56387.475	572.63	P48	PTF48R	> 20.907	...
56387.504	572.66	P48	PTF48R	> 20.812	...
56389.457	574.61	P48	PTF48R	> 20.871	...

56389.488	574.64	P48	PTF48R	> 20.817	...
56389.518	574.67	P48	PTF48R	> 20.387	...
56392.200	577.35	P48	PTF48R	> 20.636	...
56392.230	577.38	P48	PTF48R	> 20.786	...
56392.262	577.41	P48	PTF48R	> 20.802	...
56393.242	578.39	P48	PTF48R	> 21.112	...
56393.272	578.42	P48	PTF48R	> 21.204	...
56393.302	578.45	P48	PTF48R	> 21.217	...
56394.351	579.50	P48	PTF48R	> 21.158	...
56395.193	580.34	P48	PTF48R	> 20.868	...
56395.223	580.37	P48	PTF48R	> 21.024	...
56396.425	581.57	P48	PTF48R	> 20.982	...
56396.454	581.60	P48	PTF48R	> 20.910	...
56399.424	584.57	P48	PTF48R	> 20.966	...
56399.454	584.60	P48	PTF48R	> 20.912	...
56399.484	584.63	P48	PTF48R	> 20.796	...
56400.433	585.58	P48	PTF48R	> 20.856	...
56400.462	585.61	P48	PTF48R	> 20.547	...
56400.492	585.64	P48	PTF48R	> 20.530	...
56401.439	586.58	P48	PTF48R	> 20.896	...
56401.469	586.61	P48	PTF48R	> 20.919	...
56401.498	586.64	P48	PTF48R	> 20.618	...
56402.438	587.58	P48	PTF48R	> 20.740	...
56402.467	587.61	P48	PTF48R	> 20.798	...
56402.497	587.64	P48	PTF48R	> 20.758	...
56403.439	588.58	P48	PTF48R	> 21.109	...
56403.469	588.61	P48	PTF48R	> 21.192	...
56403.499	588.64	P48	PTF48R	> 21.146	...
56405.239	590.38	P48	PTF48R	> 20.437	...
56405.291	590.43	P48	PTF48R	> 20.582	...
56405.320	590.46	P48	PTF48R	> 20.634	...
56413.252	598.39	P48	PTF48R	> 20.957	...
56413.281	598.41	P48	PTF48R	> 21.144	...
56413.310	598.44	P48	PTF48R	> 20.945	...
56415.200	600.33	P48	PTF48R	> 20.508	...
56415.434	600.57	P48	PTF48R	> 20.645	...
56415.464	600.60	P48	PTF48R	> 20.604	...
56416.365	601.50	P48	PTF48R	> 21.109	...
56416.407	601.54	P48	PTF48R	> 20.989	...
56416.437	601.57	P48	PTF48R	> 20.945	...
56417.339	602.47	P48	PTF48R	> 20.979	...
56417.390	602.52	P48	PTF48R	> 20.974	...
56417.421	602.55	P48	PTF48R	> 20.844	...
56422.371	607.50	P48	PTF48R	> 21.127	...
56422.455	607.58	P48	PTF48R	> 21.049	...
56423.164	608.29	P48	PTF48R	> 21.036	...
56423.414	608.54	P48	PTF48R	> 21.013	...
56423.444	608.57	P48	PTF48R	> 21.074	...

56424.346	609.47	P48	PTF48R	> 21.323	...
56424.387	609.51	P48	PTF48R	> 21.217	...
56424.416	609.54	P48	PTF48R	> 21.097	...
56425.319	610.44	P48	PTF48R	> 21.279	...
56425.389	610.51	P48	PTF48R	> 21.146	...
56425.418	610.54	P48	PTF48R	> 21.167	...
56426.320	611.44	P48	PTF48R	> 21.081	...
56426.417	611.54	P48	PTF48R	> 20.971	...
56426.446	611.57	P48	PTF48R	> 20.883	...
56427.349	612.47	P48	PTF48R	> 20.828	...
56427.398	612.52	P48	PTF48R	> 20.831	...
56427.428	612.55	P48	PTF48R	> 20.675	...
56428.329	613.45	P48	PTF48R	> 20.947	...
56429.178	614.30	P48	PTF48R	> 21.013	...
56431.379	616.50	P48	PTF48R	> 20.801	...
56431.450	616.57	P48	PTF48R	> 20.856	...
56431.479	616.60	P48	PTF48R	> 20.663	...
56432.381	617.50	P48	PTF48R	> 21.030	...
56432.417	617.53	P48	PTF48R	> 21.071	...
56432.446	617.56	P48	PTF48R	> 20.926	...
56433.348	618.46	P48	PTF48R	> 20.910	...
56433.384	618.50	P48	PTF48R	> 21.001	...
56433.414	618.53	P48	PTF48R	20.988	0.321
56434.316	619.43	P48	PTF48R	> 20.718	...
56434.383	619.50	P48	PTF48R	> 20.677	...
56434.412	619.53	P48	PTF48R	> 20.750	...
56596.544	781.53	P48	PTF48R	> 19.754	...
56597.541	782.53	P48	PTF48R	> 20.236	...
56598.538	783.52	P48	PTF48R	> 20.463	...
56599.535	784.52	P48	PTF48R	> 20.559	...
56601.530	786.51	P48	PTF48R	> 20.307	...
56602.527	787.51	P48	PTF48R	> 20.264	...
56603.524	788.50	P48	PTF48R	> 20.397	...
56604.522	789.50	P48	PTF48R	> 20.930	...
56605.519	790.50	P48	PTF48R	> 20.753	...
56605.544	790.52	P48	PTF48R	> 20.766	...
56607.513	792.49	P48	PTF48R	> 20.619	...
56607.545	792.52	P48	PTF48R	> 20.600	...
56609.508	794.48	P48	PTF48R	> 20.665	...
56609.533	794.51	P48	PTF48R	> 20.690	...
56610.506	795.48	P48	PTF48R	> 20.476	...
56610.531	795.51	P48	PTF48R	> 20.663	...
56621.505	806.47	P48	PTF48R	> 20.316	...
56622.462	807.43	P48	PTF48R	> 19.656	...
56622.473	807.44	P48	PTF48R	> 19.864	...
56622.497	807.46	P48	PTF48R	> 20.031	...
56622.512	807.48	P48	PTF48R	> 19.997	...
56622.522	807.49	P48	PTF48R	> 19.633	...

56622.537	807.50	P48	PTF48R	> 18.893	...
56622.547	807.51	P48	PTF48R	> 19.520	...
56622.563	807.53	P48	PTF48R	> 19.005	...
56624.468	809.43	P48	PTF48R	> 20.486	...
56624.499	809.46	P48	PTF48R	> 20.597	...
56624.532	809.50	P48	PTF48R	> 20.724	...
56626.506	811.47	P48	PTF48R	> 20.884	...
56626.532	811.49	P48	PTF48R	> 21.018	...
56628.486	813.45	P48	PTF48R	> 20.637	...
56628.511	813.47	P48	PTF48R	> 20.425	...
56638.460	823.41	P48	PTF48R	> 20.604	...
56638.486	823.44	P48	PTF48R	> 20.699	...
56640.454	825.41	P48	PTF48R	> 19.487	...
56640.479	825.43	P48	PTF48R	> 19.573	...
56647.484	832.43	P48	PTF48R	> 20.418	...
56647.509	832.45	P48	PTF48R	> 20.528	...
56662.387	847.32	P48	PTF48R	> 20.161	...
56662.431	847.36	P48	PTF48R	> 20.712	...
56662.435	847.37	P48	PTF48R	> 20.795	...
56662.500	847.43	P48	PTF48R	> 20.715	...
56664.388	849.32	P48	PTF48R	> 20.599	...
56664.413	849.34	P48	PTF48R	> 20.758	...
56666.391	851.32	P48	PTF48R	> 19.866	...
56666.416	851.35	P48	PTF48R	> 20.299	...
56668.377	853.31	P48	PTF48R	> 20.610	...
56668.402	853.33	P48	PTF48R	> 20.805	...
56670.372	855.30	P48	PTF48R	> 19.841	...
56670.399	855.33	P48	PTF48R	> 19.934	...
56675.359	860.28	P48	PTF48R	> 19.374	...
56675.385	860.31	P48	PTF48R	> 18.553	...
56677.353	862.27	P48	PTF48R	> 20.457	...
56677.379	862.30	P48	PTF48R	> 20.673	...
56679.521	864.44	P48	PTF48R	> 21.124	...
56683.504	868.42	P48	PTF48R	> 21.252	...
56685.514	870.43	P48	PTF48R	> 21.015	...
56685.557	870.47	P48	PTF48R	> 21.193	...
56689.373	874.28	P48	PTF48R	> 20.758	...
56689.423	874.33	P48	PTF48R	> 20.937	...
56696.398	881.30	P48	PTF48R	> 20.868	...
56697.298	882.20	P48	PTF48R	> 20.509	...
56697.340	882.25	P48	PTF48R	> 20.655	...
56700.290	885.19	P48	PTF48R	> 19.844	...
56700.333	885.24	P48	PTF48R	> 20.130	...
56706.273	891.17	P48	PTF48R	> 20.021	...
56706.315	891.21	P48	PTF48R	> 20.371	...
56709.271	894.17	P48	PTF48R	> 19.404	...
56709.342	894.24	P48	PTF48R	> 20.608	...
56712.257	897.15	P48	PTF48R	> 21.004	...

56712.345	897.24	P48	PTF48R	> 21.010	...
56721.233	906.12	P48	PTF48R	> 20.389	...
56721.283	906.17	P48	PTF48R	> 20.719	...
56724.224	909.11	P48	PTF48R	> 20.323	...
56724.251	909.13	P48	PTF48R	> 20.613	...
56727.216	912.10	P48	PTF48R	> 20.567	...
56727.314	912.20	P48	PTF48R	> 20.784	...
56730.210	915.09	P48	PTF48R	> 20.101	...
56730.233	915.11	P48	PTF48R	> 20.208	...
56734.197	919.07	P48	PTF48R	> 19.643	...
56734.219	919.09	P48	PTF48R	> 19.524	...
56734.468	919.34	P48	PTF48R	> 19.278	...
56735.293	920.17	P48	PTF48R	> 20.526	...
56736.221	921.10	P48	PTF48R	> 20.840	...
56736.382	921.26	P48	PTF48R	> 20.636	...
56737.284	922.16	P48	PTF48R	> 20.961	...
56737.432	922.30	P48	PTF48R	> 21.079	...
56738.379	923.25	P48	PTF48R	> 21.081	...
56738.534	923.41	P48	PTF48R	> 20.916	...
56739.435	924.31	P48	PTF48R	> 20.777	...
56739.505	924.38	P48	PTF48R	> 20.642	...
56740.407	925.28	P48	PTF48R	> 19.838	...
56740.440	925.31	P48	PTF48R	> 20.310	...
56741.342	926.21	P48	PTF48R	> 21.015	...
56741.397	926.27	P48	PTF48R	> 21.197	...
56745.198	930.06	P48	PTF48R	> 20.676	...
56745.270	930.14	P48	PTF48R	> 20.838	...
56746.217	931.08	P48	PTF48R	> 20.058	...
56746.280	931.15	P48	PTF48R	> 20.264	...
56747.488	932.35	P48	PTF48R	> 21.018	...
56747.520	932.39	P48	PTF48R	> 20.928	...
56751.234	936.10	P48	PTF48R	> 20.891	...
56752.213	937.07	P48	PTF48R	> 20.821	...
56752.274	937.14	P48	PTF48R	> 20.989	...
56753.419	938.28	P48	PTF48R	> 21.036	...
56753.452	938.31	P48	PTF48R	> 21.038	...
56754.355	939.21	P48	PTF48R	> 20.887	...
56754.396	939.26	P48	PTF48R	> 20.988	...
56755.300	940.16	P48	PTF48R	> 21.003	...
56755.339	940.20	P48	PTF48R	> 21.012	...
56756.241	941.10	P48	PTF48R	> 20.319	...
56756.275	941.13	P48	PTF48R	> 20.025	...
56757.195	942.05	P48	PTF48R	> 17.703	...
56757.258	942.12	P48	PTF48R	> 18.284	...
56758.484	943.34	P48	PTF48R	> 20.957	...
56758.517	943.37	P48	PTF48R	> 20.891	...
56759.413	944.27	P48	PTF48R	> 20.656	...
56759.448	944.30	P48	PTF48R	> 20.694	...

56760.350	945.20	P48	PTF48R	> 20.168	...
56760.385	945.24	P48	PTF48R	> 20.369	...
56761.286	946.14	P48	PTF48R	> 20.453	...
56761.320	946.17	P48	PTF48R	> 20.438	...
56762.230	947.08	P48	PTF48R	> 20.258	...
56762.268	947.12	P48	PTF48R	> 21.007	...
56763.191	948.04	P48	PTF48R	> 20.427	...
56763.278	948.13	P48	PTF48R	> 20.369	...
56764.209	949.06	P48	PTF48R	> 20.548	...
56764.280	949.13	P48	PTF48R	> 20.688	...
56766.223	951.07	P48	PTF48R	> 20.634	...
56766.380	951.23	P48	PTF48R	> 20.662	...
56767.393	952.24	P48	PTF48R	> 20.982	...
56767.470	952.32	P48	PTF48R	> 20.877	...
56768.404	953.25	P48	PTF48R	> 21.063	...
56768.480	953.33	P48	PTF48R	> 21.009	...
56769.381	954.23	P48	PTF48R	> 19.786	...
56769.415	954.26	P48	PTF48R	> 19.654	...
56770.449	955.30	P48	PTF48R	> 20.838	...
56770.484	955.33	P48	PTF48R	> 20.719	...
56771.386	956.23	P48	PTF48R	> 21.139	...
56771.418	956.26	P48	PTF48R	> 20.945	...
56772.320	957.17	P48	PTF48R	> 20.726	...
56772.354	957.20	P48	PTF48R	> 20.991	...
56775.356	960.20	P48	PTF48R	> 20.913	...
56775.405	960.25	P48	PTF48R	> 20.746	...
56776.306	961.15	P48	PTF48R	> 20.890	...
56776.365	961.21	P48	PTF48R	> 20.247	...
56777.408	962.25	P48	PTF48R	> 20.369	...
56777.501	962.34	P48	PTF48R	> 19.320	...
56778.447	963.29	P48	PTF48R	> 19.990	...
56779.199	964.04	P48	PTF48R	> 21.069	...
56779.251	964.09	P48	PTF48R	> 21.076	...
56780.340	965.18	P48	PTF48R	> 21.141	...
56780.389	965.23	P48	PTF48R	> 21.061	...
56781.338	966.18	P48	PTF48R	> 21.046	...
56781.421	966.26	P48	PTF48R	> 20.966	...
56782.383	967.22	P48	PTF48R	> 21.030	...
56782.432	967.27	P48	PTF48R	> 21.007	...
56785.425	970.26	P48	PTF48R	> 21.065	...
56785.478	970.31	P48	PTF48R	> 20.852	...
56786.317	971.15	P48	PTF48R	> 20.891	...
56786.351	971.18	P48	PTF48R	> 20.892	...
56788.222	973.05	P48	PTF48R	> 20.269	...
56788.257	973.09	P48	PTF48R	> 20.160	...
56789.178	974.01	P48	PTF48R	> 20.327	...
56789.211	974.04	P48	PTF48R	> 20.362	...
56790.242	975.07	P48	PTF48R	> 20.178	...

56790.268	975.10	P48	PTF48R	> 20.206	...
56790.486	975.32	P48	PTF48R	> 19.852	...
56791.244	976.07	P48	PTF48R	> 20.123	...
56791.274	976.10	P48	PTF48R	> 20.264	...
56792.245	977.07	P48	PTF48R	> 20.241	...
56792.278	977.11	P48	PTF48R	> 20.297	...
56794.294	979.12	P48	PTF48R	> 19.578	...
56794.329	979.16	P48	PTF48R	> 19.688	...
56795.287	980.11	P48	PTF48R	> 18.792	...
56796.305	981.13	P48	PTF48R	> 20.768	...
56796.355	981.18	P48	PTF48R	> 20.698	...
56797.401	982.23	P48	PTF48R	> 20.174	...
56802.258	987.08	P48	PTF48R	> 21.249	...
56802.295	987.12	P48	PTF48R	> 21.163	...
56803.254	988.07	P48	PTF48R	> 21.199	...
56803.290	988.11	P48	PTF48R	> 21.239	...
56804.255	989.07	P48	PTF48R	> 21.275	...
56804.290	989.11	P48	PTF48R	> 21.283	...
56805.255	990.07	P48	PTF48R	> 21.247	...
56805.289	990.11	P48	PTF48R	> 20.696	...
56817.190	1002.00	P48	PTF48R	> 20.733	...
56817.217	1002.03	P48	PTF48R	> 20.958	...
56817.244	1002.05	P48	PTF48R	> 20.864	...
56854.322	1039.10	P48	PTF48R	> 19.922	...
56854.344	1039.12	P48	PTF48R	> 18.848	...
56859.171	1043.95	P48	PTF48R	> 21.109	...
56859.211	1043.99	P48	PTF48R	> 21.274	...
56860.171	1044.95	P48	PTF48R	> 21.179	...
56860.189	1044.96	P48	PTF48R	> 21.099	...
56861.170	1045.94	P48	PTF48R	> 20.871	...
56861.188	1045.96	P48	PTF48R	> 21.109	...
56862.170	1046.94	P48	PTF48R	> 20.709	...
56862.187	1046.96	P48	PTF48R	> 21.272	...
56869.166	1053.93	P48	PTF48R	> 21.019	...
56869.178	1053.94	P48	PTF48R	> 21.124	...
56874.162	1058.93	P48	PTF48R	> 20.940	...
56874.199	1058.96	P48	PTF48R	> 20.979	...
56877.160	1061.92	P48	PTF48R	> 20.507	...
56877.185	1061.95	P48	PTF48R	> 20.717	...
56877.217	1061.98	P48	PTF48R	> 20.670	...
56877.250	1062.01	P48	PTF48R	> 20.469	...
56877.270	1062.03	P48	PTF48R	> 20.430	...
56879.159	1063.92	P48	PTF48R	> 20.541	...
56879.174	1063.93	P48	PTF48R	> 20.487	...
56879.227	1063.99	P48	PTF48R	> 20.438	...
56971.547	1156.23	P48	PTF48R	> 20.063	...
57000.504	1185.17	P48	PTF48R	> 20.463	...
57000.562	1185.22	P48	PTF48R	> 20.725	...

57001.491	1186.15	P48	PTF48R	> 20.235	...
57001.550	1186.21	P48	PTF48R	> 20.555	...
57020.497	1205.14	P48	PTF48R	> 20.953	...
57020.565	1205.21	P48	PTF48R	> 20.792	...
57036.488	1221.12	P48	PTF48R	> 20.891	...
57054.486	1239.10	P48	PTF48R	> 20.712	...
57054.539	1239.16	P48	PTF48R	> 20.630	...
57059.458	1244.07	P48	PTF48R	> 18.156	...
57059.488	1244.10	P48	PTF48R	> 20.751	...
57059.519	1244.13	P48	PTF48R	> 20.722	...
57060.283	1244.90	P48	PTF48R	> 20.277	...
57060.305	1244.92	P48	PTF48R	> 20.294	...
57060.327	1244.94	P48	PTF48R	> 20.361	...
57062.285	1246.90	P48	PTF48R	> 20.407	...

[a] $\mathrm{MJD_{max}}$ = 55814.38, calculated by SiFTO

TABLE A.2: Literature *R*-band and near-IR photometric data for SN 2011fe

MJD	Phase (days)[a]	Telescope	Filter	Magnitude[b]	Magnitude system	Reference[c]	*s*-correction[d,e]
56049.50	234.93	LBT	*J*	17.18(0.10)	Vega	1	-
56257.50	442.76	LBT	*J*	17.42(0.04)	Vega	1	-
56332.50	517.70	LBT	*J*	18.23(0.18)	Vega	1	-
56337.48	522.67	LBT	*R*	22.14(0.02)	Vega	1	-0.47
56419.46	604.59	LBT	*R*	21.74(0.03)	Vega	1	0.54
56440.81	625.92	1m CAO	*R*	22.00(0.12)	Vega	2	0.37
56441.84	626.95	1m CAO	*R*	22.07(0.11)	Vega	2	0.35
56449.21	634.32	LBT	*R*	21.91(0.02)	Vega	1	0.54
56453.26	638.36	LBT	*R*	21.95(0.02)	Vega	1	0.54
56637.53	822.48	LBT	*R*	23.19(0.04)	Vega	1	0.68
56743.00	927.87	GMOS North	*r*	24.01(0.14)	AB	3	0.48
56812.35	997.17	LBT	*R*	24.31(0.08)	Vega	1	0.53
56837.28	1022.08	LBT	*R*	24.54(0.08)	Vega	1	0.54
56839.29	1024.08	LBT	*R*	24.27(0.06)	Vega	1	0.53
56939.00	1123.71	*HST*	F600LP	24.84(0.02)	Vega	1	0.68
56939.00	1123.71	*HST*	F110W	24.30(0.04)	Vega	1	-
56939.00	1123.71	*HST*	F160W	22.37(0.02)	Vega	1	-
57041.51	1226.14	LBT	*R*	25.34(0.20)	Vega	1	0.65
57071.51	1256.11	LBT	*R*	25.46(0.14)	Vega	1	0.56
57118.00	1302.57	*HST*	F600LP	25.55(0.05)	Vega	1	0.67
57118.00	1302.57	*HST*	F110W	25.28(0.09)	Vega	1	-
57118.00	1302.57	*HST*	F160W	23.12(0.02)	Vega	1	-
57135.19	1319.75	LBT	*R*	25.51(0.18)	Vega	1	0.53
57163.23	1347.76	LBT	*R*	26.07(0.26)	Vega	1	0.25
57217.00	1401.52	*HST*	F600LP	25.82(0.04)	Vega	1	0.76
57217.00	1401.52	*HST*	F110W	25.43(0.10)	Vega	1	-
57217.00	1401.52	*HST*	F160W	23.41(0.04)	Vega	1	-
57389.53	1573.88	LBT	*R*	26.39(0.41)	Vega	1	0.40
57425.49	1609.81	LBT	*R*	26.24(0.42)	Vega	1	0.31
57437.50	1621.81	*HST*	F600LP	26.51(0.09)	Vega	1	0.75
57437.50	1621.81	*HST*	F110W	26.15(0.19)	Vega	1	-
57437.50	1621.81	*HST*	F160W	24.09(0.09)	Vega	1	-

[a] Assuming maximum light at MJD 55814.30 (Mazzali et al., 2014).
[b] 1-σ uncertainties in parentheses.
[c] 1: Shappee et al. (2016); 2: Tsvetkov et al. (2013); 3: Kerzendorf et al. (2014).
[d] $Mag^{\mathrm{s-corrected}} = Mag^{\mathrm{original}} + s-\mathrm{correction}$
[e] *s*-correction term includes transformation to AB system, where appropriate.

TABLE A.3: SN 2011fe spectroscopy log

Date (UT)	Phase (days)[a]	Telescope – Instrument	Wavelength Coverage (Å)	Reference[b]
2012 04 02	205	Lick 3m – KAST	3440 – 10268	1
2012 04 23	226	Lick 3m – KAST	3438 – 10176	1
2012 04 27	230	Keck-I – LRIS	3200 – 9991	1
2012 05 01	250	LBT – Lucifer	11700 – 13100	1
2012 05 01	250	LBT – Lucifer	15500 – 17400	1
2012 05 01	250	LBT – Lucifer	20500 – 23700	1
2012 05 26	259	WHT – ISIS	3498 – 9490	1
2012 06 25	289	WHT – ISIS	3426 – 10268	1
2012 07 17	311	Lick 3m – KAST	3458 – 10254	1
2012 08 23	348	Lick 3m – KAST	3488 – 10238	1
2013 04 08	576	Keck-II – DEIMOS	4450 – 9637	2
2014 05 01	964	Keck-I – LRIS	3077 – 10328	2
2014 06 23	1034	LBT – MODS1	3100 – 10495	3

[a] Assuming maximum light at MJD 55814.30 (Mazzali et al., 2014).
[b] 1: Mazzali et al. (2015); 2: Graham et al. (2015); 3: Taubenberger et al. (2015).

TABLE A.4: The SN 2011fe pseudo-bolometric luminosity light curve

Phase (days)	$\log_{10}(L)$ (erg s^{-1})	Source (see Chapter 3 Sec. 3.4 for details)
205.00	40.676(0.035)	Spec - Mazzali et al. (2015)
212.92	40.616(0.024)	Phot - R_{P48}
226.00	40.532(0.033)	Spec - Mazzali et al. (2015)
237.99	40.514(0.034)	Phot - R_{P48}
259.00	40.312(0.037)	Spec - Mazzali et al. (2015)
262.75	40.308(0.025)	Phot - R_{P48}
287.20	40.151(0.026)	Phot - R_{P48}
289.00	40.118(0.042)	Spec - Mazzali et al. (2015)
311.00	40.002(0.039)	Spec - Mazzali et al. (2015)
311.91	39.991(0.027)	Phot - R_{P48}
331.12	39.872(0.027)	Phot - R_{P48}
348.00	39.779(0.045)	Spec - Mazzali et al. (2015)
354.90	39.732(0.028)	Phot - R_{P48}
420.32	39.333(0.030)	Phot - R_{P48}
440.69	39.218(0.031)	Phot - R_{P48}
456.88	39.102(0.031)	Phot - R_{P48}
486.84	38.892(0.032)	Phot - R_{P48}
516.39	38.663(0.033)	Phot - R_{P48}
522.67	38.546(0.034)	Phot - Shappee et al. (2016)
536.90	38.548(0.034)	Phot - R_{P48}
562.54	38.430(0.035)	Phot - R_{P48}
576.00	38.399(0.035)	Spec - Graham et al. (2015)
585.51	38.450(0.036)	Phot - R_{P48}
604.59	38.320(0.037)	Phot - Shappee et al. (2016)
610.98	38.390(0.037)	Phot - R_{P48}
625.92	38.278(0.037)	Phot - Tsvetkov et al. (2013)
626.95	38.257(0.037)	Phot - Tsvetkov et al. (2013)
634.32	38.247(0.038)	Phot - Shappee et al. (2016)
638.36	38.230(0.038)	Phot - Shappee et al. (2016)
822.48	37.604(0.045)	Phot - Shappee et al. (2016)
927.87	37.382(0.050)	Phot - Kerzendorf et al. (2014)
964.00	37.273(0.051)	Spec - Graham et al. (2015)
1034.00	37.056(0.058)	Spec - Taubenberger et al. (2015)
1123.71	36.897(0.066)	Phot - Shappee et al. (2016)-*HST*
1302.57	36.602(0.075)	Phot - Shappee et al. (2016)-*HST*
1401.52	36.453(0.087)	Phot - Shappee et al. (2016)-*HST*
1621.81	36.163(0.100)	Phot - Shappee et al. (2016)-*HST*

Appendix B

SN 201fe: The best-fitting parameters of the pseudo-bolometric light curve

TABLE B.1: The best-fitting parameters for the modelling of the pseudo-bolometric light curve (extended version)

Model	$M(56)$ ($M_\odot$)	$M(57)$ ($M_\odot$)	$M(55)$ ($M_\odot$)	$M(57)/M(56)$	$M(57)/M(56)$ $(^{57}Fe/^{56}Fe)_\odot$[a]	t^l_{56} (days)	t^l_{57} (days)	χ^2_{DOF}	DOF
Case 0	0.179(0.003)	0.004(0.001)	0.0(0.0)	0.022(0.003)	0.963(0.114)	—	—	24.09	36
Case 1	0.461(0.041)	0.014(0.005)	0.0(0.0)	0.031(0.011)	1.322(0.473)	233(30)	886(427)	2.47	34
Case 1, excluding 550-650d	0.442(0.035)	0.015(0.007)	0.0(0.0)	0.023(0.016)	1.47(0.731)	249(32)	812(551)	2.25	25
Case 2	0.355(0.017)	0.021(0.003)	0.0(0.0)	0.059(0.008)	2.571(0.346)	—	—	2.08	33
Case 2, excluding 550-650d	0.357(0.018)	0.022(0.003)	0.0(0.0)	0.060(0.009)	2.627(0.391)	—	—	1.96	24

[a] Assuming $\left(^{57}Fe/^{56}Fe\right)_\odot = 0.023$ (Asplund et al., 2009)

Appendix C

Photometric logs of SN 2014eg and SN 2016hvl

TABLE C.1: Photometry of SN 2014eg

Date (UT)	MJD[a](days)	Phase[b](days)	B mag(error)	g mag(error)	V mag(error)	r mag(error)	i mag(error)
2014 11 24	56985.23	−6.42	15.942(0.043)	15.823(0.020)	15.753(0.054)	15.758(0.012)	15.951(0.126)
2014 11 25	56986.08	−5.59	...(...)	15.732(0.017)	...(...)	15.704(0.074)	15.953(0.121)
2014 11 27	56988.17	−3.53	15.773(0.019)	15.644(0.026)	15.599(0.060)	15.577(0.042)	15.930(0.039)
2014 11 28	56989.17	−2.56	15.896(0.010)	15.542(0.014)	15.519(0.010)	15.445(0.062)	15.865(0.015)
2014 11 29	56990.18	−1.56	...(...)	15.556(0.010)	...(...)	15.303(0.014)	15.853(0.025)
2014 11 30	56991.06	−0.69	15.699(0.010)	15.521(0.024)	15.436(0.010)	15.385(0.010)	15.879(0.029)
2014 12 01	56992.11	0.33	15.711(0.018)	15.527(0.055)	15.423(0.017)	15.351(0.028)	15.881(0.041)
2014 12 02	56993.13	1.33	15.721(0.044)	15.580(0.014)	15.422(0.010)	15.344(0.021)	15.883(0.025)
2014 12 03	56994.20	2.38	15.845(0.044)	...(...)	...(...)	...(...)	...(...)
2014 12 04	56995.21	3.38	15.898(0.059)	15.603(0.061)	15.465(0.077)	15.352(0.010)	15.920(0.020)
2014 12 05	56996.94	5.08	...(...)	15.585(0.043)	...(...)	15.381(0.042)	15.934(0.048)
2014 12 08	56999.20	7.30	15.924(0.021)	15.687(0.055)	15.474(0.026)	15.449(0.013)	16.083(0.015)
2014 12 12	57003.27	11.30	16.271(0.030)	15.889(0.048)	15.677(0.020)	15.790(0.034)	16.487(0.046)
2014 12 13	57004.95	12.94	...(...)	16.053(0.025)	...(...)	15.872(0.010)	16.511(0.024)
2014 12 14	57005.95	13.93	...(...)	16.155(0.014)	...(...)	15.985(0.079)	16.567(0.031)
2014 12 16	57007.21	15.17	16.701(0.010)	16.237(0.029)	15.930(0.012)	15.955(0.023)	16.538(0.045)
2014 12 16	57007.93	15.87	...(...)	16.313(0.010)	...(...)	15.988(0.010)	16.460(0.013)
2014 12 17	57008.93	16.85	...(...)	16.405(0.023)	...(...)	15.983(0.011)	16.455(0.010)
2014 12 20	57011.20	19.09	17.181(0.022)	16.581(0.046)	16.149(0.010)	16.013(0.017)	16.411(0.062)
2014 12 22	57013.89	21.73	...(...)	16.858(0.016)	...(...)	16.067(0.014)	16.366(0.030)
2014 12 24	57015.20	23.02	17.684(0.029)	16.955(0.016)	16.372(0.010)	16.052(0.010)	16.340(0.031)
2014 12 25	57016.88	24.67	...(...)	17.182(0.010)	...(...)	16.141(0.026)	16.313(0.010)
2014 12 28	57019.07	26.81	18.125(0.019)	17.452(0.011)	...(...)	16.263(0.010)	16.366(0.010)
2014 12 28	57019.88	27.61	...(...)	17.445(0.087)	...(...)	16.218(0.010)	16.303(0.012)
2014 12 30	57021.09	28.80	18.150(0.022)	17.433(0.012)	16.659(0.024)	16.254(0.015)	16.401(0.010)
2015 01 01	57023.88	31.54	...(...)	17.687(0.138)	...(...)	16.452(0.022)	16.467(0.010)
2015 01 04	57026.99	34.60	18.431(0.021)	17.868(0.037)	17.026(0.010)	16.600(0.016)	16.638(0.061)
2015 01 07	57029.14	36.71	...(...)	17.979(0.133)	...(...)	16.822(0.010)	16.809(0.010)
2015 01 09	57031.92	39.44	...(...)	17.987(0.037)	...(...)	16.883(0.065)	16.817(0.075)
2015 01 13	57035.05	42.52	18.658(0.056)	18.148(0.043)	17.327(0.023)	17.037(0.024)	17.134(0.054)
2015 01 15	57037.92	45.33	...(...)	18.244(0.028)	...(...)	17.096(0.027)	17.245(0.042)
2015 01 19	57041.10	48.46	18.845(0.123)	18.235(0.027)	17.569(0.044)	17.207(0.028)	17.461(0.046)
2015 01 20	57042.14	49.48	18.739(0.042)	18.241(0.046)	17.557(0.022)	17.191(0.017)	17.457(0.069)
2015 01 22	57044.01	51.32	...(...)	18.304(0.079)	...(...)	17.360(0.034)	17.539(0.010)
2015 01 26	57048.04	55.27	...(...)	...(...)	17.674(0.022)	...(...)	...(...)
2015 01 27	57049.07	56.29	18.845(0.075)	18.429(0.093)	17.708(0.010)	17.503(0.106)	17.782(0.060)
2015 02 02	57055.07	62.18	18.914(0.089)	18.562(0.115)	17.832(0.056)	17.692(0.029)	18.075(0.089)
2015 02 05	57058.43	65.49	...(...)	18.554(0.071)	...(...)	17.766(0.090)	18.040(0.012)
2015 02 09	57062.09	69.07	19.138(0.026)	18.747(0.014)	18.233(0.027)	17.972(0.085)	18.430(0.010)
2015 02 11	57064.81	71.75	...(...)	...(...)	...(...)	17.977(0.023)	18.364(0.119)
2015 02 16	57069.03	75.89	19.221(0.079)	...(...)	...(...)	...(...)	...(...)
2015 02 18	57071.78	78.59	...(...)	18.802(0.058)	...(...)	18.239(0.055)	18.612(0.188)
2015 02 23	57076.04	82.78	19.389(0.053)	18.974(0.010)	18.617(0.046)	18.360(0.041)	18.997(0.089)
2015 03 02	57083.03	89.65	19.223(0.081)	18.852(0.126)	18.438(0.122)	18.341(0.040)	18.878(0.097)
2015 03 08	57089.03	95.54	19.259(0.066)	18.991(0.038)	18.696(0.122)	18.571(0.080)	19.420(0.174)
2015 03 09	57090.02	96.51	19.343(0.067)	18.933(0.010)	18.654(0.064)	18.583(0.026)	19.323(0.025)
2015 03 10	57091.01	97.48	19.427(0.063)	...(...)	18.658(0.034)	...(...)	...(...)
2015 03 12	57093.02	99.46	19.476(0.100)	19.074(0.010)	18.602(0.035)	18.760(0.199)	19.087(0.100)
2015 03 18	57099.00	105.34	...(...)	19.157(0.054)	...(...)	19.036(0.072)	...(...)

[a] Night averaged

[b] MJD_{peak} = 56991.77 from SIFTO

TABLE C.2: Photometry of SN 2016hvl

Date (UT)	MJD[a] (days)	Phase[b] (days)	B mag(error)	g mag(error)	V mag(error)	r mag(error)	i mag(error)
2016 11 09	57701.86	−8.56	...(...)	16.159(0.041)	...(...)	15.933(0.054)	16.060(0.023)
2016 11 15	57707.01	−3.47	...(...)	15.732(0.012)	...(...)	15.428(0.010)	15.686(0.012)
2016 11 16	57708.50	−1.99	...(...)	15.698(0.010)	...(...)	15.374(0.010)	15.691(0.011)
2016 11 19	57711.33	0.80	...(...)	15.645(0.010)	...(...)	15.321(0.010)	15.770(0.012)
2016 11 21	57713.34	2.78	...(...)	15.707(0.010)	...(...)	15.330(0.010)	15.762(0.010)
2016 11 22	57714.59	4.02	16.084(0.027)	15.730(0.010)	15.456(0.010)	15.338(0.010)	15.791(0.010)
2016 11 23	57715.58	4.99	16.127(0.010)	15.759(0.010)	15.461(0.010)	15.351(0.010)	15.850(0.061)
2016 11 25	57717.13	6.53	16.231(0.027)	15.825(0.028)	15.504(0.023)	15.394(0.018)	15.853(0.017)
2016 11 26	57718.95	8.32	16.376(0.010)	15.902(0.010)	15.550(0.010)	15.468(0.010)	15.947(0.010)
2016 11 29	57721.11	10.45	16.592(0.029)	16.039(0.010)	15.655(0.010)	15.587(0.010)	16.061(0.010)
2016 12 01	57723.08	12.40	16.799(0.011)	16.207(0.011)	15.778(0.010)	15.699(0.012)	16.159(0.015)
2016 12 02	57724.03	13.33	16.942(0.028)	16.299(0.010)	15.839(0.010)	15.751(0.010)	16.182(0.011)
2016 12 03	57725.08	14.37	17.043(0.023)	16.396(0.010)	15.911(0.013)	15.796(0.010)	16.205(0.010)
2016 12 04	57726.91	16.18	17.271(0.026)	16.558(0.010)	16.012(0.010)	15.846(0.010)	16.197(0.010)
2016 12 06	57728.08	17.33	17.397(0.011)	16.664(0.010)	16.079(0.011)	15.877(0.010)	16.184(0.010)
2016 12 07	57729.34	18.58	17.508(0.036)	16.717(0.012)	16.142(0.012)	15.912(0.010)	16.185(0.010)
2016 12 08	57730.25	19.47	17.582(0.030)	16.779(0.010)	16.184(0.010)	15.929(0.010)	16.183(0.010)
2016 12 11	57733.89	23.07	18.013(0.027)	17.079(0.018)	16.377(0.011)	16.039(0.010)	16.226(0.010)
2016 12 17	57739.53	28.63	18.358(0.122)	17.398(0.138)	16.630(0.058)	16.251(0.030)	16.305(0.010)
2016 12 20	57742.87	31.93	18.487(0.044)	17.661(0.032)	16.816(0.025)	16.365(0.010)	16.381(0.010)
2016 12 23	57745.27	34.30	18.517(0.040)	17.792(0.010)	16.967(0.010)	16.490(0.010)	16.475(0.010)
2016 12 24	57746.26	35.28	18.564(0.036)	17.815(0.010)	16.993(0.011)	16.562(0.010)	16.552(0.010)
2016 12 25	57747.08	36.09	18.660(0.044)	17.874(0.027)	17.044(0.017)	16.630(0.013)	16.611(0.010)
2016 12 31	57753.13	42.06	18.781(0.048)	18.072(0.010)	17.334(0.010)	16.961(0.010)	16.974(0.010)
2017 01 04	57757.85	46.72	18.915(0.028)	18.209(0.013)	17.498(0.010)	17.165(0.010)	17.251(0.010)
2017 01 06	57759.87	48.72	18.877(0.043)	18.280(0.037)	17.572(0.043)	...(...)	...(...)
2017 01 07	57760.88	49.71	18.857(0.140)	18.251(0.088)	17.593(0.010)	17.277(0.010)	17.381(0.010)
2017 01 08	57761.82	50.64	19.004(0.125)	18.340(0.010)	17.649(0.070)	17.328(0.012)	17.454(0.020)
2017 01 16	57769.84	58.56	19.132(0.023)	18.493(0.037)	17.875(0.054)	17.585(0.010)	17.689(0.029)
2017 01 17	57770.64	59.34	19.147(0.022)	18.454(0.018)	17.899(0.063)	17.618(0.023)	17.796(0.036)
2017 01 25	57778.80	67.40	19.355(0.045)	18.620(0.027)	18.101(0.047)	17.863(0.029)	18.086(0.010)
2017 01 31	57784.80	73.32	19.286(0.031)	18.670(0.010)	18.261(0.010)	18.058(0.013)	18.358(0.016)
2017 02 05	57789.88	78.34	19.418(0.165)	18.854(0.060)	18.471(0.014)	18.246(0.016)	18.510(0.010)
2017 02 11	57795.90	84.28	19.265(...)	18.803(0.143)	18.481(0.127)	18.395(0.010)	18.729(0.049)
2017 02 18	57802.53	90.82	19.543(0.049)	18.970(0.010)	18.672(0.018)	18.602(0.011)	18.887(0.099)
2017 02 24	57808.53	96.75	19.670(0.124)	19.141(0.027)	18.907(0.014)	18.763(0.042)	19.342(0.016)
2017 03 01	57813.87	102.02	19.930(0.010)	19.070(0.010)	18.974(0.108)	18.785(0.038)	19.202(0.063)
2017 03 02	57814.80	102.94	19.756(0.049)	19.171(0.010)	19.039(0.032)	19.006(0.019)	19.321(0.056)
2017 03 03	57815.80	103.93	19.840(0.068)	19.192(0.019)	19.003(0.023)	18.994(0.010)	19.404(0.031)
2017 03 09	57821.41	109.46	20.182(0.203)	19.335(0.088)	19.275(0.145)	19.120(0.010)	19.635(0.250)
2017 03 15	57827.81	115.78	20.014(0.010)	19.426(0.103)	19.264(0.102)	19.416(0.054)	19.798(0.036)
2017 03 22	57834.44	122.32	20.303(0.044)	...(...)	19.356(...)	...(...)	...(...)
2017 03 23	57835.81	123.68	20.221(0.010)	19.465(0.018)	19.490(0.109)	19.597(0.082)	19.961(0.196)
2017 03 30	57842.39	130.18	20.310(0.257)	19.568(0.278)	19.475(0.078)	19.449(0.098)	19.603(0.081)
2017 04 05	57848.75	136.45	20.395(0.098)	19.769(0.212)	19.604(0.220)	19.607(0.010)	20.011(...)

[a] Night averaged

[b] MJD_{peak} = 57710.52 from SIFTO

Bibliography

Alam S., et al., 2015, ApJS, 219, 12

Aldering G., et al., 2002, in Tyson J. A., Wolff S., eds, Proc. SPIEVol. 4836, Survey and Other Telescope Technologies and Discoveries. pp 61–72, doi:10.1117/12.458107

Aldering G., et al., 2006, ApJ, 650, 510

Altavilla G., et al., 2004, MNRAS, 349, 1344

Arnett W. D., 1979, ApJ, 230, L37

Arnett W. D., 1982, ApJ, 253, 785

Asplund M., Grevesse N., Sauval A. J., Scott P., 2009, ARA&A, 47, 481

Astier P., et al., 2006, A&A, 447, 31

Astier P., et al., 2014, A&A, 572, A80

Axelrod T. S., 1980, PhD thesis, California Univ., Santa Cruz.

Baade W., Zwicky F., 1934, Physical Review, 46, 76

Badenes C., Mullally F., Thompson S. E., Lupton R. H., 2009, ApJ, 707, 971

Benetti S., et al., 2005, ApJ, 623, 1011

Bianco F. B., et al., 2011, ApJ, 741, 20

Bildsten L., Shen K. J., Weinberg N. N., Nelemans G., 2007, ApJ, 662, L95

Blondin S., Tonry J. L., 2007, ApJ, 666, 1024

Blondin S., Prieto J. L., Patat F., Challis P., Hicken M., Kirshner R. P., Matheson T., Modjaz M., 2009, ApJ, 693, 207

Blondin S., Kasen D., Röpke F. K., Kirshner R. P., Mandel K. S., 2011, MNRAS, 417, 1280

Blondin S., et al., 2012, AJ, 143, 126

Bloom J. S., et al., 2012a, PASP, 124, 1175

Bloom J. S., et al., 2012b, ApJ, 744, L17

Bramich D. M., 2008, MNRAS, 386, L77

Branch D., van den Bergh S., 1993, AJ, 105, 2231

Branch D., et al., 2006, PASP, 118, 560

Brown T. M., et al., 2013, PASP, 125, 1031

Buzzoni B., et al., 1984, The Messenger, 38, 9

Cao Y., et al., 2015, Nature, 521, 328

Cappellaro E., Mazzali P. A., Benetti S., Danziger I. J., Turatto M., della Valle M., Patat F., 1997, A&A, 328, 203

Cappellaro E., et al., 2001, ApJ, 549, L215

Cardelli J. A., Clayton G. C., Mathis J. S., 1989, ApJ, 345, 245

Cartier R., et al., 2014, ApJ, 789, 89

Cartier R., et al., 2016, preprint, (arXiv:1609.04465)

Chambers K. C., et al., 2016, preprint, (arXiv:1612.05560)

Childress M., et al., 2013, ApJ, 770, 108

Childress M. J., et al., 2015, MNRAS, 454, 3816

Chomiuk L., et al., 2012, ApJ, 750, 164

Churazov E., et al., 2014, Nature, 512, 406

Claeys J. S. W., Pols O. R., Izzard R. G., Vink J., Verbunt F. W. M., 2014, A&A, 563, A83

Colgate S. A., McKee C., 1969, ApJ, 157, 623

Conley A., et al., 2008, ApJ, 681, 482

Corsi A., et al., 2014, ApJ, 782, 42

Crocker R. M., et al., 2016, preprint, (arXiv:1607.03495)

Di Stefano R., 2010, ApJ, 712, 728

Di Stefano R., Voss R., Claeys J. S. W., 2011, ApJ, 738, L1

Diehl R., et al., 2014, Science, 345, 1162

Dilday B., et al., 2010, ApJ, 713, 1026

Dilday B., et al., 2012, Science, 337, 942

Dimitriadis G., et al., 2016, The Astronomer's Telegram, 9720

Drozdov D., Leising M. D., Milne P. A., Pearcy J., Riess A. G., Macri L. M., Bryngelson G. L., Garnavich P. M., 2015, ApJ, 805, 71

Fenn D., Plewa T., Gawryszczak A., 2016, MNRAS, 462, 2486

Filippenko A. V., et al., 1992a, AJ, 104, 1543

Filippenko A. V., et al., 1992b, ApJ, 384, L15

Fioc M., Rocca-Volmerange B., 1997, A&A, 326, 950

Firth R. E., et al., 2015, MNRAS, 446, 3895

Fisher R., Jumper K., 2015, ApJ, 805, 150

Fitzpatrick E. L., 1999, PASP, 111, 63

Flaugher B., et al., 2015, AJ, 150, 150

Flewelling H. A., et al., 2016, preprint, (arXiv:1612.05243)

Folatelli G., et al., 2010, AJ, 139, 120

Folatelli G., et al., 2012, ApJ, 745, 74

Foley R. J., Kirshner R. P., 2013, ApJ, 769, L1

Foley R. J., et al., 2012, ApJ, 752, 101

Foley R. J., et al., 2013, ApJ, 767, 57

Foley R. J., Hounsell R., Scolnic D., WFIRST Supernova Science Investigation Team 2017, in American Astronomical Society Meeting Abstracts. p. 406.07

Fossey S. J., Cooke B., Pollack G., Wilde M., Wright T., 2014, Central Bureau Electronic Telegrams, 3792

Fransson C., Jerkstrand A., 2015, ApJ, 814, L2

Fransson C., Kozma C., 1993, ApJ, 408, L25

Friedman A. S., et al., 2015, ApJS, 220, 9

Frieman J. A., et al., 2008, AJ, 135, 338

Friesen B., et al., 2017, MNRAS, 467, 2392

Frohmaier C., Sullivan M., Nugent P. E., Goldstein D. A., DeRose J., 2017, ApJS, 230, 4

Gallagher J. S., Garnavich P. M., Caldwell N., Kirshner R. P., Jha S. W., Li W., Ganeshalingam M., Filippenko A. V., 2008, ApJ, 685, 752

Ganeshalingam M., et al., 2012, ApJ, 751, 142

Garavini G., et al., 2007, A&A, 471, 527

Gilfanov M., Bogdán Á., 2010, Nature, 463, 924

Goobar A., 2008, ApJ, 686, L103

Graham M. L., Nugent P. E., Sullivan M., Filippenko A. V., Cenko S. B., Silverman J. M., Clubb K. I., Zheng W., 2015, MNRAS, 454, 1948

Graham M. L., Harris C. E., Fox O. D., Nugent P. E., Kasen D., Silverman J. M., Filippenko A. V., 2017, ApJ, 843, 102

Graur O., et al., 2011, MNRAS, 417, 916

Graur O., Zurek D., Shara M. M., Riess A. G., Seitenzahl I. R., Rest A., 2016, ApJ, 819, 31

Guillochon J., Parrent J., Kelley L. Z., Margutti R., 2017, ApJ, 835, 64

Gunn J. E., et al., 1998, AJ, 116, 3040

Gunn J. E., et al., 2006, AJ, 131, 2332

Gupta R. R., et al., 2016, AJ, 152, 154

Guy J., et al., 2007, A&A, 466, 11

Hachisu I., Kato M., Nomoto K., 1996, ApJ, 470, L97

Hamuy M., Phillips M. M., Suntzeff N. B., Schommer R. A., Maza J., Aviles R., 1996, AJ, 112, 2391

Hamuy M., Trager S. C., Pinto P. A., Phillips M. M., Schommer R. A., Ivanov V., Suntzeff N. B., 2000, AJ, 120, 1479

Hamuy M., et al., 2003, Nature, 424, 651

Han Z., Podsiadlowski P., 2004, MNRAS, 350, 1301

Hancock P. J., Gaensler B. M., Murphy T., 2011, ApJ, 735, L35

Hayden B. T., et al., 2010, ApJ, 722, 1691

Henden A., Munari U., 2014, Contributions of the Astronomical Observatory Skalnate Pleso, 43, 518

Hicken M., Garnavich P. M., Prieto J. L., Blondin S., DePoy D. L., Kirshner R. P., Parrent J., 2007, ApJ, 669, L17

Hicken M., Wood-Vasey W. M., Blondin S., Challis P., Jha S., Kelly P. L., Rest A., Kirshner R. P., 2009, ApJ, 700, 1097

Hillebrandt W., Niemeyer J. C., 2000, ARA&A, 38, 191

Hillebrandt W., Kromer M., Röpke F. K., Ruiter A. J., 2013, Frontiers of Physics, 8, 116

Hönig S. F., et al., 2017, MNRAS, 464, 1693

Horesh A., et al., 2012, ApJ, 746, 21

Howell D. A., 2001, ApJ, 554, L193

Howell D. A., et al., 2005, ApJ, 634, 1190

Hoyle F., Fowler W. A., 1960, ApJ, 132, 565

Hsiao E. Y., Conley A., Howell D. A., Sullivan M., Pritchet C. J., Carlberg R. G., Nugent P. E., Phillips M. M., 2007, ApJ, 663, 1187

Iben Jr. I., Renzini A., 1983, ARA&A, 21, 271

Iben Jr. I., Tutukov A. V., 1984, ApJS, 54, 335

Ivezic Z., et al., 2009, in American Astronomical Society Meeting Abstracts #213. p. 366

Iwamoto K., Brachwitz F., Nomoto K., Kishimoto N., Umeda H., Hix W. R., Thielemann F.-K., 1999, ApJS, 125, 439

Jha S., et al., 2006, AJ, 131, 527

Johansson J., et al., 2014, preprint, (arXiv:1411.3332)

Kangas T., et al., 2014, The Astronomer's Telegram, 6711, 1

Kangas T., et al., 2016, MNRAS, 456, 323

Kasen D., 2010, ApJ, 708, 1025

Kasen D., Nugent P. E., 2013, Annual Review of Nuclear and Particle Science, 63, 153

Kasen D., Woosley S. E., 2007, ApJ, 656, 661

Kashi A., Soker N., 2011, MNRAS, 417, 1466

Kasliwal M. M., 2012, PASA, 29, 482

Katz B., Dong S., 2012, preprint, (arXiv:1211.4584)

Kawaler S. D., 2004, in Maeder A., Eenens P., eds, IAU Symposium Vol. 215, Stellar Rotation. p. 561

Kerzendorf W. E., Taubenberger S., Seitenzahl I. R., Ruiter A. J., 2014, ApJ, 796, L26

Khokhlov A. M., 1991, A&A, 245, 114

Kozma C., Fransson C., 1998a, ApJ, 496, 946

Kozma C., Fransson C., 1998b, ApJ, 497, 431

Krisciunas K., Hastings N. C., Loomis K., McMillan R., Rest A., Riess A. G., Stubbs C., 2000, ApJ, 539, 658

Lair J. C., Leising M. D., Milne P. A., Williams G. G., 2006, AJ, 132, 2024

Lang D., Hogg D. W., Mierle K., Blanton M., Roweis S., 2010, AJ, 139, 1782

Law N. M., et al., 2009, PASP, 121, 1395

Le Borgne D., Rocca-Volmerange B., 2002, A&A, 386, 446

Leloudas G., et al., 2009, A&A, 505, 265

Leloudas G., et al., 2015, A&A, 574, A61

Li W., et al., 2011a, MNRAS, 412, 1441

Li W., et al., 2011b, Nature, 480, 348

Liebert J., Bergeron P., Holberg J. B., 2005, ApJS, 156, 47

Lira P., et al., 1998, AJ, 115, 234

Maeda K., Iwamoto K., 2009, MNRAS, 394, 239

Maeda K., Röpke F. K., Fink M., Hillebrandt W., Travaglio C., Thielemann F.-K., 2010, ApJ, 712, 624

Magee M. R., et al., 2016, A&A, 589, A89

Maguire K., et al., 2013, MNRAS, 436, 222

Maguire K., et al., 2014, MNRAS, 444, 3258

Maguire K., Taubenberger S., Sullivan M., Mazzali P. A., 2016, MNRAS, 457, 3254

Mannucci F., Della Valle M., Panagia N., 2006, MNRAS, 370, 773

Maoz D., Mannucci F., Brandt T. D., 2012, MNRAS, 426, 3282

Maoz D., Mannucci F., Nelemans G., 2014, ARA&A, 52, 107

Marino S., González-Gaitán S., Förster F., Folatelli G., Hamuy M., Hsiao E., 2015, ApJ, 806, 134

Matheson T., et al., 2012, ApJ, 754, 19

Mattila S., Lundqvist P., Sollerman J., Kozma C., Baron E., Fransson C., Leibundgut B., Nomoto K., 2005, A&A, 443, 649

Mazzali P. A., et al., 2014, MNRAS, 439, 1959

Mazzali P. A., et al., 2015, MNRAS, 450, 2631

McClelland C. M., Garnavich P. M., Milne P. A., Shappee B. J., Pogge R. W., 2013, ApJ, 767, 119

Milne P. A., The L.-S., Leising M. D., 2001, ApJ, 559, 1019

Mohamed S., Booth R., Podsiadlowski P., 2013, in 18th European White Dwarf Workshop.. p. 323

Moore K., Bildsten L., 2012, ApJ, 761, 182

Moorwood A., Cuby J.-G., Lidman C., 1998, The Messenger, 91, 9

Munari U., Henden A., Belligoli R., Castellani F., Cherini G., Righetti G. L., Vagnozzi A., 2013, New A, 20, 30

Napiwotzki R., et al., 2007, in Napiwotzki R., Burleigh M. R., eds, Astronomical Society of the Pacific Conference Series Vol. 372, 15th European Workshop on White Dwarfs. p. 387

Nielsen M. T. B., Voss R., Nelemans G., 2012, MNRAS, 426, 2668

Nomoto K., 1982, ApJ, 253, 798

Nomoto K., Iben Jr. I., 1985, ApJ, 297, 531

Nomoto K., Thielemann F.-K., Yokoi K., 1984, ApJ, 286, 644

Nugent P., Phillips M., Baron E., Branch D., Hauschildt P., 1995, ApJ, 455, L147

Nugent P., Kim A., Perlmutter S., 2002, PASP, 114, 803

Nugent P. E., et al., 2011, Nature, 480, 344

Ofek E. O., et al., 2013, Nature, 494, 65

Ofek E. O., et al., 2014, ApJ, 789, 104

Pakmor R., Kromer M., Röpke F. K., Sim S. A., Ruiter A. J., Hillebrandt W., 2010, Nature, 463, 61

Pakmor R., Hachinger S., Röpke F. K., Hillebrandt W., 2011, A&A, 528, A117

Pakmor R., Kromer M., Taubenberger S., Sim S. A., Röpke F. K., Hillebrandt W., 2012, ApJ, 747, L10

Pan Y.-C., et al., 2014, MNRAS, 438, 1391

Pan Y.-C., Sullivan M., Maguire K., Gal-Yam A., Hook I. M., Howell D. A., Nugent P. E., Mazzali P. A., 2015, MNRAS, 446, 354

Parrent J. T., et al., 2012, ApJ, 752, L26

Patat F., et al., 2007, Science, 317, 924

Patat F., et al., 2011a, A&A, 527, A91

Patat F., Chugai N. N., Podsiadlowski P., Mason E., Melo C., Pasquini L., 2011b, A&A, 530, A63

Patat F., et al., 2013a, A&A, 549, A62

Patat F., et al., 2013b, A&A, 549, A62

Pereira R., et al., 2013, A&A, 554, A27

Perets H. B., et al., 2010, Nature, 465, 322

Perlmutter S., et al., 1998, Nature, 391, 51

Perrett K., et al., 2012, AJ, 144, 59

Phillips M. M., 1993, ApJ, 413, L105

Phillips M. M., et al., 1987, PASP, 99, 592

Phillips M. M., Lira P., Suntzeff N. B., Schommer R. A., Hamuy M., Maza J., 1999, AJ, 118, 1766

Phillips M. M., et al., 2013, ApJ, 779, 38

Pinto P. A., Eastman R. G., 2000a, ApJ, 530, 744

Pinto P. A., Eastman R. G., 2000b, ApJ, 530, 757

Rahmer G., Smith R., Velur V., Hale D., Law N., Bui K., Petrie H., Dekany R., 2008, in Ground-based and Airborne Instrumentation for Astronomy II. p. 70144Y, doi:10.1117/12.788086

Rau A., et al., 2009, PASP, 121, 1334

Reindl B., Tammann G. A., Sandage A., Saha A., 2005, ApJ, 624, 532

Richmond M. W., Smith H. A., 2012, Journal of the American Association of Variable Star Observers (JAAVSO), 40, 872

Riess A. G., et al., 1998, AJ, 116, 1009

Rigon L., et al., 2003, MNRAS, 340, 191

Röpke F. K., et al., 2012, ApJ, 750, L19

Ruiter A. J., Belczynski K., Fryer C., 2009, ApJ, 699, 2026

Russell B. R., Immler S., 2012, ApJ, 748, L29

Saio H., Nomoto K., 2004, ApJ, 615, 444

Sako M., et al., 2014, preprint, (arXiv:1401.3317)

Salim S., et al., 2007, ApJS, 173, 267

Salpeter E. E., 1955, ApJ, 121, 161

Savitzky A., Golay M. J. E., 1964, Analytical Chemistry, 36, 1627

Scalzo R., et al., 2012, ApJ, 757, 12

Scalzo R., et al., 2014a, MNRAS, 440, 1498

Scalzo R. A., Ruiter A. J., Sim S. A., 2014b, MNRAS, 445, 2535

Schaefer B. E., 2010, ApJS, 187, 275

Schaefer B. E., 2013, in American Astronomical Society Meeting Abstracts #221. p. 233.06

Schlafly E. F., Finkbeiner D. P., 2011, ApJ, 737, 103

Schlegel D. J., Finkbeiner D. P., Davis M., 1998, ApJ, 500, 525

Schmidt B. P., Kirshner R. P., Leibundgut B., Wells L. A., Porter A. C., Ruiz-Lapuente P., Challis P., Filippenko A. V., 1994, ApJ, 434, L19

Seitenzahl I. R., Townsley D. M., 2017, preprint, (arXiv:1704.00415)

Seitenzahl I. R., Taubenberger S., Sim S. A., 2009, MNRAS, 400, 531

Seitenzahl I. R., et al., 2013, MNRAS, 429, 1156

Seitenzahl I. R., Timmes F. X., Magkotsios G., 2014, ApJ, 792, 10

Shappee B. J., Stanek K. Z., 2011, ApJ, 733, 124

Shappee B. J., Stanek K. Z., Pogge R. W., Garnavich P. M., 2013, ApJ, 762, L5

Shappee B., et al., 2014, in American Astronomical Society Meeting Abstracts #223. p. 236.03

Shappee B. J., Stanek K. Z., Kochanek C. S., Garnavich P. M., 2016, preprint, (arXiv:1608.01155)

Shen K. J., Bildsten L., 2014, ApJ, 785, 61

Shen K. J., Bildsten L., Kasen D., Quataert E., 2012, ApJ, 748, 35

Shen K. J., Guillochon J., Foley R. J., 2013, ApJ, 770, L35

Siegert T., Diehl R., Khachatryan G., Krause M. G. H., Guglielmetti F., Greiner J., Strong A. W., Zhang X., 2016, A&A, 586, A84

Silverman J. M., et al., 2013a, ApJS, 207, 3

Silverman J. M., et al., 2013b, ApJ, 772, 125

Sim S. A., Röpke F. K., Hillebrandt W., Kromer M., Pakmor R., Fink M., Ruiter A. J., Seitenzahl I. R., 2010, ApJ, 714, L52

Simon J. D., et al., 2009, ApJ, 702, 1157

Smartt S. J., et al., 2015, A&A, 579, A40

Smith A. M., et al., 2011, MNRAS, 412, 1309

Smith M., et al., 2012, ApJ, 755, 61

Smith M., et al., 2014a, The Astronomer's Telegram, 6739, 1

Smith R. M., et al., 2014b, in Ground-based and Airborne Instrumentation for Astronomy V. p. 914779, doi:10.1117/12.2070014

Sollerman J., et al., 2004, A&A, 428, 555

Stern D., et al., 2004, ApJ, 612, 690

Sternberg A., et al., 2011, Science, 333, 856

Strauss M. A., et al., 2002, AJ, 124, 1810

Stritzinger M., Sollerman J., 2007, A&A, 470, L1

Stritzinger M., et al., 2002, AJ, 124, 2100

Strotjohann N. L., et al., 2015, ApJ, 811, 117

Sullivan M., et al., 2006, ApJ, 648, 868

Sullivan M., et al., 2010, MNRAS, 406, 782

Taubenberger S., 2017, preprint, (arXiv:1703.00528)

Taubenberger S., et al., 2015, MNRAS, 448, L48

Tonry J. L., 2011, PASP, 123, 58

Tripp R., 1998, A&A, 331, 815

Tsvetkov D. Y., Shugarov S. Y., Volkov I. M., Goranskij V. P., Pavlyuk N. N., Katysheva N. A., Barsukova E. A., Valeev A. F., 2013, Contributions of the Astronomical Observatory Skalnate Pleso, 43, 94

Turatto M., 2003, in Weiler K., ed., Lecture Notes in Physics, Berlin Springer Verlag Vol. 598, Supernovae and Gamma-Ray Bursters. pp 21–36 (arXiv:astro-ph/0301107), doi:10.1007/3-540-45863-8_3

Turatto M., et al., 2000, ApJ, 534, L57

Tutukov A., Yungelson L., 1996, MNRAS, 280, 1035

Vernet J., et al., 2011, A&A, 536, A105

Vink J., 2012, A&A Rev., 20, 49

Wang B., Han Z., 2012a, New A Rev., 56, 122

Wang B., Han Z., 2012b, New A Rev., 56, 122

Wang X., et al., 2009a, ApJ, 697, 380

Wang X., et al., 2009b, ApJ, 699, L139

Wang X., et al., 2012, ApJ, 749, 126

Whalen D. J., Fryer C. L., Holz D. E., Heger A., Woosley S. E., Stiavelli M., Even W., Frey L. H., 2013, ApJ, 762, L6

Wheeler J. C., 2012, ApJ, 758, 123

Wheeler J. C., Hansen C. J., 1971, APSS, 11, 373

Whelan J., Iben Jr. I., 1973, ApJ, 186, 1007

Winkler C., et al., 2003, A&A, 411, L1

Woosley S. E., Weaver T. A., 1994, ApJ, 423, 371

Yang Y., et al., 2017, preprint, (arXiv:1704.01431)

Yaron O., Gal-Yam A., 2012, PASP, 124, 668

York D. G., et al., 2000, AJ, 120, 1579

Zhang K., et al., 2016, preprint, (arXiv:1602.02951)

della Valle M., Livio M., 1996, ApJ, 473, 240

van Dokkum P. G., 2001, PASP, 113, 1420

van den Heuvel E. P. J., Bhattacharya D., Nomoto K., Rappaport S. A., 1992, A&A, 262, 97